# Beyond the Standard Model : phenomenology and LHC constraints of exotic dark matter

Gaël Alguero

THÈSE

Pour obtenir le grade de

**DOCTEUR DE L'UNIVERSITÉ GRENOBLE ALPES**

École doctorale : PHYS - Physique
Spécialité : Physique Théorique
Unité de recherche : Laboratoire de Physique Subatomique et Cosmologie

# Au-delà du modèle standard : phénoménologie de matière noire exotique et contraintes du LHC

# Beyond the Standard Model: phenomenology and LHC constraints of exotic dark matter


Présentée par :

**Gaël ALGUERO**

Direction de thèse :

**Sabine KRAML** — Directrice de thèse
DIRECTRICE DE RECHERCHE, Université Grenoble Alpes

**Geneviève BELANGER** — Co-directrice de thèse
Université de Savoie Mont-Blanc

Rapporteurs :

**FARVAH NAZILA MAHMOUDI**
Maître de conférences HDR, UNIVERSITE LYON 1 - CLAUDE BERNARD

**TILMAN PLEHN**
Professeur, Universität Heidelberg


Thèse soutenue publiquement le **2 décembre 2022**, devant le jury composé de :

| | |
|---|---|
| **FARVAH NAZILA MAHMOUDI**<br>Maître de conférences HDR, UNIVERSITE LYON 1 - CLAUDE BERNARD | Rapporteure |
| **TILMAN PLEHN**<br>Professeur, Universität Heidelberg | Rapporteur |
| **ANDREAS GOUDELIS**<br>Chargé de recherche, CNRS DELEGATION RHONE AUVERGNE | Examinateur |
| **ANA MARGARIDA TEIXEIRA**<br>Directeur de recherche, CNRS DELEGATION RHONE AUVERGNE | Examinatrice |
| **BJÖRN HERRMANN**<br>Maître de conférences HDR, UNIVERSITE CHAMBERY | Examinateur |
| **JOHANN COLLOT**<br>Professeur des Universités, UNIVERSITE GRENOBLE ALPES | Président |

# Acknowledgements

I would like to thank, first of all, Sabine Kraml and Geneviève Bélanger for accepting to supervise this thesis. Many reasons lead me to choose not to pursue a career in research, although it was my initial plan, and it was a big choice. I would like to insist on the fact that, among all the reasons, none are related to you, it is all just me. You were perfect guides, showing me ways and ideas to explore, but I can't explain how I couldn't seem to fit into the world of research. I am able at solving small problems, but I think research is about big problems and this is so overwhelming. Regardless, I enjoyed most of it and that is why it was such a big choice to quit research. I am also very grateful for the introduction to multi-pitch climbing and ski mountaineering, and all the hiking.

Humberto was one of the first to welcome me to the lab and introduced me to so many tools that I can not thank him enough! He shared a keen interest in the mountains with some of us here, and there are some hikes in the snow of the Chartreuse I will probably never forget. Mohammad was my first office mate, and I hope that we will keep being friends out of the office! We were office mates with Tim over the last year of my PhD but Tim you're one of my best friends.

Thanks a ton to all the SModelS collaborators: André, Wolfgang, Humberto, Jan. Particular thanks to Wolfgang and Jan who welcomed me in their home labs in Austria and Germany. You both learned me a lot in your field of expertise and made me gain precious time.

Thanks to all the people with whom I shared some precious time and who made my days at the lab so much better: Nathan, Maxime, Alexandre, Robin, Victor, Mirén, Hoa, Loan, and Cyprien. I will especially remember the card games and tennis table matches.

I will finally thank all the people making my life so much better. It is needless to say how much I care about those long-going relationships with family and friends, as I consider them one of the most precious things in life.

# Contents

# Chapter 1

# Introduction

In trying to describe our universe and the laws of nature, the great thinkers have come up with the craziest ideas as it seems intuition was not enough. Who could have guessed the strange behavior of quantum particles or that space-time is curved? These are only a few examples among so many strange, counterintuitive laws that nature chose to rule our universe. Leucippus of Miletus is considered the one who originated the atomic philosophy two thousand years ago, even though his student Democritus is the famous one. Tenants of this dogma thought the building blocks of matter were indivisible, solid, incompressible, and appeared in many shapes and sizes, the latter determining the properties of matter [1]. Democritus later named it "atomos", or "indivisible". More than two thousand years later, experiments and scientific deduction slowly led to our modern knowledge. We are indeed made of atoms, but they are not the elementary block of matter. It is only in the nineteenth century that Chemist John Dalton is believed to be the first to show evidence for the existence of atoms, by experimenting with gases and compounds around 1800. The components of the atom and the other fundamental particles were discovered, one after another, all along the twentieth century, electrons, nuclei, protons, neutrons, neutrinos, ...

The Higgs boson was discovered at the Large Hadron Collider (LHC) in 2012 [2, 3]. This was the last missing piece of our modern theory of Particle Physics: the Standard Model (SM). In 1964, three groups simultaneously proposed a symmetry-breaking mechanism to explain the mass of fundamental particles [4, 5, 6]. Among the three papers, one had only one author, Peter Higgs, and in the following years, physicists started to refer to this mechanism as the Higgs mechanism. The mechanism implied the existence of a new boson particle, the Higgs boson. It explained fruitfully the masses of gauge bosons and enabled to parametrize other particle masses. Nonetheless, the existence of the Higgs boson was proven only fifty years later. The Higgs breakthrough only confirmed the compelling perfection of the SM. Indeed, many experimental measurements are very close to the SM predictions. Despite this descriptive success, the SM always had conceptual caveats, such as the hierarchy problem, the absence of dark matter (DM), the impossibility to describe the gravitational force, and other open questions that will be discussed in section 2.2.1. Moreover, several measurements have revealed potential deviations with the SM predictions, like the anomalous magnetic moment of the muon, which is a long-standing problem, or like B-meson anomalies. Such missing blocks of comprehension are hints that the SM is incomplete.

Both experimentalists and theoreticians are conjugating their effort to explore beyond the limits of the SM and answer these open questions. On the one hand, many beyond the Standard Model (BSM) theories have been proposed. The concept of supersymmetry (SUSY) was invented around fifty years ago and has been the origin of many theoretical propositions over the years. SUSY extends the SM by assuming that every particle is associated with a "superpartner", while all particle and their superpartners differ by a half unit of spin. Supersymmetric theories are so compelling because they can explain most of the caveats of the SM. In addition, several BSM models have been proposed to solve one or more specific problems, for example, axions for the strong CP problem, see-saw models for neutrino masses, and new stable particles as DM candidates.

On the experimental side, a variety of experiments are looking for physics beyond the standard model, precision measurements like the muon $g-2$, DM searches, and large collider experiments. Collider experiments are searching for specific final state signatures that could reveal the existence of new physics. For example, the Higgs mechanism predicted the existence of a new particle. Theoretical studies lead physicists to think that, if Higgses could be produced at the LHC, they would partly disintegrate at a tiny rate into photon pairs. Other processes were known to produce photon pairs, but with sufficiently low rates so that a deviation, or resonance, would be observed when the invariant mass of the double photon system matched the Higgs mass. Data was accumulated between 2010 and early 2012 and an excess was observed in late 2011. A $5\sigma$ deviation was finally announced on 4 July 2012 and was confirmed to be the Higgs boson. Experimentalists rely on theoretically motivated scenarios to find significant signatures to look for at the LHC. As mentioned previously, BSM theories are designed to address conceptual caveats but also experimental deviations. The interplay between experimental and theoretical physics is therefore crucial.

The interpretation of multi-petabytes of experimental data from the LHC represents a huge effort. It can be done by statistically comparing the SM predictions with the experimental observations and looking for any deviations. One can also use the prediction from a given BSM scenario and compare them with the experimental data. However, given the number of experimental searches together with the number of BSM models, it is needless to say that experimentalists can not compare all experimental signals with every BSM models. The concept of simplified models was introduced at the LHC to interpret a large number of signatures in a generalized fashion, by extending the SM with only two or three new BSM particles.

Simplified models have been used extensively in the last decade to characterize potential new physics signals at the LHC. Such results can be reused, or reinterpreted, in other contexts, with similar particles as those of the simplified models. Reinterpreting the LHC results is crucial to get the most out of the experimental data, but it is not an easy task. Two methods will be discussed in section 3.2. The first one is based on the full simulation of particle collision events. The other one consists in reusing directly the simplified model results published by the experiments since they have already simulated the simplified model predictions. Several public tools allow computing the LHC constraints on your favorite model. Such constraints are computed using statistical methods that are particular cases of statistical hypothesis testing and will be described in section 3.3.

Most searches are cut-based analyses, *i.e.* the measured number of events are divided into bins, or so-called signal regions (SRs), aimed to be sensitive to a given scenario

(a small mass splitting for example). To use the sensitivity of the search to its full potential, non-overlapping SRs are statistically combined. However, it is not possible to perform an SR combination if the required information is not shared by the experimental collaboration. CMS sometimes provides covariance matrices to describe the correlations between SRs, which can be used to construct an approximate (simplified) likelihood. ATLAS more recently started to publish full likelihoods, in principle allowing the full reproduction of their results. Chapter 4 discusses the implementation of both methods in MadAnalysis5 while chapter 5 describes the development of an interface for ATLAS full likelihoods in SModelS.

The first potential signals of new physics that were searched at the LHC only involved prompt BSM particles. The absence of discovery and the many constraints on such hypotheses led physicists to pursue new possibilities. A recent subject of interest at the LHC is the search for long-lived particles (LLPs). They are both theoretically and experimentally motivated. Indeed, large lifetimes naturally appear in some parameter regions. For example, well-known theories can present LLPs for small mass splittings and/or small couplings. At the LHC, long-lived particles could produce recognizable signatures, such as displaced vertices, charged tracks, disappearing tracks, etc. Constraints from such LLP searches will be used in chapters 6 and 7. Dark matter models with LLPs often imply specific mechanisms to produce the DM relic. The standard picture for DM production is the freeze-out mechanism. The freeze-in mechanism is an alternative mechanism relevant the DM coupling is tiny. An in-between DM mechanism called the coscattering, which is an exception to the freeze-out calculation will be discussed in chapter 7. Chapter 8 contains a summary and conclusions.

Appendices A and B discuss additional material for chapters 6 and 7, respectively. Finally, a detailed French summary of this manuscript is available in Appendix C.

# Chapter 2

# The Standard Model and beyond

## 2.1 The Standard Model of Particle Physics

The twentieth century knew a succession of numerous breakthroughs in the world of particle physics. It leads us to identify the fundamental constituents of matter shown in table 2.1 and the laws describing their behaviors, all gathered in the Standard Model (SM) of particle physics. The SM describes the indivisible bits of matter: the fundamental,

| Names | Symbol | $SU(3)$, $SU(2)$, $U(1)_Y$ |
|---|---|---|
| **Quarks** | | |
| ($\times 3$) | $Q_i = (u_{Li}, d_{Li})^T$ | $(\mathbf{3}, \mathbf{2}, 1/6)$ |
| | $u_{Ri}$ | $(\mathbf{3}, \mathbf{1}, 2/3)$ |
| | $d_{Ri}$ | $(\mathbf{3}, \mathbf{1}, -1/3)$ |
| **Leptons** | | |
| ($\times 3$) | $L_i = (\nu_{eLi}, e_{Li})^T$ | $(\mathbf{1}, \mathbf{2}, -1/2)$ |
| | $e_{Ri}$ | $(\mathbf{1}, \mathbf{1}, 1)$ |
| **Bosons** | | |
| Higgs | $H = (h^+, h^0)^T$ | $(\mathbf{1}, \mathbf{2}, 1/2)$ |
| Gluons | $G^a$ | $(\mathbf{8}, \mathbf{1}, 0)$ |
| $W$ boson | $(W^1\ W^2\ W^3)^T$ | $(\mathbf{1}, \mathbf{3}, 0)$ |
| $B$ boson | $B$ | $(\mathbf{1}, \mathbf{1}, 0)$ |

Table 2.1: Elementary particles of the SM.

or elementary particles. The fundamental forces, or interactions, describe how particles group together to form larger matter constituents. Let us describe this paradigm by starting with the atoms, which are themselves components of larger molecules, and then plunge into the infinitesimally small. Atoms are made of a positively charged nucleus surrounded by negatively charged electrons. As described by the "planetary" model of the atom by Thomson, electrons were thought to be orbiting around the nucleus because of the electromagnetic force, similar to the planets around the sun. However, the laws of quantum mechanics revealed particles are not point-like particles but rather waves

that are spread in space-time. We hence think about an electronic "cloud" rather than orbiting particles. In the SM paradigm, electrons are part of the family of leptons along with the charged muon, the charged tau, and three neutrinos. The charged leptons all have the same properties except for their mass and the neutrinos are neutral and have very tiny masses that have not been measured precisely yet. In the SM, leptons are indivisible elementary particles. However, the positively charged nuclei have two levels of compositeness. They are made of protons and neutrons, which are held together in the nucleus by the weak force. The latter protons and neutrons are made of quarks, that are held together by the strong force. The up and down quarks are the fundamental constituents of the protons and neutrons but, similarly to leptons, quarks appear in three families by pair, adding up to a total of six quarks: up, down, charm, strange, top, and bottom, each having different masses. Quarks and leptons are the matter constituents grouped in the family of fermions. The three forces mentioned above are carried by gauge bosons, each boson being associated with its symmetry. These forces are mathematically described by the unification of three symmetries $SU(3)$, $SU(2)$ and $U(1)_Y$. The $SU(3)$ symmetry describes the strong force, while $SU(2)$ and $U(1)$ are broken through the Higgs mechanism to describe a unification of the electromagnetic and weak forces. The latter are gauge symmetries, making the SM a gauge theory. Indeed, the construction of the whole model is based on the symmetries and the mathematical terms they imply in the SM Lagrangian. The last building block of the SM is the Higgs boson, which describes the masses of other fundamental particles through the electroweak symmetry breaking (EWSB) mechanism.

The Lagrangian of the SM can be split into four terms

$$\mathcal{L}_{\text{SM}} = \mathcal{L}_{\text{gauge}} + \mathcal{L}_{\text{fermions}} + \mathcal{L}_{\text{Higgs}} + \mathcal{L}_{\text{Yukawa}}\,, \tag{2.1}$$

The gauge term describes the interactions of the bosons carriers of the fundamental forces (represented by the gauge fields $G^\mu$, $W^\mu$, and $B^\mu$). The fermion term describes the interaction between fermions but also the interaction between fermions and bosons that appear when developing the covariant derivative $D_\mu$. The Higgs term describes how the Higgs interacts with other bosons but also encapsulates the Higgs mechanism in the Higgs potential $V(H)$. Finally, the Yukawa term describes the interaction between fermions and the Higgs, from which arise the fermion masses. These terms can be written as follows

$$\mathcal{L}_{\text{gauge}} = -\frac{1}{4}G^a_{\mu\nu}G_a^{\mu\nu} - \frac{1}{4}W^a_{\mu\nu}W_a^{\mu\nu} - \frac{1}{4}B_{\mu\nu}B^{\mu\nu} \tag{2.2}$$

$$\mathcal{L}_{\text{fermions}} = i\bar{\chi}\gamma^\mu D_\mu \chi \tag{2.3}$$

$$\mathcal{L}_{\text{Higgs}} = (D_\mu H)^\dagger (D^\mu H) - V(H) \tag{2.4}$$

$$\mathcal{L}_{\text{Yukawa}} = y_e^{ij}\ \bar{L}_i\ H\ e_{Rj} + y_u^{ij}\ \bar{Q}_i\ \tilde{H}\ u_{Rj} + y_d^{ij}\ \bar{Q}_i\ H\ d_{Rj} + h.c.\,, \tag{2.5}$$

where the general expression for the covariant derivative is

$$D_\mu = \partial_\mu - ig_s\frac{\lambda_a}{2}G^a_\mu - ig\frac{\sigma_j}{2}W^j_\mu - ig'Y B_\mu\,, \tag{2.6}$$

with $a = 1..8$ and $i = 1..3$. However, the derivative depends on the particle quantum numbers. For example, left-handed (LH) leptons, being $SU(3)$ and $SU(2)$ singlets, do

not interact either with gluons or $W$ bosons, therefore their covariant derivative is only $D_\mu = \partial_\mu - ig'YB_\mu$. The Higgs potential is defined by two parameters $\mu$ and $\lambda$ as follows

$$V(H) = \mu^2 H^\dagger H + \lambda (H^\dagger H)^2 \,. \tag{2.7}$$

Figure 2.1 illustrates the shape of this potential by considering a single complex scalar field $\phi$ with $\mu^2 < 0$ and $\lambda > 0$. One can see that $|\phi|^2 = 0$ is a local maximum and there

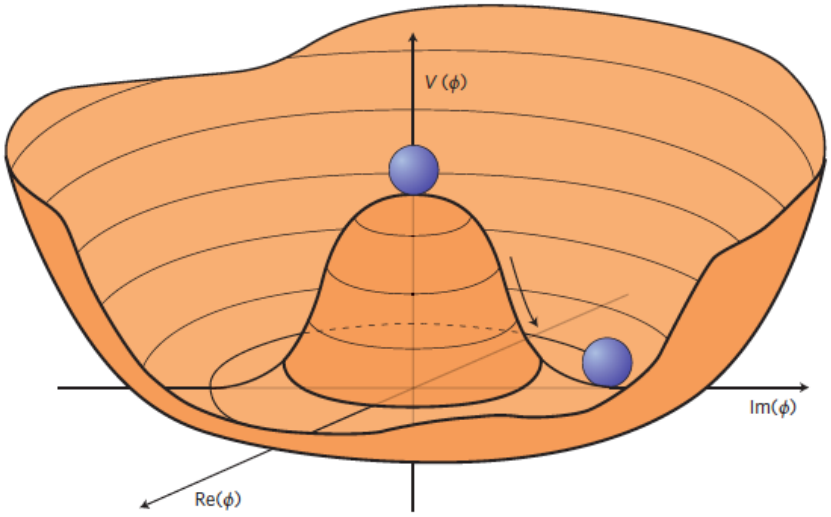


Figure 2.1: The famous "sombrero" potential from [7]

is a non-zero minimum at $|\phi|^2 = -\mu^2/(2\lambda)$. In the SM, the Higgs is a $SU(2)$ doublet $H = (\phi_1, \phi_2)^T/\sqrt{2}$ where $\phi_{1,2}$ are complex scalars. Then the Higgs doublet has the same minimum as in the single complex scalar case since $|H|^2 = (|\phi_1|^2 + |\phi_2|^2)/2$. The non-zero ground value of the Higgs fields breaks the $SU(2) \times U(1)$ electroweak symmetry into a $U(1)$ symmetry of electromagnetism. The vacuum expectation value of the Higgs is defined by the following

$$\langle H \rangle = \begin{pmatrix} 0 \\ \frac{v}{\sqrt{2}} \end{pmatrix} \text{ with } v^2 = -\frac{\mu^2}{\lambda} = (246 \text{ GeV})^2 \,, \tag{2.8}$$

where we write the Higgs as fluctuations around the minimum

$$H = \frac{1}{\sqrt{2}} \begin{pmatrix} h_1 + ih_2 \\ (v + h) + ih_3 \end{pmatrix} . \tag{2.9}$$

Among the four degrees of freedom of the complex scalar doublet, three are "absorbed" to give masses to the $W^\pm$ and $Z$ bosons

$$m_W^2 = \frac{1}{4} g^2 v^2, \quad m_Z^2 = \frac{1}{4}(g'^2 + g^2) v^2 \,. \tag{2.10}$$

The remaining degree of freedom $h$ is the physical Higgs. The quark and lepton masses, on the other hand, stem from the Yukawa terms in eq. (2.5)

$$m_e = \frac{v}{\sqrt{2}} y_e, \quad m_u = \frac{v}{\sqrt{2}} y_u, \quad m_d = \frac{v}{\sqrt{2}} y_d \,, \tag{2.11}$$

where $y_e$, $y_u$, and $y_d$ are the diagonalized Yukawa couplings. It is important to note that for quarks, the coupling matrices are not diagonal. Therefore the quark mixing matrices are the unitary matrices $V_u$ and $V_d$ that diagonalize the mass matrices $(v/\sqrt{2})y_u^{ij}$ and $(v/\sqrt{2})y_d^{ij}$. This defines the Cabbibo-Kobayashi-Maskawa (CKM) matrix $V_{\text{CKM}} = V_u V_d^\dagger$.

## 2.2 Extending the Standard Model

### 2.2.1 Motivations

Over the years, many experiments have confirmed the numerical predictions of the SM with high precision, see for example [8, 9, 10]. However, many conceptual caveats lead physicists to think that the SM is incomplete.

**Neutrinos** From the last section, it is worth noticing that neutrinos are massless in the SM. However, experiments have shown that neutrinos are massive by measuring neutrino oscillations [11, 12, 13]. Only LH neutrinos interact with the weak force, and right-handed (RH) neutrinos do not interact with other SM particles at all. Neutrinos could be Dirac particles like other SM particles but that would imply unnatural small masses, given the experimental constraints on neutrino masses. They could also be Majorana particles, allowing a more natural description through a see-saw mechanism. Deciphering the Majorana or Dirac nature of neutrinos is crucial since it would reveal if neutrinos are their own anti-particle or not. Both measuring precisely their mass and finding the mechanism that generates them are hot topics.

**The hierarchy problem** There is a large discrepancy between the weak energy scale and the gravity energy scale. This discrepancy has consequences in particle physics because the SM is a perturbative theory. This perturbativity stems from the quantum field theory (QFT) nature of the SM. Indeed, in QFT, computing the cross section for a process implies developing all possible contributions including loop contributions that appear at higher order. In loops, virtual particles do not appear in the external states as shown in figure 2.2. In such computation, the loop particle has its momentum integrated over

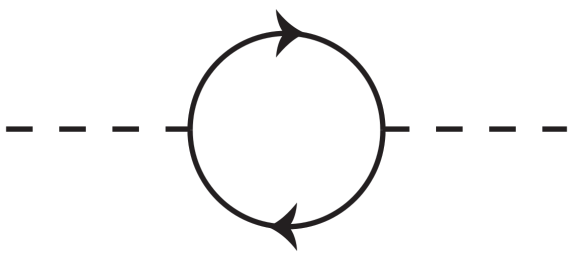

Figure 2.2: Feynman diagram of a one-loop process

all possible momenta. However, the space of possible momenta depends on the range of validity of the SM. The cut-off scale often denoted as $\Lambda_{\text{SM}}$, is defined as the scale where new physics would set in.

$\Lambda_{\text{SM}}$ is often assumed to be a high cut-off scale $\Lambda_{\text{SM}} \approx M_{\text{Planck}}$, or in other words, the SM is assumed to be valid up to the Planck scale. Loop corrections also appear in the computation of physical observables. The hierarchy problem became famous because the loop corrections on the Higgs mass are very important. For instance, the loop contribution to the Higgs mass due to a fermion is

$$\Delta m_H^2 = \frac{y_f^2}{8\pi^2}\Lambda_{\text{SM}}^2 \,. \tag{2.12}$$

Contributions from bosons are very similar except that they are negative. Overall, summing all contributions from the SM particles leads to a positive loop correction proportional to $\Lambda_{\text{SM}}^2$. Other loop contributions will come from hypothetical BSM particles, which means the "right" BSM theory will have its parameters fine-tuned to cancel the SM and get the Higgs mass to match its observed value. This is the main reason why the hierarchy problem became so important. The large discrepancy between the weak and the gravity scale can be arguably only conceptual but the consequence on the Higgs mass and the need to fine-tune is the real problem.

**The strong CP problem** In the quantum chromodynamics (QCD) sector of the SM, a term of the form $\theta_{\text{QCD}} G_{\mu\nu}\tilde{G}^{\mu\nu}$ that breaks the CP symmetry, naturally arises. However, no process bringing evidence for the presence of CP breaking was observed. For example, the electric dipole moment of the neutron is related to $\theta_{\text{QCD}}$ and the absence of such dipole moment constrains $\theta_{\text{QCD}}$ to be smaller than $10^{-10}$. This CP-breaking term could be canceled with a negative counterpart because such a term is authorized by the SM symmetries. However, that would mean this counterpart should be fine-tuned to exactly cancel the CP breaking term. The famous Peccei-Quinn theory [14, 15] is a well-known mechanism that could solve this problem and would imply the presence of a new particle called the axion.

**Grand unification** The Weinberg-Salam-Glashow theory unifying the electromagnetic and weak forces awarded the three physicists the Nobel Prize in Physics in 1979. Pursuing the dream of a Theory of everything, the problem of unifying all forces of nature has always been a matter of interest for particle physicists. Some consider the electroweak description as not being a true unification of the electromagnetic and the weak forces since both have their own gauge couplings. Moreover, the $U(1)$ symmetry of the hypercharge has an arbitrary coupling that does not explain why protons and electrons have exactly opposite charges. The first smallest symmetries encapsulating all the symmetries of the SM were found to be an $SU(5)$ or an $SO(10)$ gauge group. However, in extensions of the standard model featuring a larger symmetry group or new symmetries such as supersymmetry, couplings can unify at a high scale, see figure 2.3 for the case of supersymmetry.

**The muon $g-2$** The discrepancy between the experimentally measured value of the magnetic moment of the muon and its SM prediction has been a long-standing problem. The magnetic moment of a particle depends on its spin $\vec{S}$ as follows

$$\vec{\mu} = g\frac{q}{2m}\vec{S}\,, \tag{2.13}$$

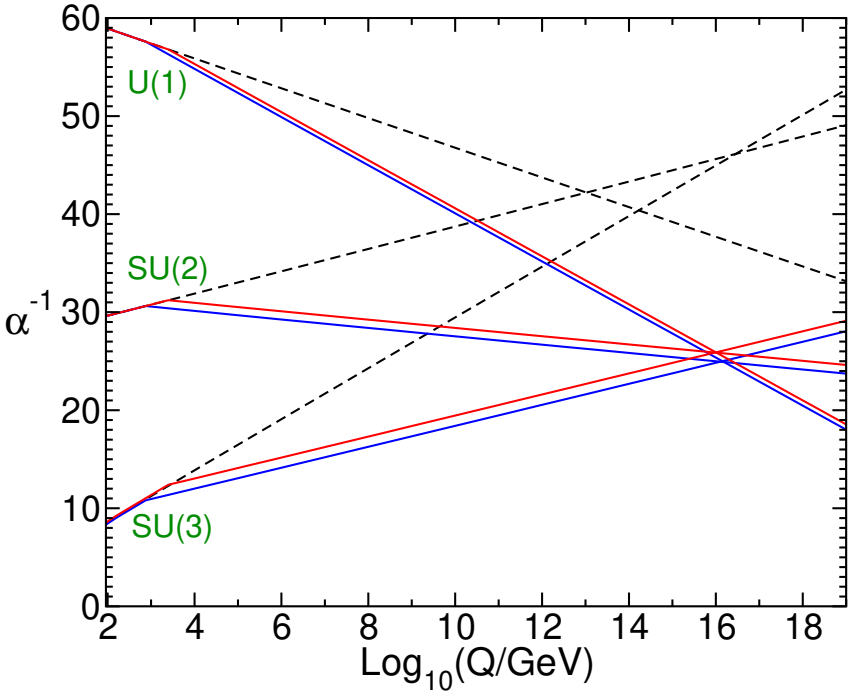


Figure 2.3: Two-loop renormalization group evolution of the SM gauge couplings from [16]. Dashed curves show the evolution of SM couplings while the continuous red and blue curves show such evolution in two cases of the MSSM.

where $q$ and $m$ denote the electric charge and the mass of the particle. $g$ is the gyromagnetic ratio and was predicted to be $g = 2$ for any half-spin elementary particle by Dirac in 1928 [17]. However, $g = 2$ appears to be only the tree-level value and $g$ receives contributions from radiative corrections. The first-order correction from quantum electrodynamics (QED) is exactly $\alpha/\pi$ [18] but higher orders are required for a precise prediction. The fractional deviation from $g_l = 2$ for a lepton $l = e, \mu, \pi$ is often used to characterize the magnetic anomaly

$$a_l = (g_l - 2)/2\,. \tag{2.14}$$

Measurements for the electron have been performed and $a_e \sim 1.159 \times 10^{-3}$ was found. However, the theoretical prediction for $a_e$ is sensitive to the experimentally measured value of the fine structure constant $\alpha$. The fine structure constant has been measured with several methods which give different results. The different SM predictions for $a_e$ give negative and positive tensions with the experimental value, depending on the experimental value of $\alpha$ that is used. Thus a clear deviation can not be confirmed.

The larger mass of the muon implies several properties which make the magnetic moment of the muon more interesting. For example, additional uncertainties make the dependence on $\alpha$ less important for $a_\mu$ than $a_e$ but also the radiative contributions are different and make $a_\mu$ more sensitive to potential BSM physics. After the first measurement of the muon $g - 2$ published in 1957 [19], other measurements always gave results deviating from the SM prediction. Two important results are from the Brookhaven National Laboratory in 2006 [20] and the Fermilab in 2021 [21]. The experimental average result is $a_\mu^{\text{exp}} = 116592061(41) \times 10^{-11}(0.35\text{ ppm})$. Statistically combining the two results gives

a tension of $4.2\sigma$ with the SM prediction, which is $a_\mu^{\rm SM} = 116591810(43) \times 10^{-11}$ [22]. The latter SM prediction includes QED contributions up to the tenth order and electroweak contributions up to the second order. However, the largest uncertainties come from hadronic contributions that are detailed in [22]. The incapability of the SM to predict the gyromagnetic ratio is not only one more caveat of the SM but can also be used to probe new physics. Indeed, it is possible to compute the radiative corrections to $a_\mu$ for a given BSM model and observe if it countervails the discrepancy.

**B-meson anomalies** The principle of lepton universality says that all three generations of leptons ($e$, $\mu$, and $\tau$) should interact identically with other particles. This principle is predicted by the SM. However it has been experimentally observed that in several B mesons decays, muons are less produced than electrons, these are referred to as B mesons anomalies. For example, the decay of a charged B meson into a charged K meson and a lepton-antilepton pair through a virtual $Z$ boson or a photon leads to such observations. In ref. [23], experimentalists of the LHCb measured the ratio

$$R_{K^+} = \frac{\mathrm{BR}(\mathrm{B}^+ \to \mathrm{K}^+\mu^+\mu^-)}{\mathrm{BR}(\mathrm{B}^+ \to \mathrm{K}^+\mathrm{e}^+\mathrm{e}^-)}\,, \tag{2.15}$$

which they found to be $R_{K^+}^{[1.1,6]} = 0.846^{+0..042+0.013}_{-0.039-0.012}$ where the first uncertainty is statistical and the second systematic. This corresponds to a significance of $\sim 2.5\sigma$. Other such measurements lead to ratios different from one for other $B$-mesons, for example, $B^0$ [24]. Measurements will continue and hopefully, confirm that this is not a statistical fluctuation but a hint for new physics.

**Dark matter** Numerous observations of the sky lead physicists to think there might be an unknown kind of matter in our universe, the so-called dark matter (DM). In all those measurements, an anomalous gravitational phenomenon is observed, and a common solution to these anomalies could be the presence of a massive particle, interacting through gravity. Astrophysical observations always reveal gravitational anomalies but nothing is observed through our telescopes. Thus the hypothetical particle would interact gravitationally but not electromagnetically, making it invisible through our standard probes that receive the light from astrophysical objects, hence the appellation of DM. An early hint for DM was the measurement of galaxy rotation curves. In the 1970s, Rubin and Ford studied several galaxies [25], and the stars orbiting around their galaxy center were found to move too fast compared to the visible mass distribution. Such a galaxy rotation curve is shown in Figure 2.4. The black dots with error bars represent the measured rotation speed in km.s$^{-1}$ for about thirty stars, with respect to their radial distance to the galaxy center. The dashed and dotted curves labeled "Disk" and "Gas" show the would-be rotation curves if the mass distribution of the galaxy is assumed to be the visible stars or gases. However, they clearly can not explain the observed speeds. The dot-dashed curve labeled "Halo" shows the contribution from an additional mass distribution that would be necessary to explain the measured data. Other observations such as gravitational lensing and hot gases in galaxy clusters are evidence that galaxies and clusters could be made of 95% of an unknown DM. Another piece of evidence for DM is the cosmic microwave background (CMB). It relies on the fact that, according to the big bang theory, the universe at its debut was very small, dense, and energetic. Such

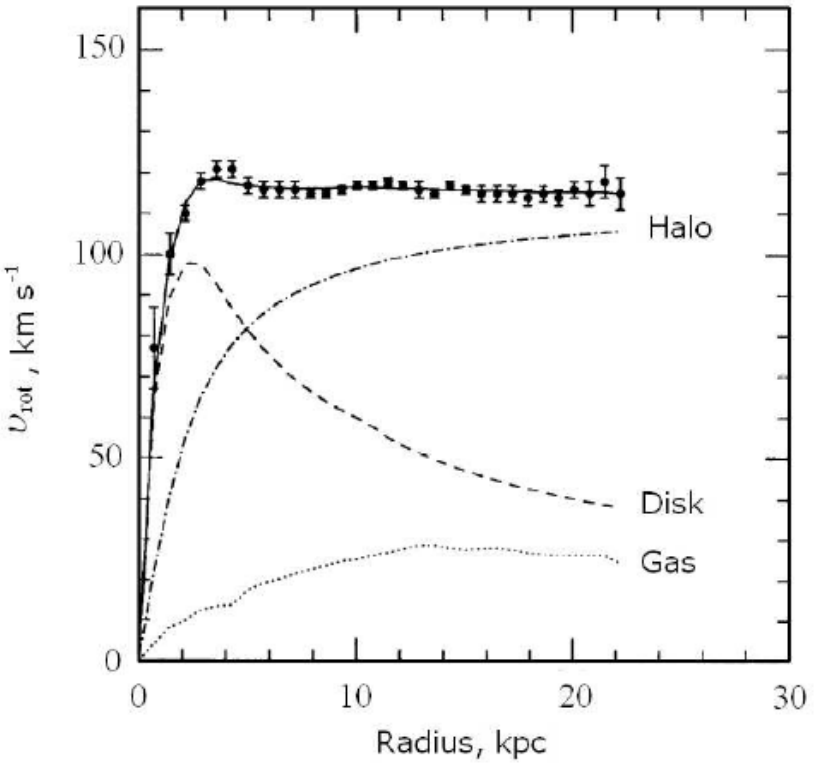


Figure 2.4: Galaxy rotation curve of NGC 6503 from [26]

energy was emitting powerful radiations. While the universe inflated and then expanded, such radiations have dispersed and lost energy. The radiation remnant is a background noise present everywhere in our universe, which is isotropic and with an almost uniform temperature of 2.7K. The CMB was the strongest evidence for the big bang theory and also allowed a very precise measurement of the cosmological parameters by studying the micro-fluctuations of its temperature. The DM density is one of these parameters and has been measured to be $\Omega h^2 = 0.12 \pm 0.0012$ by the PLANCK experiment [27].

A plethora of models propose hypothetical solutions to the DM problem, whether they are designed for DM or designed to solve a more general problem and have a DM candidate as a consequence. The theoretical ideas can be divided into a few broad categories. Popular particle physics candidates are weakly interacting massive particles (WIMPs) and axions (see paragraph about the strong CP problem above). DM could also be astrophysical objects such as massive compact halo objects (MACHOs). The latter regroups faint stars, stellar remnants but also planetary objects. Part of the work in this thesis is devoted to the phenomenology of particle DM candidates. A crucial aspect of DM phenomenology is the DM production mechanism in the early universe. The standard picture is the one of freeze-out that was developed within the WIMP paradigm. The such mechanism relies on the weak interaction of WIMPs with the SM. The typical weak coupling is such that WIMPs would interact with the SM at the early ages when the universe was dense and hot but at lower temperatures and with the expansion, the coupling becomes too small for the WIMP to interact with the SM anymore. In other words, WIMPs "kinematically decouple" from the SM at the "freeze-out temperature". Thermodynamics allows us to

describe the interactions with the SM and, as suggested by the name, the density freezes out when it can not interact anymore, thus giving the current DM relic density. This subject will be discussed more thoroughly in chapter 7, along with other possible mechanisms able to produce the current relic density.

### 2.2.2 The Minimal Supersymmetric Standard Model

As stated above, the concept of supersymmetry (SUSY), famous for its almost miraculous capacity to solve so many of the problems in the SM, has been the subject of many studies. Inspired by the matter-antimatter symmetry stating that every particle has an antiparticle partner with the same mass but opposite charge, physicists came up with the idea that the spin number could undergo a similar symmetry. Conceptually, particles split into two classes, on the one hand, fermions or matter particles with half-integer spins, and on the other hand, bosons with integer spins. Supersymmetry would then associate to each fermion a boson superpartner and to each boson a fermion superpartner. Another way to visualize it is to think about each particle as represented by fermion-boson pairs, like particle-antiparticle pairs. Imposing such a symmetry thus doubles the number of particles and theoretical reasons motivate the need for an additional Higgs doublet (and its fermionic superpartner). It is worth noticing that supersymmetry contains the SM, as it is defined with the same gauge group. Fermion superpartners are denoted sfermions and see their name changed with an s- prefix such as sneutrinos, selectrons, etc. Bosons superpartners are denoted with an -ino suffix, such as Higgsinos, binos, winos, and gluinos. Mathematically, SUSY is described with quantum operators acting on the spin of the particles they are applied to. The motivations for SUSY are numerous. The addition of new particles with opposite spins but the same couplings provides a natural cancellation of the diverging loop contributions to the Higgs mass, which solves the hierarchy problem. As shown in figure 2.3, the running of the three couplings with respect to the energy scale is different than in the SM and allows for a gauge unification around a scale of $10^{16}$ GeV. Adding an $R$-parity (see below) also makes the lightest SUSY particle stable and provides excellent DM candidates such as sneutrinos, winos, or binos. Many models based on supersymmetry have been proposed. Imposing supersymmetry can not be done trivially and involves some additional requirements, adding a Higgs doublet among others. I will introduce only the minimal supersymmetric Standard Model (MSSM), which is a SUSY model with minimal particle content to be a valid theory of particle physics. The field content of the MSSM is shown in table 2.2. A convenient mathematical description is achieved by using superfields that regroup both the fermionic and bosonic components. In the following, superfields will be denoted $\hat{S}$ with a hat and supersymmetric particles will be denoted with a tilde $\tilde{S}$.

**Two Higgs doublets** As stated above, at least two Higgs superfields $\hat{H}_u$ and $\hat{H}_d$ are required within a SUSY framework. This is due to the MSSM Lagrangian involving left-chiral superfields for the fermions, which implies the need for one Higgs for the up-type fermions and another one for the down-type fermions. Moreover, the "gauge anomalies" were canceled in the SM but it is not true anymore with the additional supersymmetric particles. Gauge anomalies coming from loop processes should cancel for the model to be renormalizable and adding a second Higgs allows for this cancellation to be re-established.

| Names | Superfield | Spin 0 | Spin 1/2 | Spin 1 | $SU(3)$, $SU(2)$, $U(1)_Y$ |
|---|---|---|---|---|---|
| **Quarks** | $\hat{Q}$ | $\tilde{Q} = (\tilde{u}_L, \tilde{d}_L)$ | $(u_L, d_L)$ | | (**3**, **2**, 1/6) |
| (×3) | $\hat{u^c}$ | $\tilde{u}^c_R$ | $u^c_R$ | | ($\overline{\mathbf{3}}$, **1**, -2/3) |
| | $\hat{d^c}$ | $\tilde{d}^c_R$ | $d^c_R$ | | ($\overline{\mathbf{3}}$, **1**, 1/3) |
| **Leptons** | $\hat{L}$ | $(\tilde{\nu}_{eL}, \tilde{e}_L)$ | $(\nu_{eL}, e_L)$ | | (**1**, **2**, -1/2) |
| (×3) | $\hat{e^c}$ | $\tilde{e}^c_R$ | $e^c_R$ | | (**1**, **1**, 1) |
| **Bosons** | | | | | |
| Higgs | $\hat{H}_u$ | $(H^+_u, H^0_u)$ | $(\tilde{H}^+_u, \tilde{H}^0_u)$ | | (**1**, **2**, 1/2) |
| | $\hat{H}_d$ | $(H^0_d, H^-_d)$ | $(\tilde{H}^0_d, \tilde{H}^-_d)$ | | (**1**, **2**, -1/2) |
| Gluons | $\hat{G}$ | | $\tilde{g}$ | $g$ | (**8**, **1**, 0) |
| W | $\hat{W}$ | | $\tilde{W}^\pm, \tilde{W}^0$ | $W^\pm, W^0$ | (**1**, **3**, 0) |
| B | $\hat{B}$ | | $\tilde{B}$ | $B$ | (**1**, **1**, 0 ) |

Table 2.2: Field content of the MSSM.

**Soft SUSY breaking** Particles and their antiparticles have the same mass but opposite charges. Likewise, particles and their superpartners should have the same mass but different spins. However, if such new particles existed, they would have been observed since they would be in the accessible energy range of the LHC. Therefore it is necessary to break supersymmetry by introducing additional mass terms for the sfermions and gauginos. Nonetheless, SUSY should be broken only "softly" in order not to fall into the hierarchy problem again. Soft breaking means that the SUSY breaking terms in the Lagrangian must not introduce any quadratic divergences. There exist many possibilities to realize soft SUSY breaking. In the MSSM, no assumption is made about the origin of the soft breaking terms, *i.e.* any possible term that softly breaks SUSY is taken into account, as will be discussed below.

***R*-parity** SUSY allows for baryon ($B$) and lepton number ($L$) violation, meaning the number of ingoing and outgoing leptons and baryons in a process does not always compensate (antiparticles contribute negatively to the lepton and baryon number). Such processes are also allowed in the SM. However, lepton and baryon number violations are experimentally constrained, *e.g.* by the proton lifetime. In the MSSM, such terms can be suppressed by introducing an $R$-parity, defined as

$$R = (-1)^{3B+L+2s}\,, \tag{2.16}$$

which is designed so that all the SM particles and the two Higgs bosons are even ($R = 1$), while their superpartners are odd ($R = -1$). Thus only Lagrangian terms with an even number of supersymmetric particles are allowed, so supersymmetric particles can only appear in pairs in any process. Moreover, this makes the lightest stable particle (LSP) stable since $R$-parity forbids decay into only SM particles. The LSP then has to be electrically and color neutral since such an exotic relic has not been observed in the universe. This is an important point because if the LSP is neutral, it can be a good DM candidate.

Having two Higgs doublets and soft SUSY breaking are the minimal conditions for a supersymmetric theory to be conceivable. With the $R$-parity added for phenomenological reasons, all the blocks of the MSSM are gathered. We can now write the different parts of the MSSM Lagrangian. First, the superpotential is defined by

$$\mathcal{W} = \mu \hat{H}_u \hat{H}_d + \mathbf{y_u} \hat{Q} \hat{H}_u \hat{U}^c + \mathbf{y_d} \hat{Q} \hat{H}_d \hat{D}^c + \mathbf{y_e} \hat{L} \hat{H}_d \hat{E}^c \,, \tag{2.17}$$

where the superfields were defined in Table 2.2 for the first generation. $\mathbf{y_u}$, $\mathbf{y_d}$, and $\mathbf{y_e}$ are $3 \times 3$ matrices acting on the three generations of quarks and leptons. $\mu$ parametrizes the two-Higgs potential. The soft-breaking Lagrangian in its most general form is

$$\begin{aligned} \mathcal{L}_{soft} = & -\frac{1}{2}(M_3 \tilde{g}\tilde{g} + M_2 \tilde{W}\tilde{W} + M_1 \tilde{B}\tilde{B} + h.c.) \\ & + (\mathbf{a_u} \epsilon_{ab} \tilde{Q}^a H_u^b \tilde{u}_R^\dagger + \mathbf{a_d} \tilde{Q} H_d \tilde{d}_R^\dagger - \mathbf{a_e} \tilde{L} H_d \tilde{e}_R^\dagger + h.c.) \\ & - \tilde{Q}^\dagger \mathbf{m_Q^2} \tilde{Q} - \tilde{L}^\dagger \mathbf{m_L^2} \tilde{L} - \tilde{u}_R^\dagger \mathbf{m_U^2} \tilde{u}_R - \tilde{d}_R^\dagger \mathbf{m_D^2} \tilde{d}_R - \tilde{e}_R^\dagger \mathbf{m_E^2} \tilde{e}_R \\ & - m_{H_u}^2 H_u^* H_u - m_{H_d}^2 H_d^* H_d + (b H_u H_d + h.c.) \,, \end{aligned} \tag{2.18}$$

where $M_1$, $M_2$, and $M_3$ are the bino, wino, and gluino mass terms, respectively. The $\mathbf{a_i}$ are the $3\times3$ Yukawa-type couplings and $\mathbf{m_i}$ are the $3\times3$ mass terms of the sfermions. The last line in the above equation is the Higgs potential part of the soft-breaking Lagrangian and $b$ is an important parameter characterizing the stability of the Higgs potential, together with $\mu$ in eq. (2.17). The last piece for the Lagrangian to be complete is the so-called Kähler potential which allows the addition of superfield kinetic terms. Such Kähler terms must be written for all superfields of the MSSM and are not detailed further here.

Once the Lagrangian is written out, electroweak symmetry breaking in the MSSM can then be made explicit and the mass spectrum of the model can be computed. The vacuum expectation values of the two Higgses are defined similarly as in the SM

$$\langle H_u \rangle = \begin{pmatrix} 0 \\ v_u/\sqrt{2} \end{pmatrix} \text{ and } \langle H_u \rangle = \begin{pmatrix} v_u/\sqrt{2} \\ 0 \end{pmatrix} \text{ with } v^2 = v_u^2 + v_d^2 = (246 \text{ GeV})^2 \,, \tag{2.19}$$

from which follows the definition of $\beta$

$$v_u = v \sin\beta, \; v_d = v \cos\beta, \tan\beta = \frac{v_u}{v_d} \,, \tag{2.20}$$

**Gauge bosons** The masses of the $W^\pm$ and $Z$ gauge bosons are defined like in the SM in eq. (2.10) but with $v^2 = v_u^2 + v_d^2$.

**Fermions** Fermion masses are defined in the superpotential 2.17. In SU(2) doublets, the masses of the upper part and the lower part are stemming from $H_u$ and $H_d$. Up-quarks hence depend on $v_u$, and down-quarks and leptons on $v_d$. It is then convenient to express the fermion masses with $v$ and $\beta$ using eq. (2.20)

$$m_u = \frac{v}{\sqrt{2}} y_u \sin\beta, \; m_d = \frac{v}{\sqrt{2}} y_d \cos\beta, \; m_e = \frac{v}{\sqrt{2}} y_e \cos\beta \,. \tag{2.21}$$

**Higgs bosons** In the SM, the single Higgs doublet has four degrees of freedom but only one corresponds to a physical Higgs since the three others are absorbed in the $W^{\pm}$ and $Z$ masses. In the MSSM, the two Higgs doublets represent a total of eight degrees of freedom. With the degrees of freedom absorbed by the gauge bosons, five physical Higgses remain in the MSSM, which are denoted $h$, $A$, $H$, and $H^{\pm}$. Their masses stem from the superpotential and the soft breaking Lagrangian, after applying electroweak symmetry breaking with the two Higgs doublets

$$m_A^2 = b\mu(\cot\beta + \tan\beta), \tag{2.22}$$

$$m_{H^{\pm}}^2 = b\mu(\cot\beta + \tan\beta) + M_W^2 \tag{2.23}$$

$$m_{h,H}^2 = \frac{1}{2}[(m_A^2 + M_Z^2) \mp \sqrt{(m_A^2 + M_Z^2)^2 - 4m_A^2 M_Z^2 \cos^2\beta}]\,. \tag{2.24}$$

**Neutralinos** The two neutral Higgsino components, the neutral wino and the bino have the same quantum numbers and therefore mix into four neutral particles called neutralinos, denoted as $\tilde{\chi}_i^0$. Indeed, their mass terms are mixed into a $4 \times 4$ mass matrix

$$M_{\tilde{\chi}^0} = \begin{pmatrix} M_1 & 0 & -g'v_d/2 & g'v_u/2 \\ 0 & M_2 & gv_d/2 & -gv_u/2 \\ -g'v_d/2 & gv_d/2 & 0 & \mu \\ g'v_u/2 & -gv_u/2 & \mu & 0 \end{pmatrix}. \tag{2.25}$$

The diagonalization of the above matrix defines a mixing matrix $V_n$ allowing to relate the interaction states to the mass eigenstates

$$\begin{pmatrix} \tilde{B} \\ \tilde{W} \\ \tilde{h}_d^0 \\ \tilde{h}_u^0 \end{pmatrix} = V_n \begin{pmatrix} \tilde{\chi}_1^0 \\ \tilde{\chi}_2^0 \\ \tilde{\chi}_3^0 \\ \tilde{\chi}_4^0 \end{pmatrix}. \tag{2.26}$$

**Charginos** Likewise neutralinos, the charged Higgs and the charged winos mix into charginos denoted $\tilde{\chi}_i^{\pm}$. The mass matrix reads

$$M_{\tilde{\chi}^{\pm}} = \begin{pmatrix} M_2 & -gv_d/\sqrt{2} \\ -gv_u/\sqrt{2} & -\mu \end{pmatrix}, \tag{2.27}$$

and upon diagonalization defines two mixing matrices $U_c$ and $V_c$

$$\begin{pmatrix} \tilde{\chi}_1^+ \\ \tilde{\chi}_2^+ \end{pmatrix} = U_c \begin{pmatrix} \tilde{W}^+ \\ \tilde{h}_u^+ \end{pmatrix}, \quad \begin{pmatrix} \tilde{\chi}_1^- \\ \tilde{\chi}_2^- \end{pmatrix} = V_c \begin{pmatrix} \tilde{W}^- \\ \tilde{h}_u^- \end{pmatrix}. \tag{2.28}$$

In such a case, the diagonalization is written as follows

$$V_c^* M_{\tilde{\chi}^{\pm}} U_c^{-1} = \begin{pmatrix} m_{\tilde{\chi}_1^{\pm}} & 0 \\ 0 & m_{\tilde{\chi}_2^{\pm}} \end{pmatrix}. \tag{2.29}$$

**Sfermions** Like for gauginos, sfermions with the same quantum numbers should in principle mix together. In the MSSM, it is assumed that only $SU(2)$ LH doublets and RH singlets of the same generation mix together, meaning there is a $2 \times 2$ mass matrix for each sfermion. However, we will see in the following that the off-diagonal terms are dependent on the mass of the associated fermion, which means they are often considered negligible except for the third generation, *i.e.* for stops, sbottoms, and staus. The stop mass matrix reads

$$M_{\tilde{t}}^2 = \begin{pmatrix} m_{\tilde{t}_L}^2 + m_t^2 + D(\tilde{t}_L) & m_t(-A_t + \mu \cot\beta) \\ m_t(-A_t + \mu \cot\beta) & m_{\tilde{t}_R}^2 + m_t^2 + D(\tilde{t}_R) \end{pmatrix} , \tag{2.30}$$

where in general

$$D = M_Z^2 \cos 2\beta (T_3 - Q \sin^2 \theta_W) . \tag{2.31}$$

The diagonal term has contributions from the superpotential with the SM top mass $m_t^2$, from the soft-breaking Lagrangian with the mass term $m_{\tilde{t}_{L,R}}^2$, and the Yukawa-type term with $D(\tilde{t}_{L,R})$. The off-diagonal terms depend on the SM top mass and $A_t \equiv (\mathbf{a_t}/y_t)$ hence the non-negligible mixing for third-generation sfermions. Finally, the stop mixing is standardly parametrized by a mixing angle $\theta_{\tilde{t}}$

$$\begin{pmatrix} \tilde{t}_1 \\ \tilde{t}_2 \end{pmatrix} = \begin{pmatrix} \cos\theta_{\tilde{t}} & \sin\theta_{\tilde{t}} \\ -\sin\theta_{\tilde{t}} & \cos\theta_{\tilde{t}} \end{pmatrix} \begin{pmatrix} \tilde{t}_L \\ \tilde{t}_R \end{pmatrix} . \tag{2.32}$$

The full MSSM contains more than a hundred free parameters. Nonetheless, it is very convenient, with a few experimentally motivated assumptions, to considerably reduce the number of parameters. A well-known list of assumptions leads to the so-called phenomenological MSSM (pMSSM) :

- new sources of CP violation are discarded,
- sources of flavor-changing neutral currents are discarded,
- first and second generation universality is preserved.

which reduces the huge number of parameters to nineteen :

- the gaugino masses: $M_1$, $M_2$ and $M_3$.
- the first and second-generation sfermion masses: $m_{\tilde{q}}$, $m_{\tilde{u}_R}$, $m_{\tilde{d}_R}$, $m_{\tilde{l}}$ and $m_{\tilde{e}_R}$.
- the third-generation sfermion masses: $m_{\tilde{Q}}$, $m_{\tilde{t}_R}$, $m_{\tilde{b}_R}$, $m_{\tilde{L}}$ and $m_{\tilde{\tau}_R}$.
- the Higgs sector parameters: $\tan\beta$, $M_A$, and $\mu$.
- the third-generation trilinear couplings: $A_t$, $A_b$, and $A_\tau$.

The pMSSM has motivated a lot of searches at the LHC. As will be discussed in section 3.1, the principle of simplified models based on the MSSM has been used at the LHC for a decade and is still the reference to interpret particle physics experiment data.

### 2.2.3 Other extensions of the SM

Supersymmetry has been one of the most promising theoretical propositions over the last fifty years. Despite the huge experimental effort, no supersymmetric particles have been observed and the allowed parameter space has been drastically reduced. However, physicists do not lack imagination and creativity when in need, and a plethora of other models have been and are still being proposed. From simple models with just a few new particles and parameters to more involved models with complicated theoretical structures. This section introduces two such ideas which will be used later in this thesis (see chapters 6 and 7).

#### Singlet-triplet model (Split-SUSY)

This model extends the Standard Model by two electroweak multiplets: a fermionic singlet $\chi$ and a fermionic $\mathrm{SU}(2)_L$ triplet $\psi$, which are both odd under a new $\mathbb{Z}_2$ symmetry, while the SM particles are even. As stated in [28], if we identify the singlet to a bino and the triplet to a wino, then the particle content of this model matches the low energy content of split supersymmetry except for gluinos that are not present in this model. The particularity of this model is the fact that the singlet and the triplet are feebly coupled to each other through a tiny mixing, which makes it phenomenologically interesting for the study of DM production mechanisms involving several dark sectors. This will be particularly relevant for the coscattering study in chapter 7.

Following the notation of [28] with four-component Majorana spinors, the most general Lagrangian for this model is

$$\mathcal{L} = \mathcal{L}_{\mathrm{SM}} + \frac{i}{2}\bar{\chi}\gamma^\mu\partial_\mu\chi + \frac{i}{2}\bar{\psi}\gamma^\mu D_\mu\psi - \frac{1}{2}\left(m\bar{\chi}\chi + M\bar{\psi}\psi\right) + \mathcal{L}_5 + \mathcal{L}_{\geq 6}\,, \tag{2.33}$$

where $\mathcal{L}_5$ contains the dimension-5 operators

$$\mathcal{L}_5 = -\frac{1}{2}\frac{\kappa}{\Lambda}\bar{\psi}\psi H^\dagger H - \frac{1}{2}\frac{\kappa'}{\Lambda}\bar{\chi}\chi H^\dagger H - \frac{\lambda}{\Lambda}\bar{\chi}\psi^a H^\dagger \tau^a H + \text{ h.c.} + \dots\,, \tag{2.34}$$

Here $H$ is the SM Higgs doublet. $\psi$ is written as a column vector $(\psi_1, \psi_2, \psi_3)^T$ with $\psi^\pm = \psi_1 \pm i\psi_2$ and $\psi^0 = \psi_3$. In the following, we will consider $\mathcal{L}_5$ only; dimension-6 and higher operators ($\mathcal{L}_{\geq 6}$) are neglected. Moreover, we take all parameters to be real and choose $M > 0$. Finally, since we are interested in scenarios where the DM is mostly the singlet $\chi$, we assume that $M > |m|$.

After electroweak symmetry breaking and upon replacing the Higgs field with its vacuum expectation value

$$\langle H \rangle = \begin{pmatrix} 0 \\ v \end{pmatrix}, \qquad v = 174\,\mathrm{GeV}\,, \tag{2.35}$$

the first two terms in eq. (2.34) induce a shift in the effective $\chi$ and $\psi$ mass parameters respectively; this can be absorbed through re-definitions of $m \to m + \kappa' v^2/\Lambda$ and $M \to M + \kappa v^2/\Lambda$. The third term induces a mixing between the singlet and the neutral component of the triplet. The respective mass matrix in the basis of the interaction

eigenstates $(\chi, \psi_3)$ is

$$\mathcal{M} = \begin{pmatrix} m & -\lambda v^2/(2\Lambda) \\ -\lambda v^2/(2\Lambda) & M \end{pmatrix} . \tag{2.36}$$

Diagonalising this mass matrix by a unitary $2 \times 2$ matrix $R$, $\mathrm{diag}(m_{\tilde{\chi}}, m_{\tilde{\psi}^0}) = R\mathcal{M}R^\dagger$ gives mass eigenstates

$$\begin{pmatrix} \tilde{\chi} \\ \tilde{\psi}^0 \end{pmatrix} = R \begin{pmatrix} \chi \\ \psi_3 \end{pmatrix}, \quad R = \begin{pmatrix} \cos\theta & -\sin\theta \\ \sin\theta & \cos\theta \end{pmatrix} \tag{2.37}$$

with physical masses

$$m_{\tilde{\chi},\tilde{\psi}^0} = \frac{1}{2}\left(m + M \mp \sqrt{(M-m)^2 + 4a^2}\right), \quad \text{where } a = \lambda v^2/(2\Lambda) . \tag{2.38}$$

The mixing angle is given by

$$\sin 2\theta \sim 2\theta = \frac{2a}{\sqrt{(M-m)^2 + 4a^2}} \quad \to \quad \theta \approx \frac{\lambda v^2}{2\Lambda(M-m)} . \tag{2.39}$$

The $\psi_3$–$\chi$ mixing also lifts the mass degeneracy between the charged and neutral triplet states, which would otherwise be exact at tree level[1].

**Interactions with gauge bosons** The interactions with the gauge bosons are settled by the term $i\psi^\dagger\bar{\sigma}^\mu D_\mu\psi$ in eq. (2.33). This develops as (notice there is no interaction with $B_\mu$ because the hypercharge is zero)

$$\mathcal{L}_{W\psi\psi} = -g\bar{\psi}\bar{\sigma}^\mu W_\mu^a T^a \psi , \tag{2.40}$$

where the generators are in the adjoint representation

$$T^1 = \frac{1}{\sqrt{2}}\begin{pmatrix} 0 & 1 & 0 \\ 1 & 0 & 1 \\ 0 & 1 & 0 \end{pmatrix}, T^2 = \frac{1}{\sqrt{2}}\begin{pmatrix} 0 & -i & 0 \\ i & 0 & -i \\ 0 & i & 0 \end{pmatrix}, T^3 = \begin{pmatrix} 1 & 0 & 0 \\ 0 & 0 & 0 \\ 0 & 0 & -1 \end{pmatrix}, \psi = \begin{pmatrix} -\psi^- \\ \psi^0 \\ \psi^+ \end{pmatrix} . \tag{2.41}$$

As a first step

$$W_\mu^a T^a = \begin{pmatrix} W_\mu^3 & \frac{W_\mu^1 - iW_\mu^2}{\sqrt{2}} & 0 \\ \frac{W_\mu^1 + iW_\mu^2}{\sqrt{2}} & 0 & \frac{W_\mu^1 - iW_\mu^2}{\sqrt{2}} \\ 0 & \frac{W_\mu^1 + iW_\mu^2}{\sqrt{2}} & -W_\mu^3 \end{pmatrix} = \begin{pmatrix} W_\mu^3 & W_\mu^- & 0 \\ W_\mu^+ & 0 & W_\mu^- \\ 0 & W_\mu^+ & -W_\mu^3 \end{pmatrix} , \tag{2.42}$$

which gives

$$\begin{aligned} \mathcal{L}_{W\psi\psi} =& g\bar{\psi}^+\bar{\sigma}^\mu W_\mu^0\psi^- + g\bar{\psi}^-\bar{\sigma}^\mu W_\mu^-\psi^3 && (2.43)\\ & - g\bar{\psi}^3\bar{\sigma}^\mu W_\mu^-\psi^+ + g\bar{\psi}^3\bar{\sigma}^\mu W_\mu^+\psi^- && (2.44)\\ & - g\bar{\psi}^+\bar{\sigma}^\mu W_\mu^+\psi^3 - g\bar{\psi}^-\bar{\sigma}^\mu W_\mu^0\psi^- && (2.45)\\ =& - g\bar{\psi}\gamma^\mu W_\mu^0\psi - \left(g\bar{\psi}^0\bar{\sigma}^\mu W_\mu^+\psi^+ + g\bar{\psi}^0\bar{\sigma}^\mu W_\mu^-\psi^- + \text{h.c.}\right) && (2.46)\\ =& \mathcal{L}_{W^0\psi\psi} + \mathcal{L}_{W^\pm\psi\psi} . && (2.47) \end{aligned}$$

[1]Here and in the following, all odd-sector physical particles are denoted with a tilde.

Developing $\psi^3$ into the eigenstates $\tilde{\psi}^0$ and $\tilde{\chi}$ and $W^0$ into $Z$ and $\gamma$, one gets the Lagrangian for the relevant vertices

$$\mathcal{L}_{\gamma\tilde{\psi}^+\tilde{\psi}^-} = g s_{\mathrm{W}} \bar{\tilde{\psi}}^+ \gamma^\mu A_\mu \tilde{\psi}^+ - g s_{\mathrm{W}} \bar{\tilde{\psi}}^- \gamma^\mu A_\mu \tilde{\psi}^-, \tag{2.48}$$

$$\mathcal{L}_{Z^0\tilde{\psi}^+\tilde{\psi}^-} = g c_{\mathrm{W}} \bar{\tilde{\psi}}^+ \gamma^\mu Z^0_\mu \tilde{\psi}^+ - g c_{\mathrm{W}} \bar{\tilde{\psi}}^- \gamma^\mu Z^0_\mu \tilde{\psi}^- \tag{2.49}$$

$$\mathcal{L}_{W^\pm\tilde{\psi}^\mp\tilde{\chi}} = -g \sin\theta \bar{\tilde{\chi}} \gamma^\mu W^+_\mu \tilde{\psi}^- + g \sin\theta \bar{\tilde{\chi}} \gamma^\mu W^-_\mu \tilde{\psi}^+ + \text{ h.c.} \tag{2.50}$$

$$\mathcal{L}_{W^\pm\tilde{\psi}^\mp\tilde{\psi}^0} = g \cos\theta \bar{\tilde{\psi}}^0 \gamma^\mu W^+_\mu \tilde{\psi}^- - g \cos\theta \bar{\tilde{\psi}}^0 \gamma^\mu W^-_\mu \tilde{\psi}^+ + \text{ h.c.}\,, \tag{2.51}$$

where $s_{\mathrm{W}} = \sin\theta_{\mathrm{W}}$ and $c_{\mathrm{W}} = \cos\theta_{\mathrm{W}}$, with $\theta_{\mathrm{W}}$ being the Weinberg angle. It is worth noticing that the neutral particles do not interact with the $Z$ boson because $\psi$ is a $\mathrm{SU}(2)_L$ triplet with a zero hypercharge.

**Interactions with the Higgs** The interactions with the Higgs come from $\mathcal{L}_5$

$$\frac{\lambda}{\Lambda}\bar{\chi}\psi^3 H^\dagger \tau^3 H + \frac{1}{2}\frac{\kappa}{\Lambda}\bar{\psi}^3\psi^3 H^\dagger H + \frac{1}{2}\frac{\kappa'}{\Lambda}\bar{\chi}\chi H^\dagger H \supset -\frac{\lambda v}{\sqrt{2}\Lambda}\bar{\chi}\psi^3 h + \frac{\kappa' v}{\sqrt{2}\Lambda}\bar{\chi}\chi h + \frac{\kappa v}{\sqrt{2}\Lambda}\bar{\psi}^3\psi^3 h\,. \tag{2.52}$$

Then $\chi$ and $\psi^3$ develop into their eigenstates with the inverse mixing matrix $\chi = \tilde{\chi}\cos\theta + \tilde{\psi}^0\sin\theta$ and $\psi_3 = -\tilde{\chi}\sin\theta + \tilde{\psi}^0\cos\theta$, which gives

$$\frac{v}{\sqrt{2}\Lambda}\Bigg[-\lambda\left(\bar{\tilde{\chi}}\cos\theta + \bar{\tilde{\psi}}^0\sin\theta\right)\left(-\tilde{\chi}\sin\theta + \tilde{\psi}^0\cos\theta\right) \tag{2.53}$$

$$+\kappa'\left(\bar{\tilde{\chi}}\cos\theta + \bar{\tilde{\psi}}^0\sin\theta\right)\left(\tilde{\chi}\cos\theta + \tilde{\psi}^0\sin\theta\right) \tag{2.54}$$

$$+\kappa\left(-\bar{\tilde{\chi}}\sin\theta + \bar{\tilde{\psi}}^0\cos\theta\right)\left(-\tilde{\chi}\sin\theta + \tilde{\psi}^0\cos\theta\right)\Bigg], \tag{2.55}$$

which then becomes

$$\mathcal{L}_{\tilde{\chi}\tilde{\chi}h} = \frac{v}{\sqrt{2}\Lambda}\left(-\frac{\lambda}{2}\sin 2\theta + \kappa\sin^2\theta + \kappa'\cos^2\theta\right)\bar{\tilde{\chi}}\tilde{\chi}h \sim -\frac{\lambda^2 v^3}{2\sqrt{2}\Lambda^2(M-m)}\bar{\tilde{\chi}}\tilde{\chi}h \tag{2.56}$$

$$\mathcal{L}_{\tilde{\psi}^0\tilde{\psi}^0 h} = \frac{v}{\sqrt{2}\Lambda}\left(\frac{\lambda}{2}\sin 2\theta + \kappa\cos^2\theta + \kappa'\sin^2\theta\right)\bar{\tilde{\psi}}^0\tilde{\psi}^0 h \sim \frac{\lambda^2 v^3}{2\sqrt{2}\Lambda^2(M-m)}\bar{\tilde{\psi}}^0\tilde{\psi}^0 h \tag{2.57}$$

$$\mathcal{L}_{\tilde{\chi}\tilde{\psi}^0 h} = \frac{v}{\sqrt{2}\Lambda}\left(\lambda\cos 2\theta - \kappa\sin 2\theta + \kappa'\sin 2\theta\right)\bar{\tilde{\chi}}\tilde{\psi}^0 h \sim \frac{\lambda v}{\sqrt{2}\Lambda}\bar{\tilde{\chi}}\tilde{\psi}^0 h \tag{2.58}$$

$$\mathcal{L}_{\tilde{\psi}^+\tilde{\psi}^- h} = \frac{2\kappa v}{\sqrt{2}\Lambda}\bar{\tilde{\psi}}^-\tilde{\psi}^- h\,. \tag{2.59}$$

The above interactions show that $\tilde{\psi}^\pm$ can decay to both $\tilde{\psi}^0$ and $\tilde{\chi}$ through a virtual $W^\pm$. However, since $\tilde{\psi}^0$ can not interact with $\tilde{\chi}$ through a $Z$, it can only decay through a virtual Higgs. Additionally, one-loop corrections induce a small mass splitting between $\psi^\pm$ and $\psi^0$. This can significantly change the $\psi^\pm$ decay width as discussed in section 7.2.

**Scotogenic model (Inert doublet model)**

The scotogenic model [29, 30] is an extension of the inert doublet model (IDM) with three generations of RH neutrinos. The IDM consists in extending the SM with an "inert" Higgs doublet, *i.e.* a Higgs doublet acquiring no vacuum expectation value. The IDM itself is a special case of the two Higgs doublet models (2HDM), in which the additional Higgs acquires a non-zero *vev* in the most general case. Overall, the scotogenic model supplements the SM by an additional SU(2) scalar doublet, $\Phi$, the *inert doublet*, and three sterile neutrinos, $N_n$. Similarly to the Singlet-Triplet model, the new fields are taken to be odd under a new $\mathcal{Z}_2$-parity, while the SM fields are even. The presence of the new scalar and fermion fields provides a radiative generation of neutrino masses via the radiative seesaw mechanism. Furthermore, the lightest $\mathcal{Z}_2$-odd particle ($H^0$ or $A^0$, or the lightest of the sterile neutrinos, $N_1$) is stable and thus a natural DM candidate. Both the scalar and the fermionic DM scenarios will be discussed in chapter 6. The model Lagrangian is given by:

$$\mathcal{L} = \mathcal{L}_{\text{SM}} + |D^\mu \Phi|^2 + \frac{i}{2}\bar{N}_n \not{\partial} N_n - \left(\frac{1}{2}M_n \bar{N}_n^c N_n + iY_{\alpha n}\bar{L}_\alpha \sigma_2 \Phi N_n + \text{h.c.}\right) - V(\Phi, H)\,, \quad (2.60)$$

where $\mathcal{L}_{\text{SM}}$ is the Lagrangian of the SM, $M_n$ is the Majorana masses of the right-handed neutrinos and $Y$ is a $3 \times 3$ complex matrix of Yukawa couplings. Finally, $V$ is the scalar potential

$$\begin{aligned} V(\Phi, H) =& \mu_1^2|H|^2 + \mu_2^2|\Phi|^2 + \lambda_1|H|^4 + \lambda_2|\Phi|^4 + \lambda_3|H|^2|\Phi|^2 \\ &+ \lambda_4|H^\dagger\Phi|^2 + \frac{1}{2}\lambda_5\left[(H^\dagger\Phi)^2 + \text{h.c.}\right]\,. \end{aligned} \quad (2.61)$$

After electroweak symmetry breaking, where $\langle\Phi\rangle = 0$ and $\langle H\rangle = v/\sqrt{2}$ with $v = 246$ GeV in this model, the particle spectrum comprises five physical scalar states ($h$, $H^0$, $A^0$, $H^\pm$) with masses:

$$\begin{aligned} m_h^2 &= \mu_1^2 + 3\lambda_1 v^2\,, \\ m_{H^0}^2 &= \mu_2^2 + \lambda_L v^2\,, \\ m_{A^0}^2 &= \mu_2^2 + \lambda_S v^2\,, \\ m_{H^\pm}^2 &= \mu_2^2 + \frac{1}{2}\lambda_3 v^2\,, \end{aligned} \quad (2.62)$$

where

$$v^2 = -\frac{\mu_1^2}{\lambda_1} \text{ and } \lambda_{L,S} = \frac{1}{2}\left(\lambda_3 + \lambda_4 \pm \lambda_5\right)\,. \quad (2.63)$$

The first scalar, $h$, is even under the new $\mathcal{Z}_2$-parity and identified with the observed SM-like Higgs boson, $m_h \simeq 125$ GeV. The other scalars are $\mathcal{Z}_2$-odd. The model is ruled by the five $\lambda_i$ parameters but it is convenient to work with the basis of the physical parameters $m_{H^0}, m_{A^0}, m_{H^\pm}, \lambda_L, \lambda_2$. Note that $\lambda_L$ and $\lambda_S$ can be physically interpreted as, respectively the $hH^0H^0$ and the $hA^0A^0$ couplings as can be seen in the vertices below.

**Interactions with the Higgs** The $\lambda_{3,4,5}$ terms in eq. (2.61) yields the following vertices between the SM Higgs and the inert scalar states

$$\mathcal{L}_{H^+H^-h} = -\lambda_3 v H^+ H^- h \tag{2.64}$$
$$\mathcal{L}_{H^0H^0h} = -\lambda_L v H^0 H^0 h \tag{2.65}$$
$$\mathcal{L}_{A^0A^0h} = -\lambda_S v A^0 A^0 h\,. \tag{2.66}$$

**Interactions with gauge bosons** The $|D^\mu\Phi|^2$ term in eq. (2.60) yields vertices between gauge bosons and the inert scalar states

$$\mathcal{L}_{H^+H^-Z} = \frac{g}{2\cos\theta_{\mathrm{W}}} H^+ H^- Z \tag{2.67}$$
$$\mathcal{L}_{H^+H^-\gamma} = g\sin\theta_{\mathrm{W}} H^+ H^- \gamma \tag{2.68}$$
$$\mathcal{L}_{H^0A^0Z} = \frac{ig}{2\cos\theta_{\mathrm{W}}} H^0 A^0 Z \tag{2.69}$$
$$\mathcal{L}_{H^\pm A^0 W\mp} = -\frac{g}{2} H^\pm A^0 W\mp \tag{2.70}$$
$$\mathcal{L}_{H^\pm H^0 W\mp} = \frac{ig}{2} H^\pm H^0 W\mp\,. \tag{2.71}$$

**Interactions with RH neutrinos** Vertices between leptons, scalars, and RH neutrinos come from the Yukawa term in eq. (2.60)

$$\mathcal{L}_{\nu_\alpha H^0 N_n} = -Y_{\alpha n}\nu_\alpha H^0 N_n \tag{2.72}$$
$$\mathcal{L}_{\nu_\alpha A^0 N_n} = -Y_{\alpha n}\nu_\alpha A^0 N_n \tag{2.73}$$
$$\mathcal{L}_{l_\alpha^- A^0 N_n} = Y_{\alpha n} l_\alpha^- H^+ N_n\,. \tag{2.74}$$

Phenomenologically, the production of odd particles at the LHC will be ruled by the gauge couplings with processes involving gauge bosons, since processes involving the Higgs will be much less probable. However, both Higgs and gauge boson-mediated processes will participate in DM production. Chapter 6 presents the LHC phenomenology for two scenarios of the scotogenic model, one where the DM candidate is the lightest RH neutrino and one where the DM candidate is the lightest neutral state of the inert Higgs doublet.

# Chapter 3

# Reinterpreting the LHC results

The LHC, located at the European organization for nuclear research (CERN) is the largest and the most energetic hadron collider. This section will introduce the LHC and the experiments at CERN. The focus will be on the two large, general-purpose LHC experiments, Compact Muon Solenoid (CMS) and A Toroïdal LHC Apparatus (ATLAS), and how they look for new physics. Particular emphasis will be placed on the interpretation and presentation of the results, and on the reinterpretation of these results by theoreticians. To complete this chapter, the statistical methods used in collider physics will be introduced.

## 3.1 Looking for new physics at the LHC

### 3.1.1 The Large Hadron Collider

Accelerating particles to collide them at high kinetic energy is an idea that was originally proposed at the end of the 1930s. The first cyclotron was invented by Ernest O. Lawrence in 1932 [31]. Cyclotrons are circular accelerators using alternating electric fields with a constant radiofrequency. They can only accelerate particles up to an energy of about 15 MeV. Synchrocyclotrons and synchrotrons were invented to increase the energy reach of colliders. To this day, synchrotron accelerators are the most energetic colliders. The Fermilab near Chicago, Illinois, hosted for decades the highest energy synchrotron: the Tevatron. It reached a record at the time of 1.96 TeV of the center of mass energy. Since 2009 the LHC is the synchrotron with the highest energy in the world, operating at a center of mass energy of 14 TeV. It consists of a circular tunnel with a circumference of 26.7 km, located a hundred meters underground on average. As sketched in Figure 3.1, protons are accelerated by a succession of three synchrotrons [32]. The linear particle accelerator Linac4 produces 160 MeV $H^-$ ions that are injected into the Proton Synchrotron Booster (PSB). The PSB takes away the electrons from the hydrogen ions and accelerates them up to 2 GeV. They are then injected successively into the Proton Synchrotron (PS), where they reach an energy of 26 GeV, and the Super Proton Synchrotron (SPS) before entering the main LHC ring with an energy of 450 GeV. In about twenty minutes, they are accelerated from 450 GeV to their maximum energy of 7 TeV (this same process is also used to accelerate and collide heavier ions at 5 TeV for the ALICE experiment). Two proton beams keep circulating in opposite directions for several hours while successively colliding. The beams collide head-on at three of the four interaction points as shown in

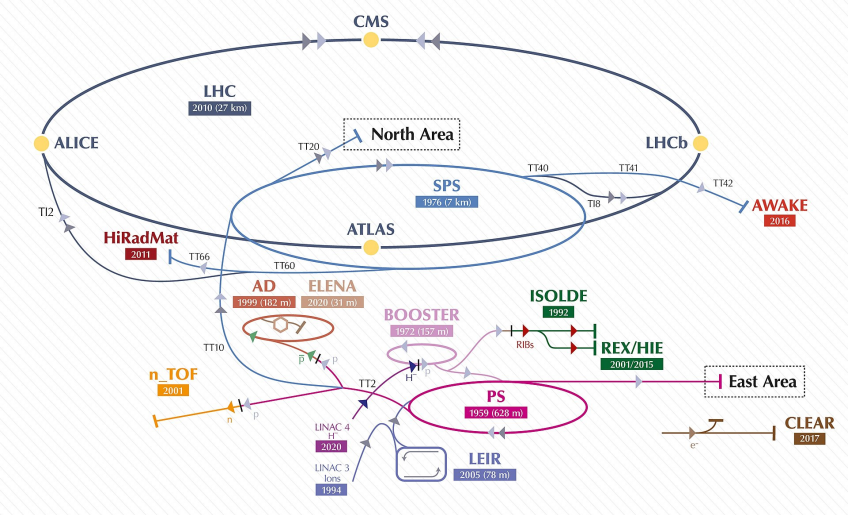


Figure 3.1: Simplified scheme of the LHC facilities from [33].

Figure 3.1, inside the three following detectors: ATLAS, CMS, and ALICE. They are cylindrical detectors placed around the beams, which are magnetically focused to locally increase the frequency of collisions. Unlike the previous experiments, LHCb is a fixed-target experiment with a forward detector that makes use of a single proton beam. The LHCb experiment has a wide physics program but it was mainly designed to measure the CP violation ratio through B-meson decays (see the paragraph about B-meson anomalies in section 2.2.1) as well as other rare B-meson branching ratios. ALICE was designed to study quark-gluon plasma (QGP) by detecting the products of lead-lead ions collisions but also performed lead-proton collisions. LHCb and ALICE will not be described further here. The focus will be given to ATLAS and CMS, them being general-purpose detectors designed for the study of fundamental particles and their interactions. The purpose of ATLAS and CMS is to detect the products of high-energy proton-proton collisions. Both have very similar designs but the main difference comes from the superconducting solenoid and the muon chamber in CMS, which was purposely designed to detect and study muons more efficiently. The successive detector systems are illustrated in Figure 3.2, each designed to identify different particles and reconstruct their properties as described below.

**Inner chamber** The precise interpolation of the interaction point and the particle tracks are keys in particle identification. A dense detector, close to the beam, is then essential. ATLAS and CMS inner tracking systems are composed of several layers, each containing silicon pixel detectors. This multilayer structure is designed to measure the tracks of the particles detected. The first pixel layers are designed for precise tracking, close to the collision point. The following layers are made of longitudinal silicon pixels, only one dimensional but allowing a wider coverage. ATLAS has in addition a straw tracker, or ionized drift tubes, as the outer layer of the inner chamber.

**Electromagnetic calorimeter (ECAL)** The ECAL is the next concentric layer. It reconstructs the energy of particles interacting electromagnetically, *i.e.* charged particles and photons. The ATLAS ECAL is a *sampling* calorimeter. It consists of an ab-

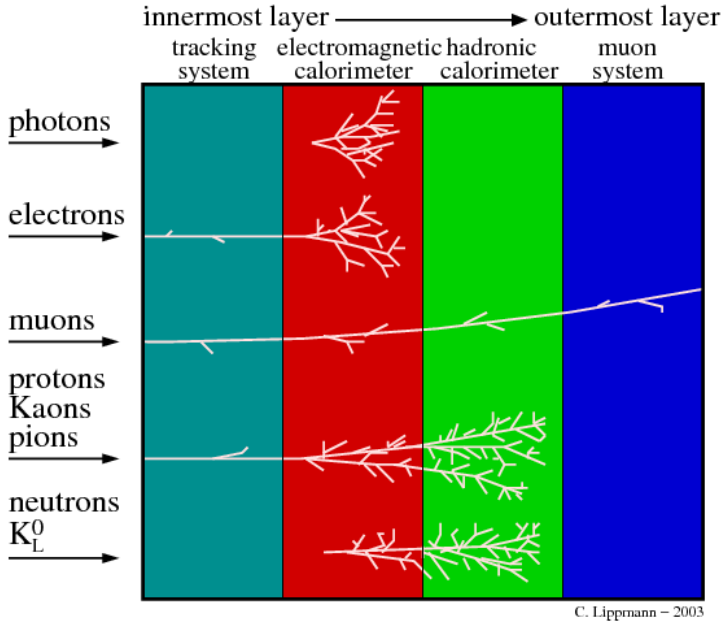


Figure 3.2: Simplified scheme of the detector designs of ATLAS and CMS, from [34].

sorber/detector alternation. The absorber is a steel material absorbing part of the particle's energy and facilitating electromagnetic shower development. The detector is a liquid Argon scintillator, enabling a precise track and energy reconstruction of the showers. The CMS ECAL however, is a *homogeneous* calorimeter, *i.e.* made of a single material ($PbWO_4$ crystal scintillator) both absorbing and measuring the energy of electrons and photons. Both ECALs are designed so that electrons and photons originate showers and deposit all their energy in the ECAL without contaminating the next detector systems.

**Hadronic calorimeter (HCAL)** High momentum hadrons deposit less energy in matter, and therefore additional material is needed to fully absorb and reconstruct their hadronic showers. The HCAL is then made of a denser material but still very similar in design to the ECAL. Both ATLAS and CMS have sampling HCAL made of plastic scintillators. However, they have different absorbing materials: steel for ATLAS and brass for CMS. Electrically charged hadrons partly interact electromagnetically and deposit some energy in the ECAL but the denser HCAL makes hadrons end their track in hadronic showers.

**Muon spectrometer** Muons being much heavier and stable at the detector scales, they can travel through all the previous systems without creating showers and being absorbed, while still leaving a recognizable charged track. Although this information can be used to measure muon properties, it can not provide enough points along the muon trajectory. A large gaseous spectrometer, with several meters of thickness, is thus placed in the outermost layer of the whole detector system of both ATLAS and CMS.

**Superconducting solenoid** In both experiments, a superconducting solenoid produces a strong magnetic field for measuring the momentum of charged particles. Indeed, charged particles see their track curved by a magnetic field, and the curvature directly depends on

the magnetic field and the momentum of the particles. This is designed to measure the momentum of the particle associated with the track. Together with a velocity measurement, particle masses can also be inferred. ATLAS's 2 Tesla solenoid is placed between the inner chamber and the calorimeters whereas CMS's 4 Tesla solenoid is between the calorimeters and the muon chamber.

The differences between ATLAS and CMS are due to different compromises that were made at the time of the detector conceptions. Scientifically, it is of great interest to cross-check results with two different apparatuses. The different detectors were presented above, and they allow the identification of particles and their properties. The following will present how SM particles interact in the detectors and how it enables the identification of each particle.

**Jets** Quarks are only stable by pairs, forming hadrons. Quarks produced by collisions will then undergo successive decays, forming showers. After each decay, they will lose more and more momentum and below a given energy scale they will start hadronizing, *i.e.* form stable hadrons. This will form bunches of hadrons called "jets". Charged jets will leave tracks in the inner tracking system and the ECAL, and deposit their remaining energy in the HCAL while ending their course. Neutral jets, however, will only be detected in the HCAL.

***b*-jets** $b$-hadrons (hadrons constituted by a bottom quark paired with an antiquark) have a significantly larger lifetime than other hadrons, about $\mathcal{O}(10^{-12})$ s. This implies that $b$-hadrons decay about $\mathcal{O}(0.1)$ mm away from the primary vertex, which is a distance that can be resolved by track reconstruction. Jets originating from a $b$-quark will then be reconstructed as coming from another interaction point, or vertex, relative to the other collision products. Such jets are called $b$-jets and can then be identified by reconstructing their tracks, up to the secondary vertex of the $b$-hadron decay.

**Photons** Because photons are electrically neutral, they are not seen in the tracker, but they will mostly be absorbed in the ECAL, where their energy will be reconstructed.

**Electrons** Similarly to photons, the energy of electrons is measured in the ECAL, but electrons also leave a charged track in the inner chamber, thus allowing to differentiate photons and electrons.

**Muons** Although muons leave a track and deposit some of their energy in the calorimeters, they are mainly detected in the muon chamber in the outer part of the detector because the calorimeters provide too few samples of the muon trajectory. It is the purpose of the large muon chamber to measure enough points of the muon trajectory. However, information from the inner tracking system is sometimes used as well. Similarly to other charged particles, the tracks allow the reconstruction of the momenta and velocities of muons.

**Missing energy** Since neutrinos interact very weakly with matter, they require very large volumes to be detected. ATLAS and CMS do not have such detectors, making

neutrinos the only particles of the SM that can not be detected. Such undetected particles are called "invisible". In BSM theories, there exist many new particle candidates that by nature would be invisible at the LHC. Although they are detector invisible, their momentum can be measured thanks to momentum conservation. Indeed, the proton beams are on the same longitudinal axis and the transverse momentum before the collision is therefore null. Thus the total momentum of the collision products must be zero by conservation. One hence defines the missing transverse energy $E_T^{\text{miss}}$ to identify the energy of invisible particles

$$E_T^{\text{miss}} = \left| \overrightarrow{p}_T^{\text{miss}} \right| \quad \text{with} \quad \overrightarrow{p}_T^{\text{miss}} = -\sum_i \overrightarrow{p}_T^{\,i}, \tag{3.1}$$

where $i$ runs over all particles detected in a given collision.

**Triggers** Finally, a crucial aspect of ATLAS and CMS is the triggers. Indeed, the frequency of collisions is about 40 MHz, which is impossible to record. A first trigger, at the hardware level and called the Level-1 trigger, is directly plugged into the calorimeters and the muon chamber. With only coarse information on the energies deposited in the detectors, it mainly selects events with a minimum transverse energy, allowing it to reduce the event frequency to about 100 kHz. The second trigger at the software level and called the high-level trigger (HLT), uses all the detector information to select relevant events for physics studies and reduces the event frequency to about 1 kHz. The HLT is an algorithm consisting of a collection of a huge number of triggers. The triggers typically select a given number of particles with a minimum transverse momentum, *e.g.* three leptons, each with certain momentum requirements. Selections are applied for all types of particles, such as leptons, photons, jets, $b$-jets, or missing transverse energy. All the triggers together aim to select the most interesting events for later physics analyses, while reducing the events rate to record, to cope with the memory capacities of the experiments. With the increase in luminosity and number of simultaneous events (pile-up), both the Level-1 trigger and the HLT have been continuously updated to keep the frequency of events recorded around 1 kHz. Table 1 in Ref. [35] gives a non-exhaustive list of ATLAS triggers in 2016 and Figure 1 in the same reference shows the evolution of events rate during the year 2016. The final triggers that are applied are analyses specific and aim to select the required final states for each analysis.

### 3.1.2 New physics searches

Once the thousands of events per second are recorded, they are analyzed and interpreted. Analyses often study one or several specific final states that are selected, as mentioned just above, with additional triggers to the HLT. These final states, defined by particular sets of collision products and their associated kinematic cuts, can be interpreted as measurements or as searches. The former considers the distributions of events for a given kinematic variable to estimate SM observables. For instance, the Higgs mass is measured with the distribution of the invariant mass of a di-photon system. Typically, the Higgs, $W$ boson, or top quark masses are crucial parameters in the SM. Searches also consider specific final states but aim their focus at phase space regions where the chances to discover new physics are higher. This is done by searching for regions in the tails of SM distributions,

where the SM event contribution can be minimized and the expected new physics events maximized. The di-photon system was a search channel where the Higgs was expected to be found. Once the Higgs was discovered, it became a channel for measuring the Higgs mass.

Since it would probably take a century to study all signatures possible, LHC physicists have to make priorities. There is then a subtle interplay between experiment and theory. For example, the enthusiasm for supersymmetry has guided experiments to look for signatures with supersymmetric particles for over two decades. Inversely, the absence of experimental observations pushes theoreticians to look for new BSM scenarios. When looking for new physics, LHC searches are then interpreted in a given theoretical context or, in other words, the data is confronted with a given BSM model. For instance, interpreting a search in a SUSY context involves the statistical comparison of the SUSY predictions with the LHC observations. In general, BSM theories are extensions of the SM since they must at least contain the SM. The new physics processes can interfere with the SM processes but these effects can often be ignored. The number of events predicted by a BSM model is in this case the addition of the SM prediction, often referred to as the SM background, and of the new BSM prediction. The computation of BSM signals will be detailed in section 3.2. Comparing the predictions with the observations then relies on the $\mathrm{CL}_s$ prescription, which is a statistical procedure discussed in section 3.3. First, we will review the typical searches performed at ATLAS and CMS.

### Prompt searches

Most SM particles detected at the LHC are emitted from prompt decays except for $b$-hadrons and taus. That means that the particle originating the decay has a too short lifetime for the daughter to be reconstructed to a secondary vertex. Thus many of the LHC searches are prompt searches, *i.e.* the searches are designed to look for promptly produced particles. Prompt searches are in the following divided into missing energy and resonance searches.

**Missing energy searches** Many BSM models are expected to produce significant $E_T^{\mathrm{miss}}$, in addition to the neutrino background. For example, the lightest neutralino in SUSY models is neutral and stable (due to $R$-parity) and thus is invisible at the LHC. The equivalent in other BSM models is the $\mathcal{Z}_2$-symmetry and it is very similar to $R$-parity. It implies that any interaction is restricted to an even number of BSM particles. That makes the LSP stable since there is no lighter BSM state available to decay into. $R$-parity or $\mathcal{Z}_2$-symmetry then makes the LSP a perfect DM candidate and therefore implies final states with large missing energy. Such missing energy searches will be subdivided into SUSY and DM searches in the following.

*SUSY* particles, due to the $R$-parity, or particles from other models with $\mathcal{Z}_2$-symmetry, can then only be produced in a certain way. Indeed, they can only be produced by pairs at the LHC. Then the two SUSY states can only decay into an SM and a SUSY state (again due to $R$-parity). Successive decay can happen but the last decay will always be to an SM state and the LSP. Since the LSP is invisible, this will lead to final states with several SM particles and missing energy. Typical final states are listed in the following

- $E_T^{\mathrm{miss}} + \mathrm{jets} + X$: inclusive jets plus missing energy ($X$ = anything).

- $E_T^{\text{miss}}$ + jets + $0l$: lepton veto.
- $E_T^{\text{miss}} + nl$: multilepton.
- $E_T^{\text{miss}}$ + jets + $1l$: jets plus one lepton.
- $E_T^{\text{miss}}$ + jets + $2l$ with $Q(l_1 = -Q(l_2))$: jets plus opposite-sign dileptons.
- $E_T^{\text{miss}}$ + jets + $2l$ with $Q(l_1 = +Q(l_2))$: jets plus same-sign dileptons.

Typically, squarks can decay into quarks and LSP. Thus direct production of squarks could lead to final states with two jets and missing energy. Electroweakino searches are also very typical. They consist of the direct production of either chargino-chargino, chargino-neutralino or neutralino-neutralino. Since the lightest neutralino is often assumed to be the LSP, we have to consider the direct production of heavier neutralinos to have a decay pattern with detectable SM particles and missing energy from the LSP neutralino. A common decay pattern is then $\tilde{\chi}_1^{\pm} \to W^{\pm}\tilde{\chi}_1^0$ or $\tilde{\chi}_2^0 \to (Z \text{ or } h)\tilde{\chi}_1^0$. Example diagrams describing such scenarios are shown in Figure 3.3.

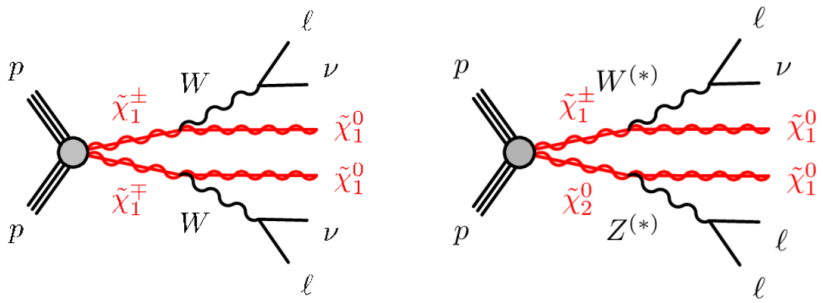


Figure 3.3: Examples of electroweakino signatures at the LHC, taken from [36]

*Dark matter* searches look for the direct production of DM candidates, in association with a heavier BSM state. However, DM candidates are invisible at the LHC since DM has to be neutral and interact very weakly with SM particles. The direct production of DM would then lead to completely invisible final states. Nonetheless, if the DM candidate is produced in association with an SM particle, it could lead to clear signatures with an SM particle and large missing energy. Thus a final state $X + E_T^{\text{miss}}$ could be observed, where $X$ is an SM particle recoiling from the $E_T^{\text{miss}}$. Such final states are called mono-$X$ final states. An example would be a recoiled hadron at the origin of a jet and leading to a mono-jet signature. Several mechanisms can lead to such signatures. The DM could be produced in association with a heavier BSM partner and the latter could decay into DM and a SM state. The $X$ particle could also be originating from initial state radiation (ISR). Ref. [37] reviews the ATLAS mono-X searches and mentions mono-jet, mono-photon, mono-W/Z, and also mono-Higgs searches.

**Resonance searches** Resonances are another way of looking for new physics. As an example, the Higgs was found through the resonance it produces in the invariant mass spectrum of the diphoton final state. In that case, the diphoton final state was a rather clean signal, *i.e.* not many particles in the SM are producing final states with two photons so the SM background was small. By looking at the distribution of events with respect

to the invariant mass $m_{\gamma\gamma}$, a resonance was found around $m_{\gamma\gamma} = 125$ GeV. This can be generalized with other final states composed of several particles. For instance, the search for dijet resonances has been a long-standing field because they are theoretically motivated in low-mass regions. It is however quite challenging since such jets are not hard enough to trigger the HCAL. However, techniques involving ISR have been developed. The idea is to measure a dijet resonance associated with an ISR photon or jet. If the ISR state is energetic enough, it can be used as the detector trigger, while the physical object of interest is the dijet system. Finally, it is also possible to measure the invariant mass of more complex systems involving invisible particles, in which case the invariant mass is dependent on the missing transverse energy. See for example [38, 39].

### Long-lived searches

Numerous BSM models naturally have long-lived particles. Famous models can generate such candidates in a part of their parameter regions. Such scenarios typically arise from small couplings and/or small mass splittings, for example in SUSY when the LSP is close in mass to the next-to-lightest supersymmetric particle (NLSP) [40]. Regarding DM models, scenarios with very weak couplings to the SM can produce the relic density required by the Planck measurement through other mechanisms than the standard freeze-out mechanism. Examples are co-annihilation, freeze-in, and others as we will see in chapter 7. Reference [41] gives an overview of BSM models involving LLPs. Depending on the free parameters of the model considered, there can be regions in which some BSM particles are sufficiently long-lived to leave distinct signatures in the LHC detectors. Depending on the decay length scale, many signatures are possible, from displaced vertices for the smallest lifetimes to heavy stable charged particles (HSCP) for the largest lifetimes. Figure 3.4 illustrates the different types of LLP signatures. The decay length of the BSM

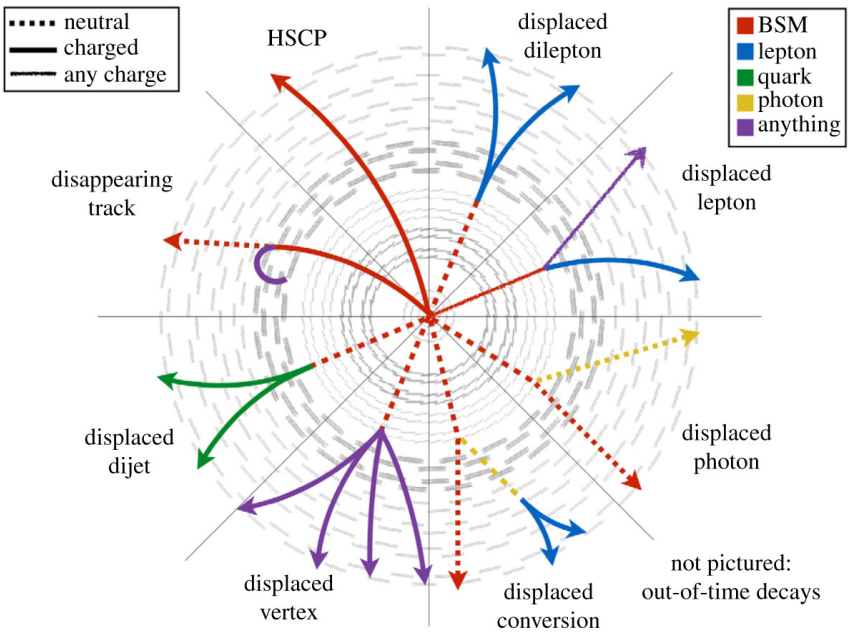


Figure 3.4: Illustration of the many LLP signatures at the LHC from [42].

candidates has to be at least of about 1 mm for the secondary vertex to be reconstructed separately from the primary vertex.

*Displaced vertices* give relevant constraints from around 1 mm up to a few meters. Both charged and neutral particles can be at the origin of displaced vertices, however, these searches are especially relevant for neutral BSM candidates since it would be the only visible signature. There are many possibilities such as displaced lepton(s), displaced jets(s), and displaced photon but also signatures with more than two states originating from the secondary vertex. ATLAS [43, 44, 45] and CMS [46] both have now published numerous displaced analyses.

*Disappearing tracks* are relevant around the same scales of decay lengths, from 1 mm up to a few meters. However, they are only sensitive to electrically charged particles. Indeed, the principle is to register events with a charged track that disappears in the outer layers of the detectors. This could happen if a long-lived BSM state decays into invisible BSM or SM states. This would leave a recognizable signature where the particle suddenly stops its track inside the detector systems. Examples are [47, 48, 49].

If the charged particle has an even longer lifetime and decays outside the detector, it will traverse the whole detector and then be seen as a heavy muon. This signature is called *heavy stable charged particles (HSCP)* and it can be relevant from decay lengths of a few meters. For larger decay lengths, the constraints do not depend on the lifetime anymore but only on the other model parameters (typically the mass of the charged particle) since the particle decays outside of the detector anyway. ATLAS has published a few HSCP searches within SUSY scenarios [50] and CMS as well [51, 52, 53]. *R-hadrons*, originating from color-charged LLPs, are a special case of HSCP. Such signatures are for example motivated in split-SUSY by long-lived gluinos. The latter gluinos hadronize and form either charge or neutral $R$-hadrons that can provoke hadron showers in the HCAL and thus can be detected. This case is rather involved since it is needed to make a hypothesis on the hadronization model, and this choice can have a significant impact on a search interpretation.

HSCP, displaced vertices, and disappearing track constraints will be used in the phenomenological studies of chapters 6 and 7. A more comprehensive list of LLP signatures is given in [54]. Reference [55] also gives an overview of the possible future LLP signatures that could be investigated by implementing new triggers at the LHC.

### 3.1.3 Interpreting the LHC results: the simplified model paradigm

Before performing a search, the LHC collaborations have several tools to split the kinematical parameters into several regions of interest, or so-called signal regions (SRs). The aim is to determine bins in the kinematic parameters that minimize the SM background and maximize the hypothetical new physics signal. The phase space that is not covered by the SRs is often used in the validation regions (VRs) and/or control regions (CRs). CRs and VRs in principle do not contain new physics signals and are then used to check SM background simulations and also estimate the background errors. After collecting collision data, the final triggers and kinematic selections are applied and a given number of events is observed in each SR. The role of the interpretation is to give sense to these numbers. The first possibility is to compare the observed events with the number of events predicted by the SM. Indeed, a significant excess of events would imply that the SM is

not enough to describe the observed data. Section 3.3 shows how statistical hypothesis testing is used in particle physics to assess the significance of an excess in the observed data. In particle physics, the requirement for discovery is a significance of $5\sigma$. However, a BSM model is often used to characterize the potential excess. To this aim, the number of events predicted by the BSM model considered is compared with the observed data. In the absence of discovery, the data is used to constrain the parameter space of the model used for interpretation. In that case, the exclusion *probability* is computed following the $\mathrm{CL}_s$ prescription, which will also be explained in section 3.3.

This section aims to focus on the simplified model paradigm that has been used for over a decade to interpret the LHC data. At the beginning of the LHC era, realistic models were used to characterize the searches of ATLAS and CMS. The constrained MSSM (cMSSM), which is an even more restrained model than the pMSSM (presented at the end of subsection 2.2.2), was the first one to be used for its limited number of five parameters. Then simplified models were proposed to have a more generic and straightforward way to characterize potential new physics signals [56]. Simplified models thus consist in models where the SM is extended with only two or three new particles and the overall decay pattern is very simple. In a lot of cases, there are only two particles, one that is pair-produced by the proton-proton collision and it decays into the other and one or several SM states with a 100% branching ratio. A SUSY example would be the pair-production of staus that decay solely into an SM tau and the lightest neutralino. This is a very simple model having only two parameters, the stau mass and the neutralino mass (since the tau mass is already fixed by its SM value). There are about a hundred publications from ATLAS and CMS presenting their results using such simplified models for interpretation. Many of these models are SUSY inspired, *i.e.* consisting of two or three supersymmetric particles. This choice was made because physicists had good reasons to think that supersymmetry would be found at the LHC. The simplicity of the models also allowed, in principle, to extrapolate the results with other BSM models having similar particles.

For each of the mass parameters, a signal prediction can be computed. For that, experimentalists simulate the collisions to compute both the SM prediction (SM background) and the simplified model prediction. There are two inputs from the theory side: the pair-production cross-section and the efficiency. The cross-section $\sigma$ is completely decided by the theory. The efficiency $\varepsilon_i$ represents the fraction between the number of events that are detected and the initial number of events for the $i^{\text{th}}$ bin. The acceptance $\mathcal{A}_i$ is defined as the fraction between the number of events that pass the kinematic selections and the number of events detected for the $i^{\text{th}}$ bin. The above are general definitions but, depending on the experiment and even sometimes the analysis, there can be various definitions. Reinterpretation tools often define a global efficiency $\epsilon_i = \varepsilon_i \times \mathcal{A}_i$, which always corresponds to the fraction of events that pass the kinematic constraints for the $i^{\text{th}}$ bin. $\epsilon_i$ then depends on the kinematics of the theory but also on the detector configuration as discussed in 3.2.1. The number of events in the $i^{\text{th}}$ bin then reads

$$N_i = \varepsilon_i \times \mathcal{A}_i \times \sigma \times \mathcal{L} = \epsilon_i \times \sigma \times \mathcal{L}\,, \tag{3.2}$$

The bin number is spelled out to show that the efficiency is bin-dependent since it contains the information on the kinematics cuts and that the cross-section and integrated luminosity $\mathcal{L}$ does not depend on the bin. Each mass parameter is then a model in itself, with its prediction for the number of events in each bin: $N_i$. The $\mathrm{CL}_s$ prescription allows

the definition of an exclusion probability for each model, or rather each parameter point. The $CL_s$ value represents the probability for the new signal hypothesis to agree with the observed data. $1 - CL_s$ is then often used because it represents the probability of excluding the model. In particle physics, the prescription is to exclude a model at a 95% exclusion level, which breaks down to $CL_s < 0.05$. Figure 3.5 shows the exclusion result obtained by ATLAS for the example cited above with pair-production of taus decaying to neutralinos. This is the standard way to present LHC results. It shows the 95% exclusion

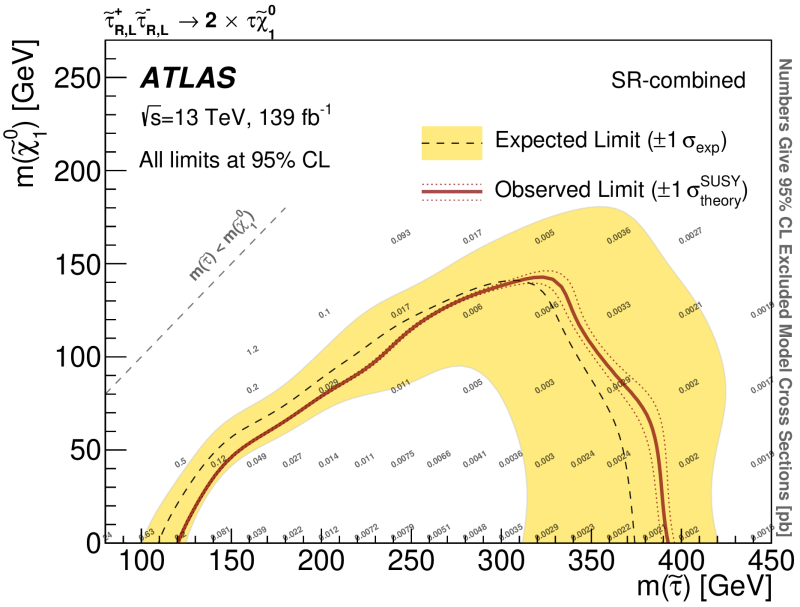


Figure 3.5: Example of an exclusion contour from ATLAS-SUSY-2018-04 [57]

limit as a red line in the plane of the tau mass and neutralino mass on the $x$ and $y$-axis. It means all mass points under the red curve have a $CL_s$ smaller than 0.05 and all the points above have a $CL_s$ larger than 0.05. The dotted line shows the same 95% exclusion limit but performed using the SM background predictions instead of the observed values. This "expected" limit is used to estimate the sensitivity of a search (see section 3.3 for more details). The yellow band shows how the expected limit would vary if the SM prediction is varied within its $1\sigma$ uncertainty. This contour is practical for comparing exclusion reaches between different analyses but it is not usable for reinterpretation. However, upper limits (ULs) on the cross-section and efficiency maps (EMs) are reusable. In the same mass plane is shown the cross-section upper limit at 95% exclusion CL[1] . The latter relies on the fact that increasing the BSM cross-section increases the new physics signal and then increases the exclusion CL (for non-excluded points *i.e.* having an exclusion CL smaller than 95%). Indeed, if the new signal increases with respect to the SM background, it will disagree more and more with the observation. The cross-section is then increased until reaching the 95% exclusion CL. For excluded points having an exclusion CL larger than 95%, the cross-section has to be decreased until the exclusion reaches down 95%. In the end, all points outside the exclusion contour have a cross-section upper limit larger than its nominal value, and vice-versa for the points inside the contour. EMs follow the same

[1] "Exclusion CL" is often used to denote $1 - CL_s$, which can be interpreted as the probability of exclusion.

principle but give efficiencies in the two-dimensional mass plane instead of the UL. How UL maps and EMs can be used for reinterpretation will be discussed in section 3.2.2.

As will be discussed in the next section, depending on the information provided by the experimental collaboration, theoreticians can reproduce and reuse the data with different levels of accuracy. Typically, UL maps are provided, but this is not always the case for EMs. Other pieces of information allowing for the combination of SRs are sometimes provided but this will be the subject of section 3.3.

## 3.2 Reinterpretation of collider data

Reinterpreting the simplified model results is not an easy task and is a field in itself. The ideal goal of reinterpretation is to be able to constrain any BSM model with experimental data that would be sensitive to it. There are two methods to reinterpret the LHC data. The first one that will be discussed is based on the full simulation of LHC collisions. This method uses a chain of reinterpretation tools to simulate the collisions, decays, and hadronization but also detector effects.

Section 3.2.2 will present the other possibility, which is to reuse the data obtained after the simulations. For that, UL maps and EMs produced by the experimental collaboration can be used, if they are provided. This method is much faster since there is no simulation. However, it is necessary to make the approximation that the kinematic distributions of the BSM model are the same as the simplified model. This is not always valid but this discussion will be addressed in 3.2.2.

### 3.2.1 Full event simulation

To characterize potential new physics signals, experimentalists confront the observed data at the LHC with simplified model predictions. The simplified model predictions then have to be computed on the theory side. The SM background is usually not simulated and the new physics signal is just added to it. For a one-to-one comparison, it is necessary to simulate the physics of colliders and detectors with the simplified model under consideration. Such simulations are performed for numerous events to get a statistically significant number of events after applying all the cuts. The cost in computational time is heavy but it is necessary if one wants to be faithful to the experimental search.

Before describing the different stages of a collision, the parton model needs to be briefly introduced. Since the initial particles colliding are two protons made of quarks, it is necessary to describe the content of the protons. In the parton model, protons are considered dynamic entities where quarks and gluons are constantly interacting. When considering for example a process with two quarks in the initial state, one must take into account for the probability to get a quark among the proton. By the QCD factorization theorem, one can decompose the hadron scattering amplitude into the parton-level scattering and the parton distribution functions (PDFs). By integrating over the phase space, scattering amplitudes are replaced with cross-sections, giving the following hadron collision cross-section

$$\sigma(AB \to F\ X) = \sum_{a,b} \int dx_a dx_b\ f_{a/A}(x_a, Q^2) f_{b/B}(x_b, Q^2)\ \hat{\sigma}(ab \to F), \tag{3.3}$$

$A$ and $B$ are the initial state hadrons. In the case of the LHC $A$ and $B$ are both protons[2]. The sum runs over all partons $a$ ($b$) contained in the hadron $A$ ($B$). In our case, the proton is composed of two up quarks and one down quark, giving $a, b \in [u, u, d]$. $f_{a/A}(x_a, Q^2)$ represents the PDF of the parton $a$ inside the hadron $A$. More concretely, this is the probability to find a parton $a$ inside $A$ with a momentum fraction $x_a$. The PDFs also depend on the energy scale $Q$ and are studied in deep inelastic scattering (DIS) experiments. Data from many DIS experiments provides the possibility to fit the PDFs. The dependence over the energy $Q$ is described by the DGLAP [58, 59, 60] equations. $\hat{\sigma}(ab \to F)$ is the cross-section of the hard process, *i.e.* the subprocess with the partons $a$ and $b$ isolated from their respective quarks.

Simulating high-energy collisions can then be divided into four stages. The first one is to implement the PDFs and the matrix elements to compute the cross-section as shown in eq. (3.3). Then the quarks form hadron showers and hadronize to form jets. The third stage is about detector effects and finally, the fourth stage is about kinematic selections.

**Parton-level event generators** Taking as input the information about the BSM model desired to be simulated, such generators compute the scattering matrix elements that characterize the hard process. The scattering matrix enters the cross-section calculation but also influences the kinematic distribution. The LHAPDF [61] framework is then used to apply eq. (3.3) and compute the hadronic process cross-section. The computed cross-sections and kinematic distributions then allow using the probability of each process to randomly generate events. At this stage, parton-level events only consist of elementary particles, mainly quarks and gluons. How to take into account quark confinement and hadronization will be discussed in the next paragraph. For a few years now, several tools have implemented the automatic computation of NLO cross-sections and some processes can even be computed at the NNLO precision. MadGraph5 [62, 63] is used widely in the field and it outputs parton-level events in the Les Houches Event file format (LHE) [64].

**Showering and hadronization** The bare quark and gluons events encoded, for example, in the LHE format will successively cascade decay into more and more quarks and gluons, each new parton having less and less momentum. They will end up forming hadrons since they can not stay isolated because of color confinement, this is called hadronization. The momentum scale at which hadronization starts is small ($\sim 200$ MeV) and at this scale, perturbativity does not hold anymore. Showering and hadronization generators (SHGs) thus use approximate models based on experimental data to describe the hadronization [65], after which all final states hadrons are colorless as dictated by color confinement. General-purpose SHGs examples are PYTHIA [66, 67], HERWIG [68, 69] and SHERPA [70, 71]. All of them produce output event files encoded under a HepMC format. They constitute what is called truth-level or particle-level events.

**Detector simulation** The physics of collisions is contained in the two previous stages. However, since the particles are detected with complex systems at the LHC, the detector response must be simulated to compare detector-level events with the observed number of

[2]In principle, the LHC also runs lead-lead and proton-lead collisions for the ALICE experiment

events at the experiments. DELPHES [72] is a commonly used tool for it can perform a fast simulation of the detector response, using the truth-level events as input. DELPHES performs a realistic detector simulation on the SM particles and applies a smearing on their momentum to simulate the energy measurement. The latter smearing is quantified using the measured detector resolution. DELPHES then constructs objects such as jets and missing energy from the results of the individual particle simulations, allowing for the description of the detected final state for each event. Another method is to apply a "smearing+efficiency" transfer function, which maps truth-level events to detector-level events. RIVET [73, 74], for instance, uses such an approach to perform the detector simulation and kinematic cuts at once. Thus RIVET directly gets the efficiencies in each SRs. With DELPHES, one has to rely on other public tools to apply the specific kinematic cuts of each analysis as is discussed in the next paragraph.

**Kinematic cuts** Many LHC searches are cut-based analyses, *i.e.* they split the events of the search into SRs by defining specific kinematic constraints using kinematic parameters. Table 3.1 shows a table specifying the cuts that are applied to define the two SRs in an ATLAS analysis looking for direct production of staus through final states with two SM taus [57]. This analysis has only two SRs which have a lot of cuts in common. The *low*

| SR-lowMass | SR-highMass |
|---|---|
| 2 tight $\tau$ (OS) | 2 medium $\tau$ (OS) , $\geq 1$ tight $\tau$ |
| asymmetric di-$\tau$ trigger | di-$\tau$+$E_{\mathrm{T}}^{\mathrm{miss}}$ trigger |
| $75 < E_{\mathrm{T}}^{\mathrm{miss}} < 150$ GeV | $E_{\mathrm{T}}^{\mathrm{miss}} > 150$ GeV |
| $\tau$ $p_{\mathrm{T}}$ cut described in Section 5 | |
| light lepton veto and 3rd medium $\tau$ veto | |
| $b$-jet veto | |
| $Z/H$ veto ($m(\tau_1, \tau_2) > 120$ GeV) | |
| $\lvert\Delta\phi(\tau_1, \tau_2)\rvert > 0.8$ | |
| $\Delta R(\tau_1, \tau_2) < 3.2$ | |
| $m_{\mathrm{T2}} > 70$ GeV | |

Table 3.1: SRs definition of ATLAS-SUSY-2018-04 [57].

*mass* SR is designed to be more sensitive to light staus while the *high mass* should be sensitive to heavier staus. This difference in sensitivity mainly comes from the selection on the missing transverse energy on the third line of table 3.1. However, there are other differences, *e.g.* different triggers or conditions on the energy of the taus. This example shows the principle of a cut-based analysis. Nonetheless, some CMS analyses can have more than a hundred SRs while ATLAS analyses often have $\mathcal{O}(10)$ SRs. Several public tools are designed to take either truth-level or detector-level events and reproduce the kinematic cuts on the input data. The output is a number of events passing all the cuts for each SR. For the analysis reimplementation to be possible, experimental collaborations must provide a clear description of all the cuts and selections of the analysis, as well as "cutflow" charts. The latter gives the number of remaining events after each successive cut. In principle, when implementing an analysis in a reinterpretation tool, one should get

the same cutflow numbers or at least close numbers by using the same simplified model. This is necessary to check or rather "validate" the implementation of the analysis. See [75] for the theorist's recommendation on how to present experimental results for later reuse. The ratio of events in an SR with the initial number of events is the efficiency $\epsilon_i$ that is relevant, together with the cross-section and luminosity, to compute the number of events in each SR (see eq. (3.2)). The final step to constrain one's model is again to use the $CL_s$ prescription (section 3.3). Physicists will typically run scans in the parameter space of their model to investigate which part of the parameter space can be excluded by LHC analyses.

The following shows a review of the current public reinterpretation tools based on full recasting.

- CheckMATE [76, 77] uses as input detector-level events from DELPHES. It also has a Pythia and MadGraph5_aMC@NLO interface to directly generate events and analyze them. The CheckMATE AnalysisManager [78] allows users to implement their own analyses.

- MadAnalysis5 [79, 80] works with truth-level events under the HepMC format. It simulates the detector response through an interface to DELPHES. Similarly to CheckMATE, MadAnalysis5 has a Public Analysis Database (PAD) [81, 80] that provides a framework for any user to implement new analyses. "Smearing+efficiency" functions have also been implemented recently in +MadAnalysis5+ [82].

- GAMBIT [83] is a multi-purpose tool. The ColliderBit module [84] is devoted to the recasting of LHC searches, which uses smearing+efficiency functions published by the experiments.

- RIVET [73, 74] was originally made to confront detector unfolded events with theory predictions. It uses detector-level input but can now use truth-level events since the implementation of smearing+efficiency functions. RIVET has since grown to the RIVET toolkit, which is an interface of a wide collection of tools.

- adl2tnm [85] and CutLang [86, 87, 88] use an analysis description language (ADL) [89, 90]. ADL is a language specifically designed to describe kinematic cuts that are used in LHC analyses. adl2tnm is an ADL to `C++` converter and CutLang directly executes code written in ADL.

See [75] for a more comprehensive list of reinterpretation tools. All these tools give physicists pretty convenient ways to reinterpret LHC analyses to constrain their favorite models. Most of these tools however only deal with prompt searches, although some are working on extensions to include LLP searches. Indeed, LLP searches use different triggers and cuts that did not exist with prompt analyses. Implementing a general treatment of LLP analyses in the fast detector simulation tools thus involves significant work. However, a few LLP analyses have been implemented and made public [91]. This will probably slowly lead to more general LLP recasting tools in the future.

### 3.2.2 Reusing simplified models

Full recasting represents a lot of work and is CPU time-consuming. To present results under the format of an exclusion contour as exemplified in figure 3.5, experimentalists run collider simulations over the two masses of the model. Since all the work of simulating collider events has already been done by the experimentalists for the simplified model they considered, the idea is to directly reuse their result without having to redo the whole simulation. As discussed in the previous section, the output information from the full simulation of collider events is an efficiency. If publicly provided, it is then possible to use the EMs provided by the experimental collaborations or also UL maps. Reusing this type of data relies on the assumption that the EMs and UL maps computed for a given simplified model stay approximately the same for the new BSM model under consideration. The main reason that could contradict this assumption would be that the BSM model has different kinematic distributions than the simplified model, which could imply that the efficiencies are not valid for the BSM model under consideration. Analyses relying heavily on shape distributions or having strong spin dependence are expected to violate this assumption. Moreover, if the model has a different $s$ or $t$-channel productions than the experimental signature, it can lead to different kinematics. This point is discussed in section 2 of ref. [92]. The following effects have been studied: different production channels in squarks simplified models, different spin structures in dijet+$E_T^{\text{miss}}$, dilepton+$E_T^{\text{miss}}$, and $t\bar{t}$ + $E_T^{\text{miss}}$ final states. In the above cases, it was found that the simplified model assumption is safe. However, the validity of this assumption is model-dependent and one still has to be cautious when using simplified model tools. Mono-$X$ searches for DM are an example for which the simplified model assumption does not hold.

The experimental limit can significantly change when applied to another model or even another scenario of the same model. Indeed, simplified models often only include one of the possible decays in the model. As discussed previously, most simplified models are SUSY-inspired but more realistic SUSY scenarios have more complicated decay patterns, with particles having several possible branchings to decay into. For example, neutralinos from simplified models decay either to a $Z$ or $h$ boson whereas, in a general SUSY scenario, neutralinos can decay with comparable branching ratios into both $Z$ and $h$ bosons. Say if for some scenario the neutralino decays into $Z$ with a 60% branching ratio, then the number of events associated with the $Z$ final states will be $64\%$[3] less than for the simplified model, and the exclusion CL will thus be weaker.

To use UL results, one must then compare $\sigma \times \text{BR}_1 \times \text{BR}_2 \times ...$ with the cross-section upper limit at 95% CL: $\sigma_{\text{UL}}^{95\%}$. For EM results, one can use the efficiency to compute the number of events in each SR by rescaling with the branching ratios, similar to the case of UL

$$N_i = \epsilon_i \times \text{BR}_1 \times \text{BR}_2 \times ... \times \sigma \times \mathcal{L}, \tag{3.4}$$

In the same way as full simulation tools do with their output efficiencies, one can then use the $\text{CL}_s$ prescription to infer the statistical agreement between the theory and the experiment.

SModelS [93, 92, 94, 95, 96] is a general tool based on simplified models that can be used with BSM models having a $\mathcal{Z}_2$-symmetry. This is the tool that will be described

[3]Since we are speaking about pair production, the branching ratio must be squared to account for the two symmetric decay branches: $(60\%)^2 = 36\%$.

among the others since a significant part of the thesis has been focusing on SModelS. Other tools are designed for specific models such as HiggsBound [97, 98, 99, 100] for multi-Higgs models, DarkCast [101] for dark photon models and ZPEED [102] for $Z'$ models.

### 3.2.3 SModelS working principle

SModelS is composed of two parts: the model decomposition and the analysis database. The analysis database contains about a hundred ATLAS and CMS simplified model analyses. The model decomposition is illustrated in the left part of figure 3.6. SModelS only

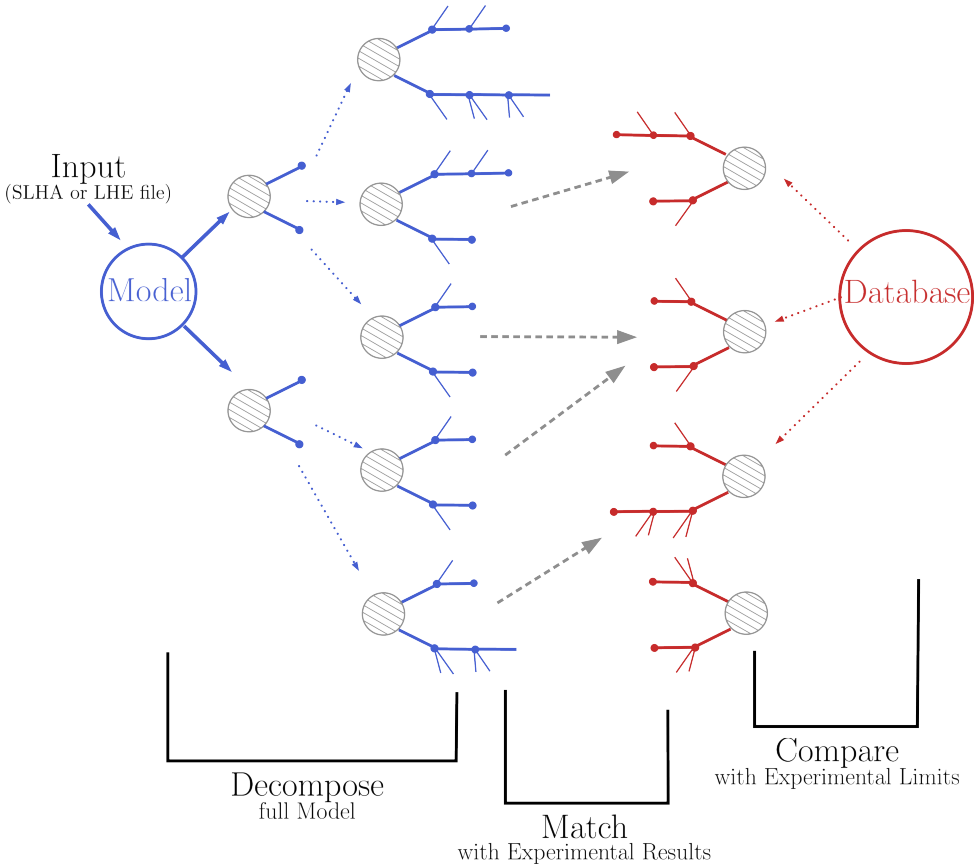


Figure 3.6: Scheme of SModelS working principle.

needs all the pair-production cross-sections, all the branching ratios, and the particle masses[4]. The first step of the decomposition is to consider all possible pair-productions $pp \to AB$. Since the BSM model is $\mathcal{Z}_2$-symmetric, $A$ and $B$ are necessarily BSM particles. The second step is to consider all the possible decays of both $A$ and $B$. Because of the $\mathcal{Z}_2$-symmetry again, the BSM particles can only decay to a BSM and an SM particle, $A \to A'X$ ($B \to B'Y$) where $X$ ($Y$) is an SM particle. The BSM particles can then decay again and again until reaching the LSP. By this decomposition process, SModelS stores all the possible combinations of pair-production and decays, most of which are asymmetrical, *i.e.* the upper and lower decay branches are different. The resulting processes are

[4]Since its version 2.0.0, SModelS can handle width-dependent results so the decay widths must be specified together with the branching ratios.

called *topologies*. Taking into account the decays, they are defined with a weight which is the cross-section rescaled with the branching ratios as explained previously in this section: $\sigma \times \mathrm{BR}_1 \times \mathrm{BR}_2 \times ...$ The last stage is the matching, which associates every topology with an analysis from the database having the same decay patterns. Since most topologies are asymmetrical, several can not be associated with a search, and contribute to the so-called *missing topologies*. Depending on if the analysis is a UL type or an EM type one, the topology is constrained using the method described just above. The output of SModelS is then the list of different constraints that originated from all the topology/analysis matches. The model is thus considered excluded if the most sensitive analysis excludes the associated topology.

To describe both types of results, UL and EM, under the same paradigm, SModelS computes a so-called $r$-value to present the different constraints. In the case of UL results, the latter is defined as

$$r = \frac{\sigma \times \mathrm{BR}_1 \times \mathrm{BR}_2 \times ...}{\sigma_{\mathrm{UL}}}, \tag{3.5}$$

By definition, $\sigma_{\mathrm{UL}}$ is the maximum value allowed for the cross-section at 95% exclusion CL. Then if $r$ is larger than one, the model is excluded, otherwise, it is allowed. Here $\sigma_{\mathrm{UL}}$ is simply taken from the UL map implemented in the SModelS database, for the given mass parameter given as inputs. In the case of EMs, the $r$-value is

$$r = \frac{\sum_a \epsilon_a \times \sigma_a \times \mathcal{BR}_a}{[\sum_a \epsilon_a \times \sigma_a \times \mathcal{BR}_a]_{\mathrm{UL}}} = \frac{N}{N_{\mathrm{UL}}}, \tag{3.6}$$

where $a$ runs over the topologies available in the same SR. Indeed, in the case of EMs, we are dealing with a number of events, hence the possibility to sum the contributions from all processes to the same SR. $\mathcal{BR}_a$ is understood to be the product of all branching ratios for the topology $a$: $\mathcal{BR}_a = \mathrm{BR}_{a1} \times \mathrm{BR}_{a2} \times ...$ The right-hand side of eq. (3.6) shows that the $r$-value in the case of EMs is exactly the ratio of the number of events and the UL on the number of events. Having the number of events, one would in principle compute a CL (using the $\mathrm{CL}_s$ prescription described in the next section) to determine if the model is excluded or not. Moreover, the denominator of eq. (3.6) is computed using the $\mathrm{CL}_s$ prescription to infer the UL. But as said previously, this is done as such in SModelS to present both EM and UL results on the same footing. Finally, let us notice that eq. (3.6) describes the $r$-value for a single SR, which brings us to an important point. Indeed, each analysis has several SRs and one needs to choose the constraint from the most sensitive SR unless information allowing the combination of the SRs is provided by the experimental collaboration[5]. This problem will be further discussed in the next section.

## 3.3 Statistical evaluation and limit setting

When confronting theoretical predictions with experimental observations, any scientific field needs the help of statistics. As mentioned multiple times, LHC experiments rely on the $\mathrm{CL}_s$ prescription to set exclusions on new physics. The $\mathrm{CL}_s$ prescription or $\mathrm{CL}_s$ method [103] is a particular case of hypothesis testing used in particle physics to avoid too strong exclusion limits. As a hypothesis test, it relies on likelihood functions which

[5]Full simulation tools also deal with this problem, as discussed in chapter 4.

represent the probability of the observed data to agree with the theoretical predictions. This section will present the principle of the $CL_s$ method employing a simple toy likelihood. Then two different ways of communicating likelihood information will be discussed; the simplified likelihoods and the full likelihoods.

### 3.3.1 The $CL_s$ method

As stated in [104], "the method's name is very descriptive, but also misleading, as the CLs exclusion region is not a confidence interval". Indeed, as we are about to discuss, the $CL_s$ is a ratio of two $p$-values, rather than a confidence level. The standard statistical method would be to take as null hypothesis $\{H_0$*: the SM model alone*$\}$ and as alternative hypothesis $\{H_1$*: the BSM model to be tested*$\}$[6], then compute the $p$-value to reject or not $H_0$ in favor of $H_1$. The $CL_s$ ratio "seeks to modify the frequentist $p$-value to avoid false exclusion when the experiment is insensitive to the signal" [104].

Let us define a very simple toy model and its likelihood, which will then serve as foundation for building more complex likelihoods. Let $n_{\text{obs}}$ be the number of events observed at the LHC for a given signature, $b$ the number of events predicted by the SM (or so-called SM background) and finally $s$ the number of events predicted by the alternative BSM model (the new physics signal). Then the standard likelihood definition is

$$\mathcal{L}(\mu) = P\left(n_{\text{obs}}|\mu s + b\right) = \frac{(\mu s + b)^{n_{\text{obs}}}}{n_{\text{obs}}!} e^{-(\mu s+b)}, \tag{3.7}$$

where $\mu$ is a free parameter called *signal strength modifier*. The above equation describes the probability to get $n_{\text{obs}}$ with a Poissonian of parameter $\mu s + b$, *i.e.* the probability to get $n_{\text{obs}}$ assuming $\mu s + b$ is the most probable outcome. $\mu = 0$ means the Poissonian parameter is $b$, hence it corresponds to the null hypothesis (also called the background-only hypothesis). $\mu = 1$ means the Poissonian parameter is $s + b$, hence corresponding to the alternative hypothesis. The signal strength modifier is then a very useful parameter to test the different hypotheses and also to infer upper limits (see below). The next step is to choose a test statistic from which to infer a $p$-value. By the Neyman-Pearson lemma, the most powerful[7] test statistic is the likelihood ratio test

$$q_\mu = -2\log\left(\frac{\mathcal{L}(\mu)}{\max_\mu \mathcal{L}(\mu)}\right) = -2\log\left(\frac{\mathcal{L}(\mu)}{\mathcal{L}(\hat{\mu})}\right), \tag{3.8}$$

where the likelihood in the denominator is maximized over $\mu$ and $\hat{\mu}$ is defined as the $\mu$ that maximizes the likelihood. To compute $p$-values, $q_\mu$ is considered a random variable that depends on the observed data. From a frequentist point of view, we could get the distribution of $q_\mu$ by repeating the experiment of measuring $n_{\text{obs}}$ a lot of times, compute $q_\mu$ each time and draw the distribution in a histogram. Finally, the $CL_s$ is defined as

$$\text{CL}_s = \frac{\text{CL}_{s+b}}{\text{CL}_b}, \tag{3.9}$$

[6] All BSM models are extensions of the SM so the new physics signal will be the addition of contributions from the SM (SM background) and the BSM signal, assuming there is no interference between the SM background and the new signal.

[7] The power of a test statistic, commonly denoted as $1 - \beta$, is the probability for the test to reject $H_0$ when $H_1$ is true. In other words, it is the probability of correctly rejecting $H_0$ when it should be rejected.

where $\mathrm{CL}_{s+b}$ is the $p$-value in the alternative hypothesis and $\mathrm{CL}_b$ in the background-only hypothesis

$$\mathrm{CL}_{s+b} = \int_{q_{\mu,\mathrm{obs}}}^{\infty} f(q_\mu|\mu = 1) \quad \text{and} \quad \mathrm{CL}_b = \int_{q_{\mu,\mathrm{obs}}}^{\infty} f(q_\mu|\mu = 0), \tag{3.10}$$

where $f(q_\mu|\mu = \mu')$ is the probability density function of $q_\mu$. Figure 3.7 illustrates eq. (3.10). The blue line shows the distribution of $q_\mu$ of the background-only hypothesis and

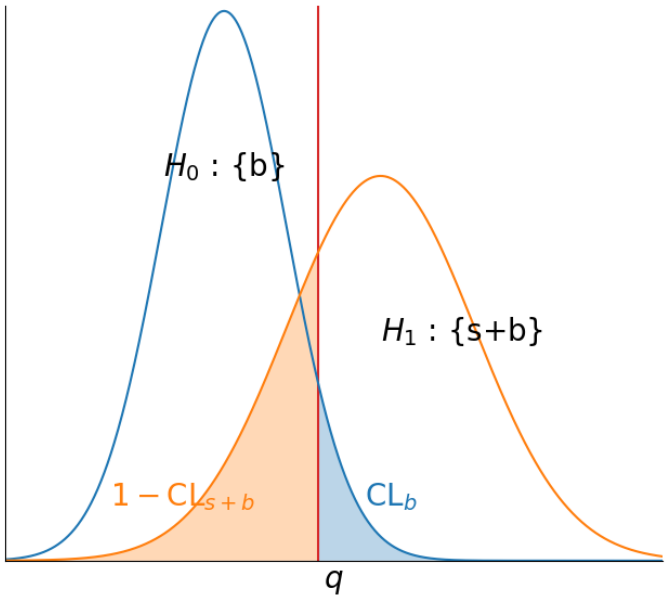


Figure 3.7: Illustration of the $\mathrm{CL}_s$ method.

the orange line of the alternative hypothesis. The vertical red line is $q_{\mu,\mathrm{obs}}$. The blue and orange shaded surfaces then correspond to $\mathrm{CL}_b$ and $1 - \mathrm{CL}_{s+b}$, respectively. If one wants to exclude a model with a CL of $\alpha$, then the obtained $\mathrm{CL}_s$ must be smaller than $1-\alpha$ for the model to be excluded. In particle physics, $\alpha$ is set to 0.95. By Wilk's theorem, the distribution for $q_\mu$ can be approximated by a $\chi^2$ and [105] uses this fact to give asymptotic approximations for the value of the $\mathrm{CL}_s$.

To compute an upper limit, one has to compute $\mathrm{CL}_{s+b}$ with an arbitrary $\mu$, $\mathrm{CL}_s(\mu)$ is thus a function depending on $\mu$. One finds $\mu_{\mathrm{UL}}$ by varying $\mu$ until $\mathrm{CL}_s(\mu_{\mathrm{UL}}) = 1-\alpha = 0.05$. This is exactly equivalent to the process of varying the cross-section to find $\sigma_{\mathrm{UL}}$ since $s = \epsilon\sigma\mathcal{L}$ directly depends on $\sigma$. It follows that $\sigma_{\mathrm{UL}} = \mu_{\mathrm{UL}}\sigma$.

One final important concept is the one of *expected* exclusion. The sensitivity of an analysis is estimated by considering the would-be constraint if the number of observed events was exactly the SM prediction. In other words, the number of observed events is replaced with the SM background, $n_{\mathrm{obs}} = b$, in the likelihood definition of eq. (3.7). The $\mathrm{CL}_s$ method is then applied to get the so-called *expected* $\mathrm{CL}_s$. BSM searches typically have many (in some cases hundreds of) SRs and the experimental collaborations use more complex likelihoods enabling the statistical combination of non-overlapping SRs. The

naive approach would be to simply multiply the individual likelihoods of each SR but the correlations between SRs must be considered. Without information about the correlations, one could naively use the most constraining SR. This is however not very robust because which SR is the most constraining can be dependent on statistical fluctuations of the observed number of events. The standard paradigm for reinterpretation is then to use the most sensitive SR to set the constraints, this is the so-called best-SR approach. Moreover, expected limits can be useful to compare the sensitivity of different analyses, *e.g.* when the same model triggers several LHC signatures.

The principle of the $CL_s$ method has been explained with a simple toy likelihood. The next section will present two ways to define more realistic likelihood definitions. The $CL_s$ method will however remain the same and will just be applied to other likelihoods.

### 3.3.2 Simplified likelihoods

With the best-SR approach, the final constraint is based on the information from a single SR. Combining the SRs using the correlation information from the likelihoods is then crucial to fully exploit the potential of the data and reproduce more precisely the experimental results since this is the approach followed by the experimental collaborations.

The CMS collaboration sometimes provides this kind of information, through covariance matrices that can be used in the "simplified likelihood" scheme [106]. The latter consists in multiplying the individual SR likelihoods and adding an uncertainty $\theta_i$ to the SM background that is constrained by a multi-variate Gaussian

$$\mathcal{L}(\mu, \theta_i) = \prod_{i=1}^{N} \frac{(\mu s_i + b_i + \theta_i)^{n^i_{\text{obs}}} e^{-(\mu s_i + b_i + \theta_i)}}{n^i_{\text{obs}}!} \exp\left(-\frac{1}{2}\vec{\theta}^T V^{-1} \vec{\theta}\right), \tag{3.11}$$

where $i$ runs over the $N$ SRs and $V$ is the covariance matrix. The $\theta_i$ are free parameters that are constrained by the Gaussian term on the very left of the above equation. Let us simplify the above to a single SR for the sake of the explanation

$$\mathcal{L}(\mu, \theta) = \frac{(\mu s + b + \theta)^{n_{\text{obs}}} e^{-(\mu s + b + \theta)}}{n_{\text{obs}}!} \exp\left(-\frac{\theta^2}{2\sigma^2}\right). \tag{3.12}$$

It is worth noticing that the above equation shows how the uncertainty is included in the single-SR case, and thus in the best-SR approach. The covariance matrix reduces to $\sigma^2$ since these are the diagonal terms of the covariance matrix. When maximizing the likelihood, $\theta$ will tend to increase in the left Poissonian term but the Gaussian on the right will keep $\theta$ from increasing too much with a Gaussian centered at zero and with a standard deviation of $\sigma$ that corresponds to the uncertainty on the SM background number of events. With the likelihood of eq. (3.11) combining the SRs, the $\theta_i$ are constrained similarly. The simple Gaussian is however replaced by a multivariate Gaussian that regulates the $\theta_i$ in a way that includes the effects of the correlations between SRs.

This method is called simplified likelihood because it is an approximation of the full likelihood which details every source of uncertainty. Indeed, experiments have to consider numerous sources of uncertainties that are often not Gaussian and therefore not always symmetric. The covariance is a quadratic sum of all the uncertainties in each SR and then the simplified likelihood assumes that this *global* uncertainty has a symmetrical Gaussian behavior.

It was part of the work of this thesis to implement simplified likelihoods in MadAnalysis5. The latter will be discussed in chapter 4.

### 3.3.3 Full likelihoods

In 2019, the ATLAS collaboration has started to provide full likelihoods [107]. Most ATLAS searches are using a `ROOT` library called `HistFactory` [108] to define their statistical models. To provide the statistical models publicly, the ATLAS collaboration implemented `pyhf` [109, 110], which is a pure `Python` implementation of `HistFactory` enabling the use of their `JSON` likelihoods in `Python`. Reference [107] defines a generic likelihood as follows

$$p(\boldsymbol{n}, \boldsymbol{a}|\boldsymbol{\eta}, \boldsymbol{\chi}) = \underbrace{\prod_{c\in\text{channels}} \prod_{b\in\text{bins}} \text{Pois}\Big(n_{cb}|\nu_{cb}(\boldsymbol{\eta}, \boldsymbol{\chi})\Big)}_{\text{measurements}} \underbrace{\prod_{\chi} c_\chi(a_\chi|\chi)}_{\text{constraints}}, \tag{3.13}$$

where the SRs correspond to the *bins* (running index $b$) that are subdivided into *channels* (running index $c$). The $n_{cb}$ parameters correspond to the observed number of events ($n^i_{\text{obs}}$ in the simplified likelihoods). The $a_\chi$ parameters are the auxiliary measurements, typically the value of a standard deviation if the constraint function is Gaussian. $\eta$ and $\chi$ are the unconstrained and constrained parameters, respectively. They are constrained by the constraint terms $c_\chi$ (in the simplified likelihood, the constraints terms were regrouped and approximated by the multi-variate Gaussian).

The concept of modifiers is used to describe uncertainties. They are split into two types: additive and multiplicative modifiers. $\nu_{cb}$ represents the total number of events (the sum of the SM background and the new physics signal) and the modifiers enter its definition of $\nu_{cb}$ as follows

$$\nu_{cb}(\boldsymbol{\eta}, \boldsymbol{\chi}) = \sum_{s\in\text{samples}} \nu_{scb}(\boldsymbol{\eta}, \boldsymbol{\chi}) = \sum_{s\in\text{samples}} \underbrace{\prod_{\kappa} \kappa_{scb}(\boldsymbol{\eta}, \boldsymbol{\chi})}_{\text{multiplicative modifiers}} \left(\nu^0_{scb}(\boldsymbol{\eta}, \boldsymbol{\chi}) + \underbrace{\sum_{\Delta} \Delta_{scb}(\boldsymbol{\eta}, \boldsymbol{\chi})}_{\text{additive modifiers}}\right), \tag{3.14}$$

where $\nu_{scb}$ are the individual sample contributions to $\nu_{cb}$. ATLAS typically provides background-only `JSON` likelihoods, where the background contributions are subdivided into samples corresponding to the different background contributions. The total number of events is the sum of the number of events in each sample after all the modifiers have been applied to the nominal number of events in the sample. The right-hand side shows the difference between multiplicative and additive modifiers. It is worth noticing that all modifiers have either Gaussian or Poissonian constraint terms. However, not all Gaussian terms are centered in zero. In other words, they are asymmetrical. This is where the simplified likelihood approximation can be inaccurate since it reduces all uncertainties to a single symmetrical Gaussian uncertainty. For more details, Table 1 in ref. [107] shows all the possible modifiers that can be defined in a `JSON` likelihood.

For comparison, in the case of simplified likelihoods, $\mu$ is the only unconstrained multiplicative modifier ($\kappa_{scb}$ in eq. (3.14)) and the $\theta_i$ are additive modifiers ($\Delta_{scb}$ in eq. (3.14)) constrained by Gaussian terms. As mentioned above, $\nu_{cb}$ is the sum of the new

physics signal and the SM background contributions which are subdivided into *samples*[8]. Simplified likelihoods only have two samples: $s$ for the new physics signal and $b$ for the SM background, while the full ATLAS likelihoods detail the full set of background contributions.

For reinterpretation, users then need the background-only `JSON` likelihood, in which they must include the new physics number of events on their own, by adding a new sample into all the SRs. A convenient way to do this is to use a `JSON` patch which can perform actions such as adding, removing, or modifying the content of `JSON` files. The interfaces to `pyhf` implemented in MadAnalysis5 (chapter 4) and SModelS (chapter 5) are based on this principle.

[8]Using again the example of the di-tau plus missing energy search [57], six background contributions lead to the same final state: multi-jet, W+jets, Z+jets, top quark, multi-boson and Higgs. Since the multi-jet contribution is divided into two samples, there are then seven samples in the associated background-only `JSON` file.

# Chapter 4

# Signal region combination with full and simplified likelihoods in MadAnalysis5

As described in the previous chapter, the combination of SRs in reinterpretation tools allows physicists to obtain more precise constraints and to use more of the physics sensitivity of the data. This topic makes an important part of the work presented in this thesis. The present chapter reproduces the paper [111], which discusses the implementation in MadAnalysis5 of the simplified likelihoods enabling the use of covariance matrices from CMS and of an interface to `pyhf` enabling the use of full likelihoods from ATLAS. The physics impact is demonstrated by a direct comparison of MadAnalysis5 results with official ATLAS and CMS results. A case study of a more realistic MSSM scenario, with more complex decay patterns than the individual simplified models, is also used for demonstrating the physics gain. My contribution to this work was the implementation of the simplified likelihood method in MadAnalysis5.

## 4.1 Introduction

Searches for new physics at the LHC are typically performed in specific bins of kinematic distributions, so-called SRs, designed to maximise the number of events from the hypothesised signal with respect to the number of "background" events originating from Standard Model processes. In parallel, control and validation regions are defined in the phase space where no or very little signal from new physics is expected. A statistical analysis is then performed to evaluate the confidence level of the hypothesised BSM scenario, and claim evidence for or set a limit on the new particles of this scenario.

Reinterpretation studies [112, 113] outside the experimental collaborations, like achieved with MadAnalysis 5 [80], aim at reproducing this process for BSM scenarios different from those considered in the original experimental publication. This makes it possible for the community as a whole to test a much larger variety of theories against LHC results than would be possible purely within the experimental collaborations. Moreover, it enables phenomenologists to pursue global analyses, give detailed feedback on the physics impact of the experimental results, and suggest target BSM scenarios for future investigations. An overview of publicly available reinterpretation tools, together with an extensive

discussion on which information is needed from the experimental collaborations, is given in [113].

Among the essential information figure the statistical models used to derive results in experimental analyses [114]. In this context, a long-standing problem for reinterpretation studies consists of the statistical combination of disjoint SRs, as the information on the correlation of uncertainties is not always provided by the experimental collaborations. In the absence of appropriate correlation information, it is common practice to use only the SR with the *best expected* sensitivity to the BSM parameter point under investigation (colloquially called the "best SR") for the statistical evaluation, *e.g.* for limit setting. The reason is that the choice of SR, and thus the conclusions drawn from data, must not depend on statistical fluctuations which affect observed data. This entails a number of problems. First of all, in the best-SR approach only a part (sometimes a very small fraction) of the available data is used, which can lead to false conclusions. Typically this causes a loss in sensitivity, but, as we will see, it can also lead to too strong exclusions. Furthermore, if the best SR changes from point to point in a scan, this can lead to numerical instabilities in global fits. We refer to [114] and references therein for more discussion of these and related issues.

The CMS collaboration provides correlation information for some of their searches for SUSY and other new particles in the form of approximate covariance matrices, designed to build a so-called *simplified likelihood* [115]. The underlying assumptions are that systematic uncertainties in the signal modelling can be neglected, and that uncertainties on the background contributions are Gaussian in shape (implying that the distribution of the number of background events is symmetric around the expectation). Although approximate, the combination of SRs through this simplified likelihood scheme greatly improves the precision and constraining power of analysis recasts relative to the usage of the best SR only.[1]

The ATLAS collaboration follows a different strategy: instead of approximate SR correlations, the collaboration recently started to provide *full statistical models* in JSON-serialised format [107]. These statistical models, based on HistFactory [108], describe the complete probabilistic dependence of the observable data on both the parameters of interest and the nuisance parameters. When the observed numbers of events are entered, this becomes the likelihood function (see [114] for details). The JSON-serialised format enables the usage of the HistFactory structure outside the Root framework, in particular within the pyhf package [110, 117]. pyhf can conveniently be used for signal patching, evaluation of likelihoods, computation of $CL_s$ values, *etc.*. Moreover, it also permits to prune a full statistical model and derive a simplified version of it. The Simplify [118] tool, for instance, takes a given full statistical model encoded in the JSON format and derives a simplified one in which all nuisance parameters are combined into a single one, and in which all contributions to the background are merged. Such simplified statistical models often (but not always) yield equivalent results for a much smaller computing time, as will be exemplified below.

It is now the task of the public reinterpretation tools to make use of this information. Statistical models from ATLAS and covariance matrices from CMS are already incorporated in SModelS [94, 119] in the context of re-using simplified-model results. In this

[1]Non-Gaussian effects, which can become important for instance when uncertainties are systematics dominated, could be accommodated in an extended simplified likelihood framework as proposed in [116].

| Analysis ID | Short description | # SRs | Statistical information |
|---|---|---|---|
| ATLAS-SUSY-2018-04 | Stau search, 2 taus | 2 | full model, all SRs |
| ATLAS-SUSY-2018-06 | EW-inos, 3 leptons | 2 | simplified model, all SRs |
| ATLAS-SUSY-2019-08 | EW-inos, $WH(\to b\bar{b})$ | 9 | full model, all SRs |
| ATLAS-SUSY-2018-31 | Multi-$b$ sbottom search | 8 | full model, 3+3+1 SRs |
| CMS-SUS-16-039 | EW-inos, multi-lepton | 158 | cov. matrix, 44 SRs |
| CMS-SUS-16-048 | OS soft leptons | 21 | cov. matrix, 12+9 SRs |
| CMS-SUS-17-001 | Stops, 2 OS lept. | 3 | cov. matrix, 3 SRs |
| CMS-SUS-19-006 | Multi-jet gluino/squarks | 174 | cov. matrix, all SRs |
| CMS-EXO-20-004 | Multi-jet SR search | 66 | cov. matrix, all SRs |

Table 4.1: Overview of MadAnalysis 5 recast codes for which SR combination is available. The last column specifies the statistical information used for the combination. Here, "full (simplified) model" stands full (simplified) JSON-serialized HistFactory model from ATLAS, to be used with pyhf, while "cov. matrix" stands for covariance matrix in the simplified likelihood approach of CMS. Details are given in section 4.3.

paper, we present their implementation and usage in MadAnalysis 5 for the purpose of full analysis recasts.[2] We first explain in section 4.2 the technical implementation through the extension of the MadAnalysis 5 `.info` XML files pertaining to each analysis. In section 4.3 we present the analyses for which SR combination is currently available (see table 4.1), comparing the limits obtained in the best-SR, simplified likelihood and/or full likelihood approaches. In section 4.4 we illustrate the gain in physics reach by means of a concrete example within the MSSM. Section 7.2.5 contains our conclusions.

## 4.2 Technical implementation

In this section we summarise how statistical models in JSON-serialised format and covariance matrices provided for a simplified likelihood treatment can be used in the MadAnalysis 5 framework. The functionality of SR combination can be turned on/off from the code's command line interface via the command:

```
set main.recast.global_likelihoods = <on or off>
```

where the default is "`on`".

The information needed for the statistical interpretation of an analysis recast is given in the `.info` XML file shipped with that analysis, which has to be located in the same directory as the analysis C++ files. For analyses implemented in the `PAD` (`PADForSFS`) format, this consists of the `PAD/Build/SampleAnalyzer/User/Analyzer` (`PADForSFS/Build/SampleAnalyzer/User/Analyzer`) directory [80, 82]. The `.info` XML file specifies for each SR the observed number of events `<nobs>`, the number of expected Standard Model events

[2]Covariance matrices can also be used in GAMBIT's ColliderBit [120]; a ColliderBit interface to pyhf is under development, as is the usage of correlation information in CheckMATE [77].

<nb> and the associated $1\sigma$ uncertainty <deltanb>; the latter might be split into its statistical and systematic components: <deltanb_stat> and <deltanb_sys> [121]. This has to be extended by the appropriate information about the JSON-serialised statistical model or covariance matrix as explained in the following.

### 4.2.1 Usage of JSON-serialised HistFactory models: interface to pyhf

In order to employ the statistical model information embedded in JSON files provided by the ATLAS collaboration, the analysis' .info file needs to be extended by <pyhf> blocks. These specify the filename(s) of the JSON file(s) and the associated channels and region names within the analysis. In the pyhf language, a channel refers to an ordered ensemble of signal regions treated correlatively in the statistical model. The structure of such a <pyhf> block reads:

```
<pyhf id="Global">
  <name>analysisID.json</name>
  <regions>
    <channel name="Channel1">Region1_1 Region1_2 Region1_3</channel>
    <channel name="Channel2">Region2_1 </channel>
    <channel name="Channel3" is_included="True"> </channel>
    <channel name="Channel4" is_included="False"> </channel>
  </regions>
</pyhf>
```

The id of a <pyhf> block is the label of the corresponding exclusion limit calculation, that is further propagated to the output file to present the results (see below). For analyses involving a single JSON file for all SRs, we recommend setting this label to "Global"; for analyses with multiple JSON files (for the combination of different subsets of SRs), each <pyhf> block needs to be assigned a unique identifier.

The following child block <name> declares the name of the JSON file. This follows the same naming convention as that employed for the analysis implementation, with an optional extra identification suffix if needed.[3] This JSON file needs to be located at the same path as the MadAnalysis 5 information file. For the ATLAS analyses discussed in section 4.3, this is automatically realised after the installation of a local version of the MadAnalysis 5 Public Analysis Database through the MadAnalysis 5 command line interface (install PAD or install PADforSFS).

In the next child of the <pyhf> block, regions are collected into multiple channels. Each channel includes the name of the recast signal regions corresponding to that specific channel. The channel names must correspond to those used in the JSON file, while the Region<i_j> names have to match the region names chosen in the recast implementation. Usually this pertains to SRs, although control and validation regions could be recast as well. The ordering of the regions is crucial and needs to follow that of the JSON file given by the ATLAS collaboration. Each channel can have a different number of regions,

[3]For instance, such suffixes can be used to distinguish between full and simplified JSON files, or JSON files combining different subsets of SRs.

but it must match the available number of regions given in the JSON file. A concrete example from the ATLAS-SUSY-2018-31[122] analysis, which has three sets of disjoint SRs (regions A, B and C), is [123]

```
<pyhf id="RegionA">
  <name>atlas_susy_2018_31_SRA.json</name>
  <regions>
    <channel name="SR_meff">SRA_L SRA_M SRA_H</channel>
    <channel name="VRtt_meff"></channel>
    <channel name="CRtt_meff"></channel>
  </regions>
</pyhf>
```

and analogously for regions B and C. Since VR and CR are not included in the recast code, the corresponding channels are left empty.

Upon execution, MadAnalysis 5 patches the region counts onto the JSON file, thus creating a JSON patchset for the particular BSM hypothesis. The latter is then evaluated through a call to pyhf. More concretely, by patching the signal yields to background samples, MadAnalysis 5 creates a dynamic statistical model which is then used to compute $p$-values and test statistics for a single parameter of interest, the signal strength $\mu$. Expected and observed limits on the cross section (in pb) are determined via optimising the signal strength to find the 95% CL upper limit, $\mu_{\rm UL}$. The $1-{\rm CL}_s$ value, on the other hand, is computed by setting $\mu = 1$. For details, see [105].

By default, the creation of the patchset includes only channels with at least one region; empty channels (which do not have any region) are removed from the statistical model. Typically this concerns control and validation regions, like for the ATLAS-SUSY-2018-31 example above. So far, MadAnalysis 5 recast codes do not emulate these regions, because they are not supposed to be sensitive to any BSM signal.[4] Removing them from the statistical model gives a good enough approximation for most purposes and considerably reduces computation time. In some cases however (for instance when the correct statistical evaluation requires a combined fit to signal and control regions), it can be relevant to keep a given channel even if it is not reproduced in the recast code. This is achieved with the `is_included` attribute in the `<channel>` element. If present, it informs MadAnalysis 5 whether or not to include a given channel while forming the statistical model, overriding the default behaviour. If `is_included` is set to `"True"` for an empty channel, it is hence included in the likelihood calculation assuming that the BSM signal yields in all its bins are zero. An example where this matters is the electroweakino (EW-ino) search ATLAS-SUSY-2018-06 [124], which has two signal and two control regions and whose `<pyhf>` block in the `atlas_susy_2018_06.info` file reads [125]

```
<pyhf id="Global">
  <name>atlas_susy_2018_06_simplified.json</name>
  <regions>
    <channel name="SRlow_cuts"> SR_low </channel>
    <channel name="SRISR_cuts"> SR_ISR </channel>
```

[4] It will, however, be good to include them in the future (whenever feasible) in order to be able to check possible signal contamination in CRs and/or to study cross-analysis correlations.

```
    <channel name="CRlow_cuts" is_included="True"> </channel>
    <channel name="CRISR_cuts" is_included="True"> </channel>
  </regions>
</pyhf>
```

This is also an example of an analysis recast which makes use of a simplified statistical model (derived with the SIMPLIFY tool from the full statistical model), as indicated by the `_simplified` suffix in the JSON filename. We come back to this feature in section 4.3.

We now turn to the format of the output file generated by MADANALYSIS 5. Whenever the exclusion is computed by means of the pyhf package, the results are reported in the `CLs_output_summary.dat` file in the form

```
<set> <tag> <SR> <best?> <exp> <obs> <CLs> ||
```

just after the results for individual SRs. The successive elements are the dataset name `<set>`, the analysis name `<tag>`, the description of the subset of combined SRs `<SR>` that contains an explicit `[pyhf]` tag, the flag for best combination (0 or 1), the expected and observed cross section upper limits at 95% CL, and finally the exclusion level, $1 - \mathrm{CL}_s$; see [80] for details. No statistical error information is printed (to the right of the double bars), as it is already accounted for in the likelihood calculation. A concrete example reads (values rounded for space reasons)

```
smpl atlas_susy_2018_31 [pyhf]-RegionA-profile  1  0.0016  0.0011  0.9787 ||
```

where `smpl` stands for the identifier of the given event sample, and where a `[pyhf]` tag identifies the combined result. If there is only one likelihood profile, it is always identified as the "best" combination. If there are several region combinations, the one with the lowest expected limit on the cross section is flagged as the "best" one.

A comment is in order regarding the meaning of "expected" limit. pyhf by default reports post-fit (or "aposteriori") expected values, *i.e.* limits after a fit of the background expectations to the observed data.[5] This differs from the usual definition of expected limits in MADANALYSIS 5, in which the observed numbers of events in each SR are set equal to the number of expected background events [80], and which we here call "apriori" expected limits. To ensure consistency between the individual and combined SRs results, MADANALYSIS 5 can now compute both "apriori" and "aposteriori" expected limits. The choice is done via the command

```
set main.recast.expectation_assumption = <apriori or aposteriori>
```

The default is "`apriori`", in which case expected limits from pyhf are determined from a patchset in which the observed numbers of events in each SR are replaced by the number of expected background events. In contrast, when setting the expected-limit computation to "`aposteriori`", the default pyhf output is taken for the combined result, while for individual SR results the numbers of background events are set equal to the observed numbers of events.

[5] For details, see the pyhf discussions #1367 and #1619 on GITHUB.

### 4.2.2 Usage of simplified likelihoods through covariance matrices

For the combination of SRs via the simplified likelihood approach [115], we adopted the implementation in SModelS [94], *i.e.* its Python module `simplified_likelihood.py`, for use in MadAnalysis 5. In order to comply with the MadAnalysis 5 framework [80], the covariance information has to be included in the `.info` XML file associated with the analysis recast code. For each SR, the covariance with every other SR can be supplied. There is thus a list of covariances with two entries: the paired regions and the value of the associated covariance. The (self-explanatory) new standard syntax of the `.info` file reads:

```
<analysis id="analysis name" cov_subset="Global">
    <lumi>...</lumi>
    <region type="signal" id="region name">
        <nobs> ... </nobs>
        <nb> ... </nb>
        <deltanb_stat> ... </deltanb_stat>
        <deltanb_syst> ... </deltanb_syst>
        <covariance region="first \acrshort{sr} name">...</covariance>
        <covariance region="second \acrshort{sr} name">...</covariance>
        ...
        <covariance region="last \acrshort{sr} name">...</covariance>
    </region>
    ...
</analysis>
```

This specifies, for each SR, the number of observed events `<nobs>`, expected background events `<nb>`, their statistical (`<deltanb_stat>`) and systematic (`<deltanb_syst>`) uncertainties,[6] as well as the covariance matrix elements linking the current region to other regions.

If a covariance element is not supplied, it is considered as a zero entry in the covariance matrix. In addition, if a region does not contain any covariance field, the region itself is omitted from the combination. This feature can be useful if the covariance matrix is available only for a subset of SRs, like for example in the CMS multilepton plus missing transverse energy search CMS-SUS-16-039 [126], which provides covariances only for the 44 SRs of type A out of a total of 158 SRs (see table 4.1). The above format also enables the use of multiple covariance matrices in the same analysis (for individually combining subsets of SRs) as in, *e.g.*, CMS-SUS-16-048 [127].[7] In order to keep trace of which subset of SRs is combined, we introduce a `cov_subset` attribute, by which users can provide a brief description of the subset of SRs to which the covariance matrix applies. If there is only one covariance matrix, `cov_subset` can conveniently be specified in the `<analysis>` tag. As in section 4.2.1, we recommend the label "`Global`" if all SRs are combined. In

[6] Instead of `<deltanb_stat>` and `<deltanb_syst>`, which are added in quadrature on run time, it is also possible to give the total uncertainty using the tag `<deltanb>` [121].

[7] This is also used in the recast implementation [128, 129] of the CMS disappearing tracks search CMS-EXO-19-010 [47] for the combination of statistically independent datasets from different years.

case of multiple covariance matrices, the `cov_subset` attributes are set directly within the `<covariance>` tags. For the CMS-SUS-16-039 example, we thus have [130]:

```
<analysis id="cms_sus_16_039" cov_subset="SRs_A">
```

and in the case of the CMS-SUS-16-048 analysis, we have [131]:

```
<analysis id="cms_sus_16_048">
  <lumi>35.9</lumi>
  <region type="signal" id="Ewkino_lowMET_M_4to9">
    <nobs>2</nobs>
    <nb>3.5</nb>
    <deltanb>1.0</deltanb>
    <covariance region="..." cov_subset="Ewkino">1.29</covariance>
    <covariance region="..." cov_subset="Ewkino">0.33</covariance>
   ...
  <region type="signal" id="stop_lowMET_PT_5to12">
    <nobs>16</nobs>
    <nb>14.0</nb>
    <deltanb>2.3</deltanb>
    <covariance region="..." cov_subset="stop">6.09</covariance>
    <covariance region="..." cov_subset="stop">4.71</covariance>
   ...
</analysis>
```

The results from the simplified likelihood combination are printed in the output file `CLs_output_summary.dat` in the form

```
  <set> <tag> <cov_subset> <best?> <exp> <obs> <CLs> ||
```

analogous to the output format described in section 4.2.1. The successive elements are the dataset name, the analysis name, the description of the subset of combined SRs (with an `[SL]` prefix indicating that SR combination is performed via the simplified likelihood approach), the flag for best combination (0 or 1), the expected and observed cross section upper limits at 95% CL, and finally the exclusion level, $1 - \mathrm{CL}_s$. A concrete example reads

```
  defaultset  cms_sus_16_039  [SL]-SRs_A  1  10.4852  11.1534  0.9997 ||
```

The statistical error, usually provided after the double bar, is not printed as it is already encoded in the simplified likelihood calculation. For the expected limits, "`apriori`" and "`aposteriori`" options are available as explained in the previous subsection.

## 4.3 Included analyses, validation

Signal region combination is currently available for four ATLAS analyses [122, 132, 133, 124] (recast codes [123, 134, 135, 125]) and five CMS analyses [126, 127, 136, 137, 138] (recast codes [130, 131, 139, 140, 141, 142]) in MadAnalysis 5. An overview is given in table 4.1. They are included in any local installation of the Public Analysis Database (PAD)

of MadAnalysis 5, achieved via the commands `install PAD` and `install PADForSFS`. In this section, we briefly describe these analyses and illustrate how SR combination improves the quality of the reinterpretation. To this end, we compare mass limits obtained in the best-SR, simplified likelihood and/or full likelihood approaches to the official limits from the ATLAS or CMS collaborations for specific simplified model scenarios used in the experimental publications.

The tool chain that we use for Monte Carlo event simulation is as follows. The hard scattering processes relevant for the investigated simplified models are simulated with MadGraph5_aMC@NLO (MG5aMC) version 2.6.5 [143]. LO matrix elements are generated from the built-in `MSSM_SLHA2` model implementation [144] for the SUSY processes considered, and from the public model file [145] for the $t$-channel dark matter example. For each process, we convolute the LO matrix element with the LO set of NNPDF 2.3 parton distribution functions [146, 61], and we generate 200,000 signal events per sample point to limit Monte Carlo uncertainties. Pythia version 8.240 [67] is used to handle unstable particle decays, parton showering, and hadronisation; the emulation of detector effects is done either with Delphes 3 [72] or the SFS framework [82], depending on the specification of each recast analysis. All SUSY particles that do not appear in the simplified model considered are assumed to be decoupled.

Finally, for a 1:1 comparison with the "official" ATLAS and CMS limits, the LO cross sections from MG5aMC are re-scaled to the reference cross sections tabulated on [147] and used by the collaborations; these tabulated cross sections have been obtained with the NNLL-fast [148, 149, 150] and Resummino [151, 152, 153] programs, that provide the most precise predictions for SUSY total rates. Simplified statistical models are derived from the full ones provided by the ATLAS collaboration, by means of Simplify [118] version 0.1.10. The `pyhf` version employed in this work is 0.6.3.

**ATLAS-SUSY-2018-31 [122]:** This is a search for SUSY in final states with multiple $b$-jets and missing transverse energy. It specifically targets sbottom pair production, $pp \to \tilde{b}\tilde{b}^*$, followed by the cascade decay $\tilde{b} \to b\tilde{\chi}_2^0 \to bh\tilde{\chi}_1^0$. The produced Higgs bosons are assumed to further decay into a pair of possibly boosted $b$-tagged jets. The analysis has 8 SRs grouped into three classes (regions A, B, C), which target mass spectra of different levels of compression. It was the first one to publish its full statistical model on HEPData [154], and was used as the showcase in [107].

The analysis is implemented in MadAnalysis 5 within the SFS framework [82]. We here use version 2.0 of the implementation [123], which is compliant with the syntax introduced in section 4.2.1. A detailed description and validation are given in [155].[8]

Figure 4.1 shows the observed (left panel) and expected (right panel) 95% CL exclusion limits obtained with MadAnalysis 5 for the $pp \to \tilde{b}\tilde{b}^*$, $\tilde{b} \to b\tilde{\chi}_2^0 \to bh(\to b\bar{b})\tilde{\chi}_1^0$ scenario in the $(m_{\tilde{b}_1}, m_{\tilde{\chi}_2^0})$ plane, with $m_{\tilde{\chi}_1^0}$ fixed to 60 GeV. Following [122], the branching ratios of the $\tilde{b} \to b\tilde{\chi}_2^0$ and $\tilde{\chi}_2^0 \to h\tilde{\chi}_1^0$ decays are set to 100%. The recasted limits are computed in three different approaches: using only the best SR (solid red lines), combination of SRs with the full statistical model (solid green lines), and combination of SRs with a simplified statistical model derived with the Simplify tool (dashed orange lines). These have to be compared to the official limits from ATLAS (in blue); in case

[8] All validation notes are also available on the PAD homepage.

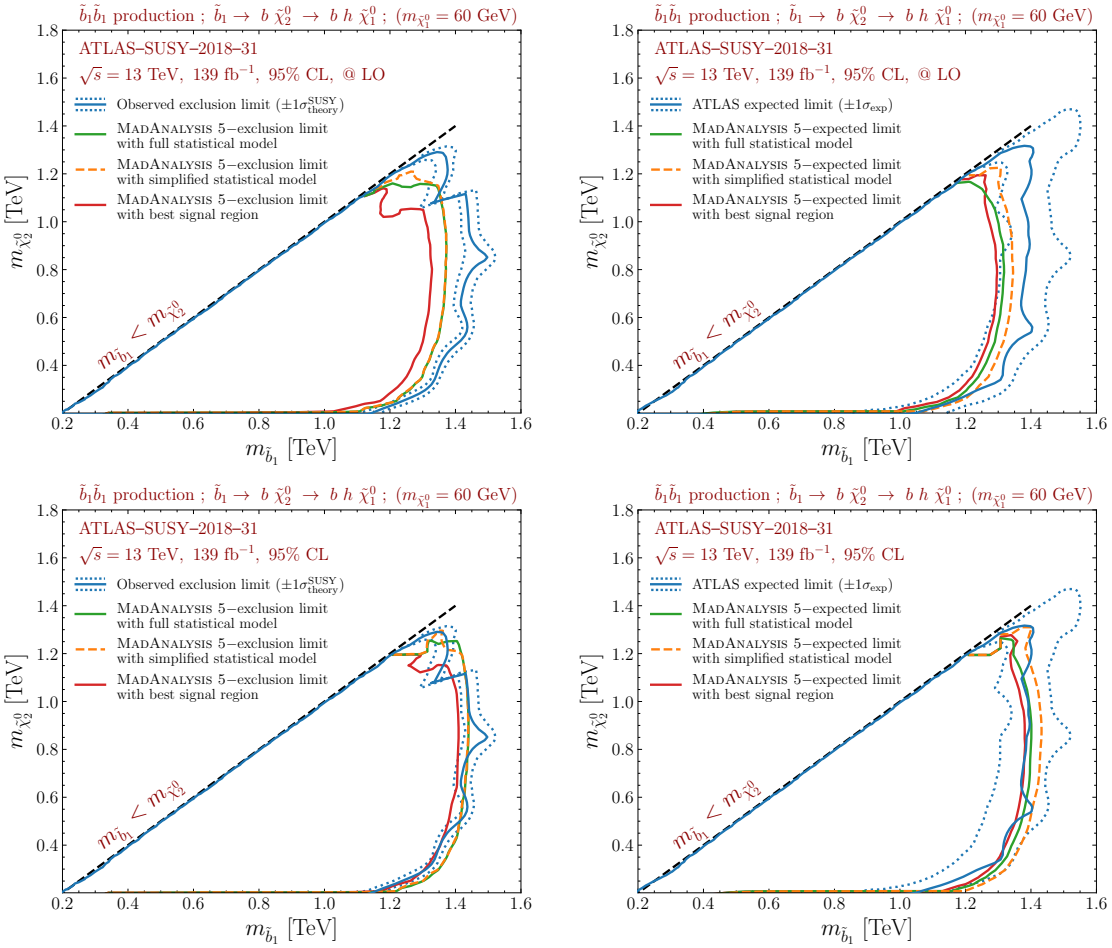


Figure 4.1: 95% CL exclusion contours for the $pp \to \tilde{b}\tilde{b}^*$, $\tilde{b} \to b\tilde{\chi}_2^0 \to bh\tilde{\chi}_1^0$ simplified model in the $(m_{\tilde{b}_1}, m_{\tilde{\chi}_2^0})$ plane, derived from the ATLAS-SUSY-2018-31 analysis. The left panels show the observed limits and the right panels the expected limits, in the upper row for LO cross sections, in the lower row using the tabulated reference cross sections from [147]. We compare the official limits from ATLAS (blue) to those obtained with MadAnalysis 5 when using the best signal region only (red), the full statistical model provided by the ATLAS collaboration (green) and an approximate version of it derived with the Simplify tool (orange).

of the *observed* exclusion, the error bands indicated for the official limits represent the $1\sigma$ theory uncertainty on sbottom-pair production, while in case of the *expected* exclusion, they represent the $1\sigma$ experimental uncertainty. In the top row of the figure, we make use of signal LO rates as returned by MG5aMC, whereas in the bottom row the results are rescaled to approximate next-to-next-to-leading-order matched with soft-gluon resummation at the next-to-next-to-leading-logarithmic accuracy (NNLO$_{\rm approx.}$+NNLL). The latter correspond to the predictions used by the ATLAS collaboration in its official publication and are taken from [147].

For the expected limits, all three approaches (best SR, full and simplified statistical model) give very similar results and agree well, at the level of about $1\sigma$, with the ATLAS result. For the observed limits, with LO cross sections the best-SR approach somewhat

under-excludes, while SR combination gives a result closer to the official limit. Employing the reference cross sections from [147], the agreement becomes almost perfect. (Henceforth, we will show results only for reference cross sections.) In this simplified-model example, the best SR performs very well. However, this need not be the case for more complicated scenarios, in which the signal may be spread to a larger extent over several SRs. The combination of SR therefore ensures a more reliable and robust interpretation than the best-SR approach. We also note that here the simplified statistical model performs very well, at significantly less CPU cost (about one fifth) than the full one. It can therefore be advantageous to use SR combination with the simplified statistical model for this analysis.

**ATLAS-SUSY-2018-04 [132]:** This analysis is a search for direct stau production in events with two hadronic taus, $pp \to \tilde{\tau}^+\tilde{\tau}^-$, $\tilde{\tau}^\pm \to \tau^\pm\tilde{\chi}^0_1$. Two event selection strategies are considered, respectively focusing on low-mass and high-mass stau production through dedicated triggers [156] and selections on the missing transverse energy $\not{E}_T$ and the stranverse mass $m_{T2}$ of the final-state system [157, 158].

The MadAnalysis 5 implementation [134] of the analysis uses Delphes 3 for the simulation of the ATLAS detector; a detailed description and validation are given in [159]. The combination of SRs through pyhf, using either the full statistical model available from HEPData [160] or its simplified version derived with Simplify 0.1.10, is enabled from version 4.0.

The effect of SR combination is illustrated in figure 4.2 for the case $pp \to \tilde{\tau}^+_{L,R}\tilde{\tau}^-_{L,R} \to \tau^+\tilde{\chi}^0_1\ \tau^-\tilde{\chi}^0_1$, with the contributions of the mass-degenerate left- and right-chiral staus summed over. The meaning of the various contours is the same as in figure 4.1. For the expected limit, shown in the right panel, SR combination based on the full statistical model reproduces very well the official ATLAS result. The simplified statistical model, however, gives an over-estimation of the sensitivity. Using the best-SR only also turns out to be slightly too aggressive, though the difference to the official expected exclusion line is within $1\sigma$ of the experimental uncertainty. For the observed limit, shown in the left panel, we observe an over-exclusion with all three approaches, although the full statistical model again performs best. This difference originates from the recasting procedure and was also noted in [159], where it was traced to a difference of up to 50% in the effect of the $m_{T2}$ cut (based on the cutflows for two benchmark points with stau masses of 120 and 280 GeV provided by the ATLAS collaboration). We must note here, however, that the analysis involves several identification and reconstruction efficiencies, which are specified only approximately in the ATLAS paper [132]. These efficiencies are used in the recast code to incorporate the multi-level tau tagging, which is not directly possible in Delphes 3. A fudge factor of 0.7 (reducing the final weights by 30%) would bring the observed limit from MadAnalysis 5 in agreement with the official ATLAS one. For the expected limit, we note that the MadAnalysis 5 results shown in the right panel of figure 4.2 are pre-fit, while the ATLAS expected limit curve seems to be post-fit. The difference between pre-fit and post-fit background numbers (*cf.* last paragraph of section 4.2.1) turns out to compensate the higher acceptance×efficiency values from the recast code. In any case, it is recommended to use the full statistical model for this analysis.

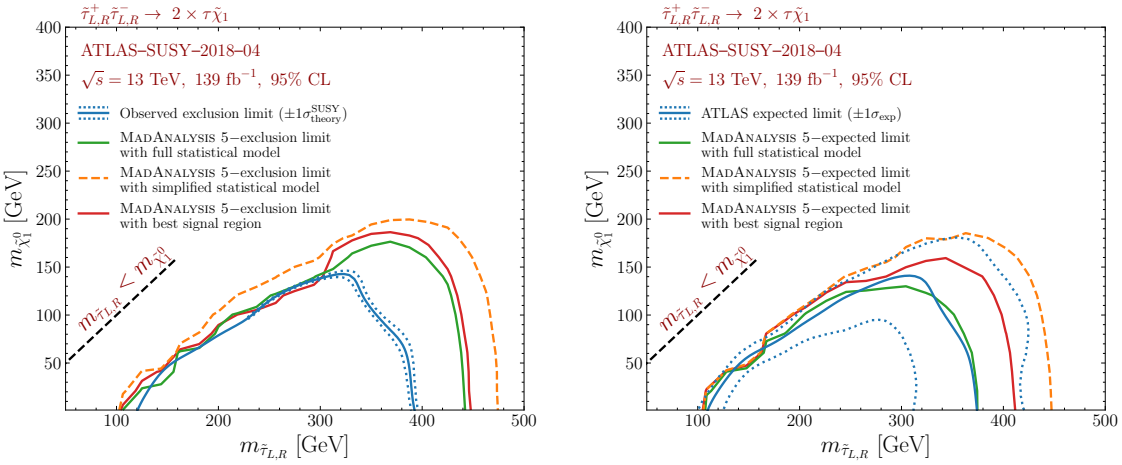


Figure 4.2: 95% CL exclusion contours as in figure 4.1, but for the $pp \to \tilde{\tau}^+_{L,R}\tilde{\tau}^-_{L,R} \to \tau^+\tau^-\tilde{\chi}^0_1\tilde{\chi}^0_1$ simplified model in the $(m_{\tilde{\tau}_{L,R}}, m_{\tilde{\chi}^0_1})$ plane and derived from the ATLAS-SUSY-2018-04 analysis.

**ATLAS-SUSY-2018-06 [124]:** This search investigates an electroweakino signal made of three leptons plus $\not{E}_T$ by means of the recursive jigsaw reconstruction technique [161, 162]. It specifically targets the production of (wino-like) charginos and neutralinos that further decay into $W$ or $Z$ bosons and the lightest neutralino, $pp \to \tilde{\chi}^\pm_1\tilde{\chi}^0_2 \to (W\tilde{\chi}^0_1)\,(Z\tilde{\chi}^0_1) \to (\ell\nu\tilde{\chi}^0_1)\,(\ell\ell\tilde{\chi}^0_1)$. The analysis has two SRs, one vetoing jets, and one requiring 1–3 jets from initial-state radiation.

The MadAnalysis 5 implementation [125] relies on Delphes 3 and is described and validated in [163]. The interface to pyhf is enabled from version 5.0 of this implementation. Note that, as mentioned in section 4.2.1, it is important in this case to include also the CRs in the combination. A complication arises from the fact that the full statistical model provided on HEPData [164] leads to issues[9] which so far could not be clarified and thus prevent us from using it for physics purposes. The simplified statistical model obtained with Simplify, however, yields reasonable results. Consequently, only the latter is included in the MadAnalysis 5 implementation.

Figure 4.3 shows the observed and expected bounds on the $pp \to \tilde{\chi}^\pm_1\tilde{\chi}^0_2 \to (W\tilde{\chi}^0_1)\,(Z\tilde{\chi}^0_1) \to (\ell\nu\tilde{\chi}^0_1)\,(\ell\ell\tilde{\chi}^0_1)$ signal obtained with MadAnalysis 5 in the $(m_{\tilde{\chi}^\pm_1/\tilde{\chi}^0_2}, m_{\tilde{\chi}^0_1})$ plane together with the official results from the ATLAS collaboration. While the best-SR approach already leads to a good agreement with the official limits, this is improved by the SR combination. Since the latter involves a combined fit to SRs and CRs, this is a case where emulating also the CRs in the recast code would be beneficial.

**ATLAS-SUSY-2019-08 [133]:** This is a search for electroweakinos in final states with one lepton, $\not{E}_T$, and two $b$-jets consistent with the decay of a Higgs boson. Like ATLAS-SUSY-2018-06, it targets the production of a chargino-neutralino pair, but with the $\tilde{\chi}^0_2$ decaying via a Higgs boson: $pp \to \tilde{\chi}^\pm_1\tilde{\chi}^0_2 \to (W\tilde{\chi}^0_1)\,(h\tilde{\chi}^0_1) \to (\ell\nu\tilde{\chi}^0_1)\,(b\bar{b}\tilde{\chi}^0_1)$. The analysis comprises 9 SRs grouped into three classes, which focus on different mass splittings between the $\tilde{\chi}^\pm_1/\tilde{\chi}^0_2$ states (assumed to be degenerate in mass) and the lightest neutralino

[9] See pyhf issue #1320 for details.

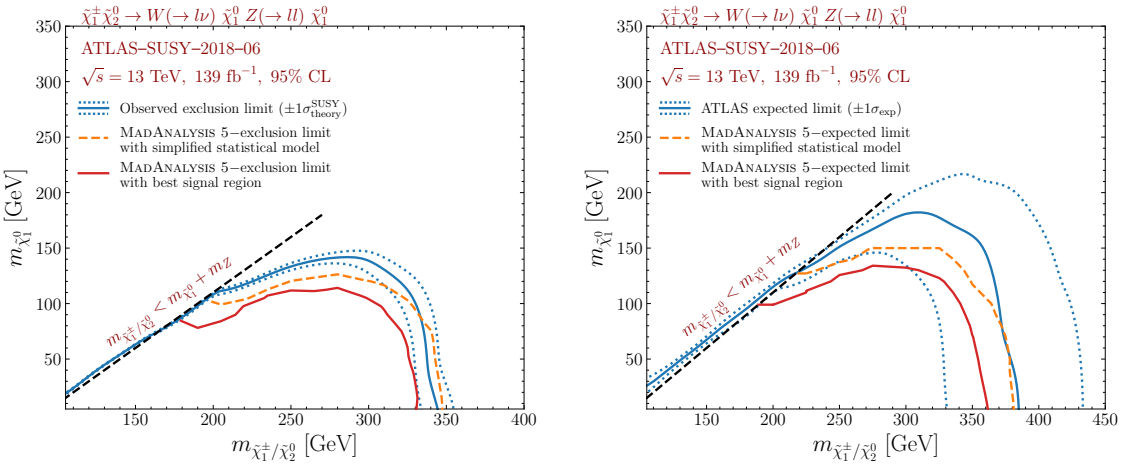


Figure 4.3: 95% CL exclusion contours as in figure 4.1, but for the $pp \to \tilde{\chi}_1^\pm\tilde{\chi}_2^0 \to (W^\pm\tilde{\chi}_1^0)\ (Z\tilde{\chi}_1^0) \to (\ell\nu\tilde{\chi}_1^0)\ (\ell\ell\tilde{\chi}_1^0)$ simplified model in the $(m_{\tilde{\chi}_1^\pm/\tilde{\chi}_2^0}, m_{\tilde{\chi}_1^0})$ plane and derived from the ATLAS-SUSY-2018-06 analysis.

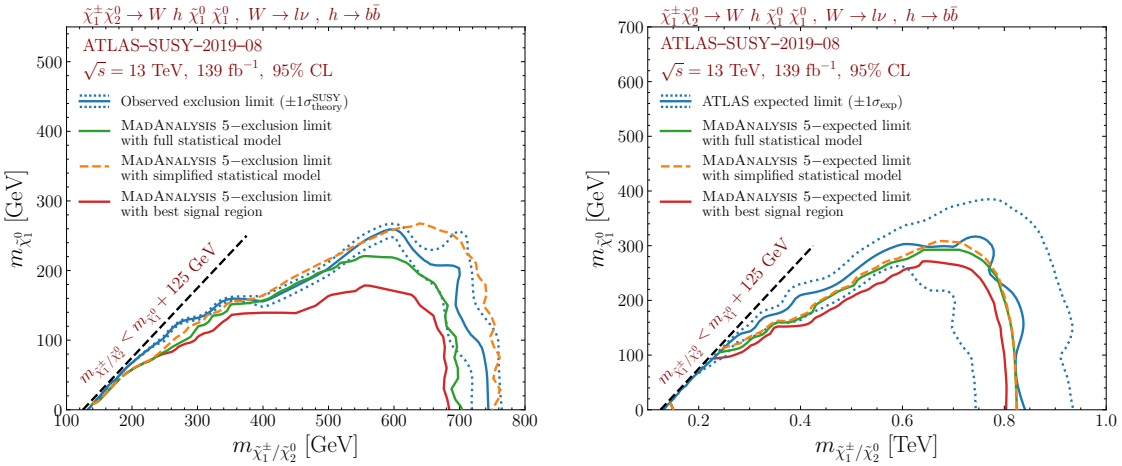


Figure 4.4: 95% CL exclusion contours as in figure 4.1, but for the $pp \to \tilde{\chi}_1^\pm\tilde{\chi}_2^0 \to (W^\pm\tilde{\chi}_1^0)\ (h\tilde{\chi}_1^0) \to (\ell\nu\tilde{\chi}_1^0)\ (b\bar{b}\tilde{\chi}_1^0)$ simplified model in the $(m_{\tilde{\chi}_1^\pm/\tilde{\chi}_2^0}, m_{\tilde{\chi}_1^0})$ plane and derived from the ATLAS-SUSY-2019-08 analysis.

$\tilde{\chi}_1^0$, and it relies on various high-level kinematic variables including the contranverse mass of the two $b$-jets [165, 166].

The MadAnalysis 5 implementation [135] of this analysis makes use of Delphes 3 for the simulation of the ATLAS detector. We refer to [167] for details and validation information. We use version 6.0, which allows for SR combination through the pyhf package, both on the basis of the full statistical model available from HEPData [168] and on that of a simplified one derived with Simplify [118].

The limits in the $(m_{\tilde{\chi}_1^\pm/\tilde{\chi}_2^0}, m_{\tilde{\chi}_1^0})$ plane obtained with the MadAnalysis 5 recast for the process $pp \to \tilde{\chi}_1^\pm\tilde{\chi}_2^0 \to (W^\pm\tilde{\chi}_1^0)\ (h\tilde{\chi}_1^0)$ are shown in figure 4.4, and compared to the official ones from the ATLAS collaboration. Signal region combination with the full statistical model clearly improves the agreement with the ATLAS result as compared to the best-SR approach. The simplified statistical model, on the other hand, performs less

well and leads to an over-exclusion. The difference however remains at the level of $1\sigma$ of the theory uncertainty. Overall it is recommended to use the full statistical model for this analysis.

**CMS-SUS-16-039 [126]:** This analysis targets the production of charginos and/or neutralinos that decay into final states comprising two or more leptons. It contains 158 SRs defined in terms of $\not{E}_T$, the number and flavours of the leptons, their electric charges and other properties of the produced multi-leptonic system like its invariant or transverse mass.

The implementation of this analysis in MadAnalysis 5 relies on Delphes 3 for the simulation of the CMS detector. Details and validation information are available from [169]. We make use of its version 3.0 [130] that includes the covariance matrix for the 44 three-lepton SRs (SRA01–SRA44) available on the analysis twiki page. This class of SRs is dedicated to final states featuring three non-tau leptons and including at least one opposite-sign same-flavour lepton pair. The correlation information for the other classes of SRs is not publicly available.

Figure 4.5 presents observed (left panel) and expected (right panel) 95% CL exclusion limits obtained with MadAnalysis 5 for the process $pp \to \tilde{\chi}_1^\pm \tilde{\chi}_2^0 \to (W\tilde{\chi}_1^0)\ (Z\tilde{\chi}_1^0) \to (\ell\nu\tilde{\chi}_1^0)\ (\ell\ell\tilde{\chi}_1^0)$ in the $(m_{\tilde{\chi}_1^\pm/\tilde{\chi}_2^0}, m_{\tilde{\chi}_1^0})$ plane. This process is the target of SRs of class A, for which the covariance matrix is publicly available. The limits are computed by MadAnalysis 5 in two different approaches, namely using the best SR (red), and combining SRs in the simplified likelihood approach by means of the covariance matrix (teal). These results are compared to the official limits from the CMS collaboration (blue). As for the analyses above, for observed limits the dashed blue lines indicate the $1\sigma$ theory uncertainty on the signal cross section, whereas for expected limits they indicate the experimental uncertainty.

The difference between the best-SR and combined results is striking. Owing to the fine binning of SRs in the CMS analysis, the hypothesised signal populates several of the analysis SRs, reducing consequently the sensitivity of any single region. Only with a statistical combination can the CMS mass limits be reproduced to a good approximation. We conclude that SR combination greatly ameliorates the reinterpretation of the results of this analysis. It would hence be great if covariance matrices were available also for the other 13 classes of SRs of this analysis.

**CMS-SUS-16-048 [127]:** This CMS search focuses on a signature with two soft leptons ($\ell = e, \mu$) of opposite electric charge and $\not{E}_T$, as is typical from compressed new physics spectra with a dark matter candidate. It relies on vetoes on a large hadronic activity and cuts on high-level observables built from the lepton properties and the missing transverse energy. Two search regions are defined: an electroweakino search region (12 SRs) through cuts on $\not{E}_T$ and the di-lepton invariant mass $M(\ell\ell)$, and a stop search region (9 SRs) through cuts on $\not{E}_T$ and the lepton transverse momenta $p_T(\ell)$. Two covariance matrices are available on the analysis twiki page, one for each of the two regions.

The analysis has been implemented in MadAnalysis 5 both in the SFS framework [82] and for use with Delphes 3. Details on the implementation and validation can be found in [82, 90]. Version 3 of the 'SFS implementation' [139] and version 2 of the 'Delphes 3 implementation' [131] include the covariance matrix information, which

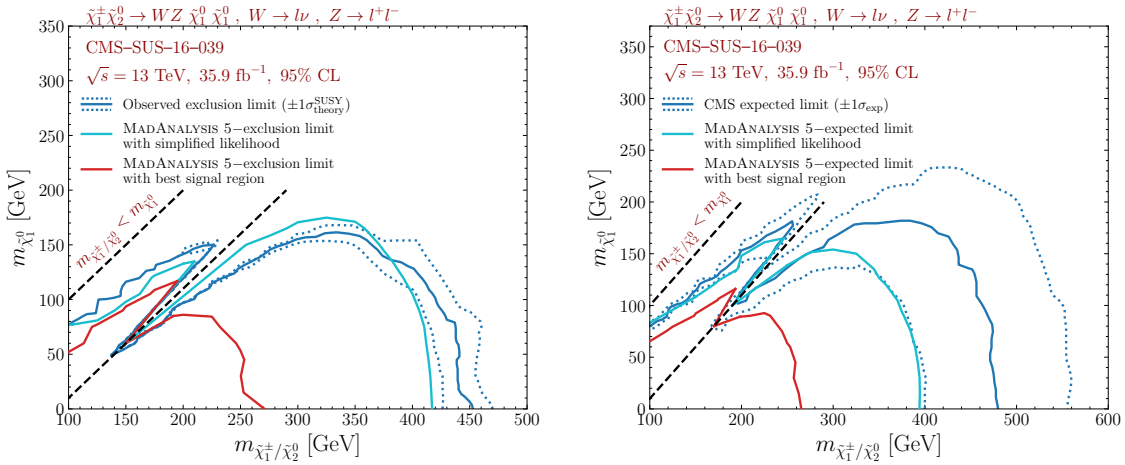


Figure 4.5: 95% CL exclusion contours for the $pp \to \tilde{\chi}_1^\pm\tilde{\chi}_2^0 \to (W\tilde{\chi}_1^0)\ (Z\tilde{\chi}_1^0) \to (\ell\nu\tilde{\chi}_1^0)\ (\ell\ell\tilde{\chi}_1^0)$ simplified model in the $(m_{\tilde{\chi}_1^\pm/\tilde{\chi}_2^0}, m_{\tilde{\chi}_1^0})$ plane, derived from the CMS-SUS-16-039 analysis. The left panel shows the observed limits, while the right panel shows the expected limits. We compare the official limits from the CMS collaboration (blue) to those obtained with MadAnalysis 5 when using the best signal region only (red) and when combining SRs with the publicly available covariance matrix information (teal).

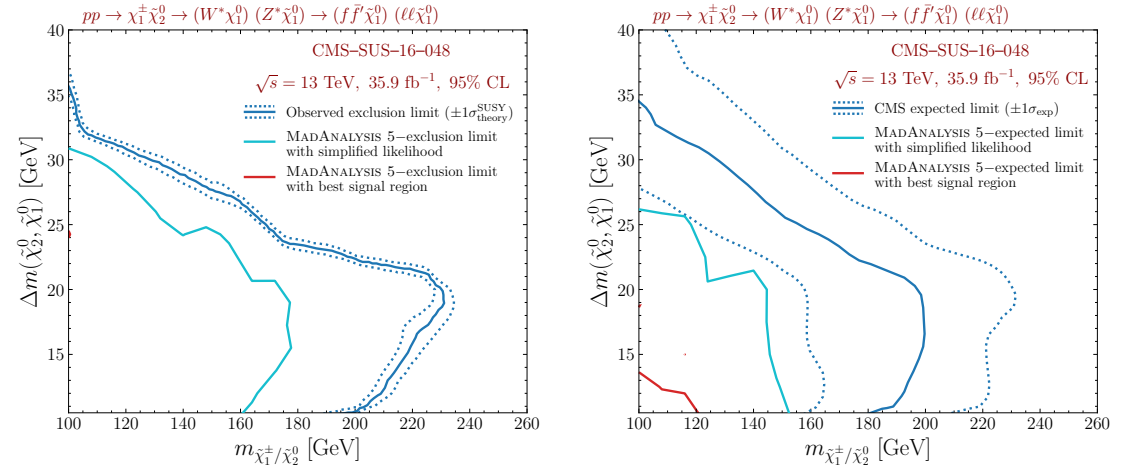


Figure 4.6: 95% CL exclusion contours as in figure 4.5, but for the $pp \to \tilde{\chi}_1^\pm\tilde{\chi}_2^0 \to f\bar{f}'\tilde{\chi}_1^0\ \ell\ell\tilde{\chi}_1^0$ simplified model in the $(m_{\tilde{\chi}_1^\pm/\tilde{\chi}_2^0},\ \Delta m = m_{\tilde{\chi}_1^\pm/\tilde{\chi}_2^0} - m_{\tilde{\chi}_1^0})$ plane and derived from the CMS-SUS-16-048 analysis.

allows for the construction of simplified likelihoods associated with subsets of the 12 electroweakino and the 9 stop SRs of the analysis. The material is again taken from the analysis twiki page.

For validation, we show in figure 4.6 exclusion contours derived with the 'SFS implementation' for the electroweakino simplified model in the plane of the $\tilde{\chi}_1^\pm/\tilde{\chi}_2^0$ mass versus its difference with the $\tilde{\chi}_1^0$ mass. The hypothesised signal is $pp \to \tilde{\chi}_1^\pm\tilde{\chi}_2^0 \to (f\bar{f}'\tilde{\chi}_1^0)\ (\ell\ell\tilde{\chi}_1^0)$, where the $\tilde{\chi}_1^\pm$ and $\tilde{\chi}_2^0$ decays proceed via off-shell $W$ and $Z$ bosons with branching ratios of 100%. The colour code is the same as in figure 4.5. As for the CMS-SUS-16-039 analysis above, the limits obtained from the best-SR and simplified likelihood approaches are

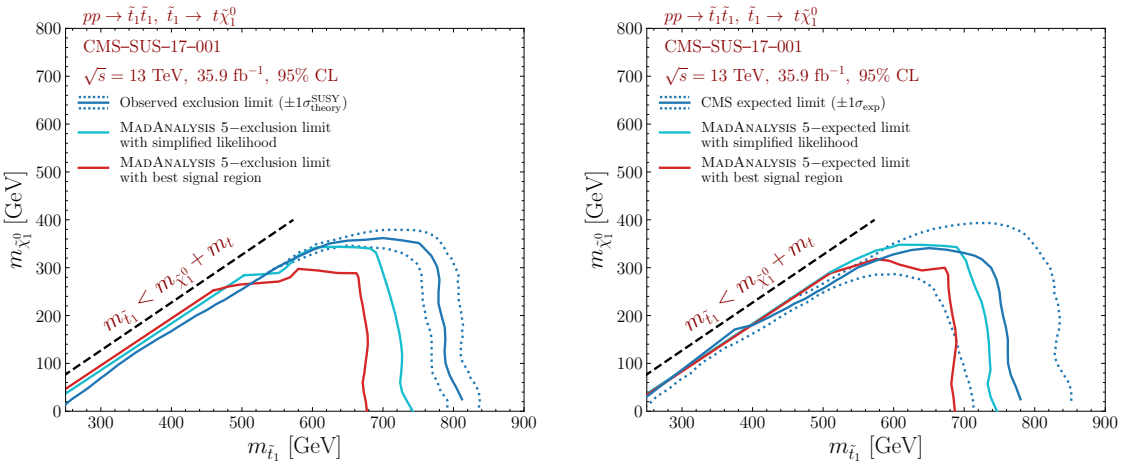


Figure 4.7: 95% CL exclusion contours as in figure 4.5, but for the $pp \to \tilde{t}^*\tilde{t} \to (t\tilde{\chi}_1^0)(\bar{t}\tilde{\chi}_1^0)$ simplified model in the $(m_{\tilde{t}}, m_{\tilde{\chi}_1^0})$ plane and derived from the CMS-SUS-17-001 analysis.

vastly different. In fact, the best SR alone has very little sensitivity to the scenario under consideration (see the expected limits, right panel in figure 4.6) and does not exclude any of it (see the observed limits, left panel in figure 4.6). The combination of SRs in the simplified likelihood approach, on the other hand, allows one to reproduce the official bounds from CMS within $1\sigma$–$2\sigma$ of the experimental uncertainty.

**CMS-SUS-17-001 [138]:** This is a search in final states with two oppositely charged leptons ($\ell = e, \mu$), $b$-jets, and $\not{E}_T$. It targets stop-pair production with the stops decaying directly into $t\tilde{\chi}_1^0$ or into $bW\tilde{\chi}_1^0$ via a chargino, as well as direct dark matter production in association with top quarks through scalar or pseudoscalar mediator exchange. The analysis has 13 SRs defined in terms of $\not{E}_T$ and the transverse mass variables $m_{T2}(b\ell b\ell)$ and $m_{T2}(\ell\ell)$. These are further split into same-flavor and different flavor SRs, totalling 26 SRs. In addition, three aggregate SRs are defined in terms of $\not{E}_T$ and $m_{T2}(\ell\ell)$.

The implementation in MadAnalysis 5 [141], described and validated in [170], is for the three aggregate SRs and relies on Delphes 3. We use version 3.0 of the code, which employs a prefit covariance matrix for the aggregate SRs constructed from the background uncertainties and correlation matrix given on the analysis twiki page.

Figure 4.7 shows observed and expected 95% CL exclusion limits for the $pp \to \tilde{t}\tilde{t}^* \to (t\tilde{\chi}_1^0)(\bar{t}\tilde{\chi}_1^0)$ scenario in the $(m_{\tilde{t}}, m_{\tilde{\chi}_1^0})$ plane. The official CMS bounds are reasonably well reproduced, as expected from the mere goal of aggregate regions. Nonetheless, the MadAnalysis 5 exclusion lines get closer to the official ones when the information from all three aggregate regions is combined. This improvement demonstrates again the importance of using correlation information whenever it is available. Notice also that the correlation between each of the three aggregate regions is about 0.4–0.5; treating them as fully correlated or fully uncorrelated would thus not be correct.

**CMS-SUS-19-006 [136]:** This analysis is dedicated to new physics signals featuring multiple jets and missing transverse energy. It includes 174 SRs defined by the number of reconstructed jets, $b$-tagged jets, the hadronic activity $H_T$ and the amount of $\not{E}_T$. The implementation in MadAnalysis 5 relies on Delphes 3; we use its version 6.0 [140] that

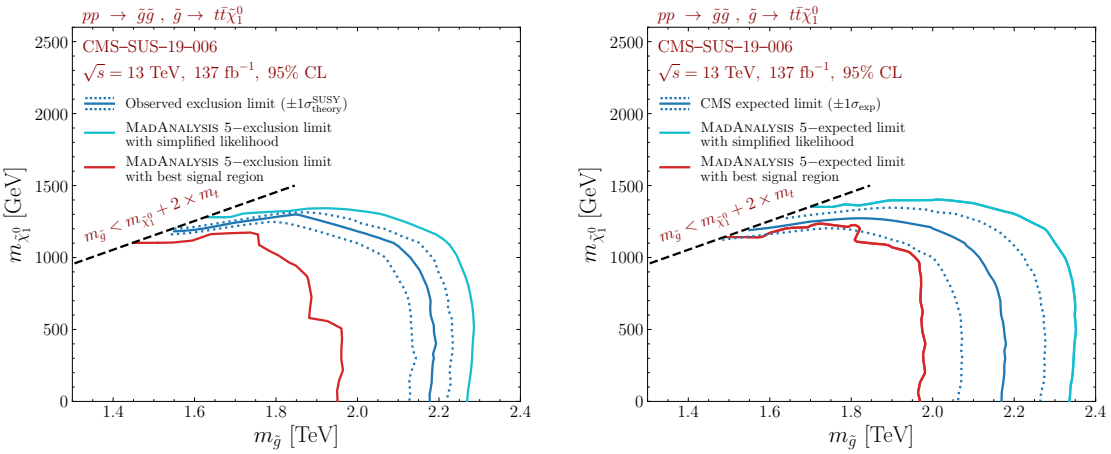


Figure 4.8: 95% CL exclusion contours as in figure 4.5, but for the $pp \to \tilde{g}\tilde{g} \to (t\bar{t}\chi_1^0)\,(t\bar{t}\tilde{\chi}_1^0)$ simplified model in the $(m_{\tilde{g}}, m_{\tilde{\chi}_1^0})$ plane and derived from the CMS-SUS-19-006 analysis.

allows for the combination of all 174 SRs of the analysis. The 12 (overlapping) aggregate regions defined in the analysis are also implemented. Details and validation material are available from [171].

CMS-SUS-19-006 generically targets gluino, stop, sbottom, and squark production. In figure 4.8, we consider the $pp \to \tilde{g}\tilde{g} \to (t\bar{t}\chi_1^0)\,(t\bar{t}\tilde{\chi}_1^0)$ scenario for validation. Whereas limits obtained by considering the best-SR approach are too conservative (under-estimating the limit on the gluino mass by about 10%), approximate likelihoods built from the covariance matrix (published on HEPData [172]) allow us to get an agreement with the CMS official results at $1\sigma - 2\sigma$. For example, at $m_{\tilde{\chi}_1^0} = 100$ GeV, the observed limit on the gluino mass improves from 1950 GeV in the best-SR approach to about 2260 GeV with combined SRs, to be compared to the official CMS limit of 2180 GeV. Despite the small over-exclusion with combined SRs, this improves the reinterpretation potential of this analysis. We note, however, that for the expected limit, the over-exclusion with combined SRs is as important as the under-exclusion with the best SR only.

**CMS-EXO-20-004 [137]:** This is a search for new particles using events with energetic jets and large missing transverse momentum. Among other signal models, the analysis targets dark matter production in association with at least one highly-energetic jet. A minimum $\not{E}_T > 250$ GeV is required, and separate categories are defined for events with narrow jets from initial-state radiation (mono-jet category) and events with large-radius jets consistent with a hadronic decay of a $W$ or $Z$ boson (low- and high-purity mono-V categories). A shape analysis is then performed of the $\not{E}_T$ spectrum.

The implementation in MadAnalysis 5 relies on Delphes 3 and has been provided by the CMS collaboration itself. It consists of the selection for the mono-jet category; a total of 66 SRs are defined, with each of the regions representing one recoil bin in one data-taking year. Information and validation details can be found in [137]; see also the related RAMP seminar by Andreas Albert [173]. We here use version 2.0 of the code [142], which allows for a $\not{E}_T$ shape analysis through the construction of a simplified likelihood based on the yields and the covariance matrix for the SR bins provided on HEPData [174].

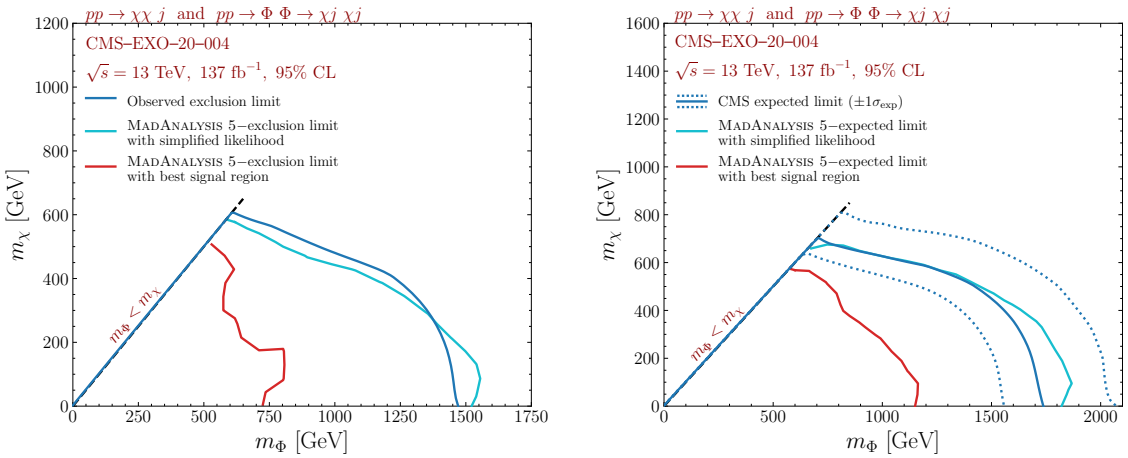


Figure 4.9: 95% CL exclusion contours as in figure 4.5, but for a $t$-channel dark matter simplified model ($pp \to \Phi\Phi \to \chi j\ \chi j$ and $pp \to \chi\chi j$) in the $(m_\Phi, m_{\tilde{\chi}})$ plane and derived from the CMS-EXO-20-004 analysis.

For validation, we reproduce in figure 4.9 the constraints on the fermion portal model considered in [137]. This is a $t$-channel dark matter signal containing two contributions, namely the production of a pair of scalar mediators $\Phi$ that decay into dark matter $\chi$ and jets ($pp \to \Phi\Phi \to \chi j\ \chi j$) and the direct production of dark matter with an energetic jet ($pp \to \chi\chi j$) through a $t$-channel mediator exchange. Whereas solely very conservative constraints are obtained when relying only on a single $\not{E}_T$ bin (the recasted mass limits being a factor of 2 smaller than the official ones), with the shape analysis based on the simplified likelihood the official limits can be reproduced quite well with MadAnalysis 5. This is explained by the topology of the signal that rarely populates a single $\not{E}_T$ bin, so that a severe loss of sensitivity in the best-SR approach is expected.

## 4.4 Physics application

In this section, we give an illustrative physics example, that goes beyond the simplified models considered by the experimental collaborations. We start from the simplified model used in ATLAS-SUSY-2018-31 [122], which assumes sbottom pair production with the sbottoms decaying into $b\tilde{\chi}_2^0$ followed by $\tilde{\chi}_2^0 \to h\chi_1^0$. This scenario is not realised in the MSSM for several reasons. First, if the $\chi_1^0$ is bino-like and the $\tilde{\chi}_2^0$ wino-like, as assumed in the simplified model, there is also always a wino-like chargino $\tilde{\chi}_1^\pm$ near in mass to the $\tilde{\chi}_2^0$. Therefore, whenever the mass difference is large enough, $\tilde{b}_1 \to t\tilde{\chi}_1^-$ decays reduce the branching ratio of the $\tilde{b}_1 \to b\tilde{\chi}_2^0$ mode. Second, for sbottoms to decay dominantly via wino-like electroweakinos (instead of directly into the LSP, *i.e.* $\tilde{b}_1 \to b\tilde{\chi}_2^0$ instead of $\tilde{b}_1 \to b\tilde{\chi}_1^0$), we need $\tilde{b}_1 \sim \tilde{b}_L$. In this case, due to $SU(2)_L$, there is always a $\tilde{t}_1$ more or less near in mass to the $\tilde{b}_1$ with leading decay modes of $\tilde{t}_1 \to b\tilde{\chi}_1^+$, $t\tilde{\chi}_2^0$ and $t\tilde{\chi}_1^0$. Since top quarks decay into $bW$ systems, all these additional modes lead to $b$-rich events, but with somewhat different kinematic features. Moreover, while $\tilde{\chi}_2^0 \to h\tilde{\chi}_1^0$ usually dominates once the neutralino mass difference is large enough, the branching ratio of $\tilde{\chi}_2^0 \to Z\tilde{\chi}_1^0$ is not zero and should be accounted for.

In a realistic MSSM setup, we therefore have a mix of final states originating from

$$pp \to \tilde{b}_1\tilde{b}_1^*, \quad \tilde{b}_1 \to b\tilde{\chi}_1^0,\ b\tilde{\chi}_2^0,\ \text{or}\ t\tilde{\chi}_1^- \qquad \text{and} \qquad pp \to \tilde{t}_1\tilde{t}_1^*, \quad \tilde{t}_1 \to t\tilde{\chi}_1^0,\ t\tilde{\chi}_2^0,\ \text{or}\ b\tilde{\chi}_1^+ . \tag{4.1}$$

It is therefore interesting to assess how the relevant analyses (in our case ATLAS-SUSY-2018-31 and CMS-SUS-19-006) pick up this signal.

Our benchmark scenario is thus the case where $\tilde{b}_1$, $\tilde{t}_1$, $\tilde{\chi}_1^\pm$, $\tilde{\chi}_2^0$ and $\tilde{\chi}_1^0$ are potentially within LHC reach, while all other supersymmetric particles are heavy, in the multi-TeV range. We call this the T6MSSM scenario.[10] The relevant parameters are the bino and wino masses ($M_1$ and $M_2$), the left squark soft mass for the third generation ($M_{\tilde{Q}_3}$), and the ratio of the two Higgs vacuum expectation values ($\tan\beta = v_2/v_1$).

For definiteness, we fix $M_1 = 60$ GeV and $\tan\beta = 10$ and scan over $M_2$ and $M_{\tilde{Q}_3}$ (with $2M_1 < M_2 < M_{\tilde{Q}_3}$). All other soft masses are set to 5 TeV, $\mu = 1.6$ TeV, and the trilinear couplings $A_{t,b} = -3.5$ TeV (to obtain $m_h \simeq 125$ GeV). This gives a mass spectrum of

$$m_{\tilde{b}_1} \simeq m_{\tilde{t}_1} \simeq M_{\tilde{Q}_3} \ > \ m_{\tilde{\chi}_1^\pm} = m_{\tilde{\chi}_2^0} = M_2 \ > \ m_{\tilde{\chi}_1^0} = 60 \text{ GeV}. \tag{4.2}$$

Masses and decay widths are computed with SOFTSUSY 4.1.12 [175, 176]. For $M_{\tilde{Q}_3} = 1200$ GeV, we find $m_{\tilde{b}_1} = 1266$ GeV and $m_{\tilde{t}_1} = 1256$ GeV. Figure 4.10 shows the decay branching ratios as a function of the wino mass parameter $M_2$. As long as these decays are not kinematically suppressed, both the sbottom and the stop decay dominantly via the chargino (which then decays to 100% into $W^\pm\tilde{\chi}_1^0$). In contrast, the decays into the $\tilde{\chi}_2^0$ only have about 20–40% branching ratio. Concretely, we find $\text{BR}(\tilde{b}_1 \to b\tilde{\chi}_2^0) \simeq 0.34$, 0.35, 0.42; $\text{BR}(\tilde{t}_1 \to t\tilde{\chi}_2^0) \simeq 0.32$, 0.31, 0.17; and $\text{BR}(\tilde{\chi}_2^0 \to h\tilde{\chi}_1^0) \simeq 0.93$, 0.84, 0.74 for $M_2 = 200$, 600, 1000 GeV, respectively.

ATLAS-SUSY-2018-31 excludes sbottoms up to about 1.4 TeV under their peculiar simplified model scenario. CMS-SUS-19-006 excludes sbottoms and stops up to about 1.2 TeV assuming direct decays into a bino LSP, but makes no statement about limits when the decays go via intermediate winos. How the simplified model limits constrain the realistic MSSM case, (4.1), can easily be checked with SMODELS [93, 94, 119, 177]. Not surprisingly, because of the variety of stop and sbottom decay modes, the constraints on the T6MSSM scenario are rather weak, with the exclusion limit reaching only up to $M_{\tilde{Q}_3} \approx 1$ TeV depending on $M_2$ (and $M_1$ being kept at 60 GeV).[11]

To evaluate the constraints on the T6MSSM scenario with MADANALYSIS 5, we generate $pp \to \tilde{b}_1\tilde{b}_1^*$ and $pp \to \tilde{t}_1\tilde{t}_1^*$ events with MG5AMC for a grid of 146 points in the $(M_{\tilde{Q}_3}, M_2)$ plane, with $M_{\tilde{Q}_3} = [1, 1.6]$ TeV and $M_2 = [0.2, 1]$ TeV ($M_1$ being kept at 60 GeV). For each point in the grid, we generate 200,000 hard-scattering events. The events are passed to PYTHIA 8.2 [67] for decays, showering and hadronisation, and then to DELPHES 3 [72] or SFS [82] for the detector simulation in the typical MADANALYSIS 5 recast chain [80], as already explained in section 4.3. The resulting limits from the ATLAS-SUSY-2018-31 and CMS-SUS-19-006 analyses are presented in figure 4.11. Here, LO cross sections from MG5AMC are used. As can be seen, the statistical combination of SRs gives a big improvement, excluding stop and sbottom masses up to 1.1–1.3 TeV

[10] This is inspired by the simplified model naming convention in SMODELS.

[11] This is easily understood by considering that, for instance, for $\text{BR}(\tilde{b}_1 \to b\tilde{\chi}_2^0) = 0.4$ and $\text{BR}(\tilde{\chi}_2^0 \to h\tilde{\chi}_1^0) = 0.8$, only 10% of sbottom events yield the $bbhh\tilde{\chi}_1^0\tilde{\chi}_1^0$ final state targeted in ATLAS-SUSY-2018-31.

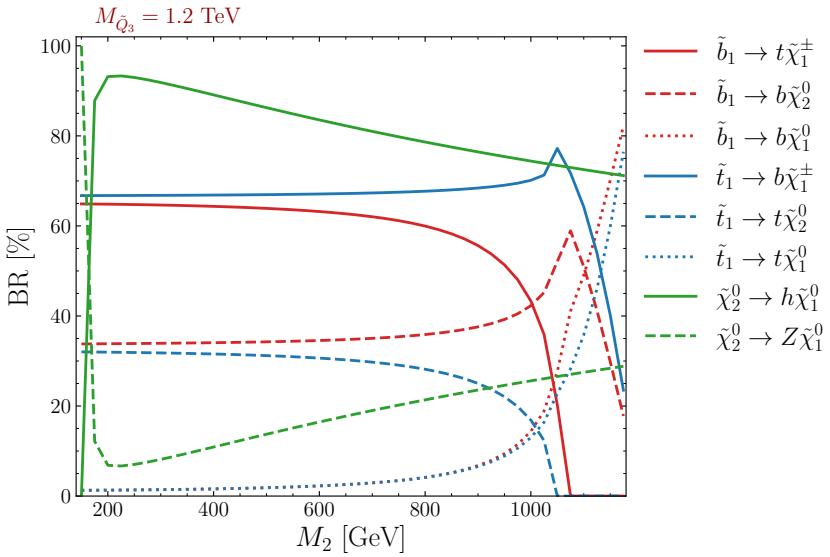


Figure 4.10: The decay branching ratios in the T6MSSM benchmark scenario as a function of $M_2$, for $M_{\tilde{Q}_3} = 1200$ GeV and $M_1 = 60$ GeV. The decay rate of $\tilde{\chi}_1^\pm \to W^\pm \tilde{\chi}_1^0$ is always 100%.

| | | $M_2 = 600$ GeV | | | $M_2 = 800$ GeV | | | $M_2 = 1$ TeV | | |
|---|---|---|---|---|---|---|---|---|---|---|
| analysis | method | $\tilde{b}_1\tilde{b}_1^*$ | $\tilde{t}_1\tilde{t}_1^*$ | total | $\tilde{b}_1\tilde{b}_1^*$ | $\tilde{t}_1\tilde{t}_1^*$ | total | $\tilde{b}_1\tilde{b}_1^*$ | $\tilde{t}_1\tilde{t}_1^*$ | total |
| ATLAS | best-SR | 0.71 | 0.66 | 0.94 | 0.70 | 0.59 | 0.91 | 0.29 | 0.21 | 0.57 |
| | combined | 0.83 | 0.80 | **0.98** | 0.84 | 0.74 | **0.97** | 0.80 | 0.56 | **0.92** |
| CMS | best-SR | 0.31 | 0.37 | 0.62 | 0.38 | 0.45 | 0.73 | 0.29 | 0.38 | 0.70 |
| | combined | 0.79 | 0.71 | **0.96** | 0.89 | 0.83 | **0.99** | 0.93 | 0.82 | **0.99** |

Table 4.2: $1 - \mathrm{CL}_s$ values from the ATLAS (SUSY-2018-31) and CMS (SUS-19-006) analyses without and with combining SRs, for $M_{\tilde{Q}_3} = 1200$ GeV and three values of $M_2$; the different columns compare sbottom production only ($\tilde{b}_1\tilde{b}_1^*$), stop production only ($\tilde{t}_1\tilde{t}_1^*$), and sbottom+stop production taken together (total). Only if the total production is considered and the SRs are combined we obtain $1 - \mathrm{CL}_s \geq 0.95$.

for wino masses of 0.2–1 TeV. In contrast, using only the best SR, the limits are considerably weaker. The effect is particularly pronounced for the CMS analysis, which has very fine-grained SRs (174 SRs as compared to 8 for the ATLAS analysis); using the 12 aggregate regions of the CMS analysis does not change the picture.

It is relevant to ask whether the limits in figure 4.11 come mostly from stop or mostly from sbottom production for one or both analyses. To answer this question we pick some points near the exclusion lines and evaluate the constraints on stop and sbottom production separately (*i.e.* considering only $pp \to \tilde{b}_1\tilde{b}_1^*$ or $pp \to \tilde{t}_1\tilde{t}_1^*$ events). The result is summarised in table 4.2. It turns out that the sensitivity to sbottoms and stops is very similar within one analysis. Moreover, we find that a $\geq 95\%$ confidence level exclusion is reached for the points in table 4.2 only if the total $pp \to \tilde{b}_1\tilde{b}_1^* + \tilde{t}_1\tilde{t}_1^*$ production is considered *and* the contributions in all SRs are combined.

Since the T6MSSM scenario features wino-like $\tilde{\chi}_1^\pm$ and $\tilde{\chi}_2^0$, complementary constraints come from electroweakino searches. Indeed, as illustrated figure 4.12, ATLAS-SUSY-2019-

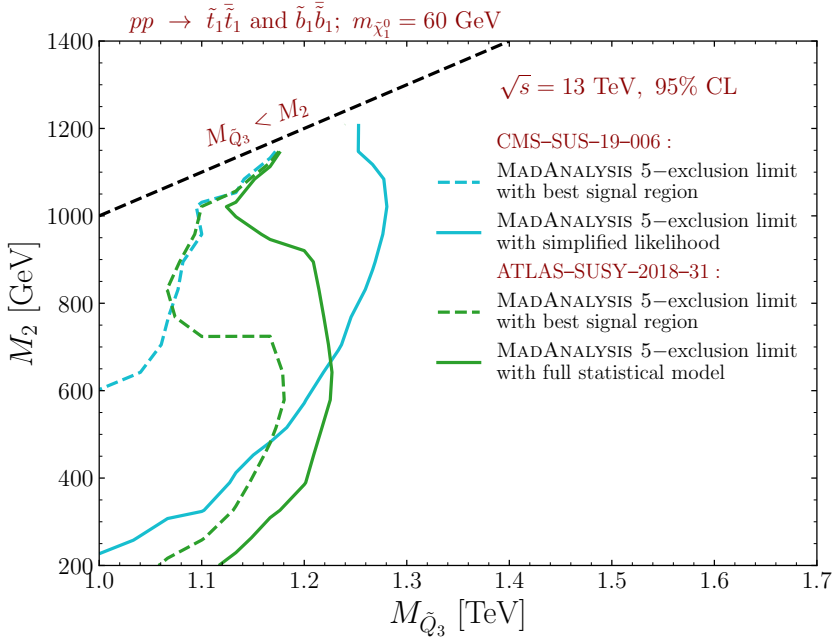


Figure 4.11: 95% confidence level exclusion limits on T6MSSM scenario in the plane of stop/sbottom *versus* wino mass parameters ($m_{\tilde{t}_1} \simeq m_{\tilde{b}_1} \simeq m_{\tilde{Q}_3}$; $m_{\chi_2^0} \simeq m_{\chi_1^\pm} \simeq M_2$; $m_{\tilde{\chi}_1^0} = M_1 = 60$ GeV). The results for ATLAS-SUSY-2018-31 are in green, the results for CMS-SUS-19-006 in blue. Full lines are the limits with, dashed lines without SR combination.

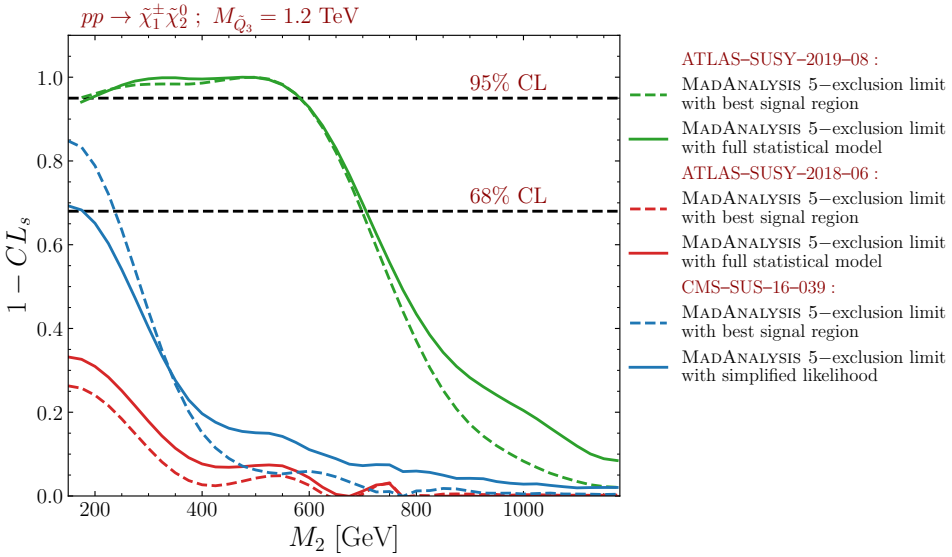


Figure 4.12: $1 - \mathrm{CL}_s$ values from electroweakino searches as function of $M_2$, for $M_1 = 60$ GeV and $\mu = 1.6$ TeV. Full lines are with, dashed lines without SR combination.

08, targeting the $Wh(\to b\bar{b}) + \not{E}_T$ final state, excludes $M_2$ (*i.e.* wino masses) up to about 600 GeV. The same result is obtained from the simplified model limits in SModelS 2.1. The multi-lepton searches targeting $WZ + \not{E}_T$ final states, on the other hand, provide no relevant constraints, as can also be seen in figure 4.12. This is no surprise as, with

decay branching ratios of $\approx$ 70–90%, $\tilde{\chi}_2^0 \to h\tilde{\chi}_1^0$ decays largely dominate over $\tilde{\chi}_2^0 \to Z\tilde{\chi}_1^0$ decays. Figure 4.12 also serves to illustrate that the best-SR approach is not always more conservative. Indeed, for $M_2 \lesssim 350$ GeV the CMS-SUS-16-039 best-SR result is too aggressive. This can happen when less events are observed than expected in the best SR, or there are small excesses in other SRs. In any case, the statistical combination of SRs is important for a reliable reinterpretation.

## 4.5 Conclusions and outlook

We presented the implementation and usage of SR combination in MadAnalysis 5 via two methods: an interface to the pyhf package making use of statistical models in JSON-serialised format provided by the ATLAS collaboration, and a simplified likelihood calculation making use of covariance matrices provided by the CMS collaboration. Currently, there are recast codes for four ATLAS and five CMS analyses in the MadAnalysis 5 Public Analysis Database for which this new functionality can be exploited.

We demonstrated the associated gain in physics reach for reinterpretation studies in two ways. First, we reproduced mass limits on simplified model scenarios as published by the ATLAS and CMS collaborations for the analyses considered. Second, we performed a case study of a realistic MSSM scenario in which stops and sbottoms have a variety of decay modes into charginos and neutralinos. Our results show that the statistical combination of disjoint SRs in reinterpretation studies, using more of the data of an analysis, gives more reliable and robust results than the best-SR approach, which uses only the most sensitive SR, for the statistical interpretation of a hypothesised signal.

Next in line of development is the statistical combination of results from different, independent analyses, a functionality that is already available in SModelS v2.2, and should soon also be adopted in MadAnalysis 5. Moreover, in order to externalise and make it available to entire HEP community, the SModelS and MadAnalysis 5 teams are currently working together to create a universal toolbox for statistics handling in the context of reinterpretation studies.

# Chapter 5

# A pyhf interface to SModelS

The subject of this chapter is also related to SR combination but for the SModelS tool. It is based on [119] and presents the implementation of an interface to `pyhf` in SModelS, enabling the use of full likelihoods provided by ATLAS in the form of `JSON` files. This improves the statistical evaluation and also the limit setting, which is demonstrated by a direct comparison of the results from SModelS with the official ATLAS simplified model results for the three analyses for which pyhf JSON files were available at the time of this work. I developed the `pyhf` interface, implemented the relevant ATLAS analyses into the SModelS database, and carried out the physics impact analysis. Chronologically, this was before [111] and the first time that statistical models from ATLAS were reused by theorists.

## 5.1 Introduction

An essential step for interpretation of experimental results is the construction of a statistical model, or *likelihood*, to compare the observed data to the target theory. Given the likelihood, all the standard statistical approaches are available for extracting information from it.

Therefore, Ref. [112] recommended for the presentation of LHC results: *"When feasible, provide a mathematical description of the final likelihood function in which experimental data and parameters are clearly distinguished, either in the publication or the auxiliary information. Limits of validity should always be clearly specified."* And furthermore *"Additionally provide a digitized implementation of the likelihood that is consistent with the mathematical description."* These are the Les Houches Recommendations 3(b) and 3(c). The necessity of detailed likelihood information was further elaborated in the recent report of the LHC Reinterpretation Forum [178].

Among the major benefits of detailed likelihood information for reinterpretation is the fact that it allows one to statistically combine disjoint SRs instead of using only the most sensitive (a.k.a. "best") SR; see, e.g., [179, 180] for the impact in physics studies.

The CMS SUSY group has been publishing SR correlation data in the form of covariance matrices for some of their analyses. This so-called simplified likelihood [181] approach assumes that uncertainties can be well approximated by Gaussians. SMod-

ELS [93, 92, 94] can make use of these correlation data since its version 1.2 [94]; their benefit for limit setting was demonstrated in [94] and contribution 15 of [90].[1]

ATLAS has recently gone a significant step further by publishing *full likelihoods* using a JSON serialization [107], which provides background estimates, changes under systematic variations, and observed data counts at the same fidelity as used in the experiment. The JSON format describes the HistFactory family of statistical models [108], which is used by the majority of ATLAS searches. The pyhf package [109] is then used to construct statistical models, and perform statistical inference, within a python environment. Note that this fulfills for the first time the Les Houches Recommendations 3(b,c)!

In the following we describe the usage of the ATLAS pyhf likelihoods in SModelS. We also demonstrate the improvements in the statistical evaluation —and thus in the constraining power—due to these likelihoods.

### 5.1.1 Usage in SModelS

The pyhf JSON files [107] from ATLAS report $L(\theta|\mathcal{D})$, where $\theta$ is the union of parameters of interest and possible nuisance parameters and $\mathcal{D}$ denotes the observed data. Encoded in this way are, in particular, background estimates, correlations, and primary data. Together with the relevant simplified model efficiency maps, they allow SModelS to evaluate the likelihood of the signal strength of a hypothesized signal in a realistic manner.

To make use of this machinery, besides `scipy` and `numpy`, which are already required by SModelS, the following python packages need to be installed:

`pyhf`, `jsonpatch`, `jsonschema`.

In addition, for speed reasons, we recommend `pytorch` as backend for `pyhf` (if not available, the default backend will be used). Details are given in the online manual at `https://smodels.readthedocs.io/en/stable/Installation.html`. Details on the pyhf package are given in [109] and at `https://scikit-hep.org/pyhf/`.

### 5.1.2 Implementation in the database

In the SModelS database, the JSON files are placed in the respective analysis folder that holds the simplified model efficiency maps (see [92] for the database structure). The information, which JSON file is used to combine which SRs, is given in the `globalInfo.txt` file in each analysis folder. For example, for the ATLAS stau search [57], which has two SRs, the `globalInfo.txt` file contains:

```
id: ATLAS-SUSY-2018-04
....
datasetOrder: "SRlow", "SRhigh"
jsonFiles: {"SRcombined.json": ["SRlow", "SRhigh"]}
```

[1] Non-Gaussian effects can also be incorporated in the simplified likelihood framework. To this end, Ref. [116] proposed a simple method to encode asymmetry information into correlations via publication of only $N_{\text{bins}}$ additional numbers (as opposed to the more common $N_{\text{bins}} \times N_{\text{bins}}$ second order correlation data).

In case the provided JSON files describe the combination of one or more subsets of SRs, as in the multi-$b$ sbottom search [182], the format is:

```
id: ATLAS-SUSY-2018-31
....
datasetOrder: "SRA_L", "SRA_M", "SRA_H", "SRB", "SRC_22",
              "SRC_24", "SRC_26", "SRC_28"
jsonFiles: {"BkgOnlyA.json": ["SRA_L", "SRA_M", "SRA_H"],
            "BkgOnlyB.json": ["SRB"],
            "BkgOnlyC.json": ["SRC_22", "SRC_24", "SRC_26",
                              "SRC_28"]}
```

Here, the likelihoods for SRs A, B and C will first be evaluated separately, and then only the most sensitive result among SRA, SRB and SRC will be used for the limit setting.

### 5.1.3 Changes/additions in the SModelS code

The interfacing of pyhf to SModelS can be summarized in two parts: the addition of an independent module `tools/pyhfInterface.py`, and the changes brought to `experiment/datasetObj.p`

The `tools/pyhfInterface.py` module is made of two classes, `PyhfData`, storing and handling informations related to the JSON files and input signal predictions, and `PyhfUpperLimitComputer`, where the upper limits are inferred given the `PyhfData` information. The constructor of `PyhfData` takes as arguments `nsignals` and `inputJsons`, which are respectively the list of BSM prediction yields and the list of workspaces, i.e., the likelihoods as python JSON objects [183]. The list of signal yields is a 2-dimensional list, so that there is a sublist for each JSON likelihood. For the previous example

```
jsonFiles: {"BkgOnlyA.json": ["SRA_L", "SRA_M", "SRA_H"],
            "BkgOnlyB.json": ["SRB"],
            "BkgOnlyC.json": ["SRC_22", "SRC_24", "SRC_26",
                              "SRC_28"]}
```

the `nsignals` would read

```
nsignals = [[<SRA_L>, <SRA_M>, <SRA_H>],
            [<SRB>],
            [<SRC_22>, <SRC_24>, <SRC_26>, <SRC_28>]]
```

where `<SRA_L>`, `<SRA_M>`, ... are the event yield predictions in the signal regions named `"SRA_L"`, `"SRA_M"`, ..., respectively.

The JSON likelihoods provided by ATLAS are written in the following python dictionary structure:

```
{"channels":[
    {"name":..., "samples":[
        {"data":[...], "modifiers":[...]},
        {"data":[...], "modifiers":[...]},
        ...
        ]
```

```
    },
    {"name":..., "samples":[...],
    ...
    ]
}
```

where the `channels` are the usual signals regions, and the `samples` contain the different background contributions. In each sample, `data` contains the event yields and `modifiers` is the list of all the modifiers representing the uncertainties. The hypothesized BSM signal will be added in the form of one of these `samples`.

The `PyhfData` constructor first collects information in the workspaces such as the number of SRs, and the paths to the `samples` where the BSM predictions are to be written, and also the VRs and CRs that are assumed not to contribute and are then removed from the workspaces. It must be noted that this approximation can imply a slight loss in accuracy because any potential leakage of the signal into the VRs or CRs is neglected. The fetched information in the `inputJsons` is then compared to the `nsignals` to check for any inconsistencies in the format of the two variables.

The `jsonpatch` package [184] allows one to easily write into an existing JSON object. The `PyhfUpperLimitComputer` class uses this feature to add the BSM prediction yields and remove the control and virtual regions from the workspaces. This procedure is dynamical so that the signal predictions can be re-scaled throughout the statistical inference.

The `pyhf.infer.hypotest` allows the computation of the $CL_s$ [185] with a signal strength modifier $\mu$ as argument, using the asymptotic formulae from [186]. Upper limits are found by varying the $CL_s$ with respect to $\mu$. Namely, our pyhf interface will look for the $\mu$ at 95% exclusion CL. $\mu$ being a multiplicative factor, the unit of the obtained upper limit will depend on the unit of the signal predictions provided. In our case, normalised signals give unitless upper limits on the event yields. We first dynamically rescale the signal predictions, so that $\mu$ at 95% CL lies in the interval [0.2, 5], and then use the `optimize` feature of the `scipy` package [187] to find the exclusion limit at 95% CL.

The independent `tools/pyhfInterface.py` module is interfaced to SModelS in `experiment/datasetObj.py`, as it is for the simplified likelihood. If combination is requested and JSON files are found in the database, the code in `datasetObj.py` will perform pyhf combination. If more than one JSON file is provided, "best expected combination" is performed, i.e., the upper limit is computed using the JSON that gives the most sensitive combination.

### 5.1.4 Running SModelS

The interface to pyhf is available from SModelS v1.2.4 onward. Running the program has not changed with respect to previous versions, apart from setting a switch to evoke the (optional) use of the JSON files in the database. When using `runSModelS.py`, one has to set

```
combineSRs = True
```

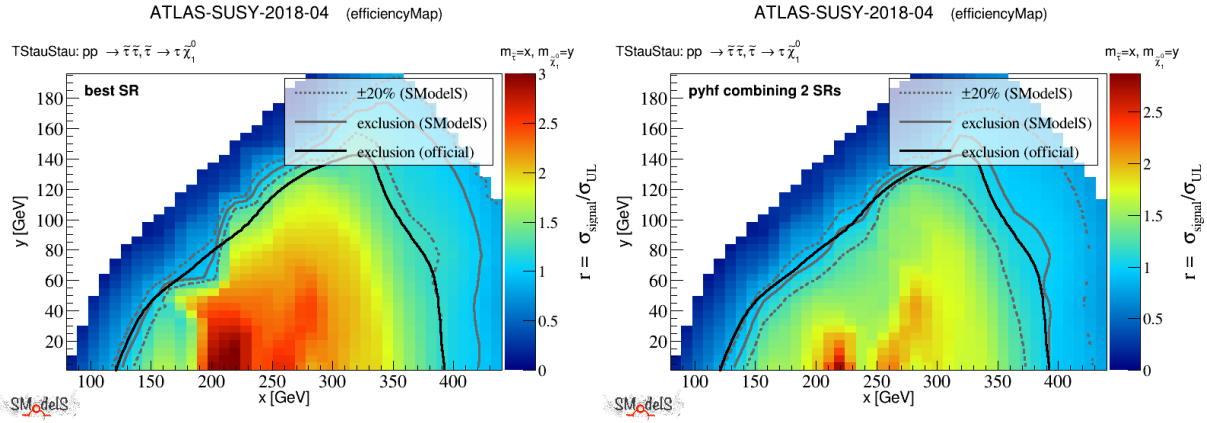


Figure 5.1: Validation of TStauStau ($pp \to \tilde{\tau}_1^+\tilde{\tau}_1^-$, $\tilde{\tau}_1^\pm \to \tau\tilde{\chi}_1^0$) result from the ATLAS stau search [57], on the left using the best SR, on the right using the full likelihood.

in the `paramerers.ini` file. Note that the same flag also turns on the SR combination in the simplified likelihood approach for CMS efficiency map results, for which a covariance matrix is available.

Alternatively, one can call `theoryPredictionsFor()` with the option `combinedResults=True` in one's own `python` program, cf. the `Example.py` file in the SModelS v1.2.4 distribution.

## 5.2 Validation and physics impact

We compare in Figure 5.1 the SModelS exclusion (grey line) with the official exclusion (black line) for the ATLAS stau search [57], using best SR (left) and using `pyhf` combination (right). As one can see, the usual procedure, which picks up the most sensitive efficiency map result, over-excludes by about 50 GeV on half the exclusion line. In contrast, a very good agreement with the official ATLAS result is obtained with the full `pyhf` likelihood.[2]

Figure 5.2 shows the same kind of validation for the ATLAS sbottom search [182], which was actually the first one to provide the full likelihood. In this case, without `pyhf`, SModelS is under-excluding by roughly 50–100 GeV.[3] Again we observe a significant improvement with the `pyhf` combination.

Our third example, shown in Figure 5.3, is for the ATLAS electroweakino search in the $W(\to \ell\nu)h(\to b\bar{b}) + E_T^{\text{miss}}$ channel [188]. Using the best exclusive SR (left panel in Figure 5.3), we face an under-exclusion over almost the entire mass plane. Using instead the best inclusive SR (not shown) would give a SModelS limit closer to the official one for large mass differences, but lead to a serious over-exclusion for small mass differences. The combination of SRs based on the full likelihood resolves these problems, and we obtain a good agreement of the SModelS exclusion line with the official one from ATLAS as shown in the right panel of Figure 5.3.

[2]The remaining small difference might be due to the (interpolated) acceptance × efficiency values from the simplified model efficiency maps not exactly matching the "true" ones of the experimental analysis.

[3]This under-exclusion is even more pronounced when using the inclusive instead of the exclusive SRs for this analysis.

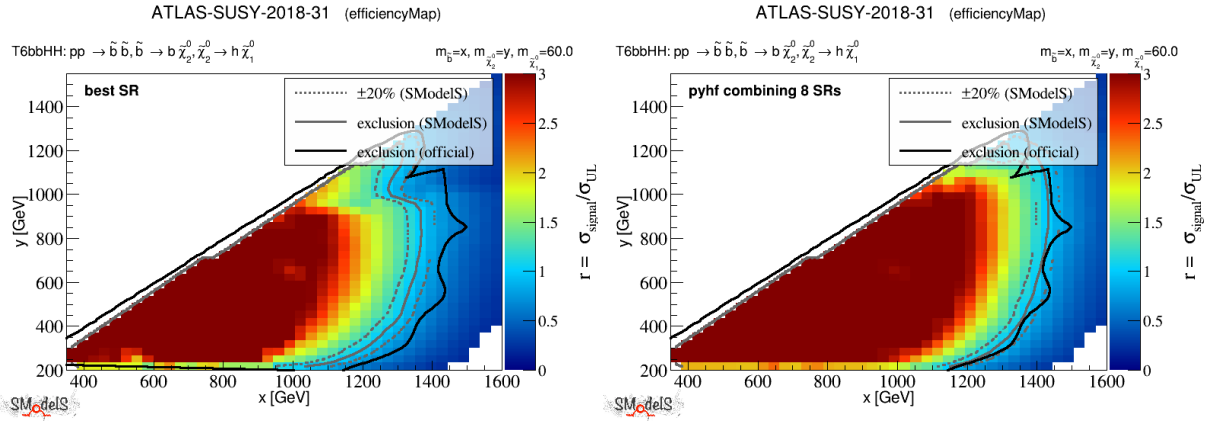


Figure 5.2: Validation of the T6bbHH ($pp \to \tilde{b}_1\tilde{b}_1^*$, $\tilde{b}_1 \to b\tilde{\chi}_2^0$, $\tilde{\chi}_2^0 \to h\tilde{\chi}_1^0$) result from the ATLAS sbottom search [182], on the left using the best SR, on the right using the full likelihood.

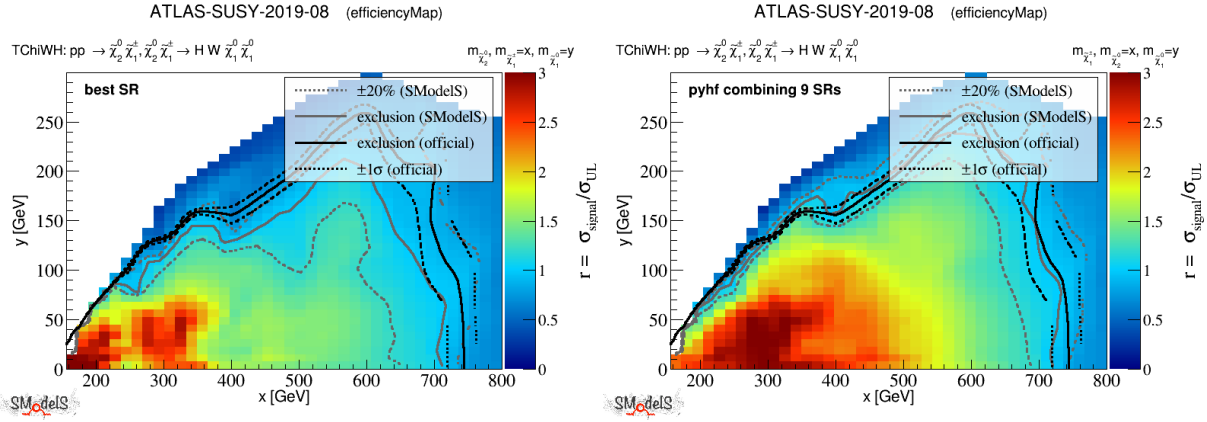


Figure 5.3: Validation of the TChiWH ($pp \to \tilde{\chi}_2^0\tilde{\chi}_1^\pm$, $\tilde{\chi}_2^0 \to h\tilde{\chi}_1^0$, $\tilde{\chi}_1^\pm \to W\tilde{\chi}_1^0$) result from the ATLAS electroweakino search [188], on the left using the best SR, on the right using the full likelihood.

Even though we only show three results here, one can appreciate the gain in accuracy one can reach with using pyhf and full likelihoods. The ATLAS collaboration is at the beginning of a huge effort to provide full statistical models for new analyses. The first analyses published already show how this can help theorists make more trustful reinterpretations. The importance of such likelihood information for, e.g., global fits, has also been emphasised in [178].

## 5.3 Conclusions

We presented an interface of SModelS to pyhf that enables the use of the full likelihoods provided by ATLAS in the form of pyhf JSON files. The SModelS database was extended by efficiency map results with the corresponding JSON files of three new ATLAS SUSY analyses [57, 182, 188] for full Run 2 luminosity (139 fb$^{-1}$).

The new version, SModelS v1.2.4, is publicly available from `https://smodels.github.io/` and can readily be employed for physics studies.

This completes the work started in contribution 15 of [90] for SModelS; the MadAnalysis5 interface to pyhf discussed in chapter 4, was developed shortly after this work.

Last but not least we note that the technical discussions with the pyhf team were handled via github's issue tracking system, see e.g. `https://github.com/scikit-hep/pyhf/issues/620`, and are thus transparent and open to all.

# Chapter 6

# Constraining new physics with SModelS version 2

In addition to the implementation of the SModelS interface to `pyhf`, several other important developments were made in the SModelS tool. Some major changes were carried out in the code, which resulted in the release of SModelS version 2. This section is based on [177] and presents these new developments as well as two case studies demonstrating their physics impact. One of the most important noveltes is the change of particle description. Any BSM state was before only represented by its mass, while in this new version, a particle object allows the definition of multiple particle properties such as quantum numbers, decay width, etc. In particular, this allows the use of width-dependent results, simultaneously with standard prompt results. Thanks to this, a few LLP results have been implemented in the SModelS database at the time of this work. The physics impact is demonstrated with the phenomenological study of two models. First, two scenarios of the scotogenic model are considered, a fermionic DM scenario and a scalar DM scenario, both of which can trigger different LLP constraints. Finally, a realistic SUSY electroweakino scenario is studied, with DM considerations as well. My contribution to this work was, first, the implementation of new ATLAS analyses with their `JSON` files. For example, one displaced leptons analysis has proven how SR combination can improve the constraints in the fermionic DM scenario of the scotogenic model. My second contribution concerned the phenomenological study of the scalar DM scenario, which was constrained by HSCP and disappearing tracks results, depending on the decay length of the charged state.

## 6.1 Introduction

Run 2 of the LHC has presented us with an incredible performance and an exciting physics programme in the quest for new physics beyond the BSM. Given the null results so far in the plethora of searches for new particles, it becomes increasingly clear that the effects of BSM physics must either be manifest at higher energy scales, or be much more subtle and/or complicated to find than originally hoped for. Consequently, searches for new physics by the LHC experimental collaborations have intensified and widened in scope. One of the directions in which many new analyses have been directed is searches for new LLPs, and many interesting new results in the pursuit of both, "prompt" and "long-lived" new physics have been coming out for the Run 2 data.

On the phenomenology side, reinterpretation efforts have intensified, with much closer theory-experiment interaction than seemed possible at the beginning of the LHC era [112, 75, 114]. It is in this spirit that public software tools for the reinterpretation of the LHC results have been developed, to allow for reinterpretation studies outside the experimental collaborations, help obtain a global and coherent view of how the experimental data constrain BSM scenarios, and guide future experimental and theoretical explorations. See Ref. [75] for the status and recommendations after Run 2, as well as an overview of reinterpretation methods and tools.

For BSM theories with a $\mathcal{Z}_2$-like symmetry, the SModelS package [93, 92, 95, 94, 96, 119, 189] provides a particularly efficient way to reuse and reinterpret the results from LHC searches for new particles. SModelS is based on the concept of simplified models; it decomposes the signatures of full BSM scenarios into simplified model components (here called *topologies*) which are then confronted against the experimental constraints from a large database of results. Since this does not involve any Monte Carlo event simulation, SModelS is extremely fast and thus particularly well suited for model surveys, including large scans. The code and its vast database were also exploited recently in a new statistical learning algorithm that aims at identifying dispersed signals in the slew of LHC results [190].

While very powerful, the SModelS approach to testing BSM theories involves a number of approximations. In particular, in the SModelS v1 series, the simplified model description involved only the structure of the topology (number of vertices in each branch, and number and type of SM final states in each vertex) and the masses of the BSM particles. Other properties like spin or color representation of the BSM particles, which might influence the kinematic distributions of the final state, were ignored. For many LHC searches with rather inclusive kinematical selection, in particular most searches for R-parity conserving SUSY, this is a reasonable approximation [93, 191, 192, 193]. Nonetheless, there is need for a more refined simplified model description in SModelS, in particular to be able to include the large variety of decay-width (lifetime) dependent LLP results.

We therefore present in this paper version 2 of SModelS.[1] The most important new development in this new version is the introduction of a *particle class*, enabling an extended topology description with a flexible number of attributes for the BSM particles, such as spin, charge, decay width, etc. As mentioned above, this allows in particular for a better treatment of LLP signatures. Moreover, constraints from prompt and long-lived searches can be evaluated simultaneously in the same run. On the database side, SModelS v2 includes results from searches for HSCPs, disappearing tracks, displaced jets and displaced leptons, in addition to a large number of prompt searches.

In the following, we describe in detail the technical novelties in SModelS v2 and demonstrate the capabilities of the program by means of two physics applications: the scotogenic model [29, 30] with either a scalar or a fermionic DM candidate, and the EW-ino sector of the MSSM [194, 195, 196, 197]. The appendices give further details on the current database, the development of home-grown HSCP efficiency maps, and the interface to micrOMEGAs [198, 199, 200]. It is assumed that the reader is familiar with the concepts and working principle of SModelS. If this is not the case, we refer to [93] and the online documentation [201] for a more detailed introduction.

[1] The concrete version which this paper is based on is v2.1.

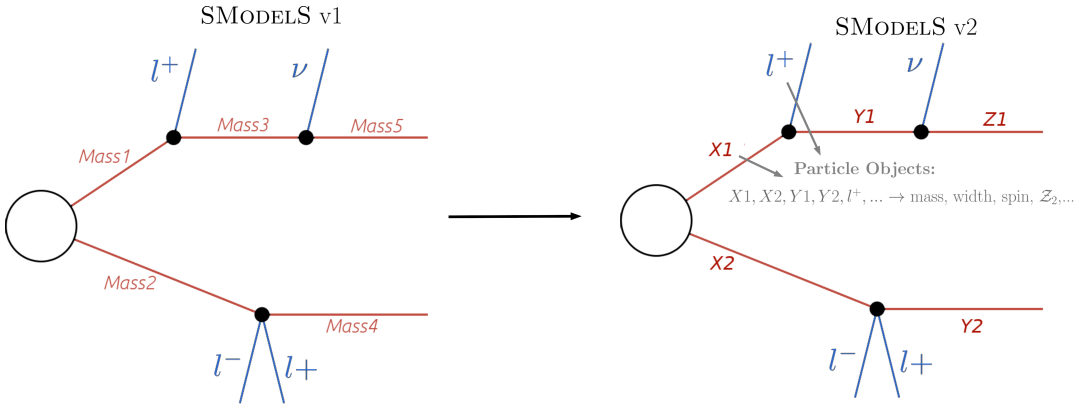


Figure 6.1: Comparison between the simplified model description in SModelS v1 (left) and in SModelS v2 (right). For the latter, the newly introduced particle class is used to describe all particles appearing in the topology.

## 6.2 Extension of the topology description in SModelS v2

The most significant novelty in SModelS v2 is the introduction of *particle objects*, which allows for more flexibility when dealing with simplified models. In the SModelS v1 series [93, 92, 94, 119], only the masses of intermediate BSM particles were used for describing the simplified model topologies tested by the database or obtained from the decomposition of the input model. Furthermore all final states, whether they are SM particles or (meta-)stable BSM particles, were described by simple labels (strings). Hence, despite the handling of a large variety of simplified model constraints, SModelS v1 was not able to deal with width-dependent results, such as searches for displaced decays, or searches which depend on additional information concerning the BSM particles, such as their spin or color representation.

### 6.2.1 Particle class

In the SModelS v2 series, the introduction of a *particle class* replaces the simple list of particle masses by full objects, which can carry any desirable number of properties, such as mass, width, spin, electric charge, etc. As illustrated in Fig. 6.1, these objects are henceforth the fundamental building blocks for describing the experimental results in the database, and for decomposing the input model. When matching the signal topologies of the input model onto those in the database, the comparison is made at the level of particle objects; particle objects with the same properties are considered as equal, independent of their labels.

At present, the following attributes (properties) are considered:

- `Z2parity`: the $\mathcal{Z}_2$-type parity of the particle ($-1$ for odd particles and $+1$ for even particles).
- `spin`: the particle spin (1/2 for fermions, 0 for scalars, ...)
- `colordim`: the color representation (1 for singlets, 3 for triplets and 8 for octets)

- `eCharge`: the electric charge ($-1$ for electrons, 0 for neutrinos, ...)
- `mass`: the particle mass
- `totalwidth`: the particle total decay width.

Note however that the number of attributes is a priori not fixed; new ones may be introduced by the user if needed.

In the database of experimental results, if a specific property has no assigned value, it is assumed to be "arbitrary". For instance, if a search is sufficiently inclusive to be, to a good approximation, insensitive to the spins of the BSM particles, the spins are left unspecified in the database entry. It is then understood that the corresponding result applies to particles of arbitrary spin.[2]

### 6.2.2 Model input

The input provided by the user is conveniently split into two files: one containing the definition of BSM particles and their properties (model specification) and one defining their masses, widths, branching ratios and production cross sections (model parameters). The list of BSM particles can be defined in two distinct ways: either by writing a simple file using Python syntax and instantiating the particle objects:[3]

```
X=Particle(Z2parity=-1,label='X',pdg=5000021,eCharge=0,colordim=8,spin=1./2)
Y=Particle(Z2parity=-1,label='Y',pdg=5000022,eCharge=0,colordim=1,spin=1./2)
...
```

or by providing a SLHA-type file with QNUMBERS blocks for each BSM particle, as shown in Fig. 6.2. Note that in the QNUMBERS blocks, whether a BSM particle is even or odd is specified by a symmetry factor $S$, $S = 0$ or 1, in key 11. This is related to the $\mathcal{Z}_2$(-like) parity, $P_{\mathcal{Z}_2}$, by $P_{\mathcal{Z}_2} = (-1)^S$. If key 11 is not defined, it will be assumed that $S = 1$ (odd particle). We point out that such SLHA files containing QNUMBERS blocks for the model definition are generated automatically by the micrOMEGAs-SModelS interface [200], see also Appendix A.3. Moreover, they can be generated by tools relying on the UFO format [202], such as MadGraph [203, 62].

As in previous versions, the model parameters (masses, decays, ...) can be provided either as an SLHA file containing MASS, DECAY and XSECTION blocks, or an LHE file containing parton level events. The typical usage is to keep the BSM model fixed and test distinct points of its parameter space. In this case, one needs a single file with the list of BSM particles (set, *e.g.*, in the `parameters.ini` file) plus the distinct parameter files for each point of parameter space, which one can also conveniently loop over. Details and explicit examples are given in the online documentation [201].

[2] This is a good approximation for many $E_T^{\text{miss}}$ searches, apart from mono-X searches, analyses relying on ISR jets, and analyses explicitly using shape information.

[3] A few specific model definitions, such as the MSSM, NMSSM and the Inert Doublet Model (IDM), are shipped with the code in the `smodels/share/models` folder and can be used as examples for defining new models.

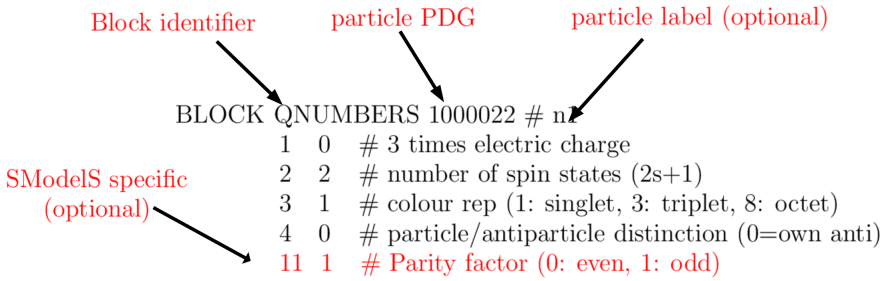


Figure 6.2: Format for the QNUMBERS block, which can be used to define new particles in SModelS v2.

### 6.2.3 Decomposition for non-prompt decays

In SModelS v2 the general procedure for decomposing the full BSM model into simplified model topologies is similar to the one in previous versions: the decomposition makes use of the production cross sections to identify the primary mothers produced in the hard scattering processes, which are then (cascade-)decayed according to the decay channels given by the input model. This procedure is followed until all unstable BSM daughters have decayed, as illustrated in Fig. 6.3. All possible cascade decays of each primary mother are then combined to generate a list of simplified model topologies (also called *elements*), which approximates the input model by a coherent sum of elements.

However, the way non-prompt decays are handled has changed significantly. The behavior is controlled by two parameters:

- `promptWidth`: minimum width for a particle to be considered decaying promptly
- `stableWidth`: maximum width for a particle to be considered detector stable

which can be set in the `parameters.ini` file. The default values are $10^{-8}$ GeV for `promptWidth` and $10^{-25}$ GeV for `stableWidth`. If the total decay width of a given BSM particle is larger than `promptWidth`, the particle is considered to decay promptly and will never appear as a final state.[4] On the other hand, if its width is smaller than `stableWidth`, the particle is considered stable on detector scales and all of its decays are ignored. Finally, if the width lies between `stableWidth` and `promptWidth`, all relevant topologies are generated where the particle can appear as an intermediate (decayed) or final-state particle. These cases are shown in Fig. 6.4. They allow the decomposition procedure to generate topologies where a meta-stable particle can appear either as an intermediate state or a final state, thus allowing SModelS v2 to simultaneously test the input model against searches for both prompt and displaced decays (see Section 6.2.4 for more details).

### 6.2.4 Results description in the database

In previous SModelS versions, the database of experimental results was limited to UL map or EM results parametrized as a function of the BSM masses ($M_i$) appearing in the simplified model topology. Consequently, only searches for promptly decaying BSM

[4] In the current version, the electric charge, color and spin of promptly decaying BSM particles are ignored, which simplifies the decomposition procedure. This is well justified for the prompt searches in the current database, which are largely insensitive to these quantum numbers.

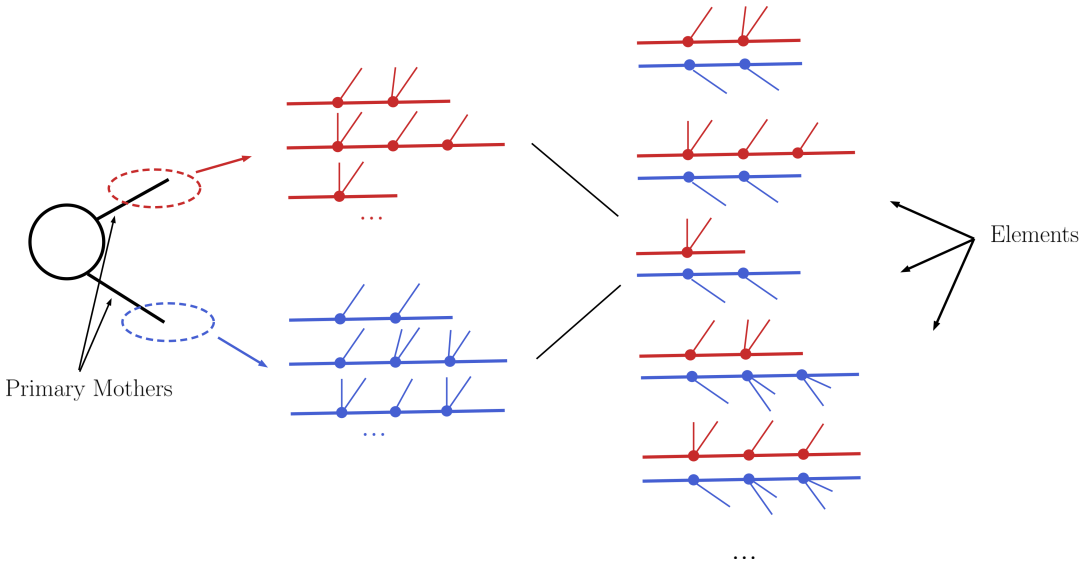


Figure 6.3: Schematic representation of how a full model is decomposed into simplified model topologies within SModelS. The input production cross sections are used to defined the primary mothers, which originate a list of possible branches for all the corresponding decay channels of the mother. The branches are then combined in pairs (according to the primary mothers appearing in the production cross sections) to form simplified model topologies, here called elements.

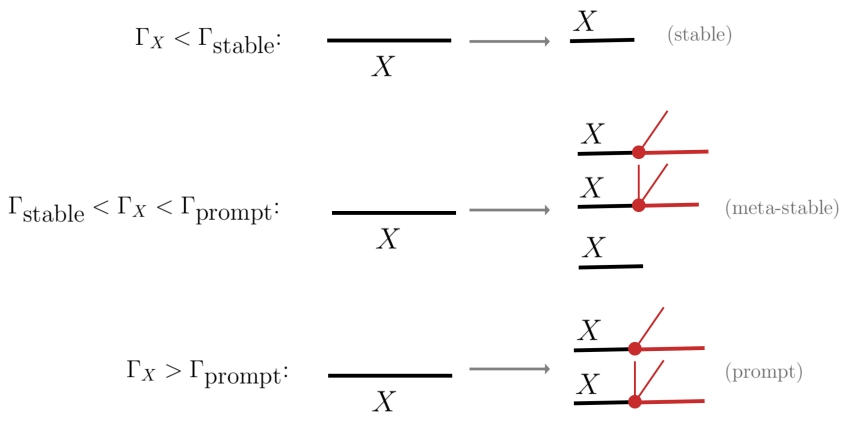


Figure 6.4: Illustration of how the decays of a given BSM particle are handled according to the particle's decay width (see text for details).

particles, or for BSM particles which are stable on detector scales could be included. In order to describe searches for non-prompt particles decaying inside the detector, in SModelS the ULs or EMs were extended to include both the mass and the width ($\Gamma_i$) of the BSM particles:

$$\epsilon(M_i) \to \epsilon(M_i, \Gamma_i) \text{ and } \sigma_{\rm UL}(M_i) \to \sigma_{\rm UL}(M_i, \Gamma_i), \tag{6.1}$$

where $\epsilon$ represents an efficiency[5] and $\sigma_{\rm UL}$ an upper limit on the production cross section.

However, most of the (prompt) results contained in the SModelS database have no explicit width dependence, since they implicitly assume all decays to be prompt and the last BSM particle in the cascade decay to be stable. In this case, if the total width of the decaying particle is smaller than `promptWidth`, it is necessary to rescale the original efficiencies or upper limits in order to take into account the width dependence given the implicit assumption of a prompt decay. Within SModelS v2 this is done by reweighting the efficiency or upper limit whenever the width dependence is not explicitly specified by the experimental result. The reweighting corresponds to evaluating the approximate fraction of prompt decays appearing in the input topology and the fraction of decays outside of the detector for the last BSM particle:[6]

$$\epsilon(M_i, \Gamma_i) = \mathcal{F}_{\rm prompt}(\Gamma_i) \times \epsilon(M_i) \text{ and } \sigma_{\rm UL}(M_i, \Gamma_i) = \sigma_{\rm UL}(M_i)/\mathcal{F}_{\rm prompt}(\Gamma_i)\,, \tag{6.2}$$

where

$$\begin{aligned} \mathcal{F}_{\rm prompt} &= \left[\prod_{i=1}^{N-1} \mathcal{F}_{\rm prompt}(\Gamma_i)\right] \mathcal{F}_{\rm stable}(\Gamma_N) \\ &= \left[\prod_{i=1}^{N-1} \left(1 - \exp(-\Gamma_i L_{\rm eff}^{\rm inner}\right)\right] \exp(-\Gamma_N L_{\rm eff}^{\rm outer})\,. \end{aligned} \tag{6.3}$$

The term in brackets corresponds to the probability that the first $N-1$ decays take place sufficiently close to the interaction point to be considered prompt while the $N$th decay takes place outside the detector. The effective inner and outer detector sizes ($L_{\rm eff} = L/\langle\gamma\beta\rangle$) are taken to be $L_{\rm eff}^{\rm inner} = 0.769$ mm and $L_{\rm eff}^{\rm outer} = 7.0$ m. We also point out that the rescaling defined in eq. (6.2) can be trivially extended to results where the efficiency (or upper limit) dependence on the widths is partially known, *e.g.*, when only the dependence on the width of the last decay is provided.

Finally, recall that in SModelS v2, the quantum numbers of the intermediate and final BSM particles can also be specified when describing an experimental search. Therefore, it is possible to restrict the search applicability to more specific scenarios, such as topologies with a particular spin assignment for the BSM particles. For instance, as discussed in Section 6.3.1, the implementation of the ATLAS disappearing track search contains distinct efficiency maps for pair production of scalar and femionic LLPs.

[5] In SModelS terminology, "efficiencies" are values of acceptance $\times$ efficiency, $\epsilon \equiv \mathcal{A}\varepsilon$.

[6] Note that since the efficiency dependence on the width scales as $\epsilon \propto \mathcal{F}_{\rm prompt}(\Gamma_i)$, the upper limit on the cross section scales as $\sigma_{\rm UL} \propto 1/\epsilon \propto 1/\mathcal{F}_{\rm prompt}(\Gamma_i)$.

### 6.2.5 Missing topologies

The constraints provided by SModelS are obviously limited by its database and the available set of simplified model interpretations provided by the experimental collaborations or computed by theory groups. Therefore it is interesting to identify classes of missing simplified models (or missing topologies) which are relevant for a given input model, but are not constrained by the database. As in previous versions, SModelS provides as output the list of the simplified models with highest cross sections which were not constrained by the database. The lack of constraints can be due to two main reasons:

1. no experimental result has considered the specific simplified model or

2. the model parameters (masses and/or widths) fall outside the range considered by the experimental result.

In SModelS v2, the classification of missing topologies has changed significantly with respect to previous versions, since inclusion of displaced results in the database makes it more difficult to uniquely classify the unconstrained topologies. The strategy adopted in SModelS v2 is to classify all experimental results into displaced or prompt results[7] and to consider the unconstrained topologies according to these types of results. They are therefore grouped according to the following *coverage groups*:

- *missing (prompt)*: not covered by any prompt-type results. This group corresponds to all topologies which did not match any of the simplified models constrained by prompt results in the database.

- *missing (displaced)*: not covered by any displaced-type results. This group corresponds to all topologies which did not match any of the simplified models constrained by displaced results in the database.

- *missing (all)*: not covered by any type of result. This group corresponds to all topologies which did not match any of the simplified models considered by the prompt and the displaced results in the database.

- *outside the grid*: this group corresponds to topologies which are matched by at least one experimental result in the database (prompt or displaced), but their parameters (masses and/or widths) fall outside the ranges considered by the results.

In addition, the *missing (prompt)* group reweights its topology cross sections by the fraction of prompt decays, as defined in eq. (6.3). The *missing (displaced)* group, on the other hand, reweights its topologies by the fraction of displaced decays. Since the grouping defined above is somewhat arbitrary, it is possible for the user to redefine them with a few simple changes in the SModelS code, as detailed in the online manual [201].

[7]Prompt results are all those which assumes all decays to be prompt and the last BSM particle to be stable (or decay outside the detector). Signatures with HSCPs, for instance, are classified as prompt, since the HSCP is assumed to decay outside the detector. Displaced results on the other hand require at least one decay to take place inside the detector.

## 6.3 Database extension

In this section, we briefly summarize the most important additions to the database. More details are provided in the release notes, which come with the program package (also available online [201]). An overview of all 13 TeV results included in the SModelS 2.1.0 database is given in Appendix A.1.

### 6.3.1 Results from searches for long-lived particles

**Heavy stable charged particles:** For HSCPs, we have newly included results from the 13 TeV ATLAS search [50] with 36 fb$^{-1}$ (ATLAS-SUSY-2016-32). On the one hand, we implemented the UL on the direct production of HSCPs and $R$-hadrons. On the other hand, we recasted the analysis employing the prescription provided in the auxiliary information of the publication and generated EM results for the 11 topologies listed in Appendix A.2. They contain directly produced HSCPs, as well as HSCPs arising from a 1- or 2-step decay. We included asymmetric and mixed HSCP/$E_T^{\text{miss}}$ branches containing up to three mass parameters. For the EMs with up to two mass parameters, we included the explicit width-dependence as a third parameter. Details are given in Appendix A.2.

**Disappearing tracks:** The SModelS database now contains efficiency maps for one or two charged tracks from searches for long-lived charginos by ATLAS [48] (ATLAS-SUSY-2016-06, 36 fb$^{-1}$) and CMS [47] (CMS-EXO-19-010, 101 fb$^{-1}$). Since these analyses can be very sensitive to the LLP decay length, which depends on the LLP boost and consequently on its spin, the disappearing track analyses were implemented for specific spin assignments. For the ATLAS analysis, we use the efficiency maps provided by [204, 205] for both the fermionic (chargino) and the scalar (charged Higgs) LLP cases. For the CMS analysis, we use the efficiency maps provided by the collaboration; here only the fermion (chargino) case is available.

**Displaced jets:** In this category, we have includedULresults from the ATLAS search [44], which targets final states with large $E_T^{\text{miss}}$ and at least one high-mass displaced vertex with five or more tracks (ATLAS-SUSY-2016-08, 32.8 fb$^{-1}$). Moreover, we have included EM results for the CMS search for non-prompt jets [46] with full Run 2 luminosity (CMS-EXO-19-001, 137 fb$^{-1}$).

**Displaced leptons:** Here, we have implemented the results from the ATLAS search [43] for charged leptons with large impact parameters, ATLAS-SUSY-2018-14, for full Run 2 luminosity (139 fb$^{-1}$). Note that this analysis provides not only EMs but also the statistical model[8] in pyhf JSON format on HEPData!

### 6.3.2 Results from conventional (prompt) SUSY searches

Newly added were UL and EM results for the ATLAS gluino/squark searches in the $1\ell$+jets and $0\ell$+jets final states, ATLAS-SUSY-2018-10 [206] and ATLAS-SUSY-2018-22 [207], and for the $0\ell$ stop search ATLAS-SUSY-2018-12 [208]. Likewise, UL results

[8] See [114] for a detailed discussion of why and how to publish the statistical models.

were added for the electroweak-ino search in the $WH + E_T^{\text{miss}}$ final state, ATLAS-SUSY-2018-23 [209] (no EMs available in this case). All these analyses are for 13 TeV and full Run 2 luminosity.

Moreover, we augmented the previously availableULresults from the 13 TeV ATLAS electroweak-ino searches in the $WZ + E_T^{\text{miss}}$ final state, ATLAS-SUSY-2017-03 [210] and ATLAS-SUSY-2018-06 [211], and the 8 TeV CMS stop search with soft leptons, CMS-SUS-14-021 [212], with the corresponding EM results.

## 6.4 Physics applications

### 6.4.1 Constraints on long-lived particles in the scotogenic model

As first showcase for the usage of the new width-dependent results, we consider the scotogenic model [29, 30]. Depending on the setup, this model features scalar or fermionic DM candidates. In either case, there can be long-lived charged scalars leading to HSCP, disappearing track, or displaced lepton signatures at the LHC.

The scotogenic model supplements the SM by an additional SU(2) scalar doublet, $\Phi$, often referred to as the *inert doublet*, and three[9] sterile neutrinos, $N_n$. The new fields are taken to be odd under a new $\mathcal{Z}_2$-parity, while the SM fields are even. The model Lagrangian is given by:

$$\mathcal{L} = \mathcal{L}_{\text{SM}} + |D^\mu \Phi|^2 + \frac{i}{2}\bar{N}_n \partial\!\!\!/ N_n - \left(\frac{1}{2} M_n \bar{N}_n^c N_n + i Y_{\alpha n} \bar{L}_\alpha \sigma_2 \Phi N_n + \text{h.c.}\right) - V(\Phi, H) \quad (6.4)$$

where $\mathcal{L}_{\text{SM}}$ is the Lagrangian of the SM, $M_n$ are the Majorana masses of the right-handed neutrinos, and $Y$ is a $3 \times 3$ complex matrix of Yukawa couplings. Finally, $V$ is the scalar potential

$$\begin{aligned} V(\Phi, H) =& \mu_1^2 |H|^2 + \mu_2^2 |\Phi|^2 + \lambda_1 |H|^4 + \lambda_2 |\Phi|^4 + \lambda_3 |H|^2 |\Phi|^2 \\ &+ \lambda_4 |H^\dagger \Phi|^2 + \frac{1}{2}\lambda_5 \left[(H^\dagger \Phi)^2 + \text{h.c.}\right] . \end{aligned} \quad (6.5)$$

After electroweak symmetry breaking, where $\langle \Phi \rangle = 0$ in this model, the particle spectrum comprises five physical scalar states ($h$, $H^0$, $A^0$, $H^\pm$) with masses:

$$\begin{aligned} m_h^2 &= \mu_1^2 + 3\lambda_1 v^2 , \\ m_{H^0}^2 &= \mu_2^2 + \lambda_L v^2 , \\ m_{A^0}^2 &= \mu_2^2 + \lambda_S v^2 , \\ m_{H^\pm}^2 &= \mu_2^2 + \frac{1}{2}\lambda_3 v^2 , \end{aligned} \quad (6.6)$$

where

$$v^2 = -\frac{\mu_1^2}{\lambda_1} \text{ and } \lambda_{L,S} = \frac{1}{2}\left(\lambda_3 + \lambda_4 \pm \lambda_5\right) . \quad (6.7)$$

[9]Variations of the model with less or more sterile neutrinos have been considered. To explain the observed oscillation in the active neutrino sector within the model, at least two sterile neutrinos need to be introduced. However, in the LHC phenomenology considered here maximally one of these states is involved, while the others are assumed to be heavy and not produced to significant amount.

The first scalar, $h$, is even under the new $\mathcal{Z}_2$-parity and identified with the observed SM-like Higgs boson, $m_h \simeq 125$ GeV. The other scalars are $\mathcal{Z}_2$-odd. Note that the scalar sector of the model has also been considered without the neutrino sector, often referred to as the IDM.

The presence of the new scalar and fermion fields provides a radiative generation of neutrino masses via the radiative seesaw mechanism [29, 30]. Furthermore, the lightest $\mathcal{Z}_2$-odd particle ($H^0$ or $A^0$, or the lightest of the sterile neutrinos, $N_1$) is stable and thus a natural DM candidate. In the following, we consider both options, *i.e.* scalar and fermionic DM candidates.

**Scalar (inert doublet) dark matter**

The scalar sector of the scotogenic model provides two possible DM particles: the scalar $H^0$ and the pseudoscalar $A^0$; in the following we will identify the $H^0$ as the DM candidate without loss of generality. The (collider) phenomenology of the scalar DM scenario is essentially the same as the one of the IDM.[10]

Regarding the relic density, for $m_{H^0} > m_W$, pair-annihilation of $H^0$s into gauge bosons is so efficient that $\Omega h^2$ is typically much (up to 2 orders of magnitude) smaller than the observed value ($\Omega h^2 = 0.12$ [27]). One way to circumvent this conclusion is a small mass splitting between the inert scalars [213, 214, 215]. Indeed, for DM masses around 500–600 GeV one needs (sub-)GeV mass splittings (plus small $\lambda_L$) to achieve $\Omega h^2 \sim 0.12$. For such small mass differences, the $H^\pm$ can become long-lived and can be constrained by HSCP and disappearing track searches. The HSCP constraints were previously discussed in [216] using SModelS v1.

In the scotogenic case, coannihilations with right-handed neutrinos close in mass to the $H^0$ can also help avoid DM under-abundance. As pointed out in [217, 218], these coannihilations tend to increase, rather than reduce, the freeze-out density and thus allow to satisfy the relic density constraint for DM masses well below 500 GeV. Finally, as studied in [219], late decays of heavy right-handed neutrinos (happening after freeze-out of the scalar DM) can be an additional, non-thermal source of DM production and bring an initial under-abundance in agreement with the observed $\Omega h^2$.

These considerations motivate us to consider long-lived charged scalars in the 100–900 GeV mass range and demonstrate how they are constrained by the width-dependent results in SModelS v2. For the numerical analysis, we use the IDM implementation in micrOMEGAs and carry out a random scan over $m_{H^0}$, $m_{H^\pm} - m_{H^0}$ and $m_{A^0}$, with the couplings fixed to $\lambda_2 = 0.01$ and $\lambda_L = 10^{-10}$. The micrOMEGAs-SModelS interface [200] (see also Appendix A.3) conveniently allows one to produce SLHA input files for SModelS including masses, decay tables, and LHC cross sections computed with CalcHep. The QNUMBER blocks are also automatically written by the interface.

Before turning to the results, a few more comments on the parameter scan are in order. First, with the above choice of small $\lambda_2$ and $\lambda_L$, the production of inert scalars at the LHC is dominated by the SM gauge interaction arising from their kinetic terms; this gives conservative estimates of the LHC constraints. In principle values of $\lambda_2, \lambda_L \sim 10^{-2}$

[10] Even if the sterile neutrinos are light, $m_{H^0} < m_{N_i} \lesssim m_{H^\pm}, m_{A^0}$, their Yukawa couplings are too small to play a role for the collider phenomenology. However, the presence of sterile neutrinos can have an effect on the relic density, see the discussion in the main text.

are small enough to this end; the particularly tiny value of $\lambda_L = 10^{-10}$ is chosen to have a vanishing Higgs portal coupling of the DM candidate, which is preferred in view of relic density constraints, see *e.g.* [219], though the precise value is actually irrelevant for the phenomenology discussed here.

Second, the overall mass spread within the inert scalars is constrained by the requirement that the quartic couplings be in the perturbative regime; here we simply require $\lambda_{3,4,5} < 4\pi$ as a rough bound. Moreover, and more importantly, the mass splittings are constrained by electroweak precision observables. For each point in the scan, we compute the oblique parameters $S$ and $T$ from eqs. (24) and (25) in [220] and demand that they fall within the 95% CL region of $S = 0 \pm 0.07$ and $T = 0.05 \pm 0.06$ with a correlation of 0.92 [221]. Very roughly, this limits $m_{A^0} \lesssim 1.4\, m_{H^0}$.

Third, regarding DM constraints, we require that $\Omega h^2 < 0.13$ from the standard thermal freeze-out calculation in micrOMEGAs (assuming $\approx 10\%$ theory uncertainty from the tree-level calculation), and that the DM-nucleon scattering cross section rescaled by a factor $\Omega h^2/0.12$ evades the DM direct detection limits implemented in micrOMEGAs v5.2.7.a. This, however, eliminates hardly any points.

All in all, we sample 29k points that fulfill the above constraints in the region of small mass splittings, $m_{H^\pm} - m_{H^0} < 0.5$ GeV, that gives long-lived charged scalars. The dominant decay modes of the $H^\pm$ are either into $\pi^\pm H^0$ (for $m_{H^\pm} - m_{H^0} > m_{\pi^\pm} = 139$ MeV) or, for $m_{H^\pm} - m_{H^0} < m_{\pi^\pm} = 139$ MeV, into $\ell^\pm H^0$ ($\ell = e, \mu$).[11] Following [225, 204] (see also [226]), we add an effective $H^\pm H^0 \pi^\mp$ vertex

$$\frac{g^2 f_\pi}{4\sqrt{2} m_W^2} (p_{H^\pm} - p_{H^0}) \cdot p_{\pi^\mp} \tag{6.8}$$

in the CalcHep model file, with $f_\pi = 0.13$ GeV the pion decay constant. This interaction arises from an effective, non pertubative $W$–$\pi$ Lagrangian $\mathcal{L} = (g f_\pi)/(2\sqrt{2}) W^+_\mu \partial^\mu \pi^-$ and gives a decay with of [204]

$$\Gamma(H^\pm \to \pi^\pm H^0) = \frac{g^4 f_\pi^2}{64\pi m_W^4} \Delta m^2 \sqrt{\Delta m^2 - m_{\pi^\pm}^2}\,, \tag{6.9}$$

where $\Delta m = m_{H^\pm} - m_{H^0}$.

The relevant long-lived signatures are disappearing tracks, which constrain lifetimes of $\mathcal{O}(1\,\text{cm})$ to $\mathcal{O}(1\,\text{m})$ for charged scalar masses of up to about 200 GeV, and HSCP signatures for lifetimes from about 2 m onward. The scan results are presented in Fig. 6.5, which shows the maximum $r$-value, $r_{\max}$, obtained from SModelS, on the left in the plane of $m_{H^\pm} - m_{H^0}$ versus $m_{H^\pm}$, and on the right in the plane of mean decay length $c\tau_{H^\pm}$ versus $m_{H^\pm}$. The $r$-value is defined as the ratio of the theory prediction for a simplified model topology over the corresponding observed upper limit; points with $r \geq 1$ are therefore considered as excluded.

The pink and white contours show the exclusion limits ($r_{\max} = 1$) from the disappearing track and HSCP searches, respectively. The HSCP limits are relevant for $c\tau_{H^\pm} \gtrsim 2$ m,

[11] For mass differences $m_{H^\pm} - m_{H^0}$ below the QCD scale of around 1.5 GeV, the $H^\pm$ decay should be computed as decay into hadrons, $H^\pm \to \pi^\pm H^0$, instead of a 3-body decay into free quarks, $H^\pm \to u\bar{d} H^0$, via an off-shell $W$-boson [222, 223, 224]. This is important for LLP studies, as $\Gamma(H^\pm \to \pi^\pm H^0) \gg \Gamma(H^\pm \to u\bar{d} H^0)$.

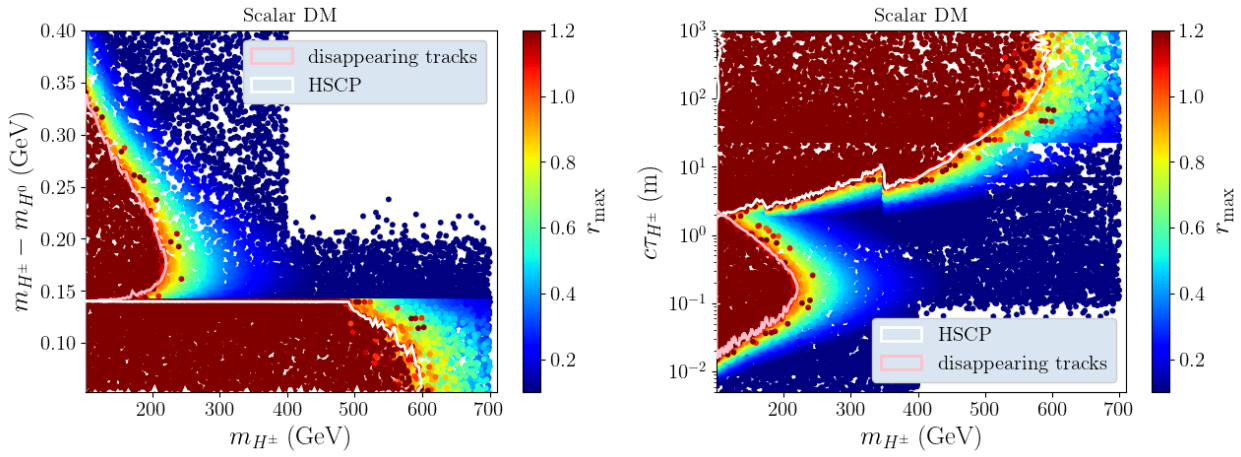


Figure 6.5: SModelS constraints on long-lived charged scalars in the scotogenic model with scalar DM, with the $H^\pm$ decaying either to $\pi^\pm H^0$ or to $\ell^\pm H^0$. The white line denotes the exclusion limit ($r_{\max} = 1$) from HSCP searches, while the pink line denotes the exclusion limit from disappearing track searches; the value of $r_{\max}$ is shown in color.

corresponding to $m_{H^\pm} - m_{H^0} < m_\pi$. The sharp cut-off at the pion mass results from the rapid change in lifetime when the $H^\pm \to \pi^\pm H^0$ decay becomes kinematically allowed. The strongest HSCP constraints come from the 13 TeV ATLAS analysis with 31.6 fb$^{-1}$ [50], the corresponding CMS analysis [227] in the SModelS database having lower luminosity (12.9 fb$^{-1}$). For long lifetimes, $c\tau_{H^\pm} \gtrsim 100$ m, this ATLAS analysis excludes charged Higgs masses up to about 600 GeV. It is worth noting, however, that the 13 TeV analyses do not cover low masses $\lesssim 160$ GeV as a result of the minimum cut on the reconstructed mass, see Appendix A.2. In this region, and for points close to the white contour up to $m_{H^\pm} \lesssim 500$ GeV, the exclusion comes from the 8 TeV CMS analysis [228, 229].

For mean decay lengths ranging from few cm to about 2 m, corresponding to $m_{H^\pm} - m_{H^0} \simeq [0.14, 0.35]$ GeV, the exclusion in Fig. 6.5 comes from the ATLAS disappearing tracks search [48] with 36 fb$^{-1}$. This reaches up to $m_{H^\pm} \approx 220$ GeV for $c\tau_{H^\pm} \approx 20$ cm. We recall that here the EMs for scalar LLPs recasted by [204, 205] are used. In principle there is also the CMS disappearing track search [47] with 101 fb$^{-1}$ of data. For this analysis, however, simplified model results are available only for the chargino/neutralino hypothesis (fermionic LLPs). Since the disappearing track searches are implemented in the SModelS database for specific spin assignments, see Section 6.3.1, by default the CMS results are not applied to the scalar LLP scenario. This is, among other considerations, motivated by the fact that the disappearing track searches make use of hard jets originating from initial-state radiation.

The picture that emerges when ignoring the spin dependence is shown in Fig. 6.6. Indeed the CMS results [47], when applied to the scalar case, significantly extend the excluded region for decay lengths above about 10 cm (blue contour). For $c\tau_{H^\pm} \sim 1$ m, masses up to almost 350 GeV are excluded. Comparing the red and orange regions in Fig. 6.6—the former being the ATLAS exclusion with EMs for the fermionic case, the latter the ATLAS exclusion with EMs for the scalar case—one sees that the effect of the spin dependence is rather small, roughly of the order of 10% in the excluded mass. Moreover, the EMs for scalar LLPs actually exclude more than those for fermionic LLPs.

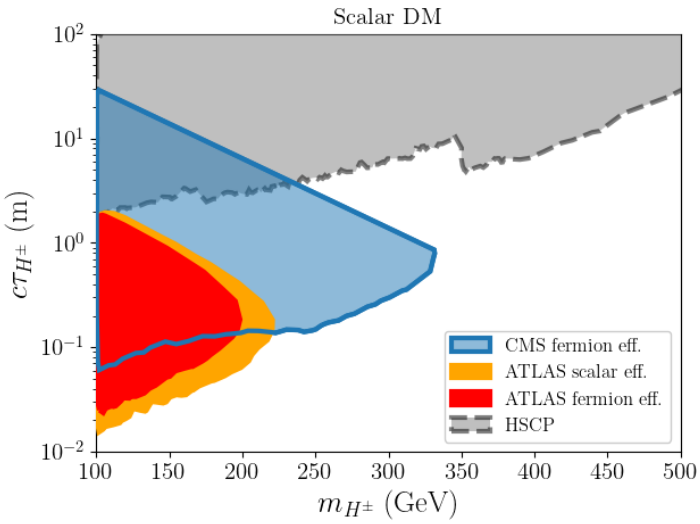


Figure 6.6: Comparison of exclusion limits for long-lived charged scalars as function of $H^\pm$ mass (in GeV) and lifetime (in m), using disappearing track EMs derived for either scalar or fermionic LLPs.

It should thus be safe to apply the simplified model constraints from [47] to scalar LLPs, although one can expect some under-exclusion in this case. In any case, it would be desirable to have dedicated EMs for both spin choices.

Another comment is in order. The alert reader will have noticed the scattered red (excluded) points, outside the white and pink contours in Fig. 6.5. These points have $m_{A^0} - m_{H^\pm} < 5$ GeV. For such small mass differences, the decay products of $A^0 \to H^\pm$ and $A^0 \to H^0$ transitions are very soft and considered as invisible in SModelS. Consequently, $A^0H^0 \to H^\pm H^0 + X_{\text{soft}}$ and $A^0H^\pm \to H^\pm H^0 + X_{\text{soft}}$ production are treated as the same topology as $H^\pm H^0$ production (the $X_{\text{soft}}$ being ignored), meaning their cross sections are added up in the simplified model decomposition. The same applies to $H^\pm H^\mp$ ($+X_{\text{soft}}$) production. This is called *mass compression* in SModelS; the behaviour is controlled by the `minmassgap` parameter, with `minmassgap` = 5 GeV being the default value. Since the cross sections are added up, the constraints typically become stronger once mass compression comes into play. There are, however, some differences between the disappearing tracks and HSCP results, which are worth explaining.

For the disappearing tracks search, results only exist for the direct production of one or two LLPs. Hence, charged scalars from the decay of the neutral inert states are not taken into account except for very small mass splittings where SModelS applies the *mass compression*. This explains why the exclusion reach increases for $m_{A^0} - m_{H^\pm} < 5$ GeV.

For the HSCP search [50], on the other hand, the database contains EM results for all topologies occurring in the IDM/scotogenic model. Hence, whether or not to apply the mass compression for small mass splittings should, in principle, not cause any difference. However, the EMs were produced using SUSY processes and it turns out that for two of the relevant 1-step topologies (concretely THSCPM8 and THSCPM11, see Fig. A.1 and Table A.3 in Appendix A.2), the choices for the production modes and spins of the involved particles are different to the ones in the model considered here. These EMs tend

to underestimate the efficiencies of the scalar case.[12] For the direct HSCP production (topologies THSCPM1b and THSCPM2b), Drell-Yan production of a scalar was used, which matches the model considered here. As a consequence, when mass compression is applied for small mass differences, one gets a slightly stronger constraint from the EM results than without mass compression. Furthermore, the database also contains the UL results provided by the ATLAS collaboration for direct HSCP production. These ULs are slightly stronger than the limits obtained from the EMs for direct HSCP production and further strengthen the constraints in the case of mass compression with respect to the case where the individual topologies are combined.

**Fermionic (sterile neutrino) dark matter**

The lightest sterile neutrino is another phenomenologically viable DM candidate in the scotogenic model. For this choice, the observed relic density can be explained by the freeze-in mechanism [230, 231, 232]. Considering freeze-in from the decays of inert scalars, to achieve $\Omega h^2 \sim 0.12$ the respective Yukawa couplings should be of the order of [233, 234]

$$\sqrt{|Y_{\alpha 1}|^2} \sim 10^{-9} \left(\frac{10\,\text{keV}}{m_{N_1}}\right)^{1/2} \left(\frac{\mu_2}{100\,\text{GeV}}\right)^{1/2}, \tag{6.10}$$

where $\alpha = 1, 2, 3$ runs over the three generations of leptons and $\mu_2$ represents the typical mass scale of the $Z_2$-odd scalars. To explain the observed oscillation of active neutrinos, the Yukawa couplings of the heavier sterile neutrinos are required to be considerably larger than the typical coupling for the lightest state, $10^{-5} < |Y_{\alpha 2}|, |Y_{\alpha 3}| < 10^{-2}$ [234].

Here, we are interested in the signatures expected from long-lived charged particles and focus on the scenario with $m_{N_1} < m_{H^\pm} < m_{H^0}, m_{A^0} < m_{N_2}, m_{N_3}$ mass hierarchy. Given its small couplings, direct production of the sterile neutrinos can be neglected and, hence, $N_2$ and $N_3$ are phenomenologically irrelevant in our considerations.

In this scenario, $H^\pm$ can only decay into $N_1$ and a lepton. The respective decay width reads [233]

$$\Gamma(H^\pm \to N_1 l_\alpha^\pm) = \frac{m_{H^\pm}|Y_{\alpha 1}|^2}{16\pi}\left(1 - \frac{m_{N_1}^2}{m_{H^+}^2}\right)^2. \tag{6.11}$$

Requiring that the $N_1$ makes up for the observed DM abundance, eq. (6.10), the proper decay length of the $H^\pm$, $c\tau_{H^\pm}$, is of the order of

$$c\tau_{H^\pm} \sim 10\,\text{m}\left(\frac{m_{N_1}}{10\,\text{keV}}\right)\left(\frac{100\,\text{GeV}}{m_{H^\pm}}\right)^2. \tag{6.12}$$

Hence, in the relevant range of masses, the charged scalar is typically long-lived. When decaying outside the detector, $H^\pm$ leads to a HSCP signature while decays inside the tracker could be detected in searches for displaced leptons.

To showcase the sensitivity of SModelS v2 for this scenario, we perform a grid scan over $m_{H^\pm}$ and $m_{N_1}$, varying $m_{H^\pm}$ from 100 to 900 GeV and $m_{N_1}$ from 1 keV to 10 GeV. The masses of the neutral $\mathcal{Z}_2$-odd scalars are taken as $m_{H^0} = m_A^0 = m_H^\pm + \Delta m$, with two choices for the mass splitting, $\Delta m = 5$ GeV and $\Delta m = 50$ GeV. Furthermore, we choose

[12] In the HSCP EMs, the spins and color charges are taken as arbirary.

$\lambda_{L,S} = 10^{-2}$. In this setup, the production of inert scalars at the LHC is dominated by SM gauge interaction arising from their kinetic terms. Finally, in our main results, we assume $Y_{\alpha 1}$ to have one non-zero entry only, such that $H^\pm$ decays to 100% into one lepton flavor, either electrons or muons. While a non-trivial mixing, in general, is subject to lepton flavor constrains, additionally, we consider the case of 50% BR into muons and electrons for illustration.

For a given particle spectrum, we compute the DM relic density arising from freeze-in production by solving the respective Boltzmann equation [232][13] taking into account the decays of all the inert scalars:

$$\Omega h^2 \simeq 2.7 \times 10^8 \, m_{N_1} \int_0^\infty \mathrm{d}x \, \frac{K_1(x)}{x K_2(x)} \sum_i \frac{Y_i^{\mathrm{eq}}(x)}{H(m_i/x)} \, \Gamma(i \to N_1 \, l^\pm/\nu) \,, \tag{6.13}$$

where $K_j$ denotes the modified Bessel functions of the second kind. The sum runs over the four inert degrees of freedom, $i \in \{H^\pm, H^0, A^0\}$, $Y_i^{\mathrm{eq}}(x)$ denotes their comoving number density in thermal equilibrium, and $\Gamma(i \to N_1 \, l^\pm/\nu)$ the partial width for their decays into $N_1$ and a charged lepton or neutrino. The latter is taken from [233]. The Hubble parameter, $H$, is evaluated at the temperature $T = m_i/x$.

Contrary to the scalar DM case, here we have less freedom for generating the DM; we therefore assume that the $N_1$ saturates the relic density constraint through freeze-in. As the partial decay widths involved in eq. (6.13) are all proportional to $|Y_{\alpha 1}|^2$, we solve for $\Omega h^2 = 0.12$ for this Yukawa coupling and compute the corresponding lifetime of the $H^\pm$ for a given set of masses. Note that for the mass splittings considered here, $H^0$ and $A^0$ promptly decay into $H^\pm$ such that their direct decays into $N_1$ can safely be neglected.

As in the previous subsection, we compute the production cross sections of the $\mathcal{Z}_2$-odd scalars with CalcHep utilizing the micrOMEGAs-SModelS interface, and then evaluate the LHC constraints with SModelS v2. Figure 6.7 shows the obtained $r_{\max}$ values in the $m_{H^\pm}$ vs. $m_{N_1}$ plane as well as the SModelS exclusion lines (contours of $r_{\max} = 1$) resulting from the HSCP and displaced lepton searches, for the two choices of $\Delta m = m_{A^0,H^0} - m_{H^\pm}$ and the $H^\pm$ decaying either 100% into $e^\pm N_1$ or 100% into $\mu^\pm N_1$.

The 13 TeV ATLAS search for displaced leptons [43] provides sensitivity in the region $c\tau \lesssim 1$ m. The HSCP limits are strongest in the detector-stable limit, while for decay lengths of $\mathcal{O}(1$ m) they suffer from the exponentially suppressed fraction of particles traversing the detector. The two exclusion regions have a minor overlap for small $m_{H^\pm}$, *i.e.* a large production cross section. The relevant HSCP analyses are the 8 TeV CMS searches [228, 229], and the 13 TeV ATLAS search [50]. As in the previous section, the 8 TeV analysis constrains the region up to $m_{H^\pm} \lesssim 160$ GeV and in the case $\Delta m = 5$ GeV, $c\tau_{H^\pm} \sim \mathcal{O}(5$ m) up to 400 GeV.

In the case $\Delta m = 50$ GeV (left panels in Fig. 6.7), both the HSCP and displaced lepton searches exclude $H^\pm$ masses up to about 700 GeV. The displaced lepton limits are slightly stronger for decays into electrons than for decays into muons. For smaller mass differences, $\Delta m = 5$ GeV (left panels), the limits are stronger, reaching up to $m_{H^\pm} \approx 800$ GeV. This is

[13] We employ the commonly made approximations that the SM degrees of freedom do not vary during the freeze-in process and that scatterings and inverse decays could be neglected. We also neglect the contribution from late decays of the lightest scalar after its freeze out (often referred to as the superWIMP contribution). We checked that this contribution only becomes relevant outside the considered range of parameters, *i.e.* for larger DM and scalar masses.

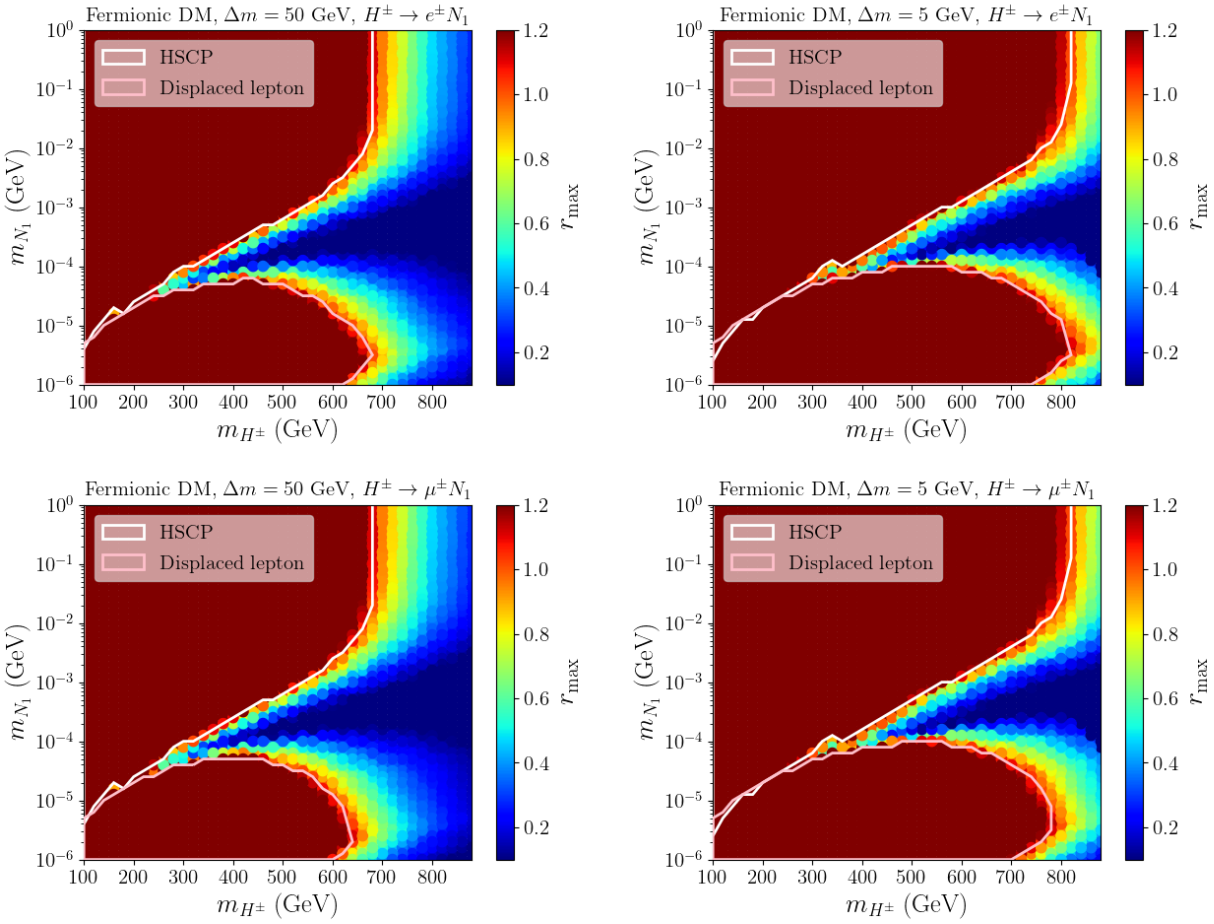


Figure 6.7: SModelS constraints on long-lived charged scalars in the scotogenic model with fermionic DM, where $H^\pm \to \ell^\pm N_1$. On the left $\Delta m \equiv m_{A^0,H^0} - m_{H^\pm} = 50$ GeV, on the right $\Delta m = 5$ GeV. The white lines denote the exclusion limit ($r_{\max} = 1$) from HSCP searches, while the pink lines denote to exclusion limit from displaced lepton searches; the value of $r_{\max}$ is shown in color. The upper panels are for $\ell^\pm = e^\pm$, the lower panels for $\ell^\pm = \mu^\pm$ with 100% branching ratio.

due to the fact that the $H^\pm$ can be produced in $pp \to H^+H^-$, $H^\pm A^0$ and $H^\pm H^0$ channels, as well as from $pp \to A^0 H^0$ with the neutral scalars decaying to the charged one, and the total $H^\pm$ signal thus increases with decreasing $\Delta m$. For the HSCP constraints, all these different signal contributions can be summed up thanks to the large variety of home-grown EMs (see however the caveat in case of mass compression explained in Section 6.4.1). In the case of displaced leptons, similar to the case of disappearing tracks considered in Section 6.4.1, simplified model results only exist for the direct production of the LLP; $H^\pm$ originating from $H^0$ or $A^0$ decays are therefore ignored unless SModelS's mass compression sets in.

Let us now turn to the question of lepton flavor. So far, we assumed that $H^\pm$ decays to 100% into one lepton flavor, concretely either electrons or muons.[14] As $m_{H^\pm} \gg m_e, m_\mu$, both scenarios provide the same $H^\pm$ decay widths. The HSCP constraints, depending

[14]Results for displaced taus are also included in the SModelS v2 database.

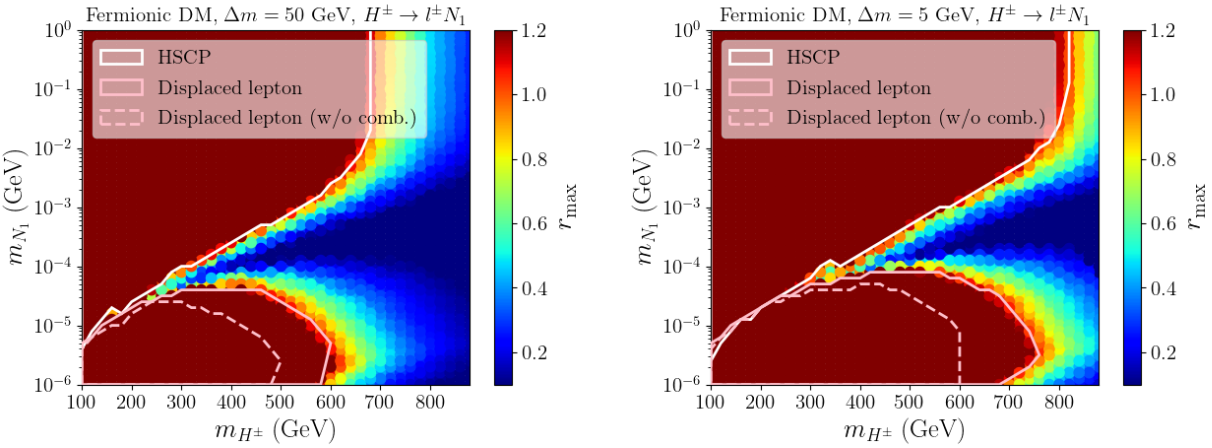


Figure 6.8: As Fig. 6.7 but for $H^\pm \to \ell^\pm N_1$ decays with equal probabilities for $\ell = e, \mu$ (50% BRs). Here, SModelS is run with `combineSRs=True` in order to combine the contributions in the SRee and SRmm signal regions of the ATLAS displaced lepton search [43]; this is made possible by the statistical model provided by the collaboration. For comparison, the pink dashed lines show the results without SR combination.

only on mass and lifetime of the LLP, stay agnostic to the type of decay products. The constraints from the displaced lepton search are, however, sensitive to the lepton flavor. Indeed, the slight difference in the displaced lepton limits in the upper and lower panels of Fig. 6.7 arises due to the larger acceptance $\times$ efficiency values in signal region SRee (two displaced electrons) as compared to SRmm (two displaced muons).

Any non-trivial structure in $Y_{\alpha 1}$, while subject to lepton flavor violation constraints, will lead to a mix of lepton flavors in the $H^\pm \to \ell^\pm N_1$ decays. Staying with $\ell = e, \mu$ for simplicity, the worst case is BR($H^\pm \to e^\pm N_1$)=BR($H^\pm \to \mu^\pm N_1$)=50%, for which only 25% of the total $H^+H^-$ production gives displaced leptons of the same flavor. This would considerably reduce the constraining power. Fortunately, the ATLAS collaboration published the statistical model for the analysis in JSON format, which allows for the combination of the SRee and SRmm signal regions in this case.[15] To demonstrate the usefulness of combining the SRs in the displaced lepton search, we consider in Fig. 6.8 the case of maximal mixture between the first two generations, such that $H^\pm \to \ell^\pm N_1$ decays give $\ell = e, \mu$ with equal probabilities. The full pink contour shows the exclusion reach when SR combination is turned on (`combineSRs=True`); this has to be compared to the dashed pink contour which represents the exclusion line without SR combination.

Before concluding this subsection, we note that the case of small DM masses is also constrained from cosmological observations independent of the scalar sector. In particular, a recent reinterpretation of warm DM constraints from the Lyman-$\alpha$ forest [235] in the freeze-in scenario excludes masses below 15 (3.5) keV [236] under nominal (conservative [237]) assumptions.

[15] With the EM results provided by ATLAS, contributions in the mixed-flavor signal region SRem can only be included in addition in case of displaced taus.

### 6.4.2 Constraints on electroweak-inos in the MSSM

Our second showcase is the EW-ino sector of the MSSM. As the lifetime of the lighter chargino $\tilde{\chi}_1^\pm$ can span a wide range of values, from prompt decays to decay lengths of several cm, this serves to illustrate the simultaneous usage of prompt and LLP results in SModelS v2.

To cover the parameter space of the EW-ino sector, we perform a random scan over the relevant Lagrangian parameters, *i.e.* the bino and wino mass parameters $M_1$ and $M_2$, the higgsino mass parameter $\mu$, and $\tan\beta = v_2/v_1$. Concretely, we vary

$$\begin{aligned} 10\text{ GeV} < \quad M_1 \quad &< 3\text{ TeV}, \\ 100\text{ GeV} < \quad M_2 \quad &< 3\text{ TeV}, \\ 100\text{ GeV} < \quad \mu \quad &< 3\text{ TeV}, \\ 5 < \quad \tan\beta \quad &< 50. \end{aligned} \tag{6.14}$$

The other SUSY breaking parameters are fixed to 10 TeV.[16] The lower limits on $M_2$ and $\mu$ are chosen so to avoid the LEP constraints on light charginos. The scan consists of close to 100k points, generated randomly within the parameter intervals above. The mass spectra and decay tables are computed with SoftSusy 4.1.12 [175, 176], which includes the $\tilde{\chi}_1^\pm \to \pi^\pm \tilde{\chi}_1^0$ decay calculation following [222, 223, 224] (see also [238]) for small mass differences below about 1.5 GeV. Cross sections are computed first at leading order (LO) with Pythia 8 [239, 67], and reevaluated at next-to-LO with Prospino [240] for all points which have $r_{\max} > 0.7$ with the LO cross sections. Furthermore, we take the lightest neutralino $\tilde{\chi}_1^0$ to be the lightest supersymmetric particle (LSP) and a DM candidate; its relic density and scattering cross sections on nucleii are computed with micrOMEGAs v5.2.7a [198, 199].

The mean decay length of the $\tilde{\chi}_1^\pm$ is shown in Fig. 6.9. As can be seen, a large fraction of the scan points feature prompt decays and can thus be tested by the conventional $E_T^{\text{miss}}$ SUSY searches. On the one hand, the wino LSP case ($M_2 \ll \mu,\ M_1$) can result in lifetimes as large as a few centimeters, which can be tested by the ATLAS and CMS disappearing track searches. The higgsino LSP scenario ($\mu \ll M_2, M_1$) can also lead to non-prompt decays, *cf.* the light blue and yellowish points in Fig. 6.9, but these remain in the sub-mm regime and are thus not probed by the current LLP results.

Figure 6.10 shows the points excluded by the LHC searches in the SModelS v2 database in the $m_{\tilde{\chi}_1^\pm}$ versus $m_{\tilde{\chi}_1^0}$ plane. The color of each excluded point denotes the most constraining analysis, that is the analysis giving the highest $r$-value, $r_{\max}$. As we can see, points in the mass-degenerate region are excluded by the ATLAS [48] and CMS [47] disappearing track searches (light and dark pink points). These points correspond to the wino LSP scenario. The compressed region, where $m_{\tilde{\chi}_1^\pm} - m_{\tilde{\chi}_1^0} \lesssim m_W$, is mostly tested by the CMS searches [241, 211] in final states with off-shell $W$ and $Z$ bosons (dark blue points). For larger mass differences, the decay $\tilde{\chi}_2^0 \to \tilde{\chi}_1^0 h$ starts to become kinematically accessible and the branching ratio $\text{BR}(\tilde{\chi}_2^0 \to \tilde{\chi}_1^0 h)$ starts to increase while $\text{BR}(\tilde{\chi}_2^0 \to \tilde{\chi}_1^0 Z)$ is reduced. In this transition region, the effective cross section for the $\tilde{\chi}_1^\pm \tilde{\chi}_2^0 \to WZ + E_T^{\text{miss}}$ simplified model is reduced and constraints from chargino-pair production [242] become

[16] We assume that stop parameters can always be adjusted such that $m_h \approx 125$ GeV without influencing the EW-ino sector.

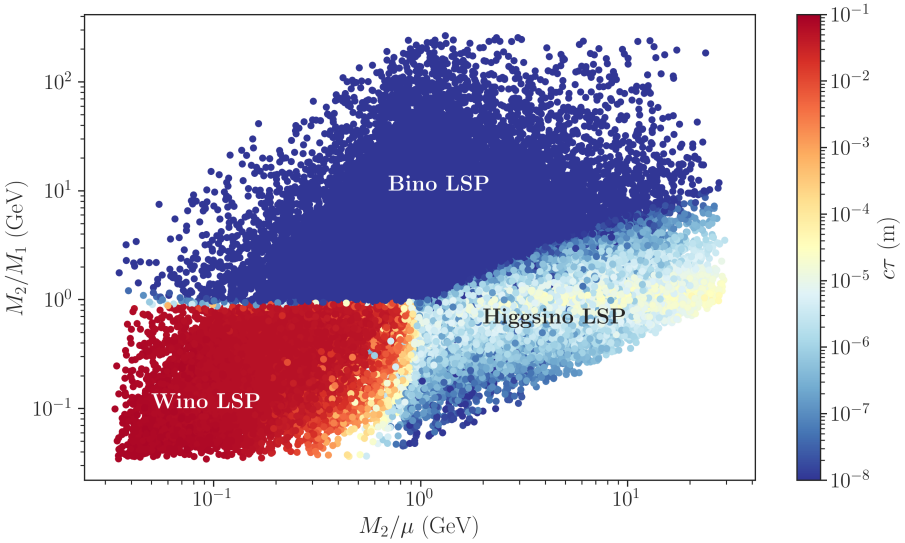


Figure 6.9: Mean decay length $c\tau$ of the lighter chargino, $\tilde{\chi}_1^\pm$, for the scan described in the text. The red points at the lower left corner correspond to the wino scenario ($M_2 \ll \mu,\ M_1$) and have the largest decay lengths (up to 8 cm). The light blue to yellowish points on the right side correspond to the higgsino scenario ($\mu \ll M_2, M_1$), resulting in decay lengths of $\sim 0.1$ mm. The dark blue points represent prompt decays.

more relevant (green points). For larger chargino masses, the decay $\tilde{\chi}_2^0 \to \tilde{\chi}_1^0 h$ becomes dominant and constraints from the $Wh$+$E_T^{\text{miss}}$ final state [188] kick in (red points). Finally, other ATLAS and CMS searches in the $WZ$+$E_T^{\text{miss}}$ final state can be more constraining for a few points in parameter space; for simplicity, they are grouped as "Others" in Fig. 6.10.

It is also instructive to consider the same points plotted in the plane of chargino mass vs. mean decay length, shown in Fig. 6.11. As discussed above, in the wino LSP case ($M_2 \ll M_1, \mu$), the lighter chargino is long-lived and can be constrained by the disappearing track searches, which are sensitive down to decay lengths of $\sim 1$ cm.

In Figs. 6.10 and 6.11, we also display the exclusion curves published by ATLAS and CMS for the corresponding simplified models. For the case of disappearing track searches, the exclusion obtained with SModelS agrees very well with the 'official' exclusion curves from the collaborations. For the prompt searches, however, SModelS seems to underestimate the reach as compared to the exclusion limits from the ATLAS and CMS collaborations. Generally, the exclusion obtained with SModelS tends to be conservative, since it is limited by the simplified models included in the database. The main reason behind the supposed under-exclusion in Fig. 6.10 is, however, the fact that the ATLAS and CMS mass limits assume a pure bino $\tilde{\chi}_1^0$ and pure wino $\tilde{\chi}_1^\pm$ and $\tilde{\chi}_2^0$, the latter assumption maximising the production cross section. Within the MSSM, this is only approximately valid if $M_1 \ll M_2 \ll \mu$. For general parameters as in our scan, the production cross sections will typically be smaller than the ones assumed by the collaborations, thus reducing the excluded region. To illustrate this point, we plot in Fig. 6.12 all the non-excluded points in the $m_{\tilde{\chi}_1^\pm}$ vs. $m_{\tilde{\chi}_1^0}$ plane. The color coding shows the $r_{\text{max}}$ value obtained for each (allowed) point rescaled by the pure wino production cross section ($\sigma_{\tilde{\chi}\tilde{\chi}}^{\text{wino}}$). In other words, it shows which would be the $r_{\text{max}}$ value if the production cross

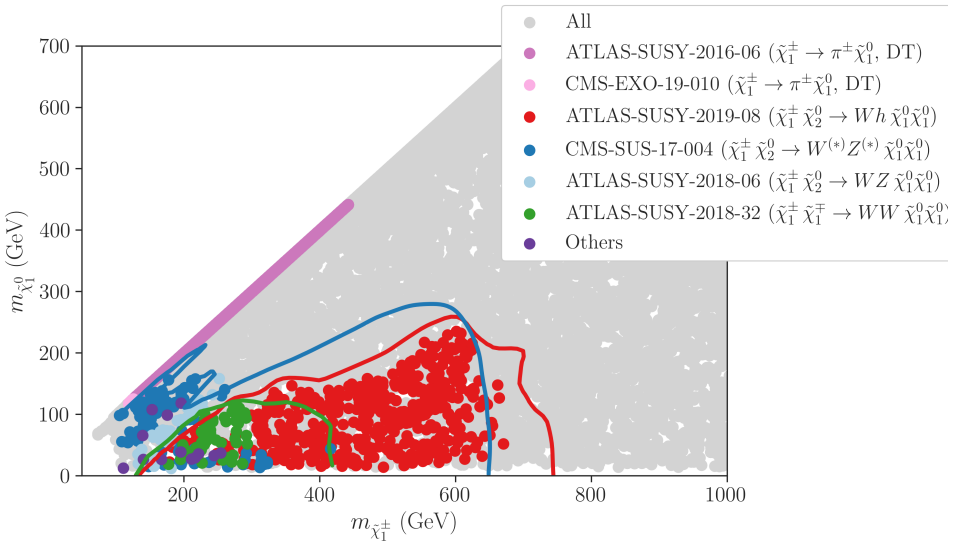


Figure 6.10: Constraints on EW-inos in the MSSM, from the scan explained in the text. The points in colour are excluded by SModelS, with the colour denoting the analysis that gives the highest $r$-value (see legend). The simplified model exclusion lines from the respective ATLAS and CMS publications are also shown for comparison.

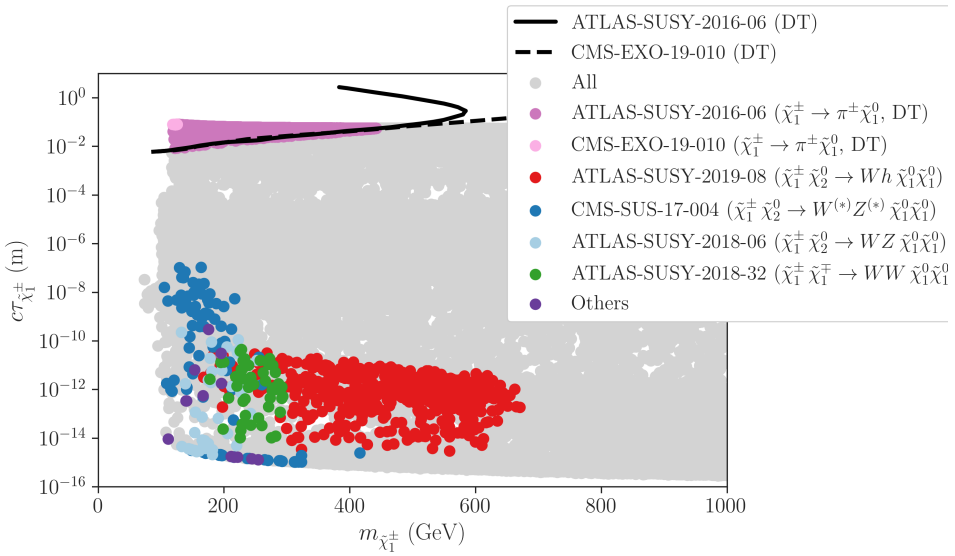


Figure 6.11: As Fig. 6.10 but in the plane of $\tilde{\chi}_1^\pm$ mass versus mean decay length. The simplified model exclusion lines from the ATLAS and CMS disappearing tracks searches are also shown for comparison.

sections for $\tilde{\chi}\tilde{\chi}$, with $\tilde{\chi} = \tilde{\chi}_1^\pm, \tilde{\chi}_2^0$, were the ones assumed in the ATLAS and CMS limit plots. As we can see, almost all non-excluded points that fall within the ATLAS and CMS exclusion curves become excluded ($r_{\max} \times \sigma^{\text{wino}}_{\tilde{\chi}\tilde{\chi}}/\sigma_{\tilde{\chi}\tilde{\chi}} \geq 1$) once their cross sections are rescaled in this way.

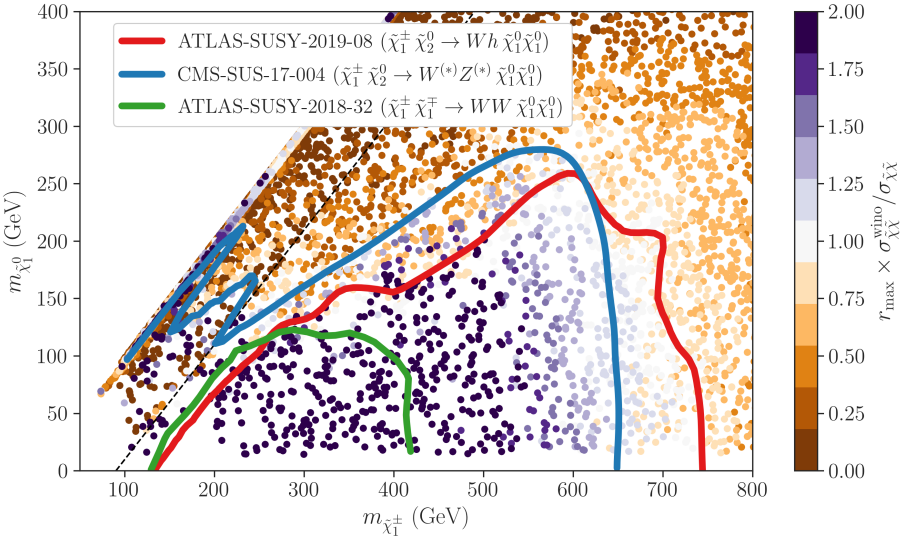


Figure 6.12: SModelS-allowed scan points in the plane of $m_{\tilde{\chi}_1^0}$ versus $m_{\tilde{\chi}_1^\pm}$; the colour code shows the highest $r$-value rescaled by the reference cross sections for pure wino production.

### LHC versus dark matter constraints

Let us next consider possible DM constraints for the EW-ino scenario, and their complementarity with the LHC constraints. To this end, we assume a standard cosmological history, so the $\tilde{\chi}_1^0$ relic abundance, $\Omega h^2$, is given by the usual WIMP freeze-out calculation. Furthermore, we allow for the $\tilde{\chi}_1^0$ to make up for just a fraction of the observed DM abundance, which may include contributions from other, non-MSSM particles. Therefore we impose only an upper bound of $\Omega h^2 < 0.13$ (assuming again $\approx 10\%$ theory uncertainty from the tree-level calculation) and rescale the DM-nucleon cross section that enters the DM direct detection constraints by a factor $\Omega h^2/0.12$.

It is well known that in the EW-ino scenario, the bino LSP case ($M_1 \ll M_2, \mu$) leads to a DM overabundance and would be excluded by the considerations above, while the wino and higgsino LSP cases lead to an under-abundance for masses below $\sim 1$ TeV. From the discussion above we know that the LHC constraints from prompt searches are more stringent for the bino LSP case, with wino-like $\tilde{\chi}_1^\pm$ and $\tilde{\chi}_2^0$. Wino LSP cases, on the other hand, are constrained by disappearing track searches. To compare the LHC and DM constraints, we show in Fig. 6.13 the $\tilde{\chi}_1^0$ relic abundance as a function of the ratio $M_1/\min(M_2, \mu)$. Values of this ratio much smaller than 1 correspond to the bino LSP scenario, while values much larger than one correspond to the wino/higgsino LSP case. As we can see, the points excluded by prompt searches are almost entirely restricted to the bino LSP region, which is already excluded by the relic abundance constraint. The exception are a few points with a mixed LSP leading to a small relic. On the other hand, the disappearing track searches are sensitive to the wino LSP case with $\Omega h^2 \lesssim 10^{-2}$.

Finally, in Fig. 6.14 we show the effective (*i.e.* rescaled) $\tilde{\chi}_1^0$-nucleon scattering cross section as a function of the $\tilde{\chi}_1^0$ mass. Points with too high a relic abundance ($\Omega h^2 > 0.13$) are shown in dark grey, while the points with $\Omega h^2 < 0.13$ but excluded by LHC results are shown in color (light and dark shades of blue, green and pink). The 90% CL direct

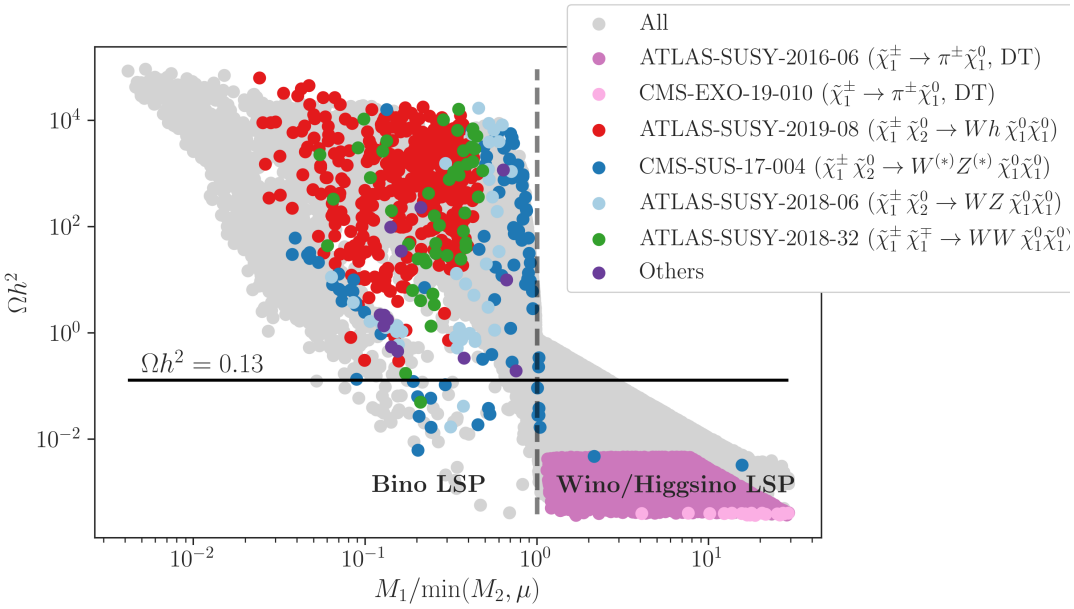


Figure 6.13: Comparison of LHC and the DM relic abundance constraint for the EW-ino scenario; see text for details. The regions with a pure bino DM corresponds to $M_1/\min(M_2, \mu) \ll 1$ and with a wino/higgsino DM to $M_1/\min(M_2, \mu) \gg 1$, as indicated by the dashed line. The upper bound on the LSP relic abundance is shown by the solid line.

detection limit from the Xenon1T experiment [243] is shown as black line. Once again, just a handful of points excluded by the prompt searches can evade the DM (relic plus direct detection) constraints. The pure wino case, however, leads to a suppressed relic abundance and, consequently, to a small effective direct detection cross section, thus evading the DM constraints. These points are only constrained by the disappearing track searches, as shown by the pink points in Fig. 6.14.

## 6.5 Conclusions

Version 2 of SModelS features a more detailed and more flexible description of simplified model topologies. Concretely, through the introduction of a *particle class*, the simple list of BSM particle masses used in SModelS v1 has been replaced by full *objects*, which can carry attributes such as mass, width, spin, electric charge, etc. This enables a refined treatment of, *e.g.*, spin-dependent results. Moreover, and more importantly for this paper, it enables the inclusion of a large variety of searches for LLPs in the form of width-dependent results. Given an input model, SModelS v2 can thus simultaneously provide prompt and long-lived results in the same run. The LLP searches currently implemented include searches for HSCPs, disappearing tracks, displaced/non-prompt jets and displaced leptons. In total, results from 62 ATLAS and CMS searches at 13 TeV are implemented in the current database, 7 of which are for LLPs.

We demonstrated the physics capabilities of SModelS v2 analysing the constraints on long-lived charged scalars in the scotogenic model with either scalar or fermionic DM.

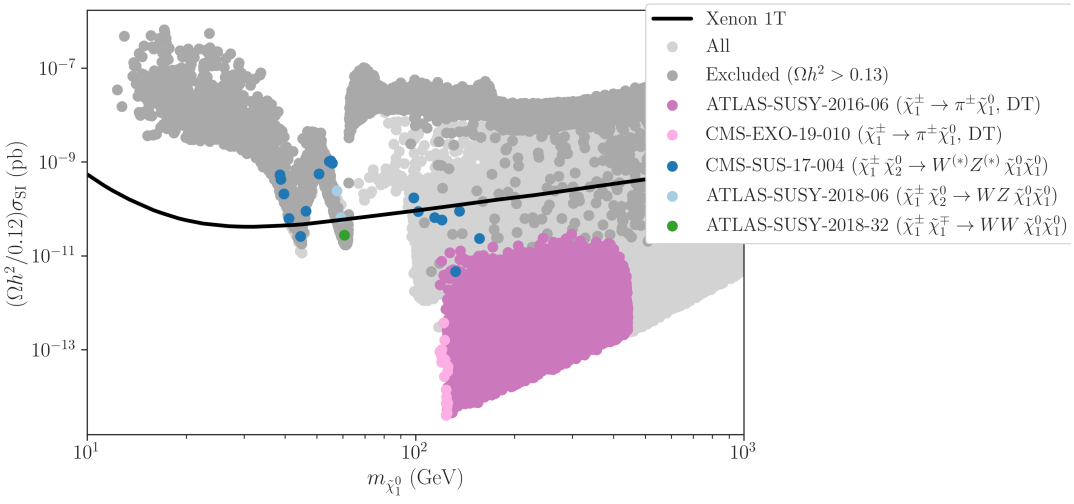


Figure 6.14: Comparison of relic density, DM direct detection and LHC constraints for the EW-ino scenario; see text for details.

In the former case, LLPs arise for sub-GeV mass splitting with the scalar DM candidate. Considering the charged scalar as the next-to-lightest $\mathcal{Z}_2$-odd state, we found that HSCP searches constrain its mass up to around 500–600 GeV for mass splittings below the pion threshold. This covers the range favoured by DM considerations for such small mass splittings. For mass splittings slightly above $m_{\pi^\pm}$, resulting in decay lengths of the order of 0.1–1 m, we found that disappearing track searches from ATLAS with 36 fb$^{-1}$ (CMS with 101 fb$^{-1}$) can exclude charged scalar masses up to around 220 (350) GeV, depending on the lifetime.

For fermionic DM in the scotogenic model, the measured relic density can be explained by freeze-in production. The smallness of the required Yukawa coupling of the lightest sterile neutrino naturally renders the next-to-lightest $\mathcal{Z}_2$-odd state long-lived in a large region of the cosmologically valid parameter space where the DM mass ranges from the keV to the GeV scale. Besides the searches for HSCP that provide sensitivity to large lifetimes (corresponding to DM masses in the MeV to GeV range) we applied constraints from searches for displaced leptons that are most sensitive towards smaller DM masses, below a few tens of keV. Both types of searches can exclude long-lived charged scalars up to about 800 GeV in mass in this scenario. For the displaced lepton search, we also demonstrated the importance of signal region combination, as enabled by the statistical model provided by ATLAS for this analysis.

As a second showcase we analysed the constraints on the EW-ino sector of the MSSM, detailing the interplay of prompt and long-lived searches, as well as the interplay of collider and DM constraints. We demonstrated to what extend the ATLAS and CMS EW-ino mass limits, which assume a pure bino $\tilde{\chi}_1^0$ and pure wino $\tilde{\chi}_1^\pm$ and $\tilde{\chi}_2^0$ (the latter in order to maximise the production cross section) are weakened in the general case. One aspect is that $\tilde{\chi}_2^0$ decays into $\tilde{\chi}_1^0 Z$ or $\tilde{\chi}_1^0 h$ compete with each other if both are kinematically allowed. More importantly, however, for general EW-ino mass parameters as in our scan, the production cross sections are typically smaller than the ones assumed by the collaborations, thus reducing the excluded region.

Regarding the interplay with DM constraints, we showed that EW-ino scenarios excluded by prompt searches are almost entirely restricted to the bino LSP region and characterised by a significant DM overabundance. Only few points with a mixed LSP, leading to a small relic, escape this conclusion and evade also the DM direct detection bounds. The disappearing track searches, on the other hand, are sensitive to the wino LSP case with $\Omega h^2 \lesssim 10^{-2}$. In this case, the suppressed relic abundance also leads a small effective direct detection cross section, evading the Xenon1T limit by order(s) of magnitude, to the effect that this scenario is best tested at colliders.

SModelS v2 is publicly available on GitHub [201] and can serve the whole community for fast testing of LHC constraints for BSM models that feature a $\mathcal{Z}_2$-like symmetry. As $\mathcal{Z}_2$-like symmetries are prevalent in DM models, SModelS is also interfaced from micrOMEGAs. A lot more work is foreseen to further extend and improve the usage of simplified model results and both, the SModelS code and the database, will continue to evolve.

# Chapter 7

# Dark matter and LHC constraints

## 7.1 DM production mechanisms in the early Universe

As introduced in section 2.2.1, many astrophysical observations hint at a new type of matter that would not be visible with standard telescopes, hence called dark matter (DM). For the case of particle DM candidates considered in this thesis, the evolution of the hypothesized DM density depends on the dynamics of the universe. The standard cosmological model ($\Lambda$CDM) is equivalent in Cosmology to the Standard Model of particle physics. It relies on general relativity (GR) to describe the theory of gravity on cosmological scales with the assumption that all observers, wherever they are, see the same universe in all directions. These are the so-called homogeneity and isotropy assumptions. These assumptions lead to the Friedmann-Lemaître-Robertson-Walker (FLRW) metric. The $\Lambda$CDM model will not be discussed further but the emphasis will be given to the Boltzmann equation that describes the evolution of the DM density in our universe. GR describes the universe as a dynamic entity, with a retroactivity between the matter-energy content and the space-time curvature. Indeed, stellar objects in GR travel in straight lines but in a curved space. At the same time, massive objects increase locally the space-time curvature. Describing the evolution of the universe then relies on the description of its energy and matter content. In the $\Lambda$CDM model, the different matter-energy components are each described by a density parameter as follows

$$\Omega_x = \frac{\rho_x}{\rho_{\text{crit}}} = \frac{8\pi G \rho_x}{3H_0^2}\,, \tag{7.1}$$

where the subscript $x$ denotes the matter-energy components that are reduced to only three for simplicity: $m$ for matter, DM for dark matter, and $\Lambda$ for dark energy. $\rho_x$ is the density of the $x$ component today, $G$ is the gravitational constant and $H_0$ is the Hubble constant today. The PLANCK experiment, by measuring the cosmic microwave background (CMB) [27], inferred these parameters. $\Omega_m \sim 0.046$ describes the ordinary matter content, $\Omega_{\text{DM}} \sim 0.23$ describes the DM density and $\Omega_\Lambda \sim 0.72$ describes the dark energy[1]. As of today, our universe is thus composed of about 72% of dark energy,

[1] $\Omega_\Lambda$ comes from the cosmological constant that describes the expansion of the universe. It is understood mathematically in GR but its conceptual meaning is not yet understood and referred to as "dark energy".

23% of dark matter and only 4.6% of ordinary matter. Rewinding time leads to the conclusion that all the energy and matter content was at the beginning concentrated in an infinitesimally small region. Then the so-called Big Bang was like an explosion during which space-time inflated very rapidly. Although a full description of the Big Bang is still missing to this day, the ΛCDM model can describe our universe from about $10^{-43}$ seconds after the Big Bang. Before that, the universe was so dense and energetic that matter at this epoch can not be described by any theory to this day, and it would probably involve a new theory that can unify gravity and quantum mechanics. At $10^{-43}$ seconds, all particles and interactions were unified in a "cosmic soup". With the universe expanding, particles differentiated. While the high temperature at early times kept all particles in thermal and kinetic equilibrium with each other, they later started to decouple and the density of each species evolved to eventually reach the densities that we can measure today. The evolution of each particle density, in the ΛCDM, is determined by thermodynamics in an expanding universe. Indeed, classic thermodynamics must be extended to take into account the expansion of the universe that has the effect to slow down chemical reactions. The success of such a description for the production of SM particles, or composite particles like heavier nuclei, hints at a similar thermal history of DM. Depending on the DM candidate properties, there can be several thermodynamic mechanisms involved. Although there is a plethora of DM models in the literature, the possible production mechanisms can be broadly classified into two categories, depending on the particle's thermal behavior. Thermal freeze-out will be addressed first as it was the first mechanism to be considered with the WIMP miracle. Finally, the freeze-in mechanism will be briefly discussed.

### 7.1.1 Freeze-out

This section describes how to produce the current DM density through the freeze-out mechanism and then why the related WIMP miracle has generated so much enthusiasm in the particle and astroparticle physics communities.

#### The freeze-out mechanism

The way DM is produced in the universe depends on the properties of the DM candidate under consideration. Besides its mass, the most significant property of the DM candidate is its coupling to the SM model. As discussed above, all SM particles are in equilibrium at early times and they constitute what is referred to as the SM bath. The case of freeze-out applies to DM candidates that are in equilibrium with the SM bath in the early universe. This is for example the case of the famous WIMP, having couplings to the SM around the weak scale ($y \sim 10^{-3}$). The freeze-out phenomenon relies on the following fact. If the DM coupling is sufficiently large, the DM candidate will be in equilibrium with the SM bath. Depending on the scenario and the properties of the DM, we will see that different processes can be responsible to keep the DM in equilibrium. The standard processes are self-annihilation processes of the form $\chi\bar{\chi} \to XX'$ where $\chi$ is the DM candidate and $X$ and $X'$ are SM particles or anti-particles[2]. However, while the Universe expands, the density of particles will decrease and thus the annihilation rate will decrease too. At

[2]If $\chi$ is a self-conjugate state, then the self-annihilation process is $\chi\chi \to XX'$.

some point, the annihilation rate can not keep up with the expansion rate and the DM candidate decouples from the SM bath. The DM density then "freezes out" and the DM candidate does not interact with the SM bath anymore. After freeze-out, the DM density keeps decreasing but only due to the expansion of the Universe. Under this paradigm, the relic DM density that is measured today can be inferred from what it was at the time of freeze-out and from the Universe expansion since then. Depending on the coupling size, the DM candidate can decouple at different times. Increasing the DM coupling will make the DM decouple later, ending up with a smaller DM density, and vice-versa.

The above paragraph discussed the concept behind freeze-out and the following will address its mathematical description, taken from [244]. First, the probability density function for a particle $\chi$ representing the DM candidate is described by the Fermi-Dirac (+) and the Bose-Einstein (-) distributions

$$f_\chi\left(\vec{p},\vec{x},t\right) = \frac{1}{\exp\left(\frac{E_\chi-\mu_\chi}{T_\chi}\right)\pm 1}\,, \tag{7.2}$$

where $\chi$ has a temperature $T_\chi$, equal to the bath temperature $T$, an energy $E_\chi$ and a chemical potential $\mu_\chi$. The density of $\chi$ is obtained by integrating $f_\chi$ over the momentum and the spatial coordinates. Given the ΛCDM assumptions of homogeneity and isotropy, $f_\chi$ does not depend on $\vec{x}$ and on the direction of $\vec{p}$, in other words $f_\chi\left(\vec{p},\vec{x},t\right) = f_\chi\left(|\vec{p}|,t\right)$, which gives

$$n_\chi(t) = \frac{g_\chi}{(2\pi)^3}\int f_\chi\left(|\vec{p}|,t\right)d\vec{p}, \tag{7.3}$$

where $g_\chi$ is the number of degrees of freedom of the DM candidate. The evolution of the DM density is determined by the Boltzmann equation

$$\mathbf{L}[f_\chi] = \mathbf{C}[f_\chi]\,, \tag{7.4}$$

where $\mathbf{L}$ and $\mathbf{C}$ are the Liouville and the collision operators, respectively. The Liouville operator represents the space-time variations of the density function $f_\chi$ and the collision operator represents how the interactions with other particles influence the density evolution. Here is used the covariant and relativistic generalization of the Liouville operator that takes into account the effects of space-time dynamics. With the FLRW metric and the space-time symmetries, it simplifies to

$$\mathbf{L}[f_\chi] = E_\chi\frac{\partial f_\chi}{\partial t} - H|\vec{p}|^2\frac{\partial f_\chi}{\partial x}\,, \tag{7.5}$$

where the effect of the metric is seen through the second term with the Hubble parameter. It is integrated in the following way

$$\frac{g_\chi}{(2\pi)^3}\int\frac{\mathbf{L}[f_\chi]}{E_\chi}d\vec{p} = \dot{n}_\chi + 3Hn_\chi\,, \tag{7.6}$$

or using 7.4 the integrated Boltzmann equation can be written as

$$\dot{n}_\chi + 3Hn_\chi = \frac{g_\chi}{(2\pi)^3}\int\frac{\mathbf{C}[f_\chi]}{E_\chi}d\vec{p}. \tag{7.7}$$

The collision operator involves a summation of all the possible processes with the particles of the SM bath. For simplification, let us consider the self-annihilation of DM into an arbitrary SM particle $X$, $\chi\bar{\chi} \to XX'$. The collision operator develops as follows

$$\frac{g_\chi}{(2\pi)^3}\int \frac{\mathbf{C}[f_\chi]}{E_\chi} = -\int d\pi_\chi d\pi_{\bar{\chi}} d\pi_X d\pi_{X'}(2\pi)^4\delta^4(p_\chi + p_{\bar{\chi}} - p_X - p_{X'}) \sum_{\text{spins}} \left[|\mathcal{M}_{\chi\bar{\chi}\leftrightarrow XX'}|^2 f_\chi f_{\bar{\chi}}(1 \pm f_X)(1 \pm f_{X'}) - (\chi\bar{\chi} \leftrightarrow XX')\right] , \tag{7.8}$$

with $d\pi_i = \frac{d\vec{p}_i}{(2\pi)^3 2E_i}$. The following series of assumptions are then applied

- at high energies $E \gg T$, the $\pm 1$ factor in the density functions can be neglected, which gives the Maxwell-Boltzmann density probability $f_i(|\vec{p}|, t) = \exp\left(-\frac{E_i}{T_i}\right)$,
- CP invariance, which implies $|\mathcal{M}_{\chi\bar{\chi}\leftrightarrow XX'}| = |\mathcal{M}_{XX'\leftrightarrow\chi\bar{\chi}}| = |\mathcal{M}|$,
- $X$ is in kinetic and chemical equilibrium and stays in kinetic equilibrium even after the loss of chemical equilibrium.

The above assumptions allow simplifying the integrated Boltzmann equation and get the famous freeze-out equation

$$\dot{n}_\chi + 3Hn_\chi = \langle\sigma_{\chi\bar{\chi}\to XX'}v\rangle\left(n_\chi^2 - n_\chi^{\text{eq}2}\right) , \tag{7.9}$$

where $\langle\sigma_{i,j\to m,n}v\rangle$ is an averaged cross-section defined by

$$\langle\sigma_{i,j\to m,n}vv\rangle = \frac{1}{n_i^{\text{eq}}n_j^{\text{eq}}}\int d\pi_i d\pi_j d\pi_m d\pi_n(2\pi)^4\delta^4(p_i + p_j - p_m - p_n)|\mathcal{M}|^2\exp\left(-\frac{E_i + E_j}{T}\right) , \tag{7.10}$$

and the equilibrium density, given the Maxwell-Boltzmann approximation, is

$$n_\chi^{\text{eq}} = g_\chi\left(\frac{m_\chi T}{2\pi}\right)^{3/2}\exp\left(-\frac{m_\chi}{T}\right) . \tag{7.11}$$

As a side note, the exponential term on the very right of eq. (7.30) can be responsible for a drastic suppression of the average cross-section. The energy of a particle $i$ is directly related to its mass and momentum, thus heavy states will see their average cross-section exponentially reduced by $\sim \exp(-m_i/T)$. This effect is referred to as Boltzmann suppression.

One defines the co-moving DM density by $Y_\chi = n_\chi/s$, allowing to get rid of the expansion term, thanks to the conservation of entropy per co-moving volume ($sa^3 =$ constant)

$$\dot{n}_\chi + 3Hn_\chi = s\dot{Y}_\chi , \tag{7.12}$$

yielding

$$\dot{Y}_\chi = s\langle\sigma_{\chi\bar{\chi}\to XX'}v\rangle\left(Y_\chi^2 - Y_\chi^{\text{eq}2}\right) . \tag{7.13}$$

Finally, the variable reflecting the course of time is often $x = m_\chi/T$

$$\frac{dY_\chi}{dx} = -\frac{1}{3H}\frac{ds}{dx}\langle\sigma_{\chi\bar{\chi}\to XX'}v\rangle\left(Y_\chi^2 - Y_\chi^{\text{eq}2}\right) . \tag{7.14}$$

With $m_\chi$ being constant and $T$ decreasing over time, $x$ increases with time. For a full description, the right-hand side of the above equation, the collision term, must be completed with the summation over all processes with the particles of the SM bath. Some scenarios have a "dark sector", that is several particles having the same discrete symmetries as the DM candidate. Such scenarios need an additional summation of the different initial states, but this will be discussed later in this section.

### The WIMP miracle

Due to the WIMP miracle, WIMPs have generated a lot of enthusiasm in the particle physics community. As the name suggests, weakly interacting massive particles (WIMPs) have weak couplings, *i.e.* their coupling to the SM bath is around the weak scale, around $y \sim 10^{-3}$. The WIMP miracle stands in the fact that, for WIMPs with a mass around the weak scale, $m_\chi \sim 100$ GeV, the relic density through the freeze-out mechanism gives a result in the ballpark of the Planck measurement, in a seemingly miraculous way. In the following, a quick calculation of the WIMP miracle is described. The temperature at which $\chi$ freezes out is denoted $x_f$. The relic density of $\chi$ depends on this value since it was only ruled by the Universe expansion after the freeze-out. Several assumptions lead to the following approximation for the relic comobile density

$$Y_0 \approx \sqrt{\frac{45 G_N}{\pi g_\star}} \frac{x_f}{m_\chi} \frac{1}{\langle \sigma_{\text{ann}} v \rangle} \,, \tag{7.15}$$

where the zero subscript represents $t = 0$, which is the current time when the DM density is measured. The relic density is computed in the following way

$$\Omega_\chi h^2 = \frac{m_\chi s_0 Y_0 h^2}{\rho_c} \,, \tag{7.16}$$

since $\Omega_\chi = \rho_\chi / \rho_c$ and $\rho_\chi = m_\chi n_\chi = m_\chi s_0 Y_0$, which gives

$$\Omega_\chi h^2 \approx \frac{3 \times 10^{-27} \text{ cm}^3\text{s}^{-1}}{\langle \sigma_{\text{ann}} v \rangle} \,. \tag{7.17}$$

If the WIMP mass is around the weak scale, $\mathcal{O}(100)$ GeV, the averaged cross-section is typically $\langle \sigma_{\text{ann}} v \rangle \sim 10^{-26}$ cm$^3$s$^{-1}$. This leads to a relic density of 0.3, which is very close to the Planck measurement $\Omega h^2 = 0.12$. The fact that the mass is around the weak scale and the coupling is weak means that the DM candidate is very similar to SM particles. Having a particle so similar to particles we already know yielding the correct relic density constitutes what is called the WIMP miracle.

### Exceptions to the standard WIMP picture

Differences in the nature of the DM candidate can lead to a significantly different phenomenology. Reference [245] lists three exceptions to the standard WIMP paradigm, i) simultaneous annihilation of multiple "dark" states (or co-annihilation), ii) annihilation to heavier states (or "forbidden channels") and iii) annihilation near a cross-section resonance. Yet still based on the freeze-out mechanism, these small variations can have a

significant effect on the relic density. For example, models with a "dark sector" consisting of several particles $\chi_i$, will have new processes involved in the relic density computation

$$\chi_i \chi_j \leftrightarrow X X' \tag{7.18}$$
$$\chi_i X \leftrightarrow \chi_j X' \tag{7.19}$$
$$\chi_j \leftrightarrow \chi_i X X' , \tag{7.20}$$

and the Boltzmann collision term has to be modified accordingly, which can have a significant effect on the final relic density. Equation (7.18) illustrates the co-annihilation processes of case i). Such co-annihilation processes offer more channels for the DM candidate to annihilate into SM particles. As mentioned above, a summation of all possible final SM states has to be included for a complete description. The framework introduced in [246, 247] is widely used in the DM community to perform this summation on the final states, but also on the initial dark states at the same time, then enabling the inclusion of co-annihilation processes as well. In this framework, the process summation is encapsulated in an effective averaged cross-section

$$\langle \sigma_{\text{eff}} v \rangle = \sum_{i,j} \langle \sigma_{ij} v \rangle \frac{n_i^{\text{eq}} n_j^{\text{eq}}}{(n^{\text{eq}})^2} , \tag{7.21}$$

where $\langle \sigma_{ij} v \rangle$ already contains a summation over all SM final states and $n^{\text{eq}} = \sum_i n_i^{\text{eq}}$. One can thus use the freeze-out equation (7.14) while replacing $\langle \sigma_{\chi\bar{\chi}\to XX'} v \rangle$ with $\langle \sigma_{\text{eff}} v \rangle$ and $Y_\chi$ with $Y = \sum_i Y_i$. Co-annihilation processes become relevant when heavier dark states are close in mass to the DM candidate. Indeed, if the other states are too heavy, they will be Boltzmann suppressed. The DM candidate will still self-annihilate, but it will also co-annihilate in association with the heavier states and the latter will eventually decay into the lightest state which is the DM. This justifies the use of the sum of all densities $Y = \sum_i Y_i$. Depending on the scenario considered, the induced effect can be either to increase or decrease the DM relic density compared to what is obtained with only self-annihilation. SUSY bino-wino scenarios are typical cases for which the relic density is reduced significantly. There are numerous examples of bino-wino co-annihilation studies, see for example [248, 249]. The effect of an increased relic density can be observed for example when there are numerous processes, because of the total number of degrees of freedom in the numerator of eq. (7.21), since $n^{\text{eq}}$ is the sum of all equilibrium densities.

The term "forbidden channels" of case ii) corresponds to scenarios where the DM candidate decays into channels that would in principle be kinematically forbidden. If some SM states are only five to ten percent heavier than the DM candidate, annihilation into these SM states can still be dominant due to the high temperature in the early Universe. Regarding case iii), the cross-section may be resonant in the relevant region, having the effect of an increased average cross-section. Thus a smaller DM coupling is required to obtain the correct relic density.

References [250, 251] introduce a fourth exception to the WIMP paradigm; the conversion-driven freeze-out. It corresponds to equations (7.19) and (7.20), which are the co-scattering and decay processes, respectively. As discussed in section 7.2, these two types of processes are part of the general freeze-out equations, but they are often irrelevant and negligible in standard co-annihilation cases. Conversion-driven freeze-out is often referred to as simply co-scattering, even though the decays can be of importance,

depending of the scenarios. If the DM candidate is very weakly coupled to the SM bath, conversion processes (co-scattering and decays) can be of importance if there is a large enough coupling between the DM candidate and heavier dark states. In such a case, the heavier states co-annihilate while the conversion processes allow it to convert into the DM candidate, which itself can not be produced through standard self-annihilation. Mathematically, this is described by a coupled set of Boltzmann equations, as detailed in section 7.2.

As a final note, solving the freeze-out equation is often done numerically. This equation is stiff, *i.e.* it can be unstable and quickly diverge if solved with naive differential equation solvers, due to the squared term on the right-hand side of eq. (7.14). For example, it can be necessary to adjust the step size to smaller values for high temperatures (small $x$). Numerically solving the freeze-out equation can thus be a challenging task and involves special numerical techniques.

### 7.1.2 Freeze-in

If the DM coupling to the SM bath is much smaller (typically $y \sim 10^{-10}$), the DM is never in equilibrium in the early universe. However, the coupling can be large enough to slowly produce DM while it is still out of equilibrium. With the expansion of the universe, the reactions will end up being inefficient and the DM density will eventually "freeze in". This section aims to briefly introduce this alternative mechanism able to produce out-of-equilibrium DM. DM candidates undergoing this mechanism are called feebly interacting massive particles (FIMPs). In contrast to freeze-out where the DM density decreases with time, the freeze-in DM density increases with time. Increasing the DM coupling then increases the final relic density and vice-versa. The main processes responsible for freeze-in are SM states decaying into DM, while $2 \to 2$ processes are often negligible, due to additional $s$ or $t$-channels couplings but also additional phase space factors [232]. The processes driving the freeze-in production depend on the mass hierarchy of the given model. Consider for example the interaction of a $\chi$ DM candidate with two SM particles $A$ and $B$, with the following mass hierarchy $m_A > m_B + m_\chi$. The decay process responsible for freeze-in will thus be $A \to B\chi$, which translates into the following integrated collision operator.

$$\frac{g_\chi}{(2\pi)^3}\int \frac{\mathbf{C}[f_\chi]}{E_\chi} = \int d\pi_i d\pi_\chi d\pi_A d\pi_B (2\pi)^4 \delta^4(p_\chi + p_B - p_A) \sum_{\text{spins}} \left[|\mathcal{M}_{A\to B+\chi}|^2 f_A(1 \pm f_B)(1 \pm f_\chi) - |\mathcal{M}_{B+\chi\to A}|^2 f_B f_\chi (1 \pm f_A)\right] . \tag{7.22}$$

Applying similar assumptions as in the case of freeze-out simplifies the freeze-in equations

$$\dot{n}_\chi + 3Hn_\chi \approx 2g_A \int d\pi_A \Gamma_{A\to B\chi} m_A f_A \approx \frac{g_A m_A^2 \Gamma_{A\to B\chi}}{2\pi^2} T K_1(m_A/T)\,, \tag{7.23}$$

where $g_A$ is the number of degrees of freedom of $A$ and $K_1$ is the first modified Bessel function of the second kind. On the above is also performed a variable change to the co-mobile density $Y_\chi = n_\chi/s$. It is worth noticing that the right-hand side of eq. (7.23) does not depend on the density $n_\chi$ while it was the case for the freeze-out. Solving this

precise freeze-in case then requires numerically integrating a function dependent on the width $\Gamma_{A\to B\chi}$, but there is no differential equation to solve.

The above only describes a single case of freeze-in production of DM but other cases are possible as described in [232]. For example, a mass hierarchy such as $m_A + m_B < m_\chi$ makes $A + B \to \chi$ the dominant decay. Even though it is rarely the case, $2 \to 2$ processes are sometimes relevant and also require different equations [232]. The above only briefly introduced the freeze-in concept and other freeze-in possibilities will not be discussed since the work of this thesis focused on the co-scattering mechanism that will be discussed in section 7.2.

The freeze-out mechanism has been implemented in many public tools such as micrOMEGAs [252], DarkSUSY [253], superISOrelic [254] or MadDM [255]. They all follow the framework developed in [246, 247] and include standard annihilation but also coannihilation. The implementation of the freeze-in mechanism is more recent and is available in micrOMEGAs [199] and DarkSUSY [256]. However, co-scattering and decay processes have not yet been included in public tools and this is the subject of the next section.

## 7.2 Coscattering in micrOMEGAs: a case study for the singlet-triplet dark matter model

This section is based on [257] and describes the micrOMEGAs machinery for multi-component DM and how it applies to the conversion-driven freeze-out mechanism. In this case, the effective average cross-section of eq. (7.21) can not be used and a coupled set of two Boltzmann equations has to be solved. After presenting the mathematical description, a case study of the Singlet-Triplet fermionic model (presented in subsection 2.2.3) is carried out to explore the transition between co-annihilation and co-scattering. The dominant conversion process is the co-scattering while decay processes are negligible. The co-scattering mechanism is found to be relevant for very small DM masses and small mass splittings, opening up a new region in the parameter space of the model. In this region, the triplet states are long-lived and SModelS is thus used to apply long-lived LHC constraints. I first rederived the coupled Boltzmann equations to later check the results obtained with the new implementation of the multi-component DM machinery in micrOMEGAs. The results were also cross-checked extensively with [28]. I finally carried out the physical analysis to explore the new coscattering region. The fruit of this work enabled the publication of a new micrOMEGAs version (v5.3.35) with the multi-component DM feature.

### 7.2.1 Introduction

In the standard DM paradigm, a single WIMP forms the DM, and the annihilation of DM into SM particles determines the DM relic abundance through the freeze-out mechanism [244]. Typically weak couplings and DM masses near the weak scale are required for this. Motivated in part by the lack of conclusive evidence for such WIMPs despite the extensive astrophysical and colliders search program underway [258, 259, 260, 261], re-

cently a much larger range of DM masses and couplings have been explored, and different mechanisms for DM formation have been proposed.

In particular, weaker couplings of the DM ($\chi$) to SM particles can lead to a value for the DM relic density that is consistent with the one extracted from measurements of the cosmic microwave background [262]. This can occur in models where the dark sector [3] contains several new particles and co-annihilation processes involving heavier states of the dark sector (which we generically denote $\psi$) can set the scale for the relic density [263, 245]. Co-annihilation of a dark particle with the DM ($\psi\chi \to \mathrm{SM\,SM}$) or self-annihilation of two dark particles ($\psi\psi \to \mathrm{SM\,SM}$) require a small mass splitting between DM and the heavier state(s) such that the number density of the $\psi s$ is not too strongly Boltzmann suppressed. The states responsible for co-annihilation have at least weak couplings, while the coupling of the DM to the SM can be suppressed. Nonetheless, however, the DM is assumed to be in thermal equilibrium with the SM, for example through processes like $\chi\,\mathrm{SM} \to \chi\,\mathrm{SM}$.

Another possibility is DM co-scattering [250] or conversion-driven freeze-out [251], where inelastic scattering processes such as $\chi\,\mathrm{SM} \to \psi\,\mathrm{SM}$ are responsible for DM formation. This also requires small mass splitting between $\chi$ and $\psi$, but involves very small couplings between the DM and the particles in the thermal bath. In such scenarios, chemical equilibrium between $\chi$ and $\psi$ is not maintained and one needs to solve separate Boltzmann equations for $\chi$ and $\psi$, which are coupled through a conversion term involving co-scattering as well as (inverse) decay processes. For even smaller DM couplings, one enters the regime of the freeze-in mechanism, where DM is so feebly interacting that it is not in equilibrium with the SM in the early Universe [264, 232].

The computation of annihilation and co-annihilation processes for DM freeze-out has long been standard in public DM tools such as micrOMEGAs [252], DarkSUSY [253], superISOrelic [254] or MadDM [255], following the framework developed in [246, 247]. The freeze-in mechanism was incorporated more recently in micrOMEGAs [199] and DarkSUSY [256], while co-scattering and decay processes have not yet been included in public tools. This is the gap that we start to fill with this work. Concretely, we present in this paper the implementation of the co-scattering mechanism[4] in micrOMEGAs together with a case study of the phenomenological implications in the singlet-triplet fermions model (STFM).

The STFM extends the SM with a singlet $\chi$ and a triplet $\psi$ of fermions, which are both odd under a new $\mathbb{Z}_2$ symmetry. In the context of supersymmetry, this has its equivalence in the bino-wino scenario of the MSSM, i.e. $\chi \approx \tilde{B}$, $(\psi^{\pm}, \psi^0) \approx (\tilde{W}^{\pm}, \tilde{W}^0)$; in particular it is realised in Split Supersymmetry [265, 266] with heavy higgsinos and a heavy gluino. It is generally a prime example of a model which can produce the dark matter relic density via either co-annihilation or co-scattering. Co-annihilation in the singlet-triplet (or bino-wino) model has been extensively discussed in the literature, see e.g. [248, 249, 267, 268, 269, 270, 271]. The same framework was also used to discuss the usage of the full momentum-dependent Boltzmann equations for co-scattering processes in [28]. On the collider side, the model can lead to signatures of long-lived particles, which

[3] Here we define each dark sector to be made of all particles that possess the same symmetry properties, in particular under the discrete symmetry that stabilizes DM, and that are in thermal equilibrium with each other.

[4] When referring to co-scattering as a mechanism, we mean the inclusion of both inelastic scattering and (inverse) decays in the conversion terms of the Boltzmann equations.

are heavily searched for at the LHC [54]. Depending on the mass splitting and on the size of the couplings involved, relevant signatures can include disappearing tracks and/or heavy stable charged particles.

The incorporation of co-scattering in micrOMEGAs relies heavily on the machinery developed to include multi-component DM as it requires to solve at least two separate Boltzmann equations, one for each set of dark particles in thermal equilibrium [272, 273]. We do, however, make the simplifying assumption that DM is maintained in kinetic equilibrium and solve the fully integrated Boltzmann equations. This presents a limitation of the current work, since, when too weak couplings are involved, departure from kinetic equilibrium in the early Universe will impact the relic density calculation [274], see also [251, 28, 275]. This can lead to a sizeable systematic uncertainty on the computed $\Omega h^2$.

The paper is organised as follows. In Section 7.2.2, we present the STFM, which is used as the showcase model in this work. In Section 7.2.3, we discuss the relic density calculation for the co-scattering mechanism as incorporated in micrOMEGAs. Section 7.2.4 then contains a numerical analysis for the STFM; this includes a discussion of co-annihilation versus co-scattering, taking into account relic density as well as LHC constraints. Our conclusions are presented in Section 7.2.5. The new micrOMEGAs routines relevant for co-scattering are described in Appendix B.

### 7.2.2 Singlet-triplet extension of the SM

As mentioned in the Introduction, we will illustrate the physics case and phenomenological implications by means of the fermionic singlet-triplet model, STFM. This model extends the SM by two electroweak multiplets: a fermionic singlet $\chi$ and a fermionic $\mathrm{SU}(2)_L$ triplet $\psi$, which are both odd under a new $\mathbb{Z}_2$ symmetry, while the SM particles are even. Following the notation of [28], but with four-component Majorana spinors, the most general Lagrangian for this model is

$$\mathcal{L} = \mathcal{L}_{\mathrm{SM}} + \frac{i}{2}\bar{\chi}\gamma^\mu\partial_\mu\chi + \frac{i}{2}\bar{\psi}\gamma^\mu D_\mu\psi - \frac{1}{2}\left(m\bar{\chi}\chi + M\bar{\psi}\psi\right) + \mathcal{L}_5 + \mathcal{L}_{\geq 6} \tag{7.24}$$

where $\mathcal{L}_5$ contains the dimension-5 operators

$$\mathcal{L}_5 = -\frac{1}{2}\frac{\kappa}{\Lambda}\bar{\psi}\psi H^\dagger H - \frac{1}{2}\frac{\kappa'}{\Lambda}\bar{\chi}\chi H^\dagger H - \frac{\lambda}{\Lambda}\bar{\chi}\psi^a H^\dagger \tau^a H + \text{ h.c.} + \dots . \tag{7.25}$$

Here $H$ is the SM Higgs doublet; $\psi$ is written as a column vector $(\psi_1, \psi_2, \psi_3)^T$ with $\psi^\pm = \psi_1 \pm i\psi_2$ and $\psi^0 = \psi_3$. In the following, we will consider $\mathcal{L}_5$ only; dimension-6 and higher operators ($\mathcal{L}_{\geq 6}$) are neglected. Moreover, we take all parameters to be real and choose $M > 0$. Finally, since we are interested in scenarios where the DM is mostly the singlet $\chi$, we assume that $M > |m|$. The Lagrangian is repeated her for convenience but it was already introduced in subsection 2.2.3 where details about the mixing calculation but also about the vertices of the model can be found.

The $\psi_3 - \chi$ mixing also lifts the mass degeneracy between the charged and neutral triplet states, which would otherwise be exact at tree level. A larger effect on the $\tilde{\psi}^\pm$ mass[5] however comes from electroweak loops, increasing it by about 160 MeV [276, 277].

[5]Here and in the following, all odd-sector physical particles are denoted with a tilde.

Since the precise $\tilde{\psi}^\pm - \tilde{\psi}^0$ mass splitting is important for phenomenology, we compute $m_{\tilde{\psi}^\pm}$ at the 2-loop level following the parametrization of [277].

Including electroweak corrections, the mass hierarchy in our model is $m_{\tilde{\psi}^\pm} > m_{\tilde{\psi}^0} > m_{\tilde{\chi}}$. The $\tilde{\psi}^\pm$ can thus decay either to the $\tilde{\chi}$ or to the $\tilde{\psi}^0$. Both transitions proceed via a virtual $W$-boson, the width of $\tilde{\psi}^\pm \to \tilde{\chi}(W^\pm)^*$ being suppressed by the small mixing, and the width of $\tilde{\psi}^\pm \to \tilde{\psi}^0(W^\pm)^*$ being suppressed by the tiny mass splitting. For the parameter ranges of interest for this study, the $\tilde{\psi}^\pm$ is thus often long-lived at collider scales.

Given that the $\tilde{\psi}^\pm$–$\tilde{\psi}^0$ mass difference is only $O(160)$ MeV, hadronic $\tilde{\psi}^\pm \to \tilde{\psi}^0(W^\pm)^*$ transitions have to be treated as decays into pions, $\tilde{\psi}^\pm \to \tilde{\psi}^0\pi^\pm$, instead of decays into quarks, $\tilde{\psi}^\pm \to \tilde{\psi}^0\, qq'$ [224]. We implement this via a non-perturbative $W$–$\pi$ mixing [225]

$$\mathcal{L}_{W\pi} = \frac{g f_\pi}{2\sqrt{2}} W_\mu^+ \partial^\mu \pi^- + \text{h.c.}\,, \tag{7.26}$$

where $f_\pi = 130$ MeV is the pion decay constant. This gives an effective $\tilde{\psi}^\pm\, \tilde{\psi}^0\, \pi^\mp$ interaction of the form

$$\mathcal{L}_{\tilde{\psi}^+\tilde{\psi}^0\pi^-} = \frac{g^2 \cos\theta f_\pi}{2\sqrt{2} m_{\rm W}^2} \bar{\tilde{\psi}}^0 \gamma^\mu \partial_\mu \pi^- \tilde{\psi}^+\,, \tag{7.27}$$

which we use to compute the 2-body decay width $\Gamma(\tilde{\psi}^\pm \to \tilde{\psi}^0\pi^\pm)$ in CalcHEP. Indeed, $\tilde{\psi}^\pm \to \tilde{\psi}^0\pi^\pm$ is often the dominant decay mode and determines the lifetime of the $\tilde{\psi}^\pm$. This will be relevant later for the LHC constraints on the model.

### 7.2.3 Relic density calculation

Since for small couplings the particles of the dark sector might not be in thermal equilibrium with each other, separate equations for the evolution of their abundances must be written. In the case of the singlet-triplet model considered in this paper, we define two dark sectors, sector 1 containing the singlet $\tilde{\chi}$ and sector 2 containing the triplet $\tilde{\psi}^\pm, \tilde{\psi}^0$ states. In addition, SM particles are assigned to sector 0.

We will always take the singlet as the lightest dark particle and thus the DM candidate. The lightest component of the triplet, which is also odd under $\mathcal{Z}_2$, will decay to the DM and SM particles. The charged component of the triplet has electromagnetic interactions and is therefore in thermal equilibrium with the SM. Moreover, processes such as $\tilde{\psi}^\pm\,\text{SM} \leftrightarrow \tilde{\psi}^0\,\text{SM}$ are always efficient so that all particles of sector 2 are in thermal equilibrium in the early Universe; they thus have the same abundance $Y_2$. The couplings of the singlet can be much weaker and the evolution of its abundance, $Y_1$, must be solved independently. The general equations for the evolution of the abundances with temperature $T$ read

$$\begin{aligned}
\frac{dY_1}{dT} \;=\; & \frac{1}{3H}\frac{ds}{dT}\Bigg[\langle\sigma_{1100}v\rangle(Y_1^2 - Y_1^{eq2}) + \langle\sigma_{1122}v\rangle\left(Y_1^2 - Y_2^2\frac{Y_1^{eq2}}{Y_2^{eq2}}\right) \\
& + \langle\sigma_{1200}v\rangle(Y_1Y_2 - Y_1^{eq}Y_2^{eq}) + \langle\sigma_{1222}v\rangle\left(Y_1Y_2 - Y_2^2\frac{Y_1^{eq}}{Y_2^{eq}}\right) \\
& - \langle\sigma_{1211}v\rangle\left(Y_1Y_2 - Y_1^2\frac{Y_2^{eq}}{Y_1^{eq}}\right) - \frac{\Gamma_{2\to1}}{s}\left(Y_2 - Y_1\frac{Y_2^{eq}}{Y_1^{eq}}\right)\Bigg]\,,
\end{aligned} \tag{7.28}$$

$$\begin{aligned}\frac{dY_2}{dT} &= \frac{1}{3H}\frac{ds}{dT}\Bigg[\langle\sigma_{2200}v\rangle(Y_2^2-Y_2^{eq2})-\langle\sigma_{1122}v\rangle\left(Y_1^2-Y_2^2\frac{Y_1^{eq2}}{Y_2^{eq2}}\right)\\ &+\langle\sigma_{1200}v\rangle(Y_1Y_2-Y_1^{eq}Y_2^{eq})-\langle\sigma_{1222}v\rangle\left(Y_1Y_2-Y_2^2\frac{Y_1^{eq}}{Y_2^{eq}}\right)\\ &+\langle\sigma_{1211}v\rangle\left(Y_1Y_2-Y_1^2\frac{Y_2^{eq}}{Y_1^{eq}}\right)+\frac{\Gamma_{2\to1}}{s}\left(Y_2-Y_1\frac{Y_2^{eq}}{Y_1^{eq}}\right)\Bigg]\,, \end{aligned} \tag{7.29}$$

where $Y_i^{eq}$ are the equilibrium abundances, $H$ is the Hubble parameter, $\langle\sigma_{\alpha\beta\gamma\delta}v\rangle$ are the thermally averaged cross-sections for processes involving annihilation of particles of sectors $\alpha\beta\to\gamma\delta$. In general, the thermally averaged cross-section is given by

$$\langle\sigma_{\alpha\beta\gamma\delta}v\rangle=\frac{1}{C_{\alpha\beta}\bar{n}_\alpha\bar{n}_\beta}\sum_{abcd}\frac{Tg_ag_b}{8\pi^4}\int\sqrt{s}p_{ab}^2(s)K_1(\frac{\sqrt{s}}{T})C_{ab}\sigma_{ab\to cd}(s)ds\,, \tag{7.30}$$

where $C_{ab}=1/2$ if $a=b$ and 1 otherwise; the sum runs over all particles in a given sector, $a\in\alpha, b\in\beta, c\in\gamma, d\in\delta$, when $\alpha=\beta$ (or $\gamma=\delta$) then the additional condition applies $a\le b$ (or $c\le d$). $\bar{n}_\alpha$ is the equilibrium number density which for non-relativistic particles reads

$$\bar{n}_\alpha=s(T)Y_\alpha^{eq}=\frac{T}{2\pi^2}\sum_{a\in\alpha}g_am_a^2K_2(\frac{m_a}{T})\,. \tag{7.31}$$

The entropy $s$ given by

$$s=\frac{2\pi^2}{45}h_{\rm eff}T^3 \tag{7.32}$$

with $h_{\rm eff}$ the effective number of degrees of freedom. Note that $Y_0^{eq}=0.238$ for the SM sector.

The conversion term $\Gamma_{2\to1}$ in Eqs. (7.28) and (7.29) includes both the co-scattering term as well as a decay term:

$$\Gamma_{2\to1}=\frac{\sum_{a\in2}\Gamma_{a\to1,0}\,g_am_a^2K_1\left(\frac{m_a}{T}\right)+\sum_{a\in1}\Gamma_{a\to2,0}\,g_am_a^2K_1\left(\frac{m_a}{T}\right)}{\sum_{a\in2}g_am_a^2K_2\left(\frac{m_a}{T}\right)}+\langle\sigma_{2010}v\rangle\bar{n}_0\,, \tag{7.33}$$

where $\Gamma_{a\to1,0}$ is the decay width of particle $a$ of sector 2 into particles of sectors 1 and 0. The processes included in the width calculation correspond to the decays into one particle of sector 1 and up to 3 particles of sector 0. $\Gamma_{a\to2,0}$ is defined analogously. However, the second term in the numerator of Eq. (7.33) does not exist in our model which contains only one stable particle in sector 1. All these terms are included in the function `darkOmegaN` of micrOMEGAs described in Appendix B. Note that by default, when 2-body decays are present, the 3-body processes are not computed by micrOMEGAs. However, there is a switch to include 3-body processes in all cases as explained in the appendix. This is important in our model, as 3-body decays of $\tilde{\psi}^\pm\to\tilde{\chi}\bar{f}f'$ compete with the 2-body decay $\tilde{\psi}^\pm\to\tilde{\psi}^0\pi^\pm$.

The total relic density is obtained after solving Eqs. (7.28) and (7.29) for the abundances today:

$$\Omega h^2=2.742\times10^8\left(m_{\tilde{\chi}}Y_1+m_{\tilde{\psi}^0}Y_2\right)\,. \tag{7.34}$$

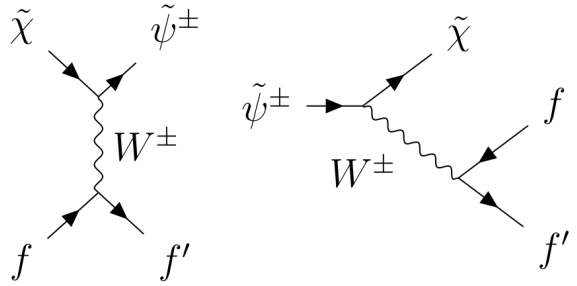


Figure 7.1: Dominant processes contributing to the co-scattering (left) and decay (right) terms in the STFM.

In the STFM, the triplet states decay fast enough such that the only relevant contribution to the relic density is from the term $Y_1$ in Eq. (7.34).

When the couplings are large enough such that both sectors are in thermal equilibrium, then $Y_1/Y_2 = Y_1^{eq}/Y_2^{eq}$ and Eqs. (7.28), (7.29) simplify considerably to recover the usual freeze-out equations. In this case the only contributions are from $\langle\sigma_{1100}v\rangle$ for DM annihilation, as well as $\langle\sigma_{1200}v\rangle$ and $\langle\sigma_{2200}v\rangle$ which are relevant for co-annihilation processes such as $\tilde{\chi}\tilde{\psi}^0 \to W^+W^-$ or $\tilde{\psi}^0\tilde{\psi}^0 \to W^+W^-$. Solving the two abundance equations will lead to the same result as solving a single abundance equation that is $Y_2 = 0$ and $Y_1 = Y$ of the single equation. On the other hand, when the coupling of the singlet, set by the Wilson coefficient $\lambda$, is small, self-annihilation of the singlet becomes negligible and the abundance equations simplify to

$$\frac{dY_1}{dT} = \frac{-\Gamma_{2\to1}}{HT}\left[Y_2 - Y_1\frac{Y_2^{eq}}{Y_1^{eq}}\right], \tag{7.35}$$

$$\frac{dY_2}{dT} = \frac{s}{HT}\left[\langle\sigma_{2200}v\rangle(Y_2^2 - Y_2^{eq2}) + \frac{\Gamma_{2\to1}}{s}\left(Y_2 - Y_1\frac{Y_2^{eq}}{Y_1^{eq}}\right)\right]. \tag{7.36}$$

The dominant processes contributing to the co-scattering and decay terms entering $\Gamma_{2\to1}$ in the STFM are scattering on SM fermions through the exchange of a $W$-boson and $\tilde{\psi}^{\pm} \to \tilde{\chi}ff'$ decays via an off-shell $W$ boson ($\tilde{\psi}^{\pm} \to \tilde{\psi}^0\pi^{\pm}$ decays do not contribute to the conversion term). The relevant diagrams are shown in Fig. 7.1. Numerically it turns out that the decays contribute at most at the level of a few percent to obtaining $\Omega h^2 \simeq 0.12$. Nonetheless they may have a relevant effect for maintaining DM in thermal equilibrium during the evolution of the number density. Scattering on SM bosons, shown in Fig. 7.2, gives a subdominant contribution, also of the level of a few percent.

For illustration, we show in Fig. 7.3 the evolution of $Y_{\chi,\psi} = Y_{1,2}$ in the STFM for two values of $\lambda = 10^{-3}$ and $10^{-5}$, for $m = 500$ GeV and $M$ chosen such that $\Omega h^2 \simeq 0.12$. For $\lambda = 10^{-3}$, co-annihilation dominates. In this case, both sectors follow their equilibrium distribution until $x \approx 25$, where freeze-out occurs. After freeze-out, the $\psi$ rapidly decay to the DM. However, since $Y_\psi \ll Y_\chi$, the decay term gives only a small contribution to the relic density. For $\lambda = 10^{-5}$ and a smaller mass splitting, co-scattering dominates and $Y_\chi$ departs from equilibrium much sooner. In this case, the decay of $\tilde{\psi}^0$ continues until small temperatures (here, the $\tilde{\psi}^{\pm}$ primarily decays into $\tilde{\psi}^0$).

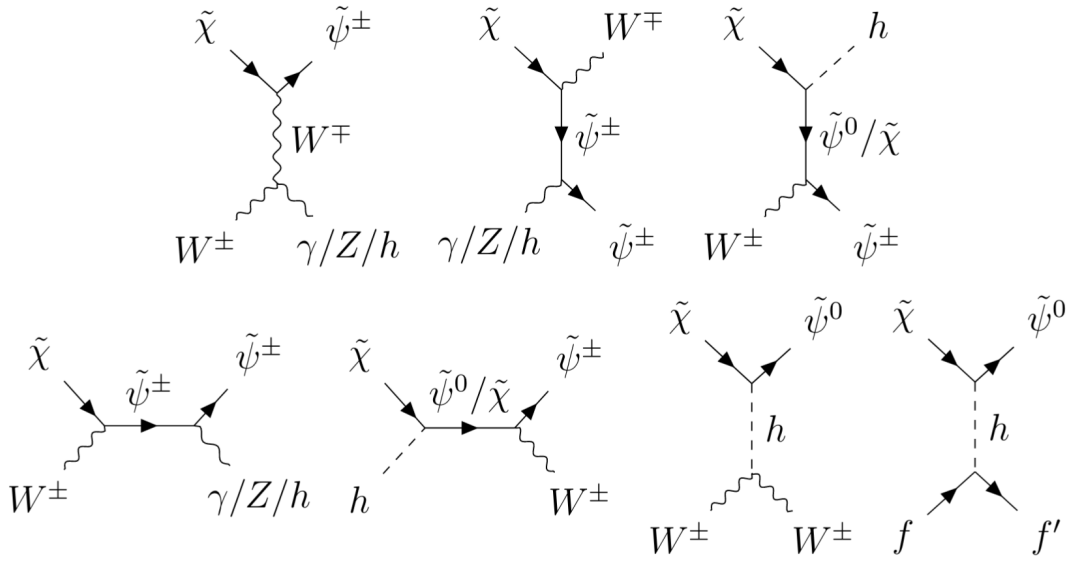


Figure 7.2: Subdominant co-scattering processes in the STFM.

The early departure of $Y_\chi$ from the equilibrium distribution in the right panel of Fig. 7.3 occurs because chemical equilibrium between $\chi$ and $\psi$, maintained by co-scattering and decay processes at high enough $T$, is lost. Quantitatively this happens when $\Gamma_{2\to1}$ is not much larger than the Hubble rate. To illustrate this in more detail, we compute $\Gamma_{2\to1}/H(T)$ for the decay and co-scattering contributions separately. The result is shown in Fig. 7.4 as a function of $x = m/T$, on the left for $\lambda = 10^{-3}$ and on the right for $\lambda = 10^{-5}$. As can be seen, for $\lambda = 10^{-3}$, both types of processes maintain equilibrium ($\Gamma/H \gg 1$) until after the freeze-out of $\psi$. However, for $\lambda = 10^{-5}$, $\Gamma_{2\to1}/H(T)$ is $\mathcal{O}(1)$ at freeze-out, thus a treatment using the one-component Boltzmann equation is not appropriate. We also see that co-scattering is more efficient at higher temperatures and decreases with increasing $x$. For completeness and as a reference, Fig. 7.4 also shows $\Gamma/H(T)$ for $\psi\psi \to \mathrm{SM\,SM}$ annihilation.

Inelastic scattering processes $\chi\,\mathrm{SM} \leftrightarrow \psi\,\mathrm{SM}$ and (inverse) decays $\psi \leftrightarrow \chi\,\mathrm{SM}$ are also involved in maintaining kinetic equilibrium. As already mentioned in the Introduction, deviations from kinetic equilibrium are expected when the DM couplings become too weak [274]. In this case, the DM distribution at freeze-out does not follow a Maxwell-Boltzmann distribution and a complete treatment involves solving the full momentum-dependent Boltzmann equation. Deviations from kinetic equilibrium in the co-scattering region were shown to have a mild ($\sim$10%) impact on the final relic density in the scenario considered in [251] (Appendix C). In [28] it was argued that there can be larger effects in the STFM because decay processes are less important than in the model considered in [251]; however, this study also made some simplifying assumptions, e.g., ignoring decays and the subdominant co-scattering processes. To reliably quantify the uncertainty introduced by using the integrated Boltzmann equations, a one-to-one comparison with the full, unintegrated approach would be needed. A complete solution to the unintegrated Boltzmann equation within MICROMEGAs is however beyond the scope of this work.

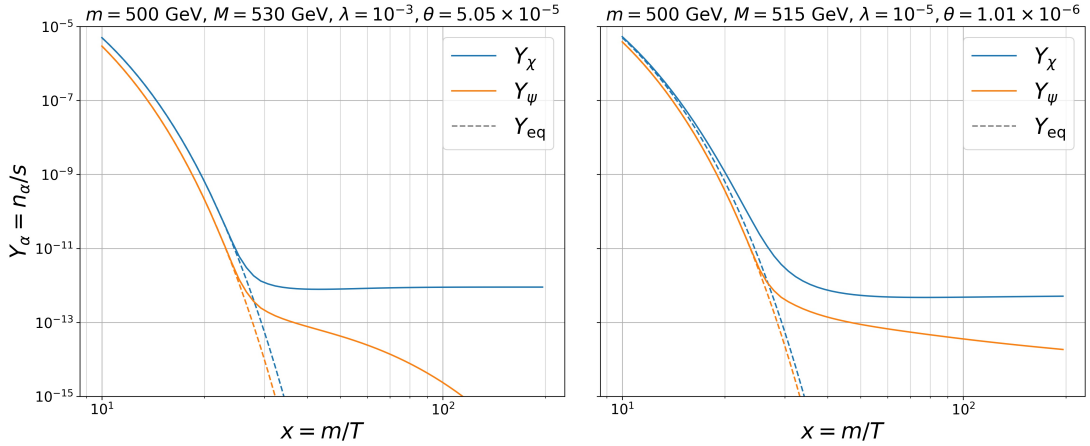


Figure 7.3: Evolution of the $\chi$ and $\psi$ abundances for $\lambda = 10^{-3}$ (left) and $\lambda = 10^{-5}$ (right); The $\chi$ mass parameter is set to $m = 500$ GeV, while $M$ is adjusted to obtain $\Omega h^2 \simeq 0.12$.

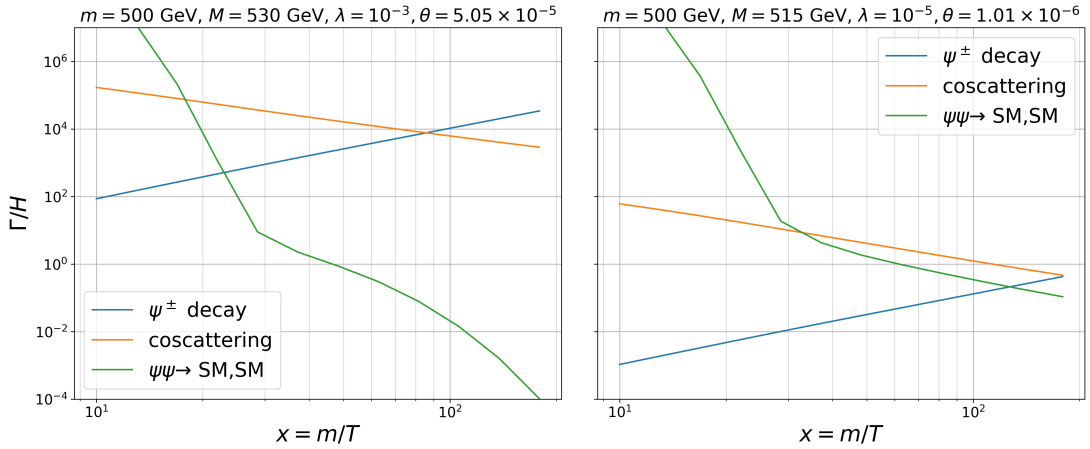


Figure 7.4: Contributions to the DM equilibrium for $\lambda = 10^{-3}$ (left) and $\lambda = 10^{-5}$ (right). Different contributions are all converted into reaction rates $\Gamma_i$ and compared to the universe expansion rate $H$; the $\chi$ mass parameter is set to $m = 500$ GeV, while $M$ is adjusted to obtain $\Omega h^2 \simeq 0.12$.

### 7.2.4 Numerical analysis

Let us now turn to the numerical analysis of the STFM parameter space. To this end, we take the mass parameters $m$ and $M$ together with the Wilson coefficient $\lambda$ from Eqs. (7.24) and (7.25) as input parameters, fixing $\kappa = \kappa' = 0$ and $\Lambda = 10$ TeV. For small $\lambda$, as relevant in this study, the singlet-triplet mixing is small and $m \simeq m_{\tilde{\chi}}$. For each choice of $(m, \lambda)$, we scan over $M$ to obtain $\Omega h^2 = 0.12$ [262]. This fixes the $\tilde{\psi}^0$–$\tilde{\chi}$ mass difference $\Delta m \equiv m_{\tilde{\psi}^0} - m_{\tilde{\chi}}$. The mixing angle is then $\theta \approx \lambda \times 1.5\,\text{GeV}/\Delta m$, cf. Eq. (2.39).

The $\tilde{\psi}^\pm$ mass is given by $m_{\tilde{\psi}^\pm} = M + \delta m_\psi^{\text{2loop}}$, where $\delta m_\psi^{\text{2loop}}$ are electroweak corrections at the 2-loop level as parametrized in [277]; they lead to a small mass splitting between the $\tilde{\psi}^\pm$ and the $\tilde{\psi}^0$ of about $150 - 165$ MeV depending on $M$. The precise value of this mass splitting is crucial for the mean lifetime $c\tau_0(\tilde{\psi}^\pm)$, which in turn determines the LHC signatures.

To evaluate LHC constraints, we use SModelS v2.2.0 [93, 92, 216, 94, 177], interfaced to micrOMEGAs [200, 278]. This interface automatically creates the input file for SModelS including all relevant LHC production cross sections at $\sqrt{s} = 8$ and 13 TeV (computed with CalcHep) and writes out the most constraining result. The collider signatures of the STFM resemble those of chargino/neutralino production in the MSSM with small mass splitting between the wino and bino states. Relevant LHC constraints therefore come from searches for long-lived charginos, in particular from disappearing track searches, for which SModelS has the ATLAS and CMS searches [48, 47] from Run 2 implemented. Searches for promptly decaying charginos/neutralinos do not give any relevant constraints for the small mass splittings relevant here. Searches for heavy stable charged particles are also not effective, because the $\tilde{\psi}^{\pm}$ mean decay length does not exceed $\mathcal{O}(10)$ cm in the parameter range we consider.

To illustrate the importance of co-scattering for obtaining the correct relic density, $\Omega h^2 = 0.12$, we introduce two quantities, $\Delta^{\Omega}_{1s}$ and $\Delta^{\Omega}_{2s}$. The former is the fractional difference of the relic densities obtained in the 1-sector or 2-sector computations:

$$\Delta^{\Omega}_{1s} \equiv 1 - \frac{\Omega h^2(\text{1 sector})}{\Omega h^2(\text{2 sectors})}\,. \tag{7.37}$$

More explicitly, $\Omega h^2$(1 sector) is the value obtained when using the standard `darkOmega` function of micrOMEGAs, which involves only one Boltzmann equation and thus includes only co-annihilation. In contrast, $\Omega h^2$(2 sectors) is the value obtained by means of `darkOmegaN` with the dark particles split in two sectors, i.e. from solving the coupled system of two Boltzmann equations including all co-scattering and decays processes. A value of $\Delta^{\Omega}_{1s} = 0.5$ means that the conventional calculation with one Boltzmann equation gives a result which is a factor of 2 too small, and one would conclude that the DM candidate is under-abundant in the scenario at hand. The second quantity, $\Delta^{\Omega}_{2s}$, is defined as

$$\Delta^{\Omega}_{2s} \equiv 1 - \frac{\Omega h^2(\text{2 sectors})}{\Omega h^2(\text{2 sectors, no co-scattering})}\,. \tag{7.38}$$

Here $\Omega h^2$(2 sectors) is the relic density from solving two Boltzmann equations as above, while $\Omega h^2$(2 sectors, no co-scattering) is the value in the same approach when the co-scattering processes (but not the decays) are neglected. The latter can be computed in micrOMEGAs via the `ExcludedFor2DM="2010"` command as explained in Appendix B. Note that $\Delta^{\Omega}_{2s} = 0.5$ means that $\Omega h^2$ increases by a factor 2 when co-scattering processes are neglected, while $\Delta^{\Omega}_{2s} = 0.9$ means an increase by a factor 10.

Figures 7.5 and 7.6 show the scan results in the plane of $\lambda$ versus $m_{\tilde{\chi}}$. At each point in the plots, $\Delta m \equiv m_{\tilde{\psi}^0} - m_{\tilde{\chi}}$ is adjusted such that $\Omega h^2 = 0.12$ within 1% precision. While the full-coloured points pass collider constraints, the points marked as crosses are excluded by the disappearing track results in SModelS. In order to focus on the transition from the co-annihilation to the co-scattering regimes, we consider the range $\lambda = [10^{-2}, 5 \times 10^{-6}]$. For smaller values of $\lambda$ the equilibrium condition becomes questionable and the calculation in micrOMEGAs may not be valid any more (see the discussion at the end of section 7.2.3). Moreover, the $\tilde{\psi}^0$ becomes very long lived, such that constraints from Big Bang Nucleosynthesis (BBN) may become relevant. In fact, for small DM masses around 100 GeV, $c\tau_0(\tilde{\psi}^0) > 100$ sec at leading order even for $\lambda \lesssim 10^{-5}$. However, this region is excluded by LHC constraints, so we do not consider BBN bounds in our analysis.

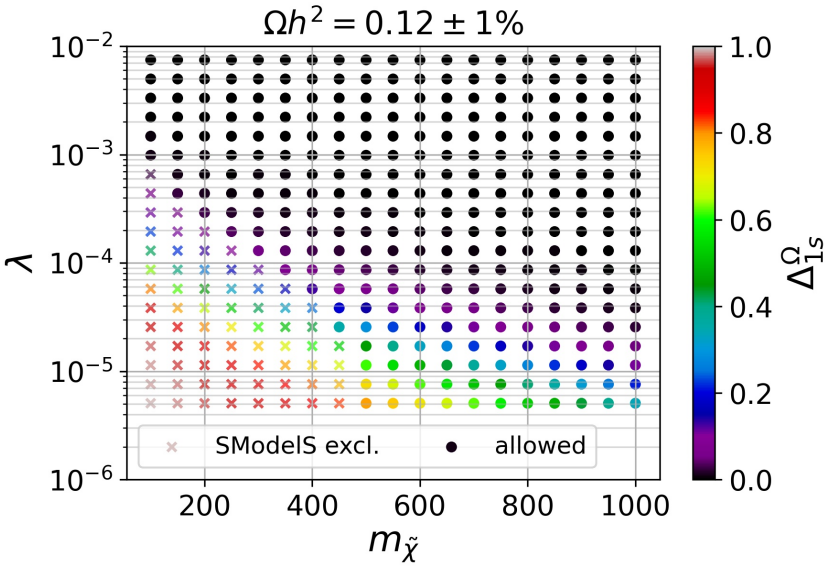


Figure 7.5: Scan result in the plane of $\lambda$ versus DM mass $m_{\tilde{\chi}}$. For each point, the triplet mass parameter $M$ is adjusted such that $\Omega h^2 = 0.12$. The colour scale indicates $\Delta^{\Omega}_{1s}$ as defined in Eq. (7.37). Full-coloured points pass collider constraints, crosses are excluded by the disappearing track results in SModelS v2.2.0.

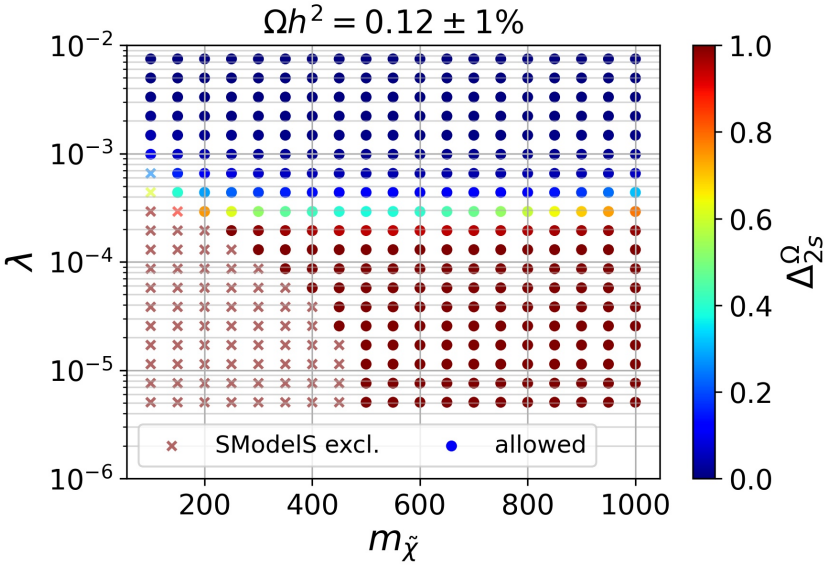


Figure 7.6: Same as Fig. 7.5 but with the colour scale showing $\Delta^{\Omega}_{2s}$ as defined in Eq. (7.38).

In Fig. 7.5, the colour code shows $\Delta^{\Omega}_{1s}$ as defined in Eq. (7.37). This indicates the importance of solving two Boltzmann equations instead of just one. We see that, for $m_{\tilde{\chi}}$ around 100–200 GeV, the splitting into two dark sectors ($1 = \tilde{\chi}$ and $2 = \tilde{\psi}^{\pm}, \tilde{\psi}^0$) is relevant already at $\lambda \sim$ (a few) $\times 10^{-4}$. With increasing mass, the importance of the two-dark-sectors treatment sets in at smaller $\lambda$. However even at $m_{\tilde{\chi}} = 1$ TeV, there is a large effect for $\lambda \lesssim 10^{-5}$. Roughly, the black points correspond to the co-annihilation dominated region, while the colourful points correspond to the co-scattering domain. The

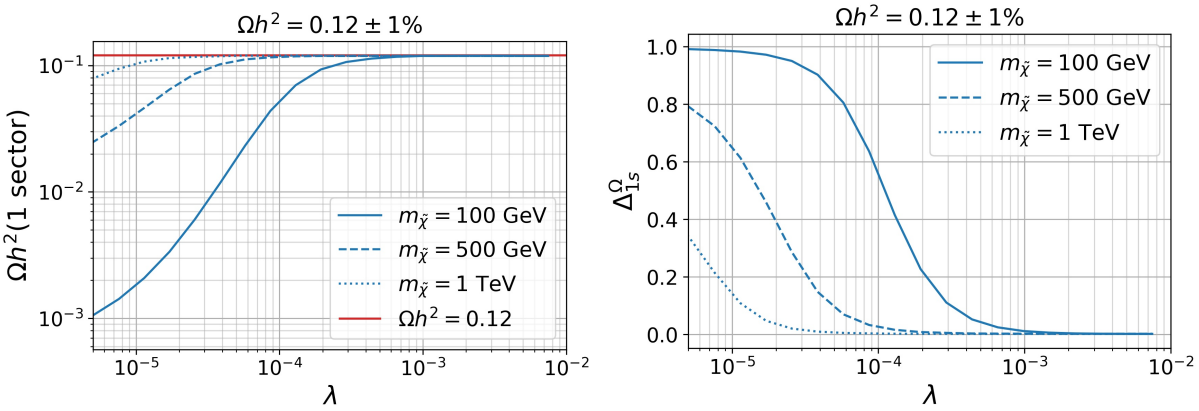


Figure 7.7: On the left $\Omega h^2$(1 sector), on the right $\Delta^{\Omega}_{1s}$ as function of $\lambda$ for $m_{\tilde{\chi}} = 100$, 500 and 1000 GeV; at each point, the triplet mass parameter $M$ is adjusted such that $\Omega h^2 = 0.12$ in the full 2-sectors calculation.

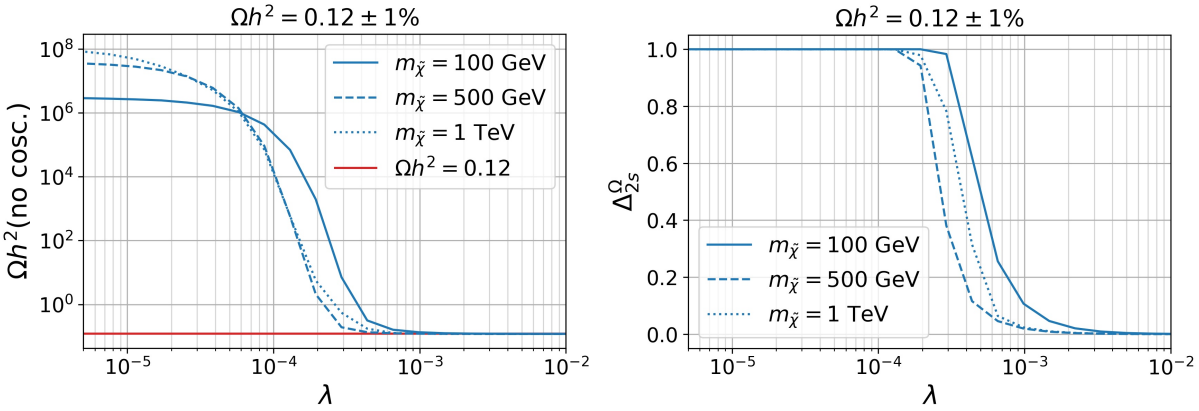


Figure 7.8: As Fig. 7.7 but showing on the left $\Omega h^2$(2 sectors, no co-scattering) and on the right the corresponding $\Delta^{\Omega}_{2s}$.

current LHC constraints challenge the co-scattering region for DM masses up to about 450 GeV, actually excluding most of this region. In the co-annihilation region, LHC constraints are not effective.

In Fig. 7.6, the colour code shows $\Delta^{\Omega}_{2s}$ as defined in Eq. (7.38). This illustrates the importance of the co-scattering term in the two-dark-sectors treatment. We observe that for $\lambda$ of the order of $10^{-2}$–$10^{-3}$ (dark blue points), the decay processes are sufficient to keep the two dark sectors in equilibrium. This rapidly changes with decreasing $\lambda$, and from $\lambda \approx 3 \times 10^{-4}$ onwards the final relic density is dominated by the co-scattering processes. This conclusion depends very little on $m_{\tilde{\chi}}$.

The behaviour of $\Omega h^2$(1 sector) and $\Delta^{\Omega}_{1s}$ as function of $\lambda$ is shown explicitly in Fig. 7.7 for three choices of DM mass, $m_{\tilde{\chi}} = 100$, 500 and 1000 GeV. Analogously, Fig. 7.8 shows the behaviour of $\Omega h^2$(2 sectors, no co-scattering) and $\Delta^{\Omega}_{2s}$ for the same choice of masses.

The singlet-triplet mass difference needed to achieve $\Omega h^2 = 0.12$ is shown in Fig. 7.9 as a function of $m_{\tilde{\chi}}$, for the same range of $\lambda$ as in Figs. 7.5 and 7.6. When co-annihilation is dominant (dark red points), a finely adjusted mass difference in the range of about 10–30 GeV is needed. The relative mass difference $\Delta m/m_{\tilde{\chi}}$ steadily decreases from 13%

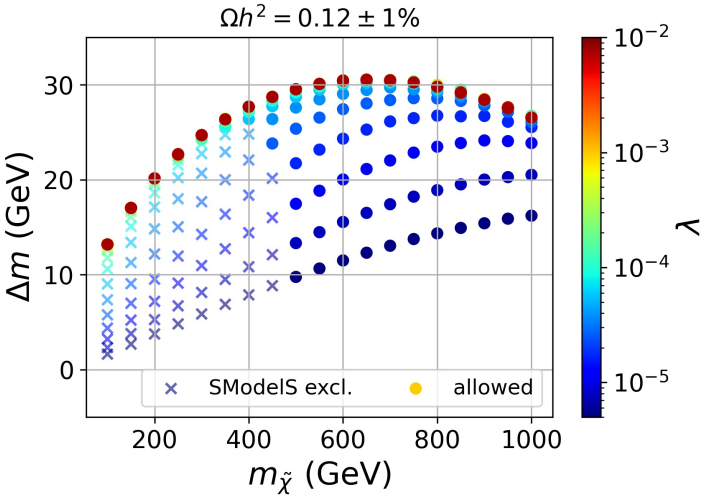


Figure 7.9: Illustration of mass difference $\Delta m$ needed to obtain $\Omega h^2 = 0.12$. Points marked as crosses are excluded by SModelS v2.2.0.

at $m_{\tilde{\chi}} = 100$ GeV to about 3% at $m_{\tilde{\chi}} = 1$ TeV. This well-known behaviour does not depend on $\lambda$ as long as co-annihilation is dominant. In the co-scattering phase, however, smaller couplings require smaller mass differences in order for $\tilde{\chi}\,\mathrm{SM} \to \tilde{\psi}\,\mathrm{SM}$ processes to remain efficient. This opens a new region of smaller mass splittings in the parameter space of the model, where the cosmologically observed DM abundance can be saturated. Without the co-scattering mechanism, one would conclude that the relic density in this region was too small and $\tilde{\chi}$ could constitute only part of the DM. As before, we also see that long-lived particle searches at the LHC exclude a large part of the co-scattering region for DM masses up to about 450 GeV.

The interdependence of $\Delta m$, the DM coupling and the importance of co-annihilation or co-scattering is further illustrated in Fig. 7.10 (top panels). This figure presents the scan points in the plane of mixing angle $\theta$ vs. singlet-triplet mass difference $\Delta m$, for $m_{\tilde{\chi}} = 100$–$600$ GeV. The left-most line of points is for $m_{\tilde{\chi}} = 100$ GeV, the right-most is for $m_{\tilde{\chi}} = 600$ GeV; in-between $m_{\tilde{\chi}}$ increases in steps of 50 GeV. We see again that, as long as co-annihilation is dominant, for a given $m_{\tilde{\chi}}$, $\Delta m$ is almost constant as the mixing decreases. Once co-scattering takes over, smaller mixing also means smaller $\Delta m$ to achieve the correct relic density. $\theta$ saturates just below $10^{-6}$, as it is inversely proportional to $\Delta m$, see Eq. (2.39). The small mixing and small mass differences make the $\tilde{\psi}^{\pm}$ long-lived in much of the co-scattering region, as can be seen in the bottom panel of Fig. 7.10. The associated decay lengths are of the order of 1–10 cm. It is this behaviour that causes constraints from disappearing track searches at the LHC to kick in.

Before concluding this analysis, we note that the computed $\Omega h^2$ is subject to systematic uncertainties, stemming in part from the usage of the momentum-integrated Boltzmann equations.[6] Quantifying this uncertainty would be a full-fledged study in itself, beyond the scope of this work. Instead, we show in Fig. 7.11 the effect of an assumed 10% theoretical uncertainty. As can be seen, this results in a widening of the range of $\Delta m$, but does not qualitatively change our results. In particular the turn-over to smaller $\Delta m$

[6] Higher-order loop corrections will also be relevant.

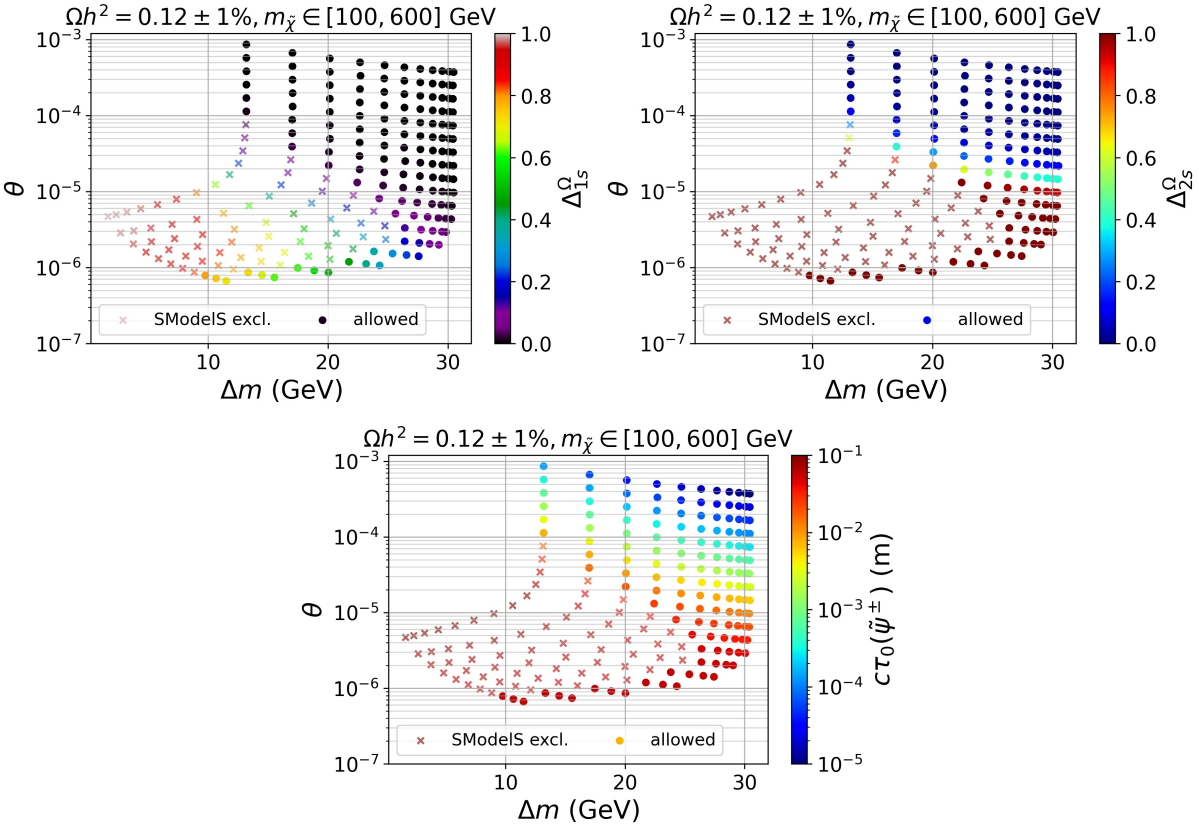


Figure 7.10: Mixing angle $\theta$ versus $\Delta m$ for $m_\chi = 100 - 600$ GeV (from left to right in steps of 50 GeV). The colour scales show $\Delta^{\Omega}_{1s}$ (top left), $\Delta^{\Omega}_{2s}$ (top right), and the $\tilde{\psi}^{\pm}$ mean decay length, $c\tau_0(\tilde{\psi}^{\pm})$, in meter (bottom). Points marked as crosses are excluded by SModelS v2.2.0.

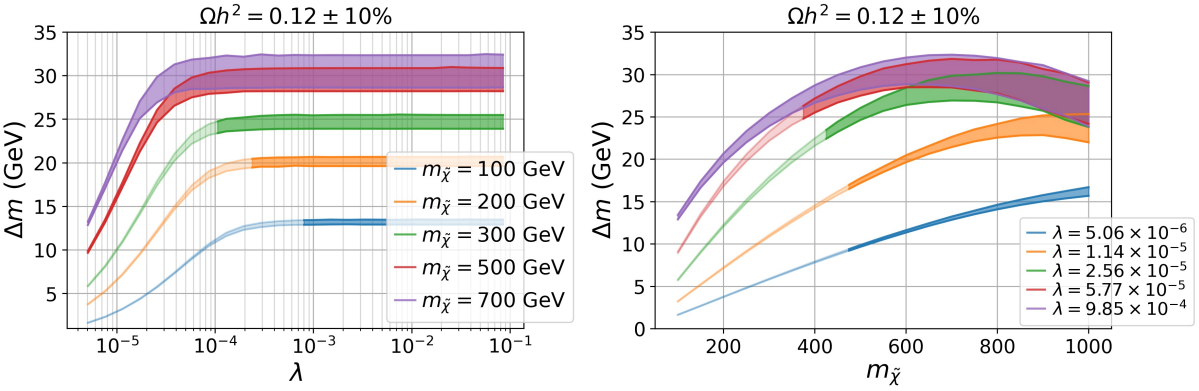


Figure 7.11: Bands of $\Omega h^2 = 0.12 \pm 10\%$ in the plane of $\Delta m$ vs $\lambda$ for several DM masses (left) and in the plane of $\Delta m$ vs $m_{\tilde{\chi}}$ for several values of $\lambda$ (right); the light-shaded areas are excluded by SModelS v2.2.0.

that indicates the transition from the co-annihilation to the co-scattering regime in the left panel of Fig. 7.11 is hardly affected. We also note that the bands of $\Omega h^2 = 0.12 \pm 10\%$ are narrower in the co-scattering region than in the co-annihilation region.

### 7.2.5 Conclusions

In scenarios with very small DM couplings and small mass splittings between the DM and other dark sector particles, so-called "co-scattering" or "conversion-driven freeze-out" can be the dominant mechanism for DM production. Characteristic for this mechanism is that freeze-out takes place out of chemical equilibrium. Self-annihilation of DM is too inefficient to achieve $\Omega h^2 \approx 0.1$. Instead, inelastic scattering processes of the type $\chi\,\mathrm{SM} \leftrightarrow \psi\,\mathrm{SM}$ are primarily responsible for DM formation. Moreover, decays and inverse decays of dark sector particles, like $\psi \leftrightarrow \chi\,\mathrm{SM}$, also have to be taken into account in the conversion terms of the Boltzmann equations.

We presented the first inclusion of this mechanism in a public DM tool, micrOMEGAs. The numerical treatment relies heavily on the machinery for multi-component DM in micrOMEGAs [272, 273] as it requires to solve at least two separate Boltzmann equations, one for each set of dark particles in thermal equilibrium. To illustrate both, the new capabilities of micrOMEGAs as well as the phenomenological implications of the co-scattering regime, we performed a case study for the singlet-triplet fermion model, STFM. This model extends the SM by two electroweak multiplets, a singlet $\chi$ and a triplet $\psi$, which are both odd under a new $\mathbb{Z}_2$ symmetry, while the SM particles are even. The $\chi$-like state is the DM candidate; it has very weak couplings induced by a small mixing with the triplet. Our numerical analysis concentrated on the transition between the co-annihilation and the co-scattering regimes, and we showed that the latter can open up a new region in the parameter space of the model.

The charged triplet states, $\tilde{\psi}^{\pm}$, are typically long-lived in the co-scattering region, leading to distinct collider signatures. Using SModelS v2.2.0 to evaluate the current LHC constraints, we found that disappearing track searches exclude DM masses up to $m_{\tilde{\chi}} \approx 200$ GeV in the transition region between co-annihilation and co-scattering, and up to $m_{\tilde{\chi}} \approx 450$ GeV for very small $\lambda$, where co-scattering dominates. A precise calculation of the mass splitting among the triplet-like states as well as the inclusion of $\tilde{\psi}^{\pm} \to \tilde{\chi}\pi^{\pm}$ decays are important to that end.

The new version of micrOMEGAs, v5.3.35, is publicly available at `https://lapth.cnrs.fr/micromegas/`. It includes the STFM implementation together with a README explaining its usage, and a demo program (`demo.c`) illustrating some of the new functionalities presented in this paper. It also includes an updated interface to SModelS v2.2 [278]. The new micrOMEGAs routines relevant for co-scattering are described in detail in the appendix.

An important caveat is that, so far, micrOMEGAs employs momentum-integrated Boltzmann equations only. For a precise calculation of the DM relic density including the effects of early kinetic decoupling, the full momentum-dependent Boltzmann equations should be solved, as advertised in [28]. This is left for future work.

# Chapter 8

# Conclusions

The SM, introduced in section 2.1, constitutes one of the most successful scientific theories, thanks to precise experimental measurements in agreement with the SM predictions. Yet several caveats hint at the incompleteness of the SM. Theoretically, the SM fails to explain several problems of modern particle physics, the hierarchy problem, the unification of fundamental interactions, the description of neutrinos, etc. Some experimental observations also contradict the SM, such as $B$-meson anomalies, or can not be explained by the SM, such as DM. Searching for new physics then founds a lot of theoretical and experimental motivations. A more detailed discussion of motivations for searching beyond the SM can be found in section 2.2.1. Answers to these questions can be looked for both theoretically and experimentally, and the two ideally work hand in hand. The communication between theoreticians and experimentalists is then crucial for the field to progress. Many BSM theories have been proposed, and supersymmetry (see section 2.2.2) was one of the most promising for its problem-solving capacity. Section 2.2.3 presented the two other BSM models used for this thesis.

On the experimental side, an intensive search program is being carried out at the ATLAS and CMS experiments, in the hope to discover new particles. Searches are interpreted with simplified models to characterize the potential new physics signals generically. In the absence of discovery, the observations are used to set constraints on the simplified models. If sufficient information is publicly provided by the experimental collaborations, theoreticians can reuse their data to constrain other theoretical scenarios. Many public tools offer the possibility for theorists to constrain their favorite models, by providing model inputs in the appropriate format. Section 3.2 described two methods for reinterpreting LHC data; i) the reinterpretation based on full simulation and ii) reusing simplified model results. Most ATLAS and CMS analyses are cut-based, *i.e.* the kinematic parameter space is divided into SRs, each defined by kinematic cuts. The latter is designed to maximize the potential new physics signal while minimizing the SM background. At the experimental level, SRs are statistically combined to get the most out of the search sensitivity. Nonetheless, with the information provided by experimentalists, reinterpretation tools can often only use one SR with the best-SR approach. Indeed, information about the correlations between SRs, reflecting the correlated effects of experimental uncertainties, is needed for a proper statistical combination. The CMS collaboration was the first to provide correlation matrices, allowing the statistical combinations through the simplified

likelihood method, which approximates the full likelihood. The ATLAS collaboration has recently started to publicly provide full likelihoods, usable with the `pyhf` package.

Chapter 4 presented the implementation of both combination methods in the MadAnalysis5 tool based on full simulation. My contribution to this work was the implementation of the simplified likelihood feature in MadAnalysis5. There are currently four ATLAS and five CMS analyses in the MadAnalysis5 Public Analysis Database for which the new combination feature can be used. The gain regarding the physics constraints was demonstrated by reproducing the mass constraints published by ATLAS and CMS, for the simplified models considered in each analysis. A case study of a more realistic MSSM scenario was also carried out. The latter showed how the SR combination allows physicists to use more of the data from analyses and give more reliable results than the best-SR approach. The logic continuation is the statistical combination of analyses, which is an endeavor already started in SModelS v2.2, and that should be adopted in MadAnalysis5 soon. Chapter 5 described the implementation of a `pyhf` interface in SModelS. This enabled the use of full likelihoods provided under a `JSON` format by the ATLAS collaboration. At the time of this work, the SModelS database was extended with three EMs results with their `JSON` file for three analyses at full Run 2 luminosity (139 $\text{fb}^{-1}$). At the time of writing this thesis, there are five such analyses implemented in the SModelS database. However, numerous analyses with full likelihoods have already been published by ATLAS and their implementation in SModelS is ongoing.

The new developments released in SModelS version 2 in 2021 were presented in chapter 6. They consisted of the extension of the topology description in SModelS with the introduction of a particle class, enabling the precise definition of the properties of a particle. In this way, quantum numbers such as spin, color, and electric charge can be described. More importantly, the width can also be stored in the particle object, while any BSM particle was only represented by its mass before version 2. This enabled the possibility to implement and use width-dependent results in SModelS, simultaneously with standard prompt results. This allowed the extension of the database with several LLP results. The new results were summarized in the same chapter, counting a few prompt results as well. The physics capabilities of SModelS v2 were then demonstrated using the scotogenic model and a SUSY electroweakino scenario, with additional DM considerations. Two scotogenic scenarios were considered, with either scalar or fermionic DM matter, both with the inert charged scalar as the second lightest state. For the scalar DM case, the charged state is long-lived for sub-GeV mass splittings with the DM and this scenario can thus be probed with HSCP and disappearing tracks, depending on the mass splitting. For the fermionic DM case, freeze-in production of DM is considered. A long-lived charged scalar states naturally arose from the small Yukawa couplings required to get the correct relic density and therefore triggered HSCP and displaced leptons results. The most sensitive displaced leptons analysis was newly implemented with a full likelihood, thus highlighting the importance of SR combination. Finally, a general SUSY electroweakino scenario was used to showcase how the LHC constraints are weakened in a realistic SUSY scenario compared to simplified models, also considering long-lived searches and DM constraints.

Chapter 7 introduced how the production of DM is described by thermodynamics in an expanding Universe. The concepts of freeze-out and freeze-in and their mathematical descriptions were presented. The two respectively correspond to extreme cases of

DM coupling to the SM; feeble couplings corresponding to FIMPs and weak couplings corresponding to WIMPs. In-between cases or exceptions to the standard feeze-out picture allow getting the required DM density for couplings between the feeble and weak scale. Namely, section 7.2 discussed the implementation of the coscattering mechanism in micrOMEGAs, which relies on its multi-component DM machinery. The physics case of the Singlet-Triplet model, similar to split-SUSY, was used to explore the transition between the coannihilation and the coscattering regimes. It was shown that coscattering opens up a new region in the parameter space of the model. In this region, the charged triplet states are long-lived and it was found with SModelS v2.2.0 that part of this new coscattering region is excluded by disappearing tracks. Coscattering in micrOMEGAs is based on the integrated Boltzmann equations, which is most of the time a good approximation. However, it could lead to wrong results in the case of early kinetic decoupling. A precise calculation would involve the full Boltzmann equation, but this is left for future work.

In particle physics, the quest for new particles is a dynamic field. Experimentalists and theoreticians both pursue this endeavor with their tools. Ideas for new searches at the LHC are constantly coming up. The reinterpretation of the LHC results by phenomenologists is crucial to use the full potential of new physics searches. Close communication between the two communities is thus very important for the field to keep going forward. The ATLAS collaboration has recently started to publish full likelihoods as complementary materials to their results. It is the first time that such detailed information is publicly provided and it allows the reuse and preservation of the results in the long term. Theorists can thus use the experimental data in a large variety of other theoretical contexts, and possibly come up with hints for new physics, guiding us toward new strategies to search for new physics at the LHC. On another note, the search for DM has been a hot topic for several decades, and many ideas have been studied and documented. However, several possibilities have not been fully explored yet, like the coscattering mechanism. More ways to produce the correct amount of DM could be found in the future. Since we can not know which mechanism or model nature has chosen, all venues must be investigated and we can only hope that someone will stumble upon a discovery that might reveal the nature of DM in the more or less near future.

# Appendix A

# SModelS version 2

## A.1 Overview of Run 2 results in the SModelS 2.1.0 database

Tables A.1 and A.2 present a list of all Run 2 results included in the SModelS database. The last column in each table displays which type of information is available (if any) for combining distinct signal regions within a given analysis.

| ID | Short Description | $\mathcal{L}$ [fb$^{-1}$] | UL$_{\text{obs}}$ | UL$_{\text{exp}}$ | EM | comb. |
|---|---|---|---|---|---|---|
| ATLAS-SUSY-2015-01 [279] | 2 $b$-jets | 3.2 | ✓ | | | |
| ATLAS-SUSY-2015-02 [280] | $1\ell$ stop | 3.2 | ✓ | | ✓ | |
| ATLAS-SUSY-2015-06 [281] | $0\ell$ + 2–6 jets | 3.2 | | | ✓ | |
| ATLAS-SUSY-2015-09 [282] | jets + 2 SS or $\geq 3\ell$ | 3.2 | ✓ | | | |
| ATLAS-SUSY-2016-06 [48] | disappearing tracks | 36.1 | | | ✓ | |
| ATLAS-SUSY-2016-07 [283] | $0\ell$ + jets | 36.1 | ✓ | | ✓ | |
| ATLAS-SUSY-2016-08 [44] | displaced vertices | 32.8 | ✓ | | | |
| ATLAS-SUSY-2016-14 [284] | 2 SS or 3 $\ell$'s + jets | 36.1 | ✓ | | | |
| ATLAS-SUSY-2016-15 [285] | $0\ell$ stop | 36.1 | ✓ | | | |
| ATLAS-SUSY-2016-16 [286] | $1\ell$ stop | 36.1 | ✓ | | ✓ | |
| ATLAS-SUSY-2016-17 [287] | 2 OS leptons | 36.1 | ✓ | | | |
| ATLAS-SUSY-2016-19 [288] | 2 $b$-jets + $\tau$'s | 36.1 | ✓ | | | |
| ATLAS-SUSY-2016-24 [289] | 2–3 $\ell$'s, EWino | 36.1 | ✓ | | ✓ | |
| ATLAS-SUSY-2016-26 [290] | $\geq 2\,c$-jets | 36.1 | ✓ | | | |
| ATLAS-SUSY-2016-27 [291] | jets + $\gamma$ | 36.1 | ✓ | | ✓ | |
| ATLAS-SUSY-2016-28 [292] | 2 $b$-jets | 36.1 | ✓ | | | |
| ATLAS-SUSY-2016-32 [50] | HSCP | 31.6 | ✓ | ✓ | ✓ | |
| ATLAS-SUSY-2016-33 [293] | 2 OSSF $\ell$'s | 36.1 | ✓ | | | |
| ATLAS-SUSY-2017-01 [294] | $WH(bb)$, EWino | 36.1 | ✓ | | | |
| ATLAS-SUSY-2017-02 [295] | $0\ell$ + jets | 36.1 | ✓ | ✓ | | |
| ATLAS-SUSY-2017-03 [210] | multi-$\ell$ EWino | 36.1 | ✓ | | ✓ | |
| ATLAS-SUSY-2018-04 [57] | 2 hadronic taus | 139.0 | ✓ | | ✓ | JSON |
| ATLAS-SUSY-2018-06 [211] | 3 leptons, EWino | 139.0 | ✓ | ✓ | ✓ | |
| ATLAS-SUSY-2018-10 [206] | $1\ell$ + jets | 139.0 | ✓ | | ✓ | |
| ATLAS-SUSY-2018-12 [208] | $0\ell$ + jets | 139.0 | ✓ | ✓ | ✓ | |
| ATLAS-SUSY-2018-14 [43] | displaced leptons | 139.0 | | | ✓ | JSON |
| ATLAS-SUSY-2018-22 [207] | multi-jets | 139.0 | ✓ | | ✓ | |
| ATLAS-SUSY-2018-23 [209] | $WH(\gamma\gamma)$, EWino | 139.0 | ✓ | ✓ | | |
| ATLAS-SUSY-2018-31 [182] | $2b + 2H(bb)$ | 139.0 | ✓ | | ✓ | JSON |
| ATLAS-SUSY-2018-32 [242] | 2 OS leptons | 139.0 | ✓ | | | |
| ATLAS-SUSY-2019-08 [188] | $1\ell + H(bb)$, EWino | 139.0 | ✓ | | ✓ | JSON |

Table A.1: List of the 31 ATLAS Run 2 analyses and their types of results in the SModelS 2.1.0 database. Apart from the HSCP, DT and displaced lepton searches, all analyses require $E_T^{\text{miss}}$ in the final state (for conciseness omitted in the short descriptions).

| ID | Short Description | $\mathcal{L}$ [fb$^{-1}$] | UL$_{\text{obs}}$ | UL$_{\text{exp}}$ | EM | comb. |
|---|---|---|---|---|---|---|
| CMS-PAS-EXO-16-036 [227] | HSCP | 12.9 | ✓ | | | |
| CMS-PAS-SUS-16-052 [296] | ISR jet + soft $\ell$ | 35.9 | ✓ | | ✓ | Cov. |
| CMS-SUS-16-009 [297] | $0\ell$ + jets, top tag | 2.3 | ✓ | ✓ | | |
| CMS-SUS-16-032 [298] | 2 $b$- or 2 $c$-jets | 35.9 | ✓ | | | |
| CMS-SUS-16-033 [299] | $0\ell$ + jets | 35.9 | ✓ | ✓ | ✓ | |
| CMS-SUS-16-034 [300] | 2 OSSF leptons | 35.9 | ✓ | | | |
| CMS-SUS-16-035 [301] | 2 SS leptons | 35.9 | ✓ | | | |
| CMS-SUS-16-036 [53] | $0\ell$ + jets | 35.9 | ✓ | ✓ | | |
| CMS-SUS-16-037 [302] | $1\ell$ + jets with MJ | 35.9 | ✓ | | | |
| CMS-SUS-16-039 [303] | multi-$\ell$, EWino | 35.9 | ✓ | | | |
| CMS-SUS-16-041 [304] | multi-$\ell$ + jets | 35.9 | ✓ | | | |
| CMS-SUS-16-042 [305] | $1\ell$ + jets | 35.9 | ✓ | | | |
| CMS-SUS-16-043 [306] | $WH(bb)$, EWino | 35.9 | ✓ | | | |
| CMS-SUS-16-045 [307] | 2 $b$ + 2 $H(\gamma\gamma)$ | 35.9 | ✓ | | | |
| CMS-SUS-16-046 [308] | high-$p_T$ $\gamma$ | 35.9 | ✓ | | | |
| CMS-SUS-16-047 [309] | $\gamma$ + jets, high $H_T$ | 35.9 | ✓ | | | |
| CMS-SUS-16-049 [310] | $0\ell$ stop | 35.9 | ✓ | ✓ | | |
| CMS-SUS-16-050 [311] | $0\ell$ + top tag | 35.9 | ✓ | ✓ | | |
| CMS-SUS-16-051 [312] | $1\ell$ stop | 35.9 | ✓ | ✓ | | |
| CMS-SUS-17-001 [313] | $2\ell$ stop | 35.9 | ✓ | | | |
| CMS-SUS-17-003 [314] | 2 taus | 35.9 | ✓ | | | |
| CMS-SUS-17-004 [241] | EWino combination | 35.9 | ✓ | | | |
| CMS-SUS-17-005 [315] | $1\ell$ + jets, top tag | 35.9 | ✓ | ✓ | | |
| CMS-SUS-17-006 [316] | jets + boosted $H(bb)$ | 35.9 | ✓ | ✓ | | |
| CMS-SUS-17-009 [317] | SFOS leptons | 35.9 | ✓ | ✓ | | |
| CMS-SUS-17-010 [318] | $2\ell$ stop | 35.9 | ✓ | ✓ | | |
| CMS-SUS-18-002 [319] | $\gamma$ + ($b$-)jets, top tag | 35.9 | ✓ | ✓ | | |
| CMS-SUS-19-006 [320] | $0\ell$ + jets, MHT | 137.0 | ✓ | ✓ | | |
| CMS-SUS-19-009 [321] | $1\ell$ + jets, MHT | 137.0 | ✓ | | | |
| CMS-EXO-19-001 [46] | non-prompt jets | 137.0 | | | ✓ | |
| CMS-EXO-19-010 [47] | disappearing tracks | 101.0 | | | ✓ | |

Table A.2: List of the 31 CMS Run 2 analyses and their types of results in the SModelS 2.1.0 database. In the last column, "Cov." stands for covariance matrix. All CMS-SUS analyses require $E_T^{\text{miss}}$ in the final state (for conciseness omitted in the short descriptions).

## A.2 Recasting of the ATLAS-SUSY-2016-32 HSCP search

For the recasting of the 13 TeV ATLAS search for HSCPs [50], we follow the prescription provided in the auxiliary information of the publication. We consider the two signal regions `SR-1Cand-FullDet` and `SR-2Cand-FullDet` that use the time-of-flight measurement for reconstructing the mass of the HSCP. The signal region `SR-1Cand-FullDet` requires one (and only one) HSCP candidate that passes the 'tight' selection criterion while the signal region `SR-2Cand-FullDet` requires candidates satisfying the 'loose' selection criteria. In the analysis, two different triggers are considered, an $E_T^{\text{miss}}$ trigger and a muon trigger. Since we consider only constraints from HSCPs decaying outside the muon chamber, the recasting assumes the muon trigger.

The probabilities for an HSCP candidate to pass the muon trigger and satisfy the loose and tight selection criteria are given as a function of its velocity, $\beta$, and pseudorapidity, $\eta$, at generator level in the auxiliary information of [50]. We denote them by $P_{\text{trig}}$, $P_{\text{loose}}$ and $P_{\text{tight}}$, respectively. (Note that $P_{\text{tight}} = P_{\text{loose}}\, P_{\text{tight-promotion}}$.) Furthermore, for each of the two signal regions, the analysis considers four different choices for the cut on the reconstructed mass, $m_{\text{reco}}$. This gives a total of eight kinematic regions for which EMs are needed for the SModelS database.

We compute the probability for the reconstructed mass to lie above the respective cut by assuming $m_{\text{reco}}$ to be Gaussian distributed. The respective mean value and variance has been provided as a function of the true mass in the auxiliary information of [50]. We denote this probability with $P_{m_{\text{cut}}}$. We furthermore have to consider the probability that the given HSCP in an event traverses the full detector, $F_{\text{long}}$. The latter is given by

$$F_{\text{long}}(\beta,\eta) = \exp\left(-\frac{L(\eta)}{c\tau\gamma\beta}\right) \tag{A.1}$$

where $\gamma$ is the relativistic boost factor according to the velocity $\beta$ and $L(\eta)$ is the $\eta$-dependent travel length of the HSCP traversing the detector. To compute $L(\eta)$, we approximate the ATLAS detector by a cylinder with a radius of 12 m and a length of 46 m.

For a given event with two HSCP candidates (that have the same mass), we compute the overall probability that the event is triggered and selected in a given signal region with $m_{\text{reco}}$ above the respective cut by

$$\begin{aligned}\mathcal{P}^{\text{event}}_{\text{1Cand},m_{\text{cut}}} = \Big\{ & F^{(1)}_{\text{long}}\left(1-F^{(2)}_{\text{long}}\right)P^{(1)}_{\text{trig}}P^{(1)}_{\text{tight}} + F^{(2)}_{\text{long}}\left(1-F^{(1)}_{\text{long}}\right)P^{(2)}_{\text{trig}}P^{(2)}_{\text{tight}} \\ & + F^{(1)}_{\text{long}}F^{(2)}_{\text{long}}\left(P^{(1)}_{\text{trig}}+P^{(2)}_{\text{trig}}-P^{(1)}_{\text{trig}}P^{(2)}_{\text{trig}}\right) \\ & \times\left[P^{(1)}_{\text{tight}}\left(1-P^{(2)}_{\text{loose}}\right)+P^{(2)}_{\text{tight}}\left(1-P^{(1)}_{\text{loose}}\right)\right]\Big\}P_{m_{\text{cut}}}\end{aligned} \tag{A.2}$$

for `SR-1Cand-FullDet`, and

$$\mathcal{P}^{\text{event}}_{\text{2Cand},m_{\text{cut}}} = F^{(1)}_{\text{long}}F^{(2)}_{\text{long}}P^{(1)}_{\text{loose}}P^{(2)}_{\text{loose}} \times \left(P^{(1)}_{\text{trig}}+P^{(2)}_{\text{trig}}-P^{(1)}_{\text{trig}}P^{(2)}_{\text{trig}}\right)P^2_{m_{\text{cut}}} \tag{A.3}$$

for `SR-2Cand-FullDet`. From the above equations, if one HSCP particle is present in each event, only the `SR-1Cand-FullDet` is applicable and $\mathcal{P}^{\text{event}}_{\text{1Cand},m_{\text{cut}}} = F_{\text{long}}P_{\text{trig}}P_{\text{tight}}P_{m_{\text{cut}}}$.

We derive the EMs for the above-mentioned eight signal regions by generating events utilizing MadGraph5_aMC@NLO [62] for the hard scattering, and Pythia 8 [67] for showering and hadronization. We do not perform any detector simulation as the recasting is based on the kinematics of the HSCP at generator level. (In fact, hadronization only affects the isolation criterion requiring the sum of the track-$p_{\mathrm{T}}$ in a cone of $\Delta R = 0.2$ around the candidate's track to be below 5 GeV. However, the effect of the isolation criterion on the EMs is small.) For each simplified model parameter point in the EM, we generate $N = 2.5 \times 10^4$ events and compute the 'efficiency', $(\mathcal{A}\varepsilon)_{\mathrm{SR}}$, for a given signal region (SR) by

$$(\mathcal{A}\varepsilon)_{\mathrm{SR}} = \frac{1}{N} \sum_{i=1}^{N} \mathcal{P}^i_{\mathrm{SR}} \,. \tag{A.4}$$

We perform the computation of EMs for the 11 topologies depicted in Fig. A.1. In four of the topologies (THSCPM2b, THSCPM4, THSCPM6, and THSCPM9) only one branch contains an HSCP, while the other branch is assumed to terminate in a neutral particle. All other topologies have two HSCP candidates. As the search relies only on the HSCP itself, it is largely[1] insensitive to the type of SM particles being emitted in the decays: the dependence on the type of topology and BSM masses involved only enters through its effect on the kinematics of the HSCP. Similarly, for the four topologies with only one HSCP, the EMs are insensitive to the $E_T^{\mathrm{miss}}$(MET) branch except for the mass of the parent particle produced by the hard scattering as it affects the kinematics of the HSCP branch. Accordingly, we only specify the first particle of the MET branch indicated by a dashed line in the respective diagrams in Fig. A.1; this representation is meant to implicitly include all possible cascade decays.

For all topologies that involve up to two mass parameters, we take into account the explicit width dependence in the database. For the three topologies which involve a 2-step cascade decay (THSCPM5, THSCPM6, and THSCPM7) and, hence, three mass parameters, we employ the detector-stable limit only, keeping the EM grids to be three-dimensional at most. This is done to limit the size of the database pickle file.

The simplified model parameters are summarized in Table A.3. For the computation of the EMs, we use realizations of the topologies within the MSSM. The respective processes are also included in Table A.3. Note that for the four topologies with one HSCP only, we re-use the events of the respective process involving two HSCPs in our analysis by taking into account only one of the candidates at a time.

[1]The isolation criterion, in principle, introduces a dependence on the type of SM particle in the event. However, the reduction of efficiencies due to the isolation criterion is small, in particular, compared to expected uncertainties introduced by the approximations associated with the simplified model assumptions.

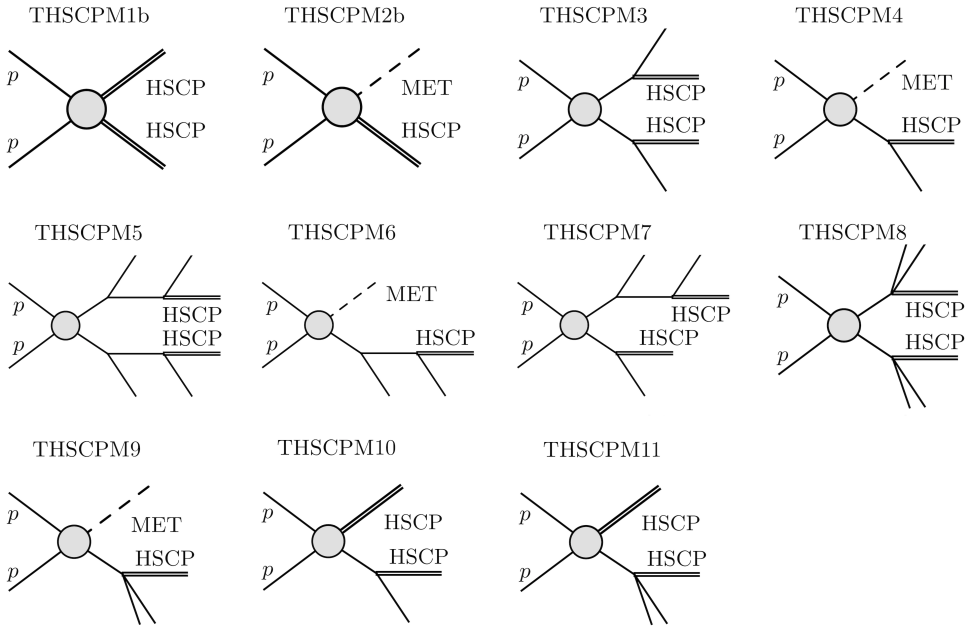


Figure A.1: Illustration of the 11 topologies for which we have generated EMs for the ATLAS-SUSY-2016-32 HSCP search.

| Topology name | free parameters | SUSY process |
|---|---|---|
| THSCPM1b | $m_{\text{HSCP}}, \Gamma_{\text{HSCP}}$ | $pp \to \tilde{\tau}\tilde{\tau}$ |
| THSCPM2b | $m_{\text{HSCP}}, \Gamma_{\text{HSCP}}$ | $pp \to \tilde{\tau}\tilde{\tau}^*$ |
| THSCPM3 | $m_{\text{prod}}, m_{\text{HSCP}}, \Gamma_{\text{HSCP}}$ | $pp \to \tilde{q}\tilde{q} \to \tilde{\chi}^{\pm}\tilde{\chi}^{\pm}$ |
| THSCPM4 | $m_{\text{prod}}, m_{\text{HSCP}}, \Gamma_{\text{HSCP}}$ | $pp \to \tilde{q}\tilde{q} \to \tilde{\chi}^{\pm}\tilde{\chi}^{\pm *}$ |
| THSCPM5 | $m_{\text{prod}}, m_{\text{int}}, m_{\text{HSCP}}$ | $pp \to \tilde{q}\tilde{q} \to \tilde{\chi}^0\tilde{\chi}^0 \to \tilde{\tau}\tilde{\tau}$ |
| THSCPM6 | $m_{\text{prod}}, m_{\text{int}}, m_{\text{HSCP}}$ | $pp \to \tilde{q}\tilde{q} \to \tilde{\chi}^0\tilde{\chi}^0 \to \tilde{\tau}\tilde{\tau}^*$ |
| THSCPM7 | $m_{\text{prod}}, m_{\text{int}}, m_{\text{HSCP}}$ | $pp \to \tilde{\chi}^0\tilde{\chi}_2^{\pm} \to \tilde{\tau}(\tilde{\chi}_1^{\pm} \to \tilde{\tau})$ |
| THSCPM8 | $m_{\text{prod}}, m_{\text{HSCP}}, \Gamma_{\text{HSCP}}$ | $pp \to \tilde{q}\tilde{q} \to \tilde{\tau}\tilde{\tau}$ |
| THSCPM9 | $m_{\text{prod}}, m_{\text{HSCP}}, \Gamma_{\text{HSCP}}$ | $pp \to \tilde{q}\tilde{q} \to \tilde{\tau}\tilde{\tau}^*$ |
| THSCPM10 | $m_{\text{prod}}, m_{\text{HSCP}}, \Gamma_{\text{HSCP}}$ | $pp \to \tilde{\chi}^{\pm}(\tilde{q} \to \tilde{\chi}^{\pm})$ |
| THSCPM11 | $m_{\text{prod}}, m_{\text{HSCP}}, \Gamma_{\text{HSCP}}$ | $pp \to \tilde{\chi}^{\pm}(\tilde{g} \to \tilde{\chi}^{\pm})$ |

Table A.3: Simplified model parameters and the SUSY processes used in the simulation of the 11 topologies shown in Fig. A.1. * Only one of the HSCP candidates is taken into account.

## A.3 Updating the micrOMEGAs v5.2.7.a interface

For using SModelS v2.1 with micrOMEGAs v5.2.7.a, the interface files
`micromegas_5.2.7.a/include/SMODELS.inc`,
`micromegas_5.2.7.a/sources/smodels.c`, and
`micromegas_5.2.7.a/Packages/SMODELS.makef`
should be replaced by the ones provided with this paper [278]. We also recommend to update the parameters file `micromegas_5.2.7.a/include/smodels_parameters.ini` with the one provided here.

In the micrOMEGAs main program, SModelS can then be called with the code snippet below (also included in the example main program on [278]).

```
#ifdef SMODELS
{ int status=0, smodelsOK=0;
  double Rvalue, Rexpected, SmoLsig, SmoLmax, SmoLSM;
  char analysis[50]={},topology[100]={},smodelsInfo[100];
  int LHCrun=LHC8|LHC13;  //  LHC8  - 8TeV; LHC13  - 13TeV;

  printf("\n\n===== LHC constraints with SModelS  =====\n\n");

#include "../include/SMODELS.inc" // SLHA interface with SModelS

  printf("SModelS %s \n",smodelsInfo);
  if(smodelsOK)
  { printf(" highest r-value = %.2E",Rvalue);

    if(Rvalue>0)
    { printf(" from %s, topology: %s ",analysis,topology);
      if(Rexpected>0)
      { printf("\n expected r = %.2E ",Rexpected);
        if(SmoLsig>0)
        { printf("\n -2log (L_signal, L_max, L_SM) = %.2E %.2E %.2E",
                  -2*log(SmoLsig),-2*log(SmoLmax),-2*log(SmoLSM)); }
      }
    }
    if(status==1) printf("\n excluded by SMS results");
    else if(status==0) printf("\n not excluded");
    else if(status==-1) printf("\n not not tested by results in SModelS database");
    printf("\n");
  } else system("cat smodels.err"); // problem: see smodels.err
}
#endif
```

For the `mssms.par` parameter point in the MSSM directory of micrOMEGAs, for instance, this will give

```
===== LHC constraints with SModelS  =====
```

```
found SM-like Higgs = h
writing mass block and decay tables ...
computing LHC cross sections ...
SLHA input file done.

SModelS v2.1.1 with database 2.1.0
 highest r-value = 1.07E+01 from ATLAS-SUSY-2018-22, topology: T2
 excluded by SMS results
```

If `#define CLEAN` is commented out in micrOMEGAs, the input and output files for SModelS (*i.e.* the `smodels.slha` file containing the mass spectrum, decay tables and cross sections, and the `smodels.slha.smodelsslha` file containing the SModelS results) will be kept. With standard settings, `smodels.slha.smodelsslha` reports all the excluding experimental results for excluded points but only the most constraining result for non-excluded points; to always have all applicable results listed, set

```
[slha-printer]
expandedOutput = True
```

in the `smodels_parameters.ini` file. Other options, like `testCoverage`, `combineSRs`, etc., can also be turned on/off via the `smodels_parameters.ini` file. Other output formats can be chosen via the

```
[printer]
outputType = ...
```

option. Available formats are `slha`, `summary`, `python`, `xml` and `stdout`; note however that `slha` output is always necessary for micrOMEGAs.

The updated interface to SModelS v2.1 (or higher) is included by default from micrOMEGAs v5.2.10 onward. Note that the exact SModelS version to be downloaded and included in micrOMEGAs `Packages/` is set in the `include/SMODELS.inc` file. Additional information is given in [200] and the manual shipped with the micrOMEGAs distribution.

# Appendix B

# MicrOMEGAs routines for co-scattering

For the computation of co-scattering, as in the case of $N$-component DM, the dark particles need to be divided into *sectors*, within each of which chemical equilibrium is observed. By default, this separation is defined by the number of ~ symbols in the beginning of the particle names. Thus, `~x1` and `~~x1` denote dark particles of two different sectors. Usually, the sector assignment corresponds to the charge of the discrete symmetry responsible for DM stability, cf. section 2 in the micrOMEGAs manual. However, in the absence of chemical equilibrium, the splitting into sectors needs to be done differently. To this end, the function

• `defThermalSet(n,particles_list)` moves all particles mentioned in *particles_list* to sector $n$. All particles that were assigned to sector $n$ before this command are returned to their default sectors specified by the number of ~ in the beginning of their names. Particles in the *particles_list* have to be separated by commas, and particle and anti-particle automatically belong to the same sector. By definition, sector 0 is the SM bath while sector $-1$ is used to define *feeble* particles which do not take part in freeze out. Such particles will be ignored when solving for the relic density. Sectors $n > 0$ are used for all other cases.

In general, `defThermalSet` can define a set which includes particles with different charges of the discrete symmetry group (different number of ~ symbols) — in particular the set could include $\mathcal{Z}_2$odd particles as well as SM particles. In this case the user must keep in mind that the abundance equations are solved for sectors $n > 0$ only. This entails that a $Z_2$ odd particle assigned to sector 0 will not be considered as potential DM candidate. The function returns an error code if *particles_list* contains a particle name which is not defined in the model.

• `printThermalSets()` prints the contents of all particle sets specified by `defThermalSet` on the screen.

To verify whether chemical equilibrium is reached in one sector, one can use

• `checkTE(n,T,mode,Beps)` which checks the condition for chemical equilibrium in the $n^{th}$ sector at temperature `T`. If mode=0, then both decay and co-scattering are taken into account. If mode=1 (2), then only decay (co-scattering) processes are taken into account. `checkTE` returns the minimal value of $\Gamma/H(T)$ obtained after testing all possible subsets of particles in sector $n$. The particle assignment corresponding to the minimal

value of $\Gamma/H(T)$ is printed on the screen. This value should be $\gg X_f$ to have chemical equilibrium; when this condition is satisfied, the correction to the abundance calculated *assuming* chemical equilibrium is approximately $\Delta Y/Y \approx X_f H/\Gamma$.

For the initialisation of the micrOMEGAs settings, one has to call the

• `sortOddParticles(outText)` command. It calculates all constrained model parameters, determines the number of sectors `Ncdm`, and fills the `Ncdm+1` dimensional array `McdmN` containing minimal masses in each sector. `McdmN[0]=0` corresponds to the SM sector.

• `YdmNEq(T,`$\alpha$`)` calculates the thermal equilibrium abundance at temperature `T` for particles of sector $\alpha$, where $\alpha$ has to be presented by a text label. For instance, `YdmNeq(T,"1")`.

• `vSigmaN(T,channel)` calculates the thermally averaged cross-section $\langle v\sigma\rangle$ in [pb·c] units. Here `channel` is a text code specifying the reaction, e.g., `vSigmaN(T,"1100")` for $1,1 \leftrightarrow 0,0$ processes.

Note that to calculate $\langle v\sigma\rangle$ for processes with incoming bath particles, micrOMEGAs uses a short cut: to avoid calculating $\bar{n}_0$ for bath particles, it substitutes $\bar{n}_0 = s$ in $\langle v\sigma_{2010}\rangle$ in Eq. (7.30). To compensate for this factor, the rate of co-scattering processes (expressed in GeV) is defined as

$$\Gamma_{2\to 1} = \texttt{vSigmaN(T,"2010")}\, s(T)/3.894\times 10^8\,. \tag{B.1}$$

To find the contribution of different processes to `vSigmaN`, one can call

• `vSigmaNCh(T,channel,Beps,&vsPb)` which returns an array of annihilation processes together with their relative contributions to the total annihilation cross-section. The cross-section is given by the return parameter `vsPb` in [pb·c] units. The elements of the array are sorted according to their weights, with the last element having weight=0. The structure of this array is identical to `vSigmaTCh` which was defined for one-DM models, see [198]. The input parameter `channel` is again written in text format. The memory allocated by `outCh` can be cleaned after usage with the command `free(outCh)`. The following lines of code give an example for how to use this function:

```
aChannel*outCh=vSigmaNCh(T, "1100", Beps, &vsPb);
for(int n=0;;n++)
{ if(outCh[n].weight==0) break;
  printf(" %.2E  %s %s -> %s %s\n", outCh[n].weight,
  outCh[n].prtcl[0],outCh[n].prtcl[1],outCh[n].prtcl[2],outCh[n].prtcl[3]);
}
free(outCh);
```

• `darkOmegaNTR(TR,Y,Beps,&err)` solves the equation of the thermal evolution of abundances starting from the initial temperature `TR` and returns the total $\Omega h^2$ in Eq. (7.34). The array `Y` has to contain the initial abundances at the temperature `TR`. After completion, `Y[k]` contains the abundances of sector $k-1$ at the temperature `Tend` defined by the user.[1] The parameter `TR` is assigned to the global variable `Tstart`.

The error code `err` is a binary code which can signal several problems simultaneously. The codes `1`, `2`, `3`, generated by the integration program `simpson`, mean

[1] By default `Tend` $= 10^{-3}$ GeV. However, when the decay contribution is important, it is preferable to choose a smaller value such as `Tend` $= 10^{-8}$ GeV.

```
1 - NaN in integrand;
2 - too deep recursion;
3 - loss of precision;
```

In general, these codes can be treated as warnings. Nonetheless it can be useful to check the calculation of integrals, which lead to problems, using e.g. the `gdb` debugging tools. For more detail, see also the explanation of the `simpson` routine in the micrOMEGAs manual. The code `128` signals a problem in the solution of the differential equation, for example this problem can arise when `TR` is too large.

• `darkOmegaN(Y,Beps,&err)` calls `darkOmegaNTR` to solve the equations of the thermal evolution of abundances in the temperature interval `[Tend,Tstart]`. In each sector, the function looks for the temperature $T_i$ where $Y_i(T_i) \approx Y_{eq}(T_i)$. `Tstart` is then defined as the minimum value of $T_i$. If `Tstart` is not found, then the error code 64 is generated and `darkOmegaN` returns NaN.

• `YdmN(T,`$\alpha$`)` presents the evolution of abundances for particles of sector $\alpha$ calculated by `darkOmegaN` or `darkOmegaNTR` for `T` $\in$ `[Tend,Tstart]`.

For the above functions, micrOMEGAs provides the possibility to selectively exclude part of the terms in the evolution equation. This is realised via the string `ExcludedFor2DM` which can be assigned specific keywords. The keyword `"DMdecay"` excludes decay processes which contribute to the DM evolution, while the keyword `"1100"` excludes $1,1 \leftrightarrow 0,0$ processes. To exclude co-scattering ($2,0 \leftrightarrow 1,0$ or $1,0 \leftrightarrow 2,0$ ) processes, set

```
ExcludedFor2DM="2010";
```

The behaviour is reset to default by `ExcludedFor2DM=NULL;` which means that all channels are included.

An option to calculate the decay width of any particle including the contributions from channels with different numbers of outgoing particle is also provided:

• `pWidthPref(particle_name, pref)` defines the switches for `pWidth`, the function which calculates the tree-level width and decay branching ratios for a given particle. By default, `pWidth` checks the value of the `useSLHAwidth` flag, if `useSLHAwidth!=0` and there are decay data in the loaded SLHA file, then `pWidth` returns the value stored in the file. Otherwise the widths are calculated at tree level including only channels with the minimal number of outgoing particles. `pref` allows to override this prescription for a single particle. It can take the values

0 – width is calculated using processes with minimal number of outgoing particles.

1 – width is calculated using processes with minimal and next to minimal number of outgoing particles excluding processes with s-channel resonances to avoid double counting.

2 – width is read from the SLHA file; if the SLHA file does not contain widths, it is calculated as in 0.

3 – width is read from the SLHA file; if the SLHA file does not contain widths, it is calculated as in 1.

4 – the default option of pWidth is used.

**Additional remarks:** In Eqs. (7.28) and (7.29) we have not included terms $\langle \sigma_{1000} v \rangle$ or $\langle \sigma_{2000} v \rangle$ since they do not appear in usual models where dark sector particles have a different discrete charge than SM particles.

Note also that, for the computation of co-scattering, the user defines which particles belong to sector 1 and sector 2. If a particle of dark sector 1 is wrongly assigned to dark sector 2 while it is in thermal equilibrium with sector 1 (for example if the singlet is in thermal equilibrium with the triplet), the two abundance equations will be solved and should give the same result as the single abundance equation, that is $Y(\text{heavier particles}) = 0$ and $Y(\text{lightest particle}) = Y$ of the single equation.

# Appendix C

# Résumé en français

## C.1 Introduction

Le Modéle Standard de la physique des particules est l'un des modèles théoriques le plus réussi de la physique moderne. En effet, nombreuses de ses prédictions sont en accord avec les observations expérimentales. Cependant, de nombreuse raisons laissent à penser que le Modèle Standard (MS) n'est pas complet. Parmi elles figurent des problèmes théoriques tel que l'unification des couplages de jauge, la masse des neutrinos, le problème de hiérarchie, etc. Le MS échoue aussi dans l'explication de certaines observations expérimentales comme la matière noire, la mesure du moment magnétique du muon, les anomalies des mésons B, etc. Toutes ces raisons poussent les physiciens à chercher la physique au-delà du MS, expérimentalement et théoriquement. La supersymétrie est l'un des modèles qui a été le plus étudié de par sa capacité à résoudre nombre de ces problèmes. Dans cette thèse, nous avons etudié le modèle singlet-triplet qui peut être vu comme une version simplifiée du modèle supersymétrique dans une certaine limite, ainsi que le modèle scotogénique.

Une autre partie importante de cette thèse est concentrée sur la réinterprétation des données du LHC et notamment le développement d'outils publiques à cette fin. L'implémentation de la combinaison des "signal regions (SRs)" dans les outils SModelS et MadAnalysis5 représente une part importante de ce travail. Des travaux de phénoménologie ont aussi été réalisés afin d'analyser l'impact physique de cette nouvelle fonctionnalité dans les deux outils.

Concernant la matière noire, de nombreuses particules candidates on été proposés. Le mécanisme le plus classique permettant d'expliquer comment la matière noire a été produite dans l'Univers primordial est le mécanisme de "freeze-out". Dans cette thèse, un mécanisme alternatif, celui de "coscattering", est étudié.

## C.2 Le Modèle Standard et au-delà

Ce chapitre présente en détail le MS de la physique des particules. Ce modèle est basé sur des symétries de jauge, une symétrie SU(3) de couleur qui décrit la force forte et deux symétries (SU(2) et SU(1)) qui fusionnent pour décrire l'unification de la force électromagnétique et de la force faible. L'ensemble des particules du MS peut être divisé en deux catégories, les fermions et les bosons. Les fermions peuvent être considérés

comme les particules de matière et se subdivisent en leptons et quarks. Les leptons sont constitués de trois générations, l'électron, le muon et le tau, ainsi que de trois générations de neutrinos. Pour chaque génération, les particules ont des propriétés identiques, excepté pour la masse. Ainsi, le muon et le tau sont deux particules identiques à l'électron, mais plus massives. Les quarks sont constitués de trois générations de type "up", up, charm et top, ainsi que trois générations de type "down", down, strange et bottom. Ce sont les quarks qui sont les constituants des protons et neutrons, eux-même constituants des noyaux atomiques.

Les bosons de jauge peuvent être considérés comme les particules porteuses des forces fondamentales, cela ne comprend donc pas le boson de Higgs qui est un boson scalaire. Les bosons de jauge comptent parmi eux le photon, porteur de la force électromagnétique, les boson $Z$ et $W^{\pm}$ porteurs de la force faible ainsi que les gluons porteurs de la force forte. Finalement, le boson de Higgs confère leurs masses aux particules du MS à travers le mécanisme de Higgs.

Plusieurs raisons poussent les physiciens à cherche la nouvelle physique expérimentalement et théoriquement. L'un des modèles qui a été le plus étudié est la supersymétrie, de par sa capacité à résoudre un grand nombre de ces problèmes. La supersymétrie consiste à étendre le MS avec une nouvelle symétrie agissant sur le spin. La supersymétrie associe donc à chaque fermion un nouveau superpartenaire bosonique et à chaque boson un nouveau superpartenaire fermionique. Un modèle supersymétrique contient donc au moins deux fois plus de particules que le MS. Cependant, certaines considérations techniques nécessitent de rajouter par exemple un second boson de Higgs. D'autres éléments sont à rajouter pour constituer un modéle supersymétrique consistant. Le MS supersymétrique minimal consiste à construire un modèle avec toutes les composantes minimales pour qu'il soit physiquement consistant. Par exemple, la supersymétrie implique que les particules et leur superpartenaires associés aient la même masse, ce qui est contredit par les expériences. Il est donc nécessaire d'introduire une brisure de supersymétrie ainsi que d'autres considérations techniques.

Dans ce chapitre sont aussi introduits deux autres modèles qui sont utilisés dans cette thèse. Le modèle Singlet-Triplet consiste à étendre le MS avec un singlet et un triplet de SU(2), tous deux étant fermioniques. Le singlet et le triplet peuvent respectivement être comparés à un bino et à un wino et l'analogie avec le modèle de split-supersymétrie peut être faite. Le faible mélange entre la composante neutre du triplet et le singlet implique des proprétés intéressantes pour l'étude de matière noire qui a été mené dans cette thèse. Finalement, le modèle scotogènique étend le MS avec un second doublet de Higgs et trois générations de neutrinos droits. En terme de matière noire, deux scénarios sont possible. Le candidat à la matière noire peut être fermionique, le neutrino droit le plus léger, ou bien scalaire, l'état neutre le plus léger du second doublet de Higgs.

## C.3 Réinterpreter les résultats du LHC

Le LHC, basé au CERN, est actuellement le collisionneur de particules le plus grand et le plus énergétique au monde avec une circonférence d'environ 27 km. Les protons, ou parfois des ions plus lourds, y sont accélérés en plusieurs étapes. Les accélérateurs conçus auparavant, atteignant des énergies plus faibles que le LHC, sont utilisés afin d'injecter des protons avec une énergie de 450 GeV dans l'anneau principal du LHC. Ils sont ensuite

accélérés jusqu'à atteindre une énergie de 7 TeV. Deux faisceaux circulent chacun dans une direction opposée, et chaque faisceau est constitué de paquets de protons. Les faisceaux circulent pendant plusieurs heures et sont progressivement mis en collisions jusqu'à ce qu'il soit nécessaire de réalimenter l'anneau principal en protons. Les quatre principales expériences sont placés à différents endroits sur l'anneau du LHC. Pour trois d'entre elles ATLAS, CMS et ALICE, les deux faisceaux sont mis en collision face à face. Les faisceaux sont focalisés à l'endroit du point d'intéraction à l'aide de champs magnétiques afin d'augmenter localement la fréquence des collisions. Pour l'expérience LHCb, un seul des deux faisceaux est mis en collision sur une cible fixe.

Dans cette thèse, seules les éxpériences ATLAS et CMS sont décrites en détail, puisque ce sont des expériences de physique généralistes et que ce sont leurs données qui ont été utilisées pour les travaux de cette thèse. Les deux détecteurs sont assez similaires et consistent en un ensemble de systèmes cylindriques multi-couches, placés autour de l'axe du faisceau à l'endroit où ceux-ci sont focalisés. La première couche du détecteur est un trajectographe qui permet de reconstruire la trajectoire des particules le traversant. Les systèmes suivant sont le calorimètre électromagnétique, pour détecter les particules chargés et les photons puis le calorimètre hadronique qui permet de détecter les jets issus des gerbes initiées par des quarks. Finalement, un spectromètre à muons est placé sur la couche la plus externe. Cet ensemble de détecteurs permet l'identification des particules, qui est une étape cruciale pour l'étude des collisions à hautes énergies. Un ensemble complexe de déclencheurs permet de réduire la fréquence des événements de collisions en ne gardant que des événements susceptible d'avoir un intérêt physique.

Les événements enregistrés après filtrage par les déclencheurs sont ensuite analysés. Pour cela les expérimentateurs se focalisent sur des états finaux bien définis, c'est-à-dire un ensemble donné de particules détéctées à l'issue d'une collision, associé à des conditions cinématiques, par example sur l'énergie transverse d'une particule. Une partie du programme de physique d'ATLAS et de CMS consiste à effectuer des mesures afin de vérifier les prédictions du MS. Par exemple, la masse du boson de Higgs est reconstruite en mesurant la distribution de la masse invariante d'un système de deux photons détectés à l'état final. Les mesures sont typiquement, comme ci-dessus, réalisées en calculant la distribution cinématique d'une certaine variable cinématique pour un état final donné. Une autre partie du programme de physique est la recherche de nouvelle physique. Les recherches sont effectuées pour les mêmes états finaux, mais contrairement aux mesures, l'objectif est de minimiser la contribution du MS et de maximiser un potentiel signal de nouvelle physique. Pour caractériser ce signal de nouvelle physique, des modèles simplifiés sont utilisés. Ce sont des modèles qui étendent le MS avec seulement deux ou trois nouvelles particules et qui considèrent des motifs de désintégration très simples. Ces modèles simplifiés permettent de caractériser la nouvelle physique de manière générique et de simplifier le travail d'analyse par les collaborations expérimentales. Lorsque aucune nouvelle physique n'est découverte, les données expérimentales sont utilisées afin de contraindre l'espace des paramètres du modèle simplifié associé à l'analyse en question. Pour cela, les expérimentateurs calculent à l'aide de simulations les prédictions du modèle simplifié et les comparent statistiquement avec les observations expérimentales.

Cependant, des modèles plus réalistes auront souvent des modes de désintégrations bien plus complexes, ce qui peut considérablement changer les contraintes obtenues. Réinterpréter les résultats du LHC est donc crucial afin d'utiliser le plein potentiel des

données expérimentales. Deux méthodes sont possible pour réaliser cette réinterprétation, réutiliser directement les données issues des analyses des modèles simplifiés ou bien reproduire les simulations effectuées par les collaborations expérimentales. SModelS est par exemple un outil publique permettant d'utiliser les résultats de modèles simplifiés sur des modèles génériques, sans avoir à reproduire les simulations. MadAnalysis5 est un exemple d'outil publique permettant de reproduire pour un modèle donné les simulations de collision et des effets des détecteurs afin d'obtenir les contraintes du LHC. Ces deux outils sont mentionnés dans les chapitres 4, 5 et 6 de cette thèse.

Finalement, la comparaison statistique des prédictions théoriques simulées avec les observations expérimentales est basée sur le test statistique d'hypothèse. Cependant, en physique des particules est utilisée une méthode dédiée appelée l'approche $CL_s$, qui est une variante de la méthode de la $p$-value. Elle consiste brièvement à calculer le ratio de deux $p$-values.

## C.4 Combinaison des "signal regions" avec des fonctions de vraisemblance complètes et simplifiées dans MadAnalysis5

Ce chapitre présente la mise en œuvre et l'utilisation de la combinaison de "signal regions (SRs)" dans MadAnalysis5 avec deux méthodes : une interface avec le code `pyhf` utilisant des fonction de vraisemblances complètes ("full likelihoods") sous un format `JSON` fourni par la collaboration ATLAS, et un calcul de vraisemblance simplifié (simplified likelihoods) utilisant des matrices de covariance fournies par la collaboration CMS. Actuellement, quatre analyses ATLAS et cinq analyses CMS sont implémentées dans la base de données d'analyses publiques (PAD) de MadAnalysis5 pour lesquelles cette nouvelle fonctionnalité peut être exploitée.

Nous avons démontré le gain associé en terme de contraintes pour les études de réinterprétation de deux façons. Premièrement, nous avons reproduit les limites de masse sur des scénarios de modèles simplifiés tels que publiés par les collaborations ATLAS et CMS pour les analyses considérées. Deuxièmement, nous avons effectué une étude de cas d'un scénario MSSM réaliste dans lequel les stops et les sbottoms ont une variété de modes de désintégration en charginos et neutralinos. Nos résultats montrent que la combinaison statistique de SRs disjointes dans les études de réinterprétation, en utilisant plus de données d'une analyse, donne des résultats plus fiables et plus robustes que l'approche "best-SR", qui n'utilise que la SR la plus sensible, pour l'interprétation statistique d'un signal hypothétique.

La prochaine ligne de développement est la combinaison statistique des résultats de différentes analyses indépendantes, une fonctionnalité qui est déjà disponible dans SModelSv2.2, et qui devrait bientôt être adoptée dans MadAnalysis5. De plus, afin de l'externaliser et de la mettre à la disposition de l'ensemble de la communauté HEP, les équipes de SModelS et de MadAnalysis5 travaillent actuellement ensemble à la création d'une boîte à outils universelle pour la manipulation des statistiques dans le contexte des études de réinterprétation. Comme discuté en détail dans [114], l'utilité des "full likelihoods" va bien au-delà de l'application pour les combinaisons de SRs, qui est

le sujet de cet article. En effet, ils ouvrent un tout nouveau domaine pour la préservation et la réutilisation des analyses.

## C.5 Une interface pyhf dans SModelS

Le sujet de cette section est également lié à la combinaison de SRs mais dans l'outil SModelS. Il y est présenté une interface pour `pyhf` dans SModelS, permettant d'utiliser les "full likelihoods" fournies par ATLAS sous la forme de fichiers `JSON`. Au moment de réaliser ce travail, la base de données de SModelS a été étendue avec les résultats et les fichiers `JSON` correspondants aux trois nouvelles analyses SUSY d'ATLAS [57, 182, 188] avec la luminosité maximum du Run 2 (139 $\text{fb}^{-1}$) du LHC.

L'impact physique a été démontré pour ces trois analyses, en comparant directement les résultats de SModelS avec les résultats officiels d'ATLAS pour les modèles simplifiés correspondants. Ces comparaisons montrent à quel point la combinaisons des SRs améliorent la précision des contraintes par rapport à l'approche best-SR. En effet, selon l'analyse, l'approche best-SR donne des exclusions soit trop fortes soit trop faibles. Dans les deux cas, la combinaison des SRs donne des résultats bien plus proches des résultats officiels d'ATLAS. De nombreuses analyses avec des "full likelihoods" ont depuis été publiés par la collaboration ATLAS et leur implémentation est toujours en cours dans SModelS.

Enfin, les discussions techniques avec l'équipe `pyhf` ont été gérées via le système de suivi des problèmes de github, voir par exemple `https://github.com/scikit-hep/pyhf/issues/620`, et sont donc transparentes et ouvertes à tous.

## C.6 Contraindre la nouvelle physique avec SModelS version 2

La version 2 de SModelS permet une description plus détaillée et plus souple des modèles simplifiés. Concrètement, grâce à l'introduction d'une classe "particules" dans le code, la simple liste de masses de particules BSM utilisée dans SModelS v1 a été remplacée par des objets complets, qui peuvent contenir des attributs tels que la masse, la largeur de désintégration, le spin, la charge électrique, etc. Par exemple, cela permet un traitement affiné des résultats dépendant du spin. Plus important encore pour cet article, cela permet d'inclure une grande variété de recherches de particules à longues durée de vie (LLPs) sous la forme de résultats dépendant de la largeur de désintégration. Étant donné un modèle en entrée, SModelSv2 peut donc fournir simultanément des résultats prompts et à longue durée de vie dans la même exécution. Les recherches de LLPs actuellement implémentées incluent des recherches de particules stables chargées et lourdes (HSCP), de traces qui disparaissent (disappearing tracks), de jets déplacés et de leptons déplacés. Au total, les résultats de 62 recherches ATLAS et CMS à 13 TeV sont implémentés dans la base de données actuelle, dont 7 résultats LLPs.

Les capacités physiques de SModelSv2 ont été démontrées en analysant les contraintes sur les scalaires chargés à longue durée de vie dans le modèle scotogènique pour deux scénarios : i) un candidat de matière noire scalaire et ii) un candidat de matière noire fermionique.

En considérant le scalaire chargé comme l'état $\mathcal{Z}_2$-impair le plus léger, les recherches HSCP contraignent sa masse jusqu'à environ 500-600 GeV pour des différences de masses inférieures au seuil du pion. Cela couvre la gamme favorisée par les considérations de matière noire pour de si petites différences de masses. Pour des différences de masses légèrement supérieurs à $m_{\pi^\pm}$, qui se traduisent par des longueurs de désintégration de l'ordre de 0,1-1 m, les recherches de traces qui disparaissent effectuées par ATLAS avec 36 fb$^{-1}$ (CMS avec 101 fb$^{-1}$) peuvent exclure des masses de scalaires chargés jusqu'à environ 220 (350) GeV, en fonction de la durée de vie.

Pour le candidat de matière noire fermionique dans le modèle scotogènique, la densité relique mesurée peut être expliquée par le mécanisme de freeze-in. Le petit couplage de Yukawa requis pour le neutrino stérile le plus léger confère naturellement une longue durée de vie à l'état $\mathcal{Z}_2$-impair le plus léger dans une grande région de l'espace des paramètres cosmologiquement valide, où la masse de la matière noire varie de l'échelle du keV à celle du GeV. En plus des recherches de HSCP qui sont sensibles aux grandes durées de vie (correspondant à des masses de matière noire dans la gamme des MeV à GeV), nous avons appliqué les contraintes des recherches de leptons déplacés qui sont plus sensibles aux plus petites masses de matière noire, inférieures à quelques dizaines de keV. Les deux types de recherche peuvent exclure les scalaires chargés à longue durée de vie dont la masse peut atteindre environ 800 GeV dans ce scénario. Pour la recherche de leptons déplacés, nous avons également démontré l'importance de la combinaison des SRs, comme le permet la "full likelihood" fourni par ATLAS pour cette analyse.

Dans un deuxième temps, nous avons analysé les contraintes sur le secteur electroweakino (EW-ino) du MSSM, en détaillant l'interaction des recherches prompts et à longue durée de vie, ainsi que l'interaction des contraintes des collisionneurs et de matière noire. Nous avons démontré dans quelle mesure les limites de la masse EW-ino d'ATLAS et de CMS, qui supposent un bino pur $\chi_1^0$ et un wino pur $\chi_1^\pm$ et $\chi_2^0$ (ce dernier afin de maximiser la section efficace de production) sont affaiblies dans le cas général. Dans ce cas, les désintégrations de $\chi_2^0$ en $\chi_1^0 Z$ ou $\chi_1^0 h$ se font concurrence si les deux sont cinématiquement autorisées. Il est cependant important de noter que pour des paramètres de masse EW-ino généraux comme dans notre analyse, les sections efficaces de production sont typiquement plus petites que celles supposées par les collaborations, réduisant ainsi la région exclue.

En ce qui concerne l'interaction avec les contraintes de matière noire, les scénarios EW-ino exclus par les recherches prompts sont presque entièrement limités à ceux où la matière noire est un bino et sont caractérisés par une surabondance de matière noire significative. Seuls quelques points avec une matière noire mixte, conduisant à une petite densité relique, échappent à cette conclusion et aux limites de détection directe de matière noire. Les recherches de traces qui disparaissent, d'autre part, sont sensibles au cas où la matière noire est un wino avec $\Omega h^2 \lesssim 10^{-2}$. Dans ce cas, la densité relique supprimée conduit également à une section efficace de détection directe faible, évitant la limite Xenon1T de plusieurs ordres de grandeurs, à tel point les contraintes des collisionneurs sont plus sensibles à ce scénario.

De nombreux travaux sont prévus pour étendre et améliorer l'utilisation des résultats des modèles simplifiés. Le code de SModelS et la base de données continueront à évoluer.

## C.7 Matière noire et contraintes du LHC

Dans les scénarios où les couplages de matière noire sont très faibles et où les différences de masse entre la matière noire et d'autres particules du secteur sombre sont faibles, la "coscattering" ou "conversion-driven freeze-out" peut être le mécanisme dominant de production de matière noire. Ce mécanisme se caractérise par le fait que le "freeze-out" a lieu hors de l'équilibre chimique. L'auto-annihilation de la matière noire est trop inefficace pour atteindre $\Omega h^2 \approx 0.1$. Au lieu de cela, les processus de diffusion inélastique de type $\chi\,\mathrm{MS} \leftrightarrow \psi\,\mathrm{MS}$ sont principalement responsables de la formation de matière noire. De plus, les désintégrations et les désintégrations inverses des particules du secteur sombre, comme $\psi \leftrightarrow \chi\,\mathrm{MS}$, doivent également être prises en compte dans les termes de conversion des équations de Boltzmann.

Nous avons présenté la première inclusion de ce mécanisme dans un outil public de matière noire, micrOMEGAs. Le traitement numérique s'appuie fortement sur la machinerie pour la matière noire multi-composantes de micrOMEGAs car il nécessite de résoudre au moins deux équations de Boltzmann séparées, une pour chaque ensemble de particules sombres en équilibre thermique. Pour illustrer à la fois les nouvelles capacités de micrOMEGAs et les implications phénoménologiques du régime de "coscattering", nous avons réalisé une étude de cas pour le modèle Singlet-Triplet fermionique, STFM. Ce modèle étend le MS avec deux multiplets électrofaibles, un singlet $\chi$ et un triplet $\psi$, qui sont tous deux impairs sous une nouvelle symétrie $\mathcal{Z}_2$, alors que les particules du SM sont $\mathcal{Z}_2$-paires. Le singlet $\chi$ est le candidat à la matière noire ; il a des couplages très faibles induits par un petit mélange avec le triplet. L'analyse numérique s'est concentrée sur la transition entre les régimes de co-annihilation et de co-scattering, et a montré que ce dernier peut ouvrir une nouvelle région dans l'espace des paramètres du modèle.

Les états triplets chargés, $\psi^\pm$, ont une durée de vie typiquement longue dans la région de co-scattering, ce qui conduirait à des signatures distinctes dans les collisionneurs. En utilisant SModelSv2.2.0 pour évaluer les contraintes actuelles du LHC, nous avons constaté que les recherches de traces qui disparaissent excluent des masses de matière noire jusqu'à $m_\chi \approx 200$ GeV dans la région de transition entre la coannihilation et le "coscattering", et jusqu'à $m_\chi \approx 450$ GeV pour les très petits $\lambda$, où le "coscattering" domine. Un calcul précis de la différence de masse interne des états de type triplet ainsi que l'inclusion des désintégrations $\tilde{\psi}^\pm \to \tilde{\chi}\pi^\pm$ sont importants à cette fin.

L'accomplissement de ce travail a donné lieu à la publication d'une nouvelle version de micrOMEGAs, v5.3.35, qui est disponible publiquement à `https://lapth.cnrs.fr/micromegas/`. Elle comprend l'implémentation du modèle STFM avec un fichier `README` expliquant son utilisation, et un programme de démonstration (`demo.c`) illustrant certaines des nouvelles fonctionnalités présentées dans ce travail. Il comprend également une interface mise à jour de SModelSv2.2. Les nouvelles routines de micrOMEGAs pertinentes pour le co-scattering sont décrites en détail en annexe.

Une mise en garde importante est que, jusqu'à présent, micrOMEGAs s'appuie uniquement sur les équations de Boltzmann intégrées sur l'impulsion. Pour un calcul précis de la densité relique de matière noire, y compris les effets d'un découplage cinétique anticipé, les équations de Boltzmann dépendantes de l'impulsion doivent être résolues. Ceci est laissé pour un travail futur.

## C.8 Conclusions

En physique des particules, la quête de nouvelles particules est un domaine dynamique. Les expérimentateurs et les théoriciens poursuivent cette quête avec leurs propres outils. Des idées de nouvelles recherches au LHC surgissent constamment. La réinterprétation des résultats du LHC par les phénoménologues est cruciale afin d'utiliser tout le potentiel des recherches de nouvelle physique. Une communication étroite entre les deux communautés est donc très importante pour que le domaine puisse continuer à progresser.

La collaboration ATLAS a récemment commencé à publier des "full likelihoods" en complément de ses résultats. C'est la première fois que des informations aussi détaillées sont fournies publiquement et cela permet la réutilisation et la préservation des résultats à long terme. Les théoriciens peuvent ainsi utiliser les données expérimentales dans une grande variété d'autres contextes théoriques, et éventuellement trouver des indices de nouvelle physique, ce qui nous guidera vers de nouvelles stratégies de recherche de nouvelle physique au LHC.

Par ailleurs, la recherche de matière noire est un sujet bouillonnant depuis plusieurs décennies, et de nombreuses idées ont été étudiées et documentées. Cependant, plusieurs possibilités n'ont pas encore été pleinement explorées, comme le mécanisme de "coscattering". Puisque nous ne pouvons pas savoir quel mécanisme ou modèle la nature a choisi, toutes les possibilités doivent être étudiées et nous pouvons seulement espérer que ceci ménera a une nouvelle découverte qui pourrait révéler la nature de la matière noire dans un avenir plus ou moins proche.

# Bibliography


[1] S. Berryman, Ancient Atomism, in: E. N. Zalta (Ed.), The Stanford Encyclopedia of Philosophy, Winter 2016 Edition, Metaphysics Research Lab, Stanford University, 2016.

[2] G. Aad, et al., Observation of a new particle in the search for the Standard Model Higgs boson with the ATLAS detector at the LHC, Phys. Lett. B 716 (2012) 1–29. arXiv:1207.7214, doi:10.1016/j.physletb.2012.08.020.

[3] S. Chatrchyan, et al., Observation of a New Boson at a Mass of 125 GeV with the CMS Experiment at the LHC, Phys. Lett. B 716 (2012) 30–61. arXiv:1207.7235, doi:10.1016/j.physletb.2012.08.021.

[4] F. Englert, R. Brout, Broken symmetry and the mass of gauge vector mesons, Phys. Rev. Lett. 13 (1964) 321–323. doi:10.1103/PhysRevLett.13.321.

[5] P. W. Higgs, Broken symmetries and the masses of gauge bosons, Phys. Rev. Lett. 13 (1964) 508–509. doi:10.1103/PhysRevLett.13.508.

[6] G. S. Guralnik, C. R. Hagen, T. W. B. Kibble, Global conservation laws and massless particles, Phys. Rev. Lett. 13 (1964) 585–587. doi:10.1103/PhysRevLett.13.585.

[7] J. Ellis, Higgs Physics, in: 2013 European School of High-Energy Physics, 2015, pp. 117–168. arXiv:1312.5672, doi:10.5170/CERN-2015-004.117.

[8] G. Aad, et al., Measurement of the high-mass Drell–Yan differential cross-section in pp collisions at sqrt(s)=7 TeV with the ATLAS detector, Phys. Lett. B 725 (2013) 223–242. arXiv:1305.4192, doi:10.1016/j.physletb.2013.07.049.

[9] G. Aad, et al., Measurement of angular correlations in Drell-Yan lepton pairs to probe Z/gamma* boson transverse momentum at sqrt(s)=7 TeV with the ATLAS detector, Phys. Lett. B 720 (2013) 32–51. arXiv:1211.6899, doi:10.1016/j.physletb.2013.01.054.

[10] V. Khachatryan, et al., Measurements of differential and double-differential Drell-Yan cross sections in proton-proton collisions at 8 TeV, Eur. Phys. J. C 75 (4) (2015) 147. arXiv:1412.1115, doi:10.1140/epjc/s10052-015-3364-2.

[11] Y. Fukuda, et al., Evidence for oscillation of atmospheric neutrinos, Phys. Rev. Lett. 81 (1998) 1562–1567. arXiv:hep-ex/9807003, doi:10.1103/PhysRevLett.81.1562.

[12] Q. R. Ahmad, et al., Measurement of the rate of $\nu_e + d \to p + p + e^-$ interactions produced by $^8$B solar neutrinos at the Sudbury Neutrino Observatory, Phys. Rev. Lett. 87 (2001) 071301. arXiv:nucl-ex/0106015, doi:10.1103/PhysRevLett.87.071301.

[13] Q. R. Ahmad, et al., Direct evidence for neutrino flavor transformation from neutral current interactions in the Sudbury Neutrino Observatory, Phys. Rev. Lett. 89 (2002) 011301. arXiv:nucl-ex/0204008, doi:10.1103/PhysRevLett.89.011301.

[14] R. D. Peccei, H. R. Quinn, CP conservation in the presence of pseudoparticles, Phys. Rev. Lett. 38 (1977) 1440–1443. doi:10.1103/PhysRevLett.38.1440.

[15] R. D. Peccei, H. R. Quinn, Constraints imposed by CP conservation in the presence of pseudoparticles, Phys. Rev. D 16 (1977) 1791–1797. doi:10.1103/PhysRevD.16.1791.

[16] S. P. Martin, A Supersymmetry primer, Adv. Ser. Direct. High Energy Phys. 18 (1998) 1–98. arXiv:hep-ph/9709356, doi:10.1142/9789812839657_0001.

[17] P. A. M. Dirac, R. H. Fowler, The quantum theory of the electron. part ii, Proceedings of the Royal Society of London. Series A, Containing Papers of a Mathematical and Physical Character 118 (779) (1928) 351–361. doi:10.1098/rspa.1928.0056.

[18] J. Schwinger, On quantum-electrodynamics and the magnetic moment of the electron, Phys. Rev. 73 (1948) 416–417. doi:10.1103/PhysRev.73.416.

[19] R. L. Garwin, L. M. Lederman, M. Weinrich, Observations of the failure of conservation of parity and charge conjugation in meson decays: the magnetic moment of the free muon, Phys. Rev. 105 (1957) 1415–1417. doi:10.1103/PhysRev.105.1415.

[20] G. W. Bennett, et al., Final Report of the Muon E821 Anomalous Magnetic Moment Measurement at BNL, Phys. Rev. D 73 (2006) 072003. arXiv:hep-ex/0602035, doi:10.1103/PhysRevD.73.072003.

[21] B. Abi, et al., Measurement of the Positive Muon Anomalous Magnetic Moment to 0.46 ppm, Phys. Rev. Lett. 126 (14) (2021) 141801. arXiv:2104.03281, doi:10.1103/PhysRevLett.126.141801.

[22] T. Aoyama, et al., The anomalous magnetic moment of the muon in the Standard Model, Phys. Rept. 887 (2020) 1–166. arXiv:2006.04822, doi:10.1016/j.physrep.2020.07.006.

[23] D. Lancierini, Updated measurement of $R_K$ at LHCbarXiv:2105.10303.

[24] R. Aaij, et al., Test of lepton universality with $B^0 \to K^{*0}\ell^+\ell^-$ decays, JHEP 08 (2017) 055. arXiv:1705.05802, doi:10.1007/JHEP08(2017)055.

[25] V. C. Rubin, W. K. Ford, N. Thonnard, Rotational properties of 21 sc galaxies with a large range of luminosities and radii, from ngc 4605 /r = 4kpc/ to ugc 2885 /r = 122 kpc/, The Astrophysical Journal 238 (1980) 471–487.

[26] K. Freese, Review of Observational Evidence for Dark Matter in the Universe and in upcoming searches for Dark Stars, EAS Publ. Ser. 36 (2009) 113–126. arXiv:0812.4005, doi:10.1051/eas/0936016.

[27] N. Aghanim, et al., Planck 2018 results. VI. Cosmological parameters, Astron. Astrophys. 641 (2020) A6, [Erratum: Astron.Astrophys. 652, C4 (2021)]. arXiv:1807.06209, doi:10.1051/0004-6361/201833910.

[28] F. Brümmer, Coscattering in next-to-minimal dark matter and split supersymmetry, JHEP 01 (2020) 113. arXiv:1910.01549, doi:10.1007/JHEP01(2020)113.

[29] E. Ma, Verifiable radiative seesaw mechanism of neutrino mass and dark matter, Phys. Rev. D 73 (2006) 077301. arXiv:hep-ph/0601225, doi:10.1103/PhysRevD.73.077301.

[30] J. Kubo, E. Ma, D. Suematsu, Cold Dark Matter, Radiative Neutrino Mass, $\mu \to e\gamma$, and Neutrinoless Double Beta Decay, Phys. Lett. B 642 (2006) 18–23. arXiv:hep-ph/0604114, doi:10.1016/j.physletb.2006.08.085.

[31] E. O. Lawrence, M. S. Livingston, The production of high speed light ions without the use of high voltages, Phys. Rev. 40 (1932) 19–35. doi:10.1103/PhysRev.40.19. URL https://link.aps.org/doi/10.1103/PhysRev.40.19

[32] N. Anh Ky, N. T. H. Van, Was the Higgs Boson Discovered?, Commun. in Phys. 25 (1) (2015) 1–20. arXiv:1503.08630, doi:10.15625/0868-3166/25/1/5941.

[33] R. Vanden Broeck, THE CERN ACCELERATOR COMPLEX. Complexe des accélérateurs du CERN (Sep 2019).
URL https://cds.cern.ch/record/2693837

[34] C. Lippmann, Particle identification, Nucl. Instrum. Methods Phys. Res., A 666 (2011) 148–172. 61 p. arXiv:1101.3276.

[35] The ATLAS Collaboration, Trigger Menu in 2016, Tech. rep., CERN, Geneva (Jan 2017).
URL https://cds.cern.ch/record/2242069

[36] G. Aad, et al., Search for chargino–neutralino pair production in final states with three leptons and missing transverse momentum in $\sqrt{s} = 13$ TeV pp collisions with the ATLAS detector, Eur. Phys. J. C 81 (12) (2021) 1118. arXiv:2106.01676, doi:10.1140/epjc/s10052-021-09749-7.

[37] E. Tolley, Dark Matter searches with Mono-X signatures at the ATLAS experiment, PoS DIS2016 (2016) 107. doi:10.22323/1.265.0107.

[38] The ATLAS Collaboration, Search for new light resonances decaying to jet pairs and produced in association with a photon or a jet in proton-proton collisions at $\sqrt{s} = 13$ TeV with the ATLAS detector, Tech. rep., CERN, Geneva (2016).
URL https://cds.cern.ch/record/2206221

[39] The CMS Collaboration, Search for light vector resonances decaying to a quark pair produced in association with a jet in proton-proton collisions at $\sqrt{s} = 13$ TeV, Tech. rep., CERN, Geneva (2017).
URL https://cds.cern.ch/record/2264843

[40] A. R. Raklev, Massive Metastable Charged (S)Particles at the LHC, Mod. Phys. Lett. A 24 (2009) 1955–1969. arXiv:0908.0315, doi:10.1142/S0217732309031648.

[41] D. Curtin, et al., Long-Lived Particles at the Energy Frontier: The MATHUSLA Physics Case, Rept. Prog. Phys. 82 (11) (2019) 116201. arXiv:1806.07396, doi:10.1088/1361-6633/ab28d6.

[42] A. De Roeck, Searching for long-lived particles at the Large Hadron Collider and beyond, Phil. Trans. Roy. Soc. Lond. A 377 (2161) (2019) 20190047. doi:10.1098/rsta.2019.0047.

[43] G. Aad, et al., Search for Displaced Leptons in $\sqrt{s} = 13$ TeV $pp$ Collisions with the ATLAS Detector, Phys. Rev. Lett. 127 (5) (2021) 051802. arXiv:2011.07812, doi:10.1103/PhysRevLett.127.051802.

[44] M. Aaboud, et al., Search for long-lived, massive particles in events with displaced vertices and missing transverse momentum in $\sqrt{s} = 13$ TeV $pp$ collisions with the ATLAS detector, Phys. Rev. D97 (5) (2018) 052012. arXiv:1710.04901, doi:10.1103/PhysRevD.97.052012.

[45] G. Aad, et al., Search for long-lived, massive particles in events with a displaced vertex and a muon with large impact parameter in $pp$ collisions at $\sqrt{s} = 13$ TeV with the ATLAS detector, Phys. Rev. D 102 (3) (2020) 032006. arXiv:2003.11956, doi:10.1103/PhysRevD.102.032006.

[46] A. M. Sirunyan, et al., Search for long-lived particles using nonprompt jets and missing transverse momentum with proton-proton collisions at $\sqrt{s} = 13$ TeV, Phys. Lett. B797 (2019) 134876. arXiv:1906.06441, doi:10.1016/j.physletb.2019.134876.

[47] A. M. Sirunyan, et al., Search for disappearing tracks in proton-proton collisions at $\sqrt{s} = 13$ TeV, Phys. Lett. B 806 (2020) 135502. arXiv:2004.05153, doi:10.1016/j.physletb.2020.135502.

[48] M. Aaboud, et al., Search for long-lived charginos based on a disappearing-track signature in pp collisions at $\sqrt{s} = 13$ TeV with the ATLAS detector, JHEP 06 (2018) 022. arXiv:1712.02118, doi:10.1007/JHEP06(2018)022.

[49] G. Aad, et al., Search for long-lived charginos based on a disappearing-track signature using 136 fb$^{-1}$ of pp collisions at $\sqrt{s} = 13$ TeV with the ATLAS detector, Eur. Phys. J. C 82 (7) (2022) 606. arXiv:2201.02472, doi:10.1140/epjc/s10052-022-10489-5.

[50] M. Aaboud, et al., Search for heavy charged long-lived particles in the ATLAS detector in 36.1 fb$^{-1}$ of proton-proton collision data at $\sqrt{s}$ = 13 TeV, Phys. Rev. D99 (9) (2019) 092007. arXiv:1902.01636, doi:10.1103/PhysRevD.99.092007.

[51] S. Chatrchyan, et al., Searches for long-lived charged particles in pp collisions at $\sqrt{s}$=7 and 8 TeV, JHEP 07 (2013) 122. arXiv:1305.0491, doi:10.1007/JHEP07(2013)122.

[52] V. Khachatryan, et al., Searches for electroweak production of charginos, neutralinos, and sleptons decaying to leptons and W, Z, and Higgs bosons in pp collisions at 8 TeV, Eur.Phys.J. C74 (9) (2014) 3036. arXiv:1405.7570, doi:10.1140/epjc/s10052-014-3036-7.

[53] A. M. Sirunyan, et al., Search for new phenomena with the $M_{\mathrm{T2}}$ variable in the all-hadronic final state produced in proton–proton collisions at $\sqrt{s}$ = 13 TeV, Eur. Phys. J. C77 (10) (2017) 710. arXiv:1705.04650, doi:10.1140/epjc/s10052-017-5267-x.

[54] J. Alimena, et al., Searching for long-lived particles beyond the Standard Model at the Large Hadron Collider, J. Phys. G 47 (9) (2020) 090501. arXiv:1903.04497, doi:10.1088/1361-6471/ab4574.

[55] D. Acosta, et al., Review of opportunities for new long-lived particle triggers in Run 3 of the Large Hadron ColliderarXiv:2110.14675.

[56] D. Alves, Simplified Models for LHC New Physics Searches, J. Phys. G 39 (2012) 105005. arXiv:1105.2838, doi:10.1088/0954-3899/39/10/105005.

[57] G. Aad, et al., Search for direct stau production in events with two hadronic $\tau$-leptons in $\sqrt{s}$ = 13 TeV $pp$ collisions with the ATLAS detector, Phys. Rev. D 101 (3) (2020) 032009. arXiv:1911.06660, doi:10.1103/PhysRevD.101.032009.

[58] Asymptotic freedom in parton language, Nuclear Physics B 126 (2) (1977) 298–318. doi:https://doi.org/10.1016/0550-3213(77)90384-4.

[59] Y. L. Dokshitzer, Calculation of the Structure Functions for Deep Inelastic Scattering and e+ e- Annihilation by Perturbation Theory in Quantum Chromodynamics., Sov. Phys. JETP 46 (1977) 641–653.

[60] V. N. Gribov, L. N. Lipatov, Deep inelastic e p scattering in perturbation theory, Sov. J. Nucl. Phys. 15 (1972) 438–450.

[61] A. Buckley, J. Ferrando, S. Lloyd, K. Nordström, B. Page, M. Rüfenacht, M. Schönherr, G. Watt, LHAPDF6: parton density access in the LHC precision era, Eur. Phys. J. C 75 (2015) 132. arXiv:1412.7420, doi:10.1140/epjc/s10052-015-3318-8.

[62] J. Alwall, R. Frederix, S. Frixione, V. Hirschi, F. Maltoni, O. Mattelaer, H. S. Shao, T. Stelzer, P. Torrielli, M. Zaro, The automated computation of tree-level and next-to-leading order differential cross sections, and their matching to parton shower

simulations, JHEP 07 (2014) 079. arXiv:1405.0301, doi:10.1007/JHEP07(2014)079.

[63] R. Frederix, S. Frixione, V. Hirschi, D. Pagani, H. S. Shao, M. Zaro, The automation of next-to-leading order electroweak calculations, JHEP 07 (2018) 185, [Erratum: JHEP 11, 085 (2021)]. arXiv:1804.10017, doi:10.1007/JHEP11(2021)085.

[64] J. Alwall, A. Ballestrero, P. Bartalini, S. Belov, E. Boos, et al., A Standard format for Les Houches event files, Comput.Phys.Commun. 176 (2007) 300–304. arXiv:hep-ph/0609017, doi:10.1016/j.cpc.2006.11.010.

[65] M. A. Dobbs, et al., Les Houches guidebook to Monte Carlo generators for hadron collider physics, in: 3rd Les Houches Workshop on Physics at TeV Colliders, 2004, pp. 411–459. arXiv:hep-ph/0403045.

[66] T. Sjostrand, S. Mrenna, P. Z. Skands, PYTHIA 6.4 Physics and Manual, JHEP 05 (2006) 026. arXiv:hep-ph/0603175, doi:10.1088/1126-6708/2006/05/026.

[67] T. Sjöstrand, S. Ask, J. R. Christiansen, R. Corke, N. Desai, P. Ilten, S. Mrenna, S. Prestel, C. O. Rasmussen, P. Z. Skands, An Introduction to PYTHIA 8.2, Comput. Phys. Commun. 191 (2015) 159–177. arXiv:1410.3012, doi:10.1016/j.cpc.2015.01.024.

[68] M. Bahr, et al., Herwig++ Physics and Manual, Eur. Phys. J. C 58 (2008) 639–707. arXiv:0803.0883, doi:10.1140/epjc/s10052-008-0798-9.

[69] J. Bellm, et al., Herwig 7.0/Herwig++ 3.0 release note, Eur. Phys. J. C 76 (4) (2016) 196. arXiv:1512.01178, doi:10.1140/epjc/s10052-016-4018-8.

[70] T. Gleisberg, S. Hoeche, F. Krauss, M. Schonherr, S. Schumann, F. Siegert, J. Winter, Event generation with SHERPA 1.1, JHEP 02 (2009) 007. arXiv:0811.4622, doi:10.1088/1126-6708/2009/02/007.

[71] E. Bothmann, et al., Event Generation with Sherpa 2.2, SciPost Phys. 7 (3) (2019) 034. arXiv:1905.09127, doi:10.21468/SciPostPhys.7.3.034.

[72] J. de Favereau, C. Delaere, P. Demin, A. Giammanco, V. Lemaître, A. Mertens, M. Selvaggi, DELPHES 3, A modular framework for fast simulation of a generic collider experiment, JHEP 02 (2014) 057. arXiv:1307.6346, doi:10.1007/JHEP02(2014)057.

[73] A. Buckley, J. Butterworth, L. Lonnblad, D. Grellscheid, H. Hoeth, J. Monk, H. Schulz, F. Siegert, Rivet user manual, Comput. Phys. Commun. 184 (2013) 2803–2819. arXiv:1003.0694, doi:10.1016/j.cpc.2013.05.021.

[74] C. Bierlich, et al., Robust Independent Validation of Experiment and Theory: Rivet version 3, SciPost Phys. 8 (2020) 026. arXiv:1912.05451, doi:10.21468/SciPostPhys.8.2.026.

[75] W. Abdallah, et al., Reinterpretation of LHC Results for New Physics: Status and Recommendations after Run 2, SciPost Phys. 9 (2) (2020) 022. arXiv:2003.07868, doi:10.21468/SciPostPhys.9.2.022.

[76] M. Drees, H. Dreiner, D. Schmeier, J. Tattersall, J. S. Kim, CheckMATE: Confronting your Favourite New Physics Model with LHC Data, Comput. Phys. Commun. 187 (2015) 227–265. arXiv:1312.2591, doi:10.1016/j.cpc.2014.10.018.

[77] D. Dercks, N. Desai, J. S. Kim, K. Rolbiecki, J. Tattersall, T. Weber, CheckMATE 2: From the model to the limit. arXiv:1611.09856.

[78] J. S. Kim, D. Schmeier, J. Tattersall, K. Rolbiecki, A framework to create customised LHC analyses within CheckMATE, Comput. Phys. Commun. 196 (2015) 535–562. arXiv:1503.01123, doi:10.1016/j.cpc.2015.06.002.

[79] E. Conte, B. Fuks, G. Serret, MadAnalysis 5, A User-Friendly Framework for Collider Phenomenology, Comput. Phys. Commun. 184 (2013) 222–256. arXiv:1206.1599, doi:10.1016/j.cpc.2012.09.009.

[80] E. Conte, B. Fuks, Confronting new physics theories to LHC data with MADANALYSIS 5, Int. J. Mod. Phys. A 33 (28) (2018) 1830027. arXiv:1808.00480, doi:10.1142/S0217751X18300272.

[81] B. Dumont, B. Fuks, S. Kraml, S. Bein, G. Chalons, E. Conte, S. Kulkarni, D. Sengupta, C. Wymant, Toward a public analysis database for LHC new physics searches using MADANALYSIS 5, Eur. Phys. J. C75 (2) (2015) 56. arXiv:1407.3278, doi:10.1140/epjc/s10052-014-3242-3.

[82] J. Y. Araz, B. Fuks, G. Polykratis, Simplified fast detector simulation in MADANALYSIS 5, Eur. Phys. J. C 81 (4) (2021) 329. arXiv:2006.09387, doi:10.1140/epjc/s10052-021-09052-5.

[83] P. Athron, et al., GAMBIT: The Global and Modular Beyond-the-Standard-Model Inference Tool. arXiv:1705.07908.

[84] C. Balazs, et al., ColliderBit: a GAMBIT module for the calculation of high-energy collider observables and likelihoods. arXiv:1705.07919.

[85] G. Brooijmans, et al., Les Houches 2017: Physics at TeV Colliders New Physics Working Group Report, in: 10th Les Houches Workshop on Physics at TeV Colliders, 2018. arXiv:1803.10379.

[86] S. Sekmen, G. Ünel, CutLang: A Particle Physics Analysis Description Language and Runtime Interpreter, Comput. Phys. Commun. 233 (2018) 215–236. arXiv:1801.05727, doi:10.1016/j.cpc.2018.06.023.

[87] G. Unel, S. Sekmen, A. M. Toon, CutLang: a cut-based HEP analysis description language and runtime interpreter, J. Phys. Conf. Ser. 1525 (1) (2020) 012025. arXiv:1909.10621, doi:10.1088/1742-6596/1525/1/012025.

[88] G. Unel, S. Sekmen, A. M. Toon, B. Gokturk, B. Orgen, A. Paul, N. Ravel, J. Setpal, CutLang v2: Advances in a Runtime-Interpreted Analysis Description Language for HEP Data, Front. Big Data 4 (2021) 659986. arXiv:2101.09031, doi:10.3389/fdata.2021.659986.

[89] G. Brooijmans, et al., Les Houches 2015: Physics at TeV colliders - new physics working group report, in: 9th Les Houches Workshop on Physics at TeV Colliders, 2016. arXiv:1605.02684.

[90] G. Brooijmans, et al., Les Houches 2019 Physics at TeV Colliders: New Physics Working Group Report, in: 11th Les Houches Workshop on Physics at TeV Colliders: PhysTeV Les Houches, 2020. arXiv:2002.12220.

[91] Y. Cui, B. Shuve, Probing Baryogenesis with Displaced Vertices at the LHC, JHEP 02 (2015) 049. arXiv:1409.6729, doi:10.1007/JHEP02(2015)049.

[92] F. Ambrogi, S. Kraml, S. Kulkarni, U. Laa, A. Lessa, V. Magerl, J. Sonneveld, M. Traub, W. Waltenberger, SModelS v1.1 user manual: Improving simplified model constraints with efficiency maps, Comput. Phys. Commun. 227 (2018) 72–98. arXiv:1701.06586, doi:10.1016/j.cpc.2018.02.007.

[93] S. Kraml, S. Kulkarni, U. Laa, A. Lessa, W. Magerl, D. Proschofsky, W. Waltenberger, SModelS: a tool for interpreting simplified-model results from the LHC and its application to supersymmetry, Eur.Phys.J. C74 (2014) 2868. arXiv:1312.4175, doi:10.1140/epjc/s10052-014-2868-5.

[94] F. Ambrogi, et al., SModelS v1.2: long-lived particles, combination of signal regions, and other novelties, Comput. Phys. Commun. 251 (2020) 106848. arXiv:1811.10624, doi:10.1016/j.cpc.2019.07.013.

[95] J. Dutta, S. Kraml, A. Lessa, W. Waltenberger, SModelS extension with the CMS supersymmetry search results from Run 2, LHEP 1 (1) (2018) 5–12. arXiv:1803.02204, doi:10.31526/LHEP.1.2018.02.

[96] C. K. Khosa, S. Kraml, A. Lessa, P. Neuhuber, W. Waltenberger, SModelS database update v1.2.3, to appear in LHEP. arXiv:2005.00555.

[97] P. Bechtle, O. Brein, S. Heinemeyer, G. Weiglein, K. E. Williams, HiggsBounds: Confronting Arbitrary Higgs Sectors with Exclusion Bounds from LEP and the Tevatron, Comput. Phys. Commun. 181 (2010) 138–167. arXiv:0811.4169, doi:10.1016/j.cpc.2009.09.003.

[98] P. Bechtle, O. Brein, S. Heinemeyer, G. Weiglein, K. E. Williams, HiggsBounds 2.0.0: Confronting Neutral and Charged Higgs Sector Predictions with Exclusion Bounds from LEP and the Tevatron, Comput. Phys. Commun. 182 (2011) 2605–2631. arXiv:1102.1898, doi:10.1016/j.cpc.2011.07.015.

[99] P. Bechtle, O. Brein, S. Heinemeyer, O. Stål, T. Stefaniak, G. Weiglein, K. E. Williams, HiggsBounds – 4: Improved Tests of Extended Higgs Sectors against Exclusion Bounds from LEP, the Tevatron and the LHC, Eur. Phys. J. C 74 (3) (2014) 2693. arXiv:1311.0055, doi:10.1140/epjc/s10052-013-2693-2.

[100] P. Bechtle, D. Dercks, S. Heinemeyer, T. Klingl, T. Stefaniak, G. Weiglein, J. Wittbrodt, HiggsBounds-5: Testing Higgs Sectors in the LHC 13 TeV Era, Eur. Phys. J. C 80 (12) (2020) 1211. arXiv:2006.06007, doi:10.1140/epjc/s10052-020-08557-9.

[101] P. Ilten, Y. Soreq, M. Williams, W. Xue, Serendipity in dark photon searches, JHEP 06 (2018) 004. arXiv:1801.04847, doi:10.1007/JHEP06(2018)004.

[102] F. Kahlhoefer, A. Mück, S. Schulte, P. Tunney, Interference effects in dilepton resonance searches for $Z'$ bosons and dark matter mediators, JHEP 03 (2020) 104. arXiv:1912.06374, doi:10.1007/JHEP03(2020)104.

[103] A. L. Read, Modified frequentist analysis of search results (the $CL_s$ method), in: 1st Workshop on Confidence Limits. 17 - 18 Jan 2000., CERN, Geneva, 2000. doi:10.5170/CERN-2000-005.

[104] A. Harel, Statistical methods in CMS searches, in: PHYSTAT 2011, CERN, Geneva, 2011, pp. 88–93. doi:10.5170/CERN-2011-006.88.

[105] G. Cowan, K. Cranmer, E. Gross, O. Vitells, Asymptotic formulae for likelihood-based tests of new physics, Eur. Phys. J. C 71 (2011) 1554, erratum: Eur. Phys. J. C **73** (2013) 2501. arXiv:1007.1727, doi:10.1140/epjc/s10052-011-1554-0.

[106] The CMS Collaboration, Simplified likelihood for the re-interpretation of public CMS results, Tech. rep., CERN, Geneva (Jan 2017).
URL https://cds.cern.ch/record/2242860

[107] ATLAS Collaboration, Reproducing searches for new physics with the ATLAS experiment through publication of full statistical likelihoods, Tech. Rep. ATL-PHYS-PUB-2019-029, CERN, Geneva, https://cds.cern.ch/record/2684863 (Aug 2019).

[108] K. Cranmer, G. Lewis, L. Moneta, A. Shibata, W. Verkerke, HistFactory: A tool for creating statistical models for use with RooFit and RooStats (CERN-OPEN-2012-016), https://cds.cern.ch/record/1456844.

[109] L. Heinrich, M. Feickert, G. Stark, scikit-hep/pyhf, https://github.com/scikit-hep/pyhf, DOI: 10.5281/zenodo.1169739. doi:10.5281/zenodo.1169739.

[110] L. Heinrich, M. Feickert, G. Stark, K. Cranmer, pyhf: pure-Python implementation of HistFactory statistical models, J. Open Source Softw. 6 (58) (2021) 2823. doi:10.21105/joss.02823.

[111] G. Alguero, J. Y. Araz, B. Fuks, S. Kraml, Signal region combination with full and simplified likelihoods in MadAnalysis 5. arXiv:2206.14870.

[112] S. Kraml, et al., Searches for New Physics: Les Houches Recommendations for the Presentation of LHC Results, Eur. Phys. J. C 72 (2012) 1976. arXiv:1203.2489, doi:10.1140/epjc/s10052-012-1976-3.

[113] W. Abdallah, et al., Reinterpretation of LHC Results for New Physics: Status and Recommendations after Run 2, SciPost Phys. 9 (2) (2020) 022. arXiv:2003.07868, doi:10.21468/SciPostPhys.9.2.022.

[114] K. Cranmer, S. Kraml, H. Prosper, et al., Publishing statistical models: Getting the most out of particle physics experiments, SciPost Phys. 12 (2022) 037. arXiv:2109.04981, doi:10.21468/SciPostPhys.12.1.037.

[115] CMS Collaboration, Simplified likelihood for the re-interpretation of public CMS results, Tech. Rep. CMS-NOTE-2017-001, CERN, Geneva (Jan 2017).

[116] A. Buckley, M. Citron, S. Fichet, S. Kraml, W. Waltenberger, N. Wardle, The Simplified Likelihood Framework, JHEP 04 (2019) 064. arXiv:1809.05548, doi:10.1007/JHEP04(2019)064.

[117] L. Heinrich, M. Feickert, G. Stark, pyhf: v0.6.3. doi:10.5281/zenodo.1169739. URL https://github.com/scikit-hep/pyhf/releases/tag/v0.6.3

[118] ATLAS Collaboration, Implementation of simplified likelihoods in HistFactory for searches for supersymmetry, Tech. Rep. ATL-PHYS-PUB-2021-038 (2021).

[119] G. Alguero, S. Kraml, W. Waltenberger, A SModelS interface for pyhf likelihoods, Comput. Phys. Commun. 264 (2021) 107909. arXiv:2009.01809, doi:10.1016/j.cpc.2021.107909.

[120] C. Balázs, et al., ColliderBit: a GAMBIT module for the calculation of high-energy collider observables and likelihoods, Eur. Phys. J. C 77 (11) (2017) 795. arXiv:1705.07919, doi:10.1140/epjc/s10052-017-5285-8.

[121] J. Y. Araz, M. Frank, B. Fuks, Reinterpreting the results of the LHC with MadAnalysis 5: uncertainties and higher-luminosity estimates, Eur. Phys. J. C 80 (6) (2020) 531. arXiv:1910.11418, doi:10.1140/epjc/s10052-020-8076-6.

[122] G. Aad, et al., Search for bottom-squark pair production with the ATLAS detector in final states containing Higgs bosons, $b$-jets and missing transverse momentum, JHEP 12 (2019) 060. arXiv:1908.03122, doi:10.1007/JHEP12(2019)060.

[123] B. Fuks, J. Y. Araz, Implementation of a search for sbottoms in the multibottom + missing energy channel (139/fb; ATLAS-SUSY-2018-31) (2020). doi:10.14428/DVN/IHALED.

[124] G. Aad, et al., Search for chargino-neutralino production with mass splittings near the electroweak scale in three-lepton final states in $\sqrt{s} = 13$ TeV $pp$ collisions with the ATLAS detector, Phys. Rev. D 101 (7) (2020) 072001. arXiv:1912.08479, doi:10.1103/PhysRevD.101.072001.

[125] J. Kim, T. G. Lee, J. Kim, H. Jang, Implementation of the electroweakino search with Jigsaw variables (139 fb-1; ATLAS-SUSY-2018-06) (2020). doi:10.14428/DVN/LYQMUJ.

[126] A. M. Sirunyan, et al., Search for electroweak production of charginos and neutralinos in multilepton final states in proton-proton collisions at $\sqrt{s} = 13$ TeV, JHEP 03 (2018) 166. arXiv:1709.05406, doi:10.1007/JHEP03(2018)166.

[127] A. M. Sirunyan, et al., Search for new physics in events with two soft oppositely charged leptons and missing transverse momentum in proton-proton collisions at $\sqrt{s} = 13$ TeV, Phys. Lett. B 782 (2018) 440–467. arXiv:1801.01846, doi:10.1016/j.physletb.2018.05.062.

[128] M. Goodsell, Implementation of a search for disappearing tracks (139/fb; 13 TeV; CMS-EXO-19-010) (2021). doi:10.14428/DVN/P82DKS.

[129] J. Y. Araz, B. Fuks, M. D. Goodsell, M. Utsch, Recasting LHC searches for long-lived particles with MadAnalysis 5. arXiv:2112.05163.

[130] B. Fuks, S. Mondal, Implementation of a search for electroweakinos in the multi-lepton + missing energy channel (35.9 fb-1; 13 TeV; CMS-SUS-16-039) (2021). doi:10.14428/DVN/E8WN3G.

[131] B. Fuks, Re-implementation of the soft lepton + missing energy analysis of CMS (35.9 fb-1; CMS-SUS-16-048) (2020). doi:10.14428/DVN/YA8E9V.

[132] G. Aad, et al., Search for direct stau production in events with two hadronic $\tau$-leptons in $\sqrt{s} = 13$ TeV $pp$ collisions with the ATLAS detector, Phys. Rev. D 101 (3) (2020) 032009. arXiv:1911.06660, doi:10.1103/PhysRevD.101.032009.

[133] G. Aad, et al., Search for direct production of electroweakinos in final states with one lepton, missing transverse momentum and a Higgs boson decaying into two $b$-jets in $pp$ collisions at $\sqrt{s} = 13$ TeV with the ATLAS detector, Eur. Phys. J. C 80 (8) (2020) 691. arXiv:1909.09226, doi:10.1140/epjc/s10052-020-8050-3.

[134] J. Lim, C.-T. Lu, J.-H. Park, J. Park, Re-implementation of a search for staus in the ditau + MET channel (139 fb-1; ATLAS-SUSY-2018-04) (2020). doi:10.14428/DVN/UN3NND.

[135] M. Goodsell, Re-implementation of the H (into b bbar) + 1 lepton + missing transverse momentum analysis (139 fb-1; ATLAS-SUSY-2019-08) (2020). doi:10.14428/DVN/BUN2UX.

[136] A. M. Sirunyan, et al., Search for supersymmetry in proton-proton collisions at 13 TeV in final states with jets and missing transverse momentum, JHEP 10 (2019) 244. arXiv:1908.04722, doi:10.1007/JHEP10(2019)244.

[137] A. Tumasyan, et al., Search for new particles in events with energetic jets and large missing transverse momentum in proton-proton collisions at $\sqrt{s} = 13$ TeV, JHEP 11 (2021) 153. arXiv:2107.13021, doi:10.1007/JHEP11(2021)153.

[138] A. M. Sirunyan, et al., Search for top squarks and dark matter particles in opposite-charge dilepton final states at $\sqrt{s} = 13$ TeV, Phys. Rev. D 97 (3) (2018) 032009. arXiv:1711.00752, doi:10.1103/PhysRevD.97.032009.

[139] J. Y. Araz, Implementation of the soft lepton + missing energy analysis of CMS (35.9 fb-1; 13 TeV; CMS-SUS-16-048) (2020). doi:10.14428/DVN/4WVPNQ.

[140] M. Malte, S. Bein, J. Sonneveld, Re-implementation of a search for supersymmetry in the HT/missing HT channel (137 fb-1; CMS-SUSY-19-006) (2020). doi:10.14428/DVN/4DEJQM.

[141] S. Bein, S.-M. Choi, B. Fuks, S. Jeong, D. W. Kang, J. Li, J. Sonneveld, Implementation of a search for stops in the di-lepton + missing energy channel (35.9 fb-1; 13 TeV; CMS-SUS-17-001) (2021). doi:10.14428/DVN/BQM0T3.

[142] A. Albert, Implementation of a search for new phenomena in events featuring energetic jets and missing transverse energy (137 fb-1; 13 TeV; CMS-EXO-20-004) (2021). doi:10.14428/DVN/IRF7ZL.

[143] J. Alwall, C. Duhr, B. Fuks, O. Mattelaer, D. G. Öztürk, C.-H. Shen, Computing decay rates for new physics theories with FeynRules and MadGraph 5_aMC@NLO, Comput. Phys. Commun. 197 (2015) 312–323. arXiv:1402.1178, doi:10.1016/j.cpc.2015.08.031.

[144] C. Duhr, B. Fuks, A superspace module for the FeynRules package, Comput. Phys. Commun. 182 (2011) 2404–2426. arXiv:1102.4191, doi:10.1016/j.cpc.2011.06.009.

[145] C. Arina, B. Fuks, L. Mantani, A universal framework for t-channel dark matter models, Eur. Phys. J. C 80 (5) (2020) 409, http://feynrules.irmp.ucl.ac.be/wiki/DMsimpt. arXiv:2001.05024, doi:10.1140/epjc/s10052-020-7933-7.

[146] R. D. Ball, V. Bertone, S. Carrazza, L. Del Debbio, S. Forte, A. Guffanti, N. P. Hartland, J. Rojo, Parton distributions with QED corrections, Nucl. Phys. B 877 (2013) 290–320. arXiv:1308.0598, doi:10.1016/j.nuclphysb.2013.10.010.

[147] LHC SUSY Cross Section Working Group, Cross sections for various subprocesses - 13 TeV, https://twiki.cern.ch/twiki/bin/view/LHCPhysics/SUSYCrossSections#Cross_sections_for_various_subpr (2021).

[148] C. Borschensky, M. Krämer, A. Kulesza, M. Mangano, S. Padhi, T. Plehn, X. Portell, Squark and gluino production cross sections in pp collisions at $\sqrt{s}$ = 13, 14, 33 and 100 TeV, Eur. Phys. J. C 74 (12) (2014) 3174. arXiv:1407.5066, doi:10.1140/epjc/s10052-014-3174-y.

[149] W. Beenakker, C. Borschensky, R. Heger, M. Krämer, A. Kulesza, E. Laenen, NNLL resummation for stop pair-production at the LHC, JHEP 05 (2016) 153. arXiv:1601.02954, doi:10.1007/JHEP05(2016)153.

[150] W. Beenakker, C. Borschensky, M. Krämer, A. Kulesza, E. Laenen, NNLL-fast: predictions for coloured supersymmetric particle production at the LHC with threshold and Coulomb resummation, JHEP 12 (2016) 133. arXiv:1607.07741, doi:10.1007/JHEP12(2016)133.

[151] B. Fuks, M. Klasen, D. R. Lamprea, M. Rothering, Gaugino production in proton-proton collisions at a center-of-mass energy of 8 TeV, JHEP 10 (2012) 081. arXiv:1207.2159, doi:10.1007/JHEP10(2012)081.

[152] B. Fuks, M. Klasen, D. R. Lamprea, M. Rothering, Precision predictions for electroweak superpartner production at hadron colliders with Resummino, Eur. Phys. J. C 73 (2013) 2480. arXiv:1304.0790, doi:10.1140/epjc/s10052-013-2480-0.

[153] B. Fuks, M. Klasen, D. R. Lamprea, M. Rothering, Revisiting slepton pair production at the Large Hadron Collider, JHEP 01 (2014) 168. arXiv:1310.2621, doi:10.1007/JHEP01(2014)168.

[154] ATLAS Collaboration, "HEPData_workspaces.tar.gz" of "Search for bottom-squark pair production with the ATLAS detector in final states containing Higgs bosons, $b$-jets and missing transverse momentum" (Version 3), HEPData (other), https://doi.org/10.17182/hepdata.89408.v3/r2 (2021).

[155] J. Y. Araz, B. Fuks, Implementation of the ATLAS-SUSY-2018-31 analysis in the MadAnalysis 5 framework (sbottoms with multi-bottoms and missing transverse energy; 139 fb$^{-1}$), Mod. Phys. Lett. A 36 (01) (2021) 2141010. doi:10.1142/S0217732321410108.

[156] ATLAS Collaboration, The ATLAS Tau Trigger in Run 2, Tech. Rep. ATLAS-CONF-2017-061 (July 2017).

[157] C. G. Lester, D. J. Summers, Measuring masses of semiinvisibly decaying particles pair produced at hadron colliders, Phys. Lett. B 463 (1999) 99–103. arXiv:hep-ph/9906349, doi:10.1016/S0370-2693(99)00945-4.

[158] H.-C. Cheng, Z. Han, Minimal Kinematic Constraints and m(T2), JHEP 12 (2008) 063. arXiv:0810.5178, doi:10.1088/1126-6708/2008/12/063.

[159] J. Lim, C.-T. Lu, J.-H. Park, J. Park, Implementation of the ATLAS-SUSY-2018-04 analysis in the MadAnalysis 5 framework (staus in the di-tau plus missing transverse energy channel; 139 fb$^{-1}$), Mod. Phys. Lett. A 36 (01) (2021) 2141009. doi:10.1142/S0217732321410091.

[160] ATLAS Collaboration, "SUSY-2018-04_likelihoods.tar.gz" of "Search for direct stau production in events with two hadronic $\tau$-leptons in $\sqrt{s} = 13$ TeV $pp$ collisions with the ATLAS detector" (Version 2), HEPData (other), https://doi.org/10.17182/hepdata.92006.v2/r2 (2020).

[161] P. Jackson, C. Rogan, M. Santoni, Sparticles in motion: Analyzing compressed SUSY scenarios with a new method of event reconstruction, Phys. Rev. D 95 (3) (2017) 035031. arXiv:1607.08307, doi:10.1103/PhysRevD.95.035031.

[162] P. Jackson, C. Rogan, Recursive Jigsaw Reconstruction: HEP event analysis in the presence of kinematic and combinatoric ambiguities, Phys. Rev. D 96 (11) (2017) 112007. arXiv:1705.10733, doi:10.1103/PhysRevD.96.112007.

[163] J. Kim, T. Lee, J. Kim, H. Jang, Implementation of the ATLAS-SUSY-2018-06 analysis in the MadAnalysis 5 framework (electroweakinos with Jigsaw variables; 139 fb$^{-1}$), Mod. Phys. Lett. A 36 (01) (2021) 2141004. doi:10.1142/S0217732321410042.

[164] ATLAS Collaboration, Search for chargino-neutralino production with mass splittings near the electroweak scale in three-lepton final states in $\sqrt{s}$=13 TeV $pp$ collisions with the ATLAS detector (Version 2), HEPData (collection), https://doi.org/10.17182/hepdata.91127.v2 (2020).

[165] D. R. Tovey, On measuring the masses of pair-produced semi-invisibly decaying particles at hadron colliders, JHEP 04 (2008) 034. arXiv:0802.2879, doi:10.1088/1126-6708/2008/04/034.

[166] G. Polesello, D. R. Tovey, Supersymmetric particle mass measurement with the boost-corrected contransverse mass, JHEP 03 (2010) 030. arXiv:0910.0174, doi:10.1007/JHEP03(2010)030.

[167] M. D. Goodsell, Implementation of the ATLAS-SUSY-2019-08 analysis in the MadAnalysis 5 framework (electroweakinos with a Higgs decay into a $b\bar{b}$ pair, one lepton and missing transverse energy; 139 fb$^{-1}$), Mod. Phys. Lett. A 36 (01) (2021) 2141006. doi:10.1142/S0217732321410066.

[168] ATLAS Collaboration, "1Lbb-likelihoods-hepdata.tar.gz" of "Search for direct production of electroweakinos in final states with one lepton, missing transverse momentum and a Higgs boson decaying into two $b$-jets in $pp$ collisions at $\sqrt{s} = 13$ TeV with the ATLAS detector" (Version 4), HEPData (other), https://doi.org/10.17182/hepdata.90607.v4/r3 (2021).

[169] A. Chatterjee, M. Frank, B. Fuks, K. Huitu, S. Mondal, S. K. Rai, H. Waltari, Multileptonic signals of co-annihilating left-right supersymmetric dark matter, Phys. Rev. D 99 (3) (2019) 035017. arXiv:1810.03891, doi:10.1103/PhysRevD.99.035017.

[170] B. Fuks (Ed.), Proceedings of the first MadAnalysis 5 workshop on LHC recasting in Korea, 2018. arXiv:1806.02537.

[171] M. Mrowietz, S. Bein, J. Sonneveld, Implementation of the CMS-SUS-19-006 analysis in the MadAnalysis 5 framework (supersymmetry with large hadronic activity and missing transverse energy; 137 fb$^{-1}$), Mod. Phys. Lett. A 36 (01) (2021) 2141007. doi:10.1142/S0217732321410078.

[172] CMS Collaboration, "Covariance matrix" of "Search for supersymmetry in proton-proton collisions at 13 TeV in final states with jets and missing transverse momentum" (Version 1), HEPData (dataset), https://doi.org/10.17182/hepdata.90835.v1/t7 (2020).

[173] A. Albert, Material for the CMS monojet analysis for 101+36/fb (PAS-EXO-20-004). Reinterpretation: Auxiliary Material Presentation (RAMP) #3, https://cds.cern.ch/record/2774586 (Jun 2021).

[174] CMS Collaboration, Search for new particles in events with energetic jets and large missing transverse momentum in proton-proton collisions at $\sqrt{s} = 13$ TeV, HEPData (collection), https://doi.org/10.17182/hepdata.106115 (2022).

[175] B. C. Allanach, SOFTSUSY: a program for calculating supersymmetric spectra, Comput. Phys. Commun. 143 (2002) 305–331. arXiv:hep-ph/0104145, doi:10.1016/S0010-4655(01)00460-X.

[176] B. C. Allanach, T. Cridge, The Calculation of Sparticle and Higgs Decays in the Minimal and Next-to-Minimal Supersymmetric Standard Models: SOFTSUSY4.0, Comput. Phys. Commun. 220 (2017) 417–502. arXiv:1703.09717, doi:10.1016/j.cpc.2017.07.021.

[177] G. Alguero, J. Heisig, C. K. Khosa, S. Kraml, S. Kulkarni, A. Lessa, H. Reyes-González, W. Waltenberger, A. Wongel, Constraining new physics with SModelS version 2, JHEP 08 (2022) 068. arXiv:2112.00769, doi:10.1007/JHEP08(2022)068.

[178] W. Abdallah, et al., Reinterpretation of LHC Results for New Physics: Status and Recommendations after Run 2, SciPost Phys. 9 (2020) 22. arXiv:2003.07868, doi:10.21468/SciPostPhys.9.2.022.

[179] P. Asadi, M. R. Buckley, A. DiFranzo, A. Monteux, D. Shih, Digging Deeper for New Physics in the LHC Data, JHEP 11 (2017) 194. arXiv:1707.05783, doi:10.1007/JHEP11(2017)194.

[180] P. Athron, et al., Combined collider constraints on neutralinos and charginos, Eur. Phys. J. C 79 (5) (2019) 395. arXiv:1809.02097, doi:10.1140/epjc/s10052-019-6837-x.

[181] CMS Collaboration, Simplified likelihood for the re-interpretation of public CMS results, Tech. Rep. CMS-NOTE-2017-001, CERN, Geneva, https://cds.cern.ch/record/2242860 (Jan 2017).

[182] G. Aad, et al., Search for bottom-squark pair production with the ATLAS detector in final states containing Higgs bosons, $b$-jets and missing transverse momentum, JHEP 12 (2019) 060, HEPData entry: https://doi.org/10.17182/hepdata.89408. arXiv:1908.03122, doi:10.1007/JHEP12(2019)060.

[183] F. Pezoa, J. L. Reutter, F. Suarez, M. Ugarte, D. Vrgoč, Foundations of json schema, in: Proceedings of the 25th International Conference on World Wide Web, International World Wide Web Conferences Steering Committee, 2016, pp. 263–273.

[184] S. Kögl, jsonpatch (6 2020).
URL https://github.com/stefankoegl/python-json-patch

[185] A. L. Read, Presentation of search results: The CL(s) technique, J. Phys. G 28 (2002) 2693–2704. doi:10.1088/0954-3899/28/10/313.

[186] G. Cowan, K. Cranmer, E. Gross, O. Vitells, Asymptotic formulae for likelihood-based tests of new physics, The European Physical Journal C 71 (2). doi:10.1140/epjc/s10052-011-1554-0.

[187] P. Virtanen, R. Gommers, T. E. Oliphant, et al., SciPy 1.0: Fundamental Algorithms for Scientific Computing in Python, Nature Methods 17 (2020) 261–272. doi:https://doi.org/10.1038/s41592-019-0686-2.

[188] G. Aad, et al., Search for direct production of electroweakinos in final states with one lepton, missing transverse momentum and a Higgs boson decaying into two $b$-jets in (pp) collisions at $\sqrt{s} = 13$ TeV with the ATLAS detector, Eur. Phys. J. C 80 (8) (2020) 691, HEPData entry: https://doi.org/10.17182/hepdata.90607.v2. arXiv:1909.09226.

[189] G. Alguero, J. Heisig, C. K. Khosa, S. Kraml, S. Kulkarni, A. Lessa, P. Neuhuber, H. Reyes-González, W. Waltenberger, A. Wongel, New developments in SModelS, PoS TOOLS2020 (2021) 022. arXiv:2012.08192, doi:10.22323/1.392.0022.

[190] W. Waltenberger, A. Lessa, S. Kraml, Artificial Proto-Modelling: Building Precursors of a Next Standard Model from Simplified Model Results, JHEP 03 (2021) 207. arXiv:2012.12246, doi:10.1007/JHEP03(2021)207.

[191] L. Edelhauser, J. Heisig, M. Krämer, L. Oymanns, J. Sonneveld, Constraining supersymmetry at the LHC with simplified models for squark production, JHEP 12 (2014) 022. arXiv:1410.0965, doi:10.1007/JHEP12(2014)022.

[192] L. Edelhäuser, M. Krämer, J. Sonneveld, Simplified models for same-spin new physics scenarios, JHEP 04 (2015) 146. arXiv:1501.03942, doi:10.1007/JHEP04(2015)146.

[193] S. Kraml, U. Laa, L. Panizzi, H. Prager, Scalar versus fermionic top partner interpretations of $t\bar{t} + E_T^{\mathrm{miss}}$ searches at the LHC, JHEP 11 (2016) 107. arXiv:1607.02050, doi:10.1007/JHEP11(2016)107.

[194] H. E. Haber, Introductory low-energy supersymmetry, in: Theoretical Advanced Study Institute (TASI 92): From Black Holes and Strings to Particles, 1993, pp. 589–686. arXiv:hep-ph/9306207.

[195] H. Baer, et al., Low-energy supersymmetry phenomenology. arXiv:hep-ph/9503479, doi:10.2172/72994.

[196] M. Drees, S. P. Martin, Implications of SUSY model building, 1995, pp. 146–215. arXiv:hep-ph/9504324, doi:10.1142/9789812830265_0003.

[197] H. P. Nilles, Phenomenological aspects of supersymmetry, in: Workshop on Gauge Theories, Applied Supersymmetry, and Quantum Gravity, 1995, pp. 81–105. arXiv:hep-ph/9511313.

[198] G. Belanger, F. Boudjema, A. Pukhov, A. Semenov, micrOMEGAs_3: A program for calculating dark matter observables, Comput. Phys. Commun. 185 (2014) 960–985. arXiv:1305.0237, doi:10.1016/j.cpc.2013.10.016.

[199] G. Bélanger, F. Boudjema, A. Goudelis, A. Pukhov, B. Zaldivar, micrOMEGAs5.0 : Freeze-in, Comput. Phys. Commun. 231 (2018) 173–186. arXiv:1801.03509, doi:10.1016/j.cpc.2018.04.027.

[200] D. Barducci, G. Belanger, J. Bernon, F. Boudjema, J. Da Silva, S. Kraml, U. Laa, A. Pukhov, Collider limits on new physics within micrOMEGAs_4.3, Comput. Phys. Commun. 222 (2018) 327–338. arXiv:1606.03834, doi:10.1016/j.cpc.2017.08.028.

[201] http://smodels.hephy.at.

[202] C. Degrande, C. Duhr, B. Fuks, D. Grellscheid, O. Mattelaer, T. Reiter, UFO - The Universal FeynRules Output, Comput. Phys. Commun. 183 (2012) 1201–1214. arXiv:1108.2040, doi:10.1016/j.cpc.2012.01.022.

[203] J. Alwall, M. Herquet, F. Maltoni, O. Mattelaer, T. Stelzer, MadGraph 5 : Going Beyond, JHEP 06 (2011) 128. arXiv:1106.0522, doi:10.1007/JHEP06(2011)128.

[204] A. Belyaev, S. Prestel, F. Rojas-Abbate, J. Zurita, Probing dark matter with disappearing tracks at the LHC, Phys. Rev. D 103 (9) (2021) 095006. arXiv:2008.08581, doi:10.1103/PhysRevD.103.095006.

[205] A. Belyaev, S. Prestel, F. Rojas-Abbate, J. Zurita, Probing Dark Matter with Disappearing Tracks at the LHC (Zenodo dataset) (Aug. 2020). doi:10.5281/zenodo.4288736.

[206] G. Aad, et al., Search for squarks and gluinos in final states with one isolated lepton, jets, and missing transverse momentum at $\sqrt{s} = 13$ with the ATLAS detector, Eur. Phys. J. C 81 (7) (2021) 600. arXiv:2101.01629, doi:10.1140/epjc/s10052-021-09344-w.

[207] G. Aad, et al., Search for squarks and gluinos in final states with jets and missing transverse momentum using 139 fb$^{-1}$ of $\sqrt{s}$ =13 TeV $pp$ collision data with the ATLAS detector, JHEP 02 (2021) 143. arXiv:2010.14293, doi:10.1007/JHEP02(2021)143.

[208] G. Aad, et al., Search for a scalar partner of the top quark in the all-hadronic $t\bar{t}$ plus missing transverse momentum final state at $\sqrt{s} = 13$ TeV with the ATLAS detector, Eur. Phys. J. C 80 (8) (2020) 737. arXiv:2004.14060, doi:10.1140/epjc/s10052-020-8102-8.

[209] G. Aad, et al., Search for direct production of electroweakinos in final states with missing transverse momentum and a Higgs boson decaying into photons in pp collisions at $\sqrt{s} = 13$ TeV with the ATLAS detector, JHEP 10 (2020) 005. arXiv:2004.10894, doi:10.1007/JHEP10(2020)005.

[210] M. Aaboud, et al., Search for chargino-neutralino production using recursive jigsaw reconstruction in final states with two or three charged leptons in proton-proton collisions at $\sqrt{s} = 13$ TeV with the ATLAS detector, Phys. Rev. D98 (9) (2018) 092012. arXiv:1806.02293, doi:10.1103/PhysRevD.98.092012.

[211] G. Aad, et al., Search for chargino-neutralino production with mass splittings near the electroweak scale in three-lepton final states in $\sqrt{s}$=13 TeV $pp$ collisions with the ATLAS detector, Phys. Rev. D 101 (7) (2020) 072001, HEPData entry: https://doi.org/10.17182/hepdata.91127. arXiv:1912.08479, doi:10.1103/PhysRevD.101.072001.

[212] V. Khachatryan, et al., Search for supersymmetry in events with soft leptons, low jet multiplicity, and missing transverse energy in proton–proton collisions at $\sqrt{s}$=8 TeV, Phys. Lett. B759 (2016) 9–35. arXiv:1512.08002, doi:10.1016/j.physletb.2016.05.033.

[213] L. Lopez Honorez, E. Nezri, J. F. Oliver, M. H. G. Tytgat, The Inert Doublet Model: An Archetype for Dark Matter, JCAP 02 (2007) 028. arXiv:hep-ph/0612275, doi:10.1088/1475-7516/2007/02/028.

[214] A. Goudelis, B. Herrmann, O. Stål, Dark matter in the Inert Doublet Model after the discovery of a Higgs-like boson at the LHC, JHEP 09 (2013) 106. arXiv:1303.3010, doi:10.1007/JHEP09(2013)106.

[215] B. Eiteneuer, A. Goudelis, J. Heisig, The inert doublet model in the light of Fermi-LAT gamma-ray data: a global fit analysis, Eur. Phys. J. C 77 (9) (2017) 624. arXiv:1705.01458, doi:10.1140/epjc/s10052-017-5166-1.

[216] J. Heisig, S. Kraml, A. Lessa, Constraining new physics with searches for long-lived particles: Implementation into SModelS, Phys. Lett. B788 (2019) 87–95. arXiv:1808.05229, doi:10.1016/j.physletb.2018.10.049.

[217] M. Klasen, C. E. Yaguna, J. D. Ruiz-Alvarez, D. Restrepo, O. Zapata, Scalar dark matter and fermion coannihilations in the radiative seesaw model, JCAP 04 (2013) 044. arXiv:1302.5298, doi:10.1088/1475-7516/2013/04/044.

[218] I. M. Ávila, G. Cottin, M. A. Díaz, Revisiting the scotogenic model with scalar dark matter, J. Phys. G 49 (6) (2022) 065001. arXiv:2108.05103, doi:10.1088/1361-6471/ac5fb4.

[219] D. Borah, A. Gupta, New viable region of an inert Higgs doublet dark matter model with scotogenic extension, Phys. Rev. D 96 (11) (2017) 115012. arXiv:1706.05034, doi:10.1103/PhysRevD.96.115012.

[220] M. Baak, M. Goebel, J. Haller, A. Hoecker, D. Ludwig, K. Moenig, M. Schott, J. Stelzer, Updated Status of the Global Electroweak Fit and Constraints on New Physics, Eur. Phys. J. C 72 (2012) 2003. arXiv:1107.0975, doi:10.1140/epjc/s10052-012-2003-4.

[221] P. A. Zyla, et al., Review of Particle Physics, PTEP 2020 (8) (2020) 083C01. doi:10.1093/ptep/ptaa104.

[222] C. H. Chen, M. Drees, J. F. Gunion, Searching for invisible and almost invisible particles at e+ e- colliders, Phys. Rev. Lett. 76 (1996) 2002–2005. arXiv:hep-ph/9512230, doi:10.1103/PhysRevLett.76.2002.

[223] C. H. Chen, M. Drees, J. F. Gunion, A Nonstandard string / SUSY scenario and its phenomenological implications, Phys. Rev. D 55 (1997) 330–347, [Erratum: Phys.Rev.D 60, 039901 (1999)]. arXiv:hep-ph/9607421, doi:10.1103/PhysRevD.60.039901.

[224] C. H. Chen, M. Drees, J. F. Gunion, Addendum/erratum for 'searching for invisible and almost invisible particles at e+ e- colliders' [hep-ph/9512230] and 'a nonstandard string/SUSY scenario and its phenomenological implications' [hep-ph/9607421]arXiv:hep-ph/9902309.

[225] A. Belyaev, G. Cacciapaglia, I. P. Ivanov, F. Rojas-Abatte, M. Thomas, Anatomy of the Inert Two Higgs Doublet Model in the light of the LHC and non-LHC Dark Matter Searches, Phys. Rev. D 97 (3) (2018) 035011. arXiv:1612.00511, doi:10.1103/PhysRevD.97.035011.

[226] G. Belanger, A. Mjallal, A. Pukhov, Two dark matter candidates: The case of inert doublet and singlet scalars, Phys. Rev. D 105 (3) (2022) 035018. arXiv:2108.08061, doi:10.1103/PhysRevD.105.035018.

[227] Search for heavy stable charged particles with 12.9 $\text{fb}^{-1}$ of 2016 data, Tech. Rep. CMS-PAS-EXO-16-036, CERN, Geneva, https://cds.cern.ch/record/2205281 (2016).

[228] S. Chatrchyan, et al., Searches for Long-Lived Charged Particles in *pp* Collisions at $\sqrt{s}$=7 and 8 TeV, JHEP 07 (2013) 122. arXiv:1305.0491, doi:10.1007/JHEP07(2013)122.

[229] V. Khachatryan, et al., Constraints on the pMSSM, AMSB model and on other models from the search for long-lived charged particles in proton-proton collisions at sqrt(s) = 8 TeV, Eur. Phys. J. C 75 (7) (2015) 325. arXiv:1502.02522, doi:10.1140/epjc/s10052-015-3533-3.

[230] J. McDonald, Thermally generated gauge singlet scalars as selfinteracting dark matter, Phys. Rev. Lett. 88 (2002) 091304. arXiv:hep-ph/0106249, doi:10.1103/PhysRevLett.88.091304.

[231] T. Asaka, K. Ishiwata, T. Moroi, Right-handed sneutrino as cold dark matter, Phys. Rev. D 73 (2006) 051301. arXiv:hep-ph/0512118, doi:10.1103/PhysRevD.73.051301.

[232] L. J. Hall, K. Jedamzik, J. March-Russell, S. M. West, Freeze-In Production of FIMP Dark Matter, JHEP 03 (2010) 080. arXiv:0911.1120, doi:10.1007/JHEP03(2010)080.

[233] E. Molinaro, C. E. Yaguna, O. Zapata, FIMP realization of the scotogenic model, JCAP 07 (2014) 015. arXiv:1405.1259, doi:10.1088/1475-7516/2014/07/015.

[234] A. G. Hessler, A. Ibarra, E. Molinaro, S. Vogl, Probing the scotogenic FIMP at the LHC, JHEP 01 (2017) 100. arXiv:1611.09540, doi:10.1007/JHEP01(2017)100.

[235] N. Palanque-Delabrouille, C. Yèche, N. Schöneberg, J. Lesgourgues, M. Walther, S. Chabanier, E. Armengaud, Hints, neutrino bounds and WDM constraints from SDSS DR14 Lyman-$\alpha$ and Planck full-survey data, JCAP 04 (2020) 038. arXiv:1911.09073, doi:10.1088/1475-7516/2020/04/038.

[236] Q. Decant, J. Heisig, D. C. Hooper, L. Lopez-Honorez, Lyman-$\alpha$ constraints on freeze-in and superWIMPs, JCAP 03 (2022) 041. arXiv:2111.09321, doi:10.1088/1475-7516/2022/03/041.

[237] A. Garzilli, A. Magalich, O. Ruchayskiy, A. Boyarsky, How to constrain warm dark matter with the Lyman-$\alpha$ forest, Mon. Not. Roy. Astron. Soc. 502 (2) (2021) 2356–2363. arXiv:1912.09397, doi:10.1093/mnras/stab192.

[238] M. D. Goodsell, S. Kraml, H. Reyes-González, S. L. Williamson, Constraining Electroweakinos in the Minimal Dirac Gaugino Model, SciPost Phys. 9 (4) (2020) 047. arXiv:2007.08498, doi:10.21468/SciPostPhys.9.4.047.

[239] T. Sjostrand, S. Mrenna, P. Z. Skands, A Brief Introduction to PYTHIA 8.1, Comput. Phys. Commun. 178 (2008) 852–867. arXiv:0710.3820, doi:10.1016/j.cpc.2008.01.036.

[240] W. Beenakker, R. Hopker, M. Spira, PROSPINO: A Program for the production of supersymmetric particles in next-to-leading order QCD. arXiv:hep-ph/9611232.

[241] A. M. Sirunyan, et al., Combined search for electroweak production of charginos and neutralinos in proton-proton collisions at $\sqrt{s} = 13$ TeV, JHEP 03 (2018) 160. arXiv:1801.03957, doi:10.1007/JHEP03(2018)160.

[242] G. Aad, et al., Search for electroweak production of charginos and sleptons decaying into final states with two leptons and missing transverse momentum in $\sqrt{s} = 13$ TeV $pp$ collisions using the ATLAS detector, Eur. Phys. J. C80 (2) (2020) 123. arXiv:1908.08215, doi:10.1140/epjc/s10052-019-7594-6.

[243] E. Aprile, et al., Dark Matter Search Results from a One Ton-Year Exposure of XENON1T, Phys. Rev. Lett. 121 (11) (2018) 111302. arXiv:1805.12562, doi:10.1103/PhysRevLett.121.111302.

[244] E. W. Kolb, M. S. Turner, The Early Universe, Vol. 69, 1990. doi:10.1201/9780429492860.

[245] K. Griest, D. Seckel, Three exceptions in the calculation of relic abundances, Phys. Rev. D 43 (1991) 3191–3203. doi:10.1103/PhysRevD.43.3191.

[246] P. Gondolo, G. Gelmini, Cosmic abundances of stable particles: Improved analysis, Nucl. Phys. B 360 (1991) 145–179. doi:10.1016/0550-3213(91)90438-4.

[247] J. Edsjo, P. Gondolo, Neutralino relic density including coannihilations, Phys. Rev. D 56 (1997) 1879–1894. arXiv:hep-ph/9704361, doi:10.1103/PhysRevD.56.1879.

[248] H. Baer, T. Krupovnickas, A. Mustafayev, E.-K. Park, S. Profumo, X. Tata, Exploring the BWCA (bino-wino co-annihilation) scenario for neutralino dark matter, JHEP 12 (2005) 011. arXiv:hep-ph/0511034, doi:10.1088/1126-6708/2005/12/011.

[249] N. Arkani-Hamed, A. Delgado, G. F. Giudice, The Well-tempered neutralino, Nucl. Phys. B 741 (2006) 108–130. arXiv:hep-ph/0601041, doi:10.1016/j.nuclphysb.2006.02.010.

[250] R. T. D'Agnolo, D. Pappadopulo, J. T. Ruderman, Fourth Exception in the Calculation of Relic Abundances, Phys. Rev. Lett. 119 (6) (2017) 061102. arXiv:1705.08450, doi:10.1103/PhysRevLett.119.061102.

[251] M. Garny, J. Heisig, B. Lülf, S. Vogl, Coannihilation without chemical equilibrium, Phys. Rev. D 96 (10) (2017) 103521. arXiv:1705.09292, doi:10.1103/PhysRevD.96.103521.

[252] G. Belanger, F. Boudjema, A. Pukhov, A. Semenov, MicrOMEGAs: A Program for calculating the relic density in the MSSM, Comput. Phys. Commun. 149 (2002) 103–120. arXiv:hep-ph/0112278, doi:10.1016/S0010-4655(02)00596-9.

[253] P. Gondolo, J. Edsjo, P. Ullio, L. Bergstrom, M. Schelke, E. A. Baltz, DarkSUSY: Computing supersymmetric dark matter properties numerically, JCAP 07 (2004) 008. arXiv:astro-ph/0406204, doi:10.1088/1475-7516/2004/07/008.

[254] A. Arbey, F. Mahmoudi, G. Robbins, SuperIso Relic v4: A program for calculating dark matter and flavour physics observables in Supersymmetry, Comput. Phys. Commun. 239 (2019) 238–264. arXiv:1806.11489, doi:10.1016/j.cpc.2019.01.014.

[255] F. Ambrogi, C. Arina, M. Backovic, J. Heisig, F. Maltoni, L. Mantani, O. Mattelaer, G. Mohlabeng, MadDM v.3.0: a Comprehensive Tool for Dark Matter Studies, Phys. Dark Univ. 24 (2019) 100249. arXiv:1804.00044, doi:10.1016/j.dark.2018.11.009.

[256] T. Bringmann, J. Edsjö, DarkSUSY 6.3: Freeze-in, out-of-equilibrium freeze-out, cosmic-ray upscattering and further new feature, in: Computational Tools for High Energy Physics and Cosmology, 2022. arXiv:2203.07439.

[257] G. Alguero, G. Belanger, S. Kraml, A. Pukhov, Co-scattering in micrOMEGAs: a case study for the singlet-triplet dark matter model. arXiv:2207.10536.

[258] G. Bertone, T. Tait, M. P., A new era in the search for dark matter, Nature 562 (7725) (2018) 51–56. arXiv:1810.01668, doi:10.1038/s41586-018-0542-z.

[259] J. K. Behr, Searches for Dark Matter with the ATLAS and CMS Experiments using LHC Run 2 (2015–2018) Data, PoS PANIC2021 (2022) 137. doi:10.22323/1.380.0137.

[260] H. Abdalla, et al., Combined dark matter searches towards dwarf spheroidal galaxies with Fermi-LAT, HAWC, H.E.S.S., MAGIC, and VERITAS, PoS ICRC2021 (2021) 528. arXiv:2108.13646, doi:10.22323/1.395.0528.

[261] J. Aalbers, et al., First Dark Matter Search Results from the LUX-ZEPLIN (LZ) Experiment. arXiv:2207.03764.

[262] N. Aghanim, et al., Planck 2018 results. VI. Cosmological parameters, Astron. Astrophys. 641 (2020) A6, [Erratum: Astron.Astrophys. 652, C4 (2021)]. arXiv:1807.06209, doi:10.1051/0004-6361/201833910.

[263] P. Binetruy, G. Girardi, P. Salati, Constraints on a System of Two Neutral Fermions From Cosmology, Nucl. Phys. B 237 (1984) 285–306. doi:10.1016/0550-3213(84)90161-5.

[264] J. McDonald, Gauge singlet scalars as cold dark matter, Phys. Rev. D 50 (1994) 3637–3649. arXiv:hep-ph/0702143, doi:10.1103/PhysRevD.50.3637.

[265] N. Arkani-Hamed, S. Dimopoulos, Supersymmetric unification without low energy supersymmetry and signatures for fine-tuning at the LHC, JHEP 06 (2005) 073. arXiv:hep-th/0405159, doi:10.1088/1126-6708/2005/06/073.

[266] G. F. Giudice, A. Romanino, Split supersymmetry, Nucl. Phys. B 699 (2004) 65–89, [Erratum: Nucl.Phys.B 706, 487–487 (2005)]. arXiv:hep-ph/0406088, doi:10.1016/j.nuclphysb.2004.08.001.

[267] M. Ibe, A. Kamada, S. Matsumoto, Mixed (cold+warm) dark matter in the bino-wino coannihilation scenario, Phys. Rev. D 89 (12) (2014) 123506. arXiv:1311.2162, doi:10.1103/PhysRevD.89.123506.

[268] K. Harigaya, K. Kaneta, S. Matsumoto, Gaugino coannihilations, Phys. Rev. D 89 (11) (2014) 115021. arXiv:1403.0715, doi:10.1103/PhysRevD.89.115021.

[269] A. Bharucha, F. Brümmer, R. Ruffault, Well-tempered n-plet dark matter, JHEP 09 (2017) 160. arXiv:1703.00370, doi:10.1007/JHEP09(2017)160.

[270] J. Bramante, N. Desai, P. Fox, A. Martin, B. Ostdiek, T. Plehn, Towards the Final Word on Neutralino Dark Matter, Phys. Rev. D 93 (6) (2016) 063525. arXiv:1510.03460, doi:10.1103/PhysRevD.93.063525.

[271] T. T. Yanagida, W. Yin, N. Yokozaki, Bino-wino coannihilation as a prediction in the $E_7$ unification of families, JHEP 12 (2019) 169. arXiv:1907.07168, doi:10.1007/JHEP12(2019)169.

[272] G. Bélanger, F. Boudjema, A. Pukhov, A. Semenov, micrOMEGAs4.1: two dark matter candidates, Comput. Phys. Commun. 192 (2015) 322–329. arXiv:1407.6129, doi:10.1016/j.cpc.2015.03.003.

[273] G. Belanger, A. Mjallal, A. Pukhov, WIMP and FIMP dark matter in the inert doublet plus singlet model. arXiv:2205.04101.

[274] T. Binder, T. Bringmann, M. Gustafsson, A. Hryczuk, Early kinetic decoupling of dark matter: when the standard way of calculating the thermal relic density fails, Phys. Rev. D 96 (11) (2017) 115010, [Erratum: Phys.Rev.D 101, 099901 (2020)]. arXiv:1706.07433, doi:10.1103/PhysRevD.96.115010.

[275] G. Bélanger, C. Delaunay, A. Pukhov, B. Zaldivar, Dark matter abundance from the sequential freeze-in mechanism, Phys. Rev. D 102 (3) (2020) 035017. arXiv:2005.06294, doi:10.1103/PhysRevD.102.035017.

[276] M. Ibe, S. Matsumoto, R. Sato, Mass Splitting between Charged and Neutral Winos at Two-Loop Level, Phys. Lett. B 721 (2013) 252–260. arXiv:1212.5989, doi:10.1016/j.physletb.2013.03.015.

[277] J. McKay, P. Scott, Two-loop mass splittings in electroweak multiplets: winos and minimal dark matter, Phys. Rev. D 97 (5) (2018) 055049. arXiv:1712.00968, doi:10.1103/PhysRevD.97.055049.

[278] https://doi.org/10.5281/zenodo.5747107 (Dec. 2021). doi:10.5281/zenodo.5747107.

[279] M. Aaboud, et al., Search for bottom squark pair production in proton–proton collisions at $\sqrt{s} = 13$ TeV with the ATLAS detector, Eur. Phys. J. C76 (10) (2016) 547. arXiv:1606.08772, doi:10.1140/epjc/s10052-016-4382-4.

[280] M. Aaboud, et al., Search for top squarks in final states with one isolated lepton, jets, and missing transverse momentum in $\sqrt{s} = 13$ TeV $pp$ collisions with the ATLAS detector, Phys. Rev. D94 (5) (2016) 052009. arXiv:1606.03903, doi:10.1103/PhysRevD.94.052009.

[281] M. Aaboud, et al., Search for squarks and gluinos in final states with jets and missing transverse momentum at $\sqrt{s} = 13$ TeV with the ATLAS detector, Eur. Phys. J. C76 (7) (2016) 392. arXiv:1605.03814, doi:10.1140/epjc/s10052-016-4184-8.

[282] G. Aad, et al., Search for supersymmetry at $\sqrt{s} = 13$ TeV in final states with jets and two same-sign leptons or three leptons with the ATLAS detector, Eur. Phys. J. C76 (5) (2016) 259. arXiv:1602.09058, doi:10.1140/epjc/s10052-016-4095-8.

[283] M. Aaboud, et al., Search for squarks and gluinos in final states with jets and missing transverse momentum using 36 fb$^{-1}$ of $\sqrt{s} = 13$ TeV pp collision data with the ATLAS detector, Phys. Rev. D97 (11) (2018) 112001. arXiv:1712.02332, doi:10.1103/PhysRevD.97.112001.

[284] M. Aaboud, et al., Search for supersymmetry in final states with two same-sign or three leptons and jets using 36 fb$^{-1}$ of $\sqrt{s} = 13$ TeV $pp$ collision data with the ATLAS detector, JHEP 09 (2017) 084, [Erratum: JHEP08,121(2019)]. arXiv:1706.03731, doi:10.1007/JHEP09(2017)084,10.1007/JHEP08(2019)121.

[285] M. Aaboud, et al., Search for a scalar partner of the top quark in the jets plus missing transverse momentum final state at $\sqrt{s}$=13 TeV with the ATLAS detector, JHEP 12 (2017) 085. arXiv:1709.04183, doi:10.1007/JHEP12(2017)085.

[286] M. Aaboud, et al., Search for top-squark pair production in final states with one lepton, jets, and missing transverse momentum using 36 fb$^{-1}$ of $\sqrt{s} = 13$ TeV pp collision data with the ATLAS detector, JHEP 06 (2018) 108. arXiv:1711.11520, doi:10.1007/JHEP06(2018)108.

[287] M. Aaboud, et al., Search for direct top squark pair production in final states with two leptons in $\sqrt{s} = 13$ TeV $pp$ collisions with the ATLAS detector, Eur. Phys. J. C77 (12) (2017) 898. arXiv:1708.03247, doi:10.1140/epjc/s10052-017-5445-x.

[288] M. Aaboud, et al., Search for top squarks decaying to tau sleptons in $pp$ collisions at $\sqrt{s} = 13$ TeV with the ATLAS detector, Phys. Rev. D98 (3) (2018) 032008. arXiv:1803.10178, doi:10.1103/PhysRevD.98.032008.

[289] M. Aaboud, et al., Search for electroweak production of supersymmetric particles in final states with two or three leptons at $\sqrt{s} = 13\,\text{TeV}$ with the ATLAS detector, Eur. Phys. J. C78 (12) (2018) 995. arXiv:1803.02762, doi:10.1140/epjc/s10052-018-6423-7.

[290] M. Aaboud, et al., Search for supersymmetry in final states with charm jets and missing transverse momentum in 13 TeV $pp$ collisions with the ATLAS detector, JHEP 09 (2018) 050. arXiv:1805.01649, doi:10.1007/JHEP09(2018)050.

[291] M. Aaboud, et al., Search for photonic signatures of gauge-mediated supersymmetry in 13 TeV $pp$ collisions with the ATLAS detector, Phys. Rev. D97 (9) (2018) 092006. arXiv:1802.03158, doi:10.1103/PhysRevD.97.092006.

[292] M. Aaboud, et al., Search for supersymmetry in events with $b$-tagged jets and missing transverse momentum in $pp$ collisions at $\sqrt{s} = 13$ TeV with the ATLAS detector, JHEP 11 (2017) 195. arXiv:1708.09266, doi:10.1007/JHEP11(2017)195.

[293] M. Aaboud, et al., Search for new phenomena using the invariant mass distribution of same-flavour opposite-sign dilepton pairs in events with missing transverse momentum in $\sqrt{s} = 13$ TeV pp collisions with the ATLAS detector, Eur. Phys. J. C78 (8) (2018) 625. arXiv:1805.11381, doi:10.1140/epjc/s10052-018-6081-9.

[294] M. Aaboud, et al., Search for chargino and neutralino production in final states with a Higgs boson and missing transverse momentum at $\sqrt{s} = 13$ TeV with the ATLAS detector, Phys. Rev. D100 (1) (2019) 012006. arXiv:1812.09432, doi:10.1103/PhysRevD.100.012006.

[295] M. Aaboud, et al., Search for pair production of higgsinos in final states with at least three $b$-tagged jets in $\sqrt{s} = 13$ TeV $pp$ collisions using the ATLAS detector, Phys. Rev. D98 (9) (2018) 092002. arXiv:1806.04030, doi:10.1103/PhysRevD.98.092002.

[296] Search for supersymmetry in events with at least one soft lepton, low jet multiplicity, and missing transverse momentum in proton-proton collisions at $\sqrt{s} = 13$ TeV, Tech. Rep. CMS-PAS-SUS-16-052, https://cds.cern.ch/record/2273394 (2017).

[297] V. Khachatryan, et al., Search for supersymmetry in the all-hadronic final state using top quark tagging in pp collisions at $\sqrt{s} = 13$ TeV, Phys. Rev. D96 (1) (2017) 012004. arXiv:1701.01954, doi:10.1103/PhysRevD.96.012004.

[298] A. M. Sirunyan, et al., Search for the pair production of third-generation squarks with two-body decays to a bottom or charm quark and a neutralino in proton–proton collisions at $\sqrt{s} = 13$ TeV, Phys. Lett. B778 (2018) 263–291. arXiv:1707.07274, doi:10.1016/j.physletb.2018.01.012.

[299] A. M. Sirunyan, et al., Search for supersymmetry in multijet events with missing transverse momentum in proton-proton collisions at 13 TeV, Phys. Rev. D96 (3) (2017) 032003. arXiv:1704.07781, doi:10.1103/PhysRevD.96.032003.

[300] A. M. Sirunyan, et al., Search for new phenomena in final states with two opposite-charge, same-flavor leptons, jets, and missing transverse momentum in pp collisions at $\sqrt{s} = 13$ TeV, JHEP 03 (2018) 076. arXiv:1709.08908, doi:10.1007/s13130-018-7845-2,10.1007/JHEP03(2018)076.

[301] A. M. Sirunyan, et al., Search for physics beyond the standard model in events with two leptons of same sign, missing transverse momentum, and jets in proton–proton collisions at $\sqrt{s} = 13\,\text{TeV}$, Eur. Phys. J. C77 (9) (2017) 578. arXiv:1704.07323, doi:10.1140/epjc/s10052-017-5079-z.

[302] A. M. Sirunyan, et al., Search for Supersymmetry in $pp$ Collisions at $\sqrt{s} = 13$ TeV in the Single-Lepton Final State Using the Sum of Masses of Large-Radius Jets, Phys. Rev. Lett. 119 (15) (2017) 151802. arXiv:1705.04673, doi:10.1103/PhysRevLett.119.151802.

[303] A. M. Sirunyan, et al., Search for electroweak production of charginos and neutralinos in multilepton final states in proton-proton collisions at $\sqrt{s} = 13$ TeV, JHEP 03 (2018) 166. arXiv:1709.05406, doi:10.1007/JHEP03(2018)166.

[304] A. M. Sirunyan, et al., Search for supersymmetry in events with at least three electrons or muons, jets, and missing transverse momentum in proton-proton collisions at $\sqrt{s} = 13$ TeV, JHEP 02 (2018) 067. arXiv:1710.09154, doi:10.1007/JHEP02(2018)067.

[305] A. M. Sirunyan, et al., Search for supersymmetry in events with one lepton and multiple jets exploiting the angular correlation between the lepton and the missing transverse momentum in proton-proton collisions at $\sqrt{s} = 13$ TeV, Phys. Lett. B780 (2018) 384–409. arXiv:1709.09814, doi:10.1016/j.physletb.2018.03.028.

[306] A. M. Sirunyan, et al., Search for electroweak production of charginos and neutralinos in WH events in proton-proton collisions at $\sqrt{s} = 13$ TeV, JHEP 11 (2017) 029. arXiv:1706.09933, doi:10.1007/JHEP11(2017)029.

[307] A. M. Sirunyan, et al., Search for supersymmetry with Higgs boson to diphoton decays using the razor variables at $\sqrt{s} = 13$ TeV, Phys. Lett. B779 (2018) 166–190. arXiv:1709.00384, doi:10.1016/j.physletb.2017.12.069.

[308] A. M. Sirunyan, et al., Search for gauge-mediated supersymmetry in events with at least one photon and missing transverse momentum in pp collisions at $\sqrt{s}$ = 13 TeV, Phys. Lett. B780 (2018) 118–143. arXiv:1711.08008, doi:10.1016/j.physletb.2018.02.045.

[309] A. M. Sirunyan, et al., Search for supersymmetry in events with at least one photon, missing transverse momentum, and large transverse event activity in proton-proton collisions at $\sqrt{s} = 13$ TeV, JHEP 12 (2017) 142. arXiv:1707.06193, doi:10.1007/JHEP12(2017)142.

[310] A. M. Sirunyan, et al., Search for direct production of supersymmetric partners of the top quark in the all-jets final state in proton-proton collisions at $\sqrt{s} = 13$ TeV, JHEP 10 (2017) 005. arXiv:1707.03316, doi:10.1007/JHEP10(2017)005.

[311] A. M. Sirunyan, et al., Search for supersymmetry in proton-proton collisions at 13 TeV using identified top quarks, Phys. Rev. D97 (1) (2018) 012007. arXiv:1710.11188, doi:10.1103/PhysRevD.97.012007.

[312] A. M. Sirunyan, et al., Search for top squark pair production in pp collisions at $\sqrt{s} = 13$ TeV using single lepton events, JHEP 10 (2017) 019. arXiv:1706.04402, doi:10.1007/JHEP10(2017)019.

[313] A. M. Sirunyan, et al., Search for top squarks and dark matter particles in opposite-charge dilepton final states at $\sqrt{s}$ = 13 TeV, Phys. Rev. D97 (3) (2018) 032009. arXiv:1711.00752, doi:10.1103/PhysRevD.97.032009.

[314] A. M. Sirunyan, et al., Search for supersymmetry in events with a $\tau$ lepton pair and missing transverse momentum in proton-proton collisions at $\sqrt{s}$ = 13 TeV, JHEP 11 (2018) 151. arXiv:1807.02048, doi:10.1007/JHEP11(2018)151.

[315] A. M. Sirunyan, et al., Search for top squarks decaying via four-body or chargino-mediated modes in single-lepton final states in proton-proton collisions at $\sqrt{s} = 13$ TeV, JHEP 09 (2018) 065. arXiv:1805.05784, doi:10.1007/JHEP09(2018)065.

[316] A. M. Sirunyan, et al., Search for Physics Beyond the Standard Model in Events with High-Momentum Higgs Bosons and Missing Transverse Momentum in Proton-Proton Collisions at 13 TeV, Phys. Rev. Lett. 120 (24) (2018) 241801. arXiv:1712.08501, doi:10.1103/PhysRevLett.120.241801.

[317] A. M. Sirunyan, et al., Search for supersymmetric partners of electrons and muons in proton-proton collisions at $\sqrt{s}$ = 13 TeV, Phys. Lett. B790 (2019) 140–166. arXiv:1806.05264, doi:10.1016/j.physletb.2019.01.005.

[318] A. M. Sirunyan, et al., Searches for pair production of charginos and top squarks in final states with two oppositely charged leptons in proton-proton collisions at $\sqrt{s} = 13$ TeV, JHEP 11 (2018) 079. arXiv:1807.07799, doi:10.1007/JHEP11(2018)079.

[319] A. M. Sirunyan, et al., Search for supersymmetry in events with a photon, jets, b -jets, and missing transverse momentum in proton–proton collisions at 13 TeV, Eur. Phys. J. C79 (5) (2019) 444. arXiv:1901.06726, doi:10.1140/epjc/s10052-019-6926-x.

[320] A. M. Sirunyan, et al., Search for supersymmetry in proton-proton collisions at 13 TeV in final states with jets and missing transverse momentum, JHEP 10 (2019) 244. arXiv:1908.04722, doi:10.1007/JHEP10(2019)244.

[321] A. M. Sirunyan, et al., Search for direct top squark pair production in events with one lepton, jets, and missing transverse momentum at 13 TeV with the CMS experiment, JHEP 05 (2020) 032. arXiv:1912.08887, doi:10.1007/JHEP05(2020)032.

# Acronyms

**2HDM** two Higgs doublet models. 23

**ADL** analysis description language. 39

**ALICE** A Large Ion Collider. 25, 26, 37, 140

**ATLAS** A Toroïdal LHC Apparatus. 6, 25–31, 33–35, 38, 41, 46–49, 51, 55–60, 67, 69–72, 74, 75, 77, 83, 85, 86, 89, 91, 92, 94–97, 99, 100, 117, 123–125, 127, 129, 140–143, 145, 173

**BSM** beyond the Standard Model. 5, 6, 11–13, 29–37, 40, 41, 43, 44, 48, 49, 52, 72, 73, 77–84, 99, 101, 123, 124, 130, 142, 173

**ΛCDM** standard cosmological model. 102–104

**CERN** European organization for nuclear research. 25, 139

**CKM** Cabbibo-Kobayashi-Maskawa. 10

**CL** confidence level. 35, 40, 42, 44, 52

**CMB** cosmic microwave background. 13, 14, 102

**CMS** Compact Muon Solenoid. 6, 25–30, 33, 34, 38, 41, 45, 48, 49, 54–56, 61–64, 67, 69, 70, 74, 85, 86, 89, 92, 95–97, 99, 100, 117, 123, 124, 128, 140–142, 173

**cMSSM** constrained MSSM. 34

**CP** charge-parity. 5, 11, 14, 19, 26, 105

**CR** control region. 52

**CRs** control regions. 33, 52, 59, 73

**DGLAP** Dokshitzer–Gribov–Lipatov–Altarelli–Parisi. 37

**DIS** deep inelastic scattering. 37

**DM** dark matter. 4–6, 13–16, 20, 23, 24, 30–32, 40, 77, 86–88, 91, 92, 94, 95, 98–112, 114–125, 134, 136, 173

**ECAL** Electromagnetic calorimeter. 26–28

**ECALs** Electromagnetic calorimeters. 27

**EM** efficiency map. 40, 42, 83, 85, 86, 90, 91, 94, 130

**EMs** efficiency maps. 35, 36, 40, 42, 83, 85, 86, 89–91, 93, 124, 129–131

**EW-ino** electroweakino. 143

**EWSB** electroweak symmetry breaking. 8

**FIMPs** feebly interacting massive particles. 108, 125

**FLRW** Friedmann-Lemaître-Robertson-Walker. 102, 104

**GR** general relativity. 102

**HCAL** Hadronic calorimeter. 27, 28, 32, 33

**HepMC** high energy physics Monte Carlo. 37, 39

**HLT** high-level trigger. 29

**HSCP** heavy stable charged particles. 32, 33, 77, 78, 84, 87–93, 100, 124, 129–131, 142, 143

**IDM** inert doublet model. 23, 87

**ISR** initial state radiation. 31, 32

**LH** left-handed. 8, 10, 19

**LHC** Large Hadron Collider. 4–6, 16, 19, 24–26, 29–39, 42, 43, 45, 48, 66, 70, 77, 78, 86, 87, 92, 95, 98–101, 109, 111, 112, 116, 117, 119, 120, 122–125, 138–142, 144, 145, 173

**LHCb** LHC beauty. 13, 26, 140

**LHE** Les Houches Event file format. 37

**LLP** long-lived particle. 6, 32, 33, 39, 77, 78, 85, 88, 89, 95, 99, 124

**LLPs** long-lived particles. 6, 32, 33, 77, 83, 89, 90, 99, 100, 142

**LO** Leading-order. 56

**LSP** lightest stable particle. 16, 30–32, 41

**MACHOs** massive compact halo objects. 14

**MS** Modèle Standard. 138–140, 144, 173

**MSSM** minimal supersymmetric Standard Model. 12, 15–19, 48, 50, 65, 66, 69, 117, 124, 132, 141

**NLSP** next-to-lightest supersymmetric particle. 32

**PDF** parton distribution function. 37

**PDFs** parton distribution functions. 36, 37

**pMSSM** phenomenological MSSM. 19, 34

**PS** Proton Synchrotron. 25

**PSB** Proton Synchrotron Booster. 25

**QCD** quantum chromodynamics. 11, 36

**QED** quantum electrodynamics. 12, 13

**QFT** quantum field theory. 10

**QGP** quark-gluon plasma. 26

**RH** right-handed. 10, 19, 23, 24

**SHGs** Showering and hadronization generators. 37

**SM** Standard Model. 4, 5, 7–19, 23, 24, 28–36, 38, 41, 43–47, 103–108, 123, 125, 173

**SPS** Super Proton Synchrotron. 25

**SR** signal region. 6, 33, 38–40, 42, 44, 45, 49, 50, 53–62, 64, 68–70, 74, 77, 94, 123, 124, 141, 142, 173

**SRs** signal regions. 5, 6, 33, 36, 38, 42, 44–50, 52–56, 58, 59, 61–64, 66, 67, 69, 72, 74, 94, 123, 138, 141–143, 173

**SUSY** supersymmetry. 5, 15–17, 30, 32–34, 40, 49, 77, 107, 124, 125

**UL** upper limit. 36, 40, 42, 83, 85, 86, 91

**ULs** upper limits. 35, 83, 91

**VR** validation region. 52

**VRs** validation regions. 33, 73

**WIMP** weakly interacting massive particle. 14, 98, 103, 106, 107, 173

**WIMPs** weakly interacting massive particles. 14, 106, 109, 125, 173

**Abstract.** The Standard Model (SM) of particle physics is one of the most successful theories in science. Indeed, numerous SM predictions have been observed to be consistent with experimental measurements. However, some caveats hint at the incompleteness of the SM and push physicists to search for new physics. The ATLAS and CMS collaborations are carrying out an extensive and exciting physics program at the LHC. Searches for new physics constitute a relevant part of this program. Simplified models are used to characterize the potential new physics signal. Reinterpreting the LHC results in more realistic scenarios than the simplified models is crucial to use most of the physics sensitivity of the data. The work of this thesis focused on two aspects of reinterpretation, the improvement of reinterpretation tools and the phenomenology of models beyond the Standard Model (BSM). The statistical combination of signal regions (SRs) allows using more of the physics sensitivity of the experimental data in public tools. This thesis participated in the implementation of this feature in MadAnalysis5 and SModelS. Part of the focus was also given to phenomenological studies to demonstrate the impact of SR combination. Explaining the nature of dark matter (DM) is another area where the SM fails. Although many hypothetical particles with different properties are good DM candidates, the way they are produced in the early Universe can be classified into a few main mechanisms. The standard WIMP picture is based on the freeze-out mechanism, which is based on several assumptions that are valid in general cases. However, these assumptions can be broken for some scenarios, leading to exceptions to the standard WIMP picture. The DM portion of this thesis focused on a recently proposed mechanism, which is the conversion-driven freeze-out mechanism.

**Résumé.** Le Modèle Standard (MS) de la physique des particules est l'une des théories les plus réussies de la science. En effet, de nombreuses prédictions du MS se sont révélées cohérentes avec les mesures expérimentales. Cependant, certaines exceptions laissent entrevoir l'incomplétude du SM et poussent les physiciens à rechercher une nouvelle physique. Les collaborations ATLAS et CMS mènent un vaste et passionnant programme de physique au LHC. La recherche d'une nouvelle physique constitue une partie importante de ce programme. Des modèles simplifiés sont utilisés pour caractériser les potentiels signaux d'une nouvelle physique. La réinterprétation des résultats du LHC dans des scénarios plus réalistes que les modèles simplifiés est cruciale afin d'utiliser au mieux le potentiel des données expérimentales. Le travail de cette thèse s'est concentré sur deux aspects de la réinterprétation, l'amélioration des outils de réinterprétation et la phénoménologie au-delà du Modèle Standard (BSM). La combinaison statistique des "signal regions (SRs)" permet d'utiliser davantage la sensibilité physique des données expérimentales dans les outils publics. Cette thèse a participé à l'implémentation de cette fonctionnalité dans MadAnalysis5 et SModelS. Une partie de l'attention a également été accordée aux études phénoménologiques afin de démontrer l'impact de la combinaison de SRs. Expliquer la nature de la matière noire est un autre domaine où le MS échoue. Bien que de nombreuses particules hypothétiques ayant des propriétés différentes soient de bons candidats pour la matière noire, la façon dont elles sont produites dans l'Univers primitif peut être classée en quelques mécanismes principaux. Le paradigme standard des WIMPs est basé sur le mécanisme de "freeze-out", qui repose sur plusieurs hypothèses valables dans les cas les plus généraux. La partie "matière noire" de cette thèse s'est concentrée sur un mécanisme récemment proposé, qui est le mécanisme de freeze-out par conversion, ou "coscattering".